



PLASMONIQUE MOLÉCULAIRE : SPECTROSCOPIE SUR SURFACE MÉTALLIQUE ET MATÉRIAUX HYBRIDES POUR LA PHOTONIQUE INTÉGRÉE

Gérard Colas Des Francs

► To cite this version:

Gérard Colas Des Francs. PLASMONIQUE MOLÉCULAIRE : SPECTROSCOPIE SUR SURFACE MÉTALLIQUE ET MATÉRIAUX HYBRIDES POUR LA PHOTONIQUE INTÉGRÉE. Physique [physics]. Université de Bourgogne, 2009. tel-00437161

HAL Id: tel-00437161

<https://theses.hal.science/tel-00437161>

Submitted on 29 Nov 2009

HAL is a multi-disciplinary open access archive for the deposit and dissemination of scientific research documents, whether they are published or not. The documents may come from teaching and research institutions in France or abroad, or from public or private research centers.

L'archive ouverte pluridisciplinaire **HAL**, est destinée au dépôt et à la diffusion de documents scientifiques de niveau recherche, publiés ou non, émanant des établissements d'enseignement et de recherche français ou étrangers, des laboratoires publics ou privés.

HABILITATION À DIRIGER DES RECHERCHES

**PLASMONIQUE MOLÉCULAIRE :
SPECTROSCOPIE SUR SURFACE MÉTALLIQUE
ET MATÉRIAUX HYBRIDES POUR LA PHOTONIQUE INTÉGRÉE**

GÉRARD COLAS DES FRANCS

Chargé de Recherches au CNRS
Institut Carnot de Bourgogne
(UMR 5209 CNRS - Université de Bourgogne)

Soutenue le 16 novembre 2009, à l'Université de Bourgogne

Devant le jury composé de

MM. Rémi CARMINATI	Rapporteur
Gérald DUJARDIN	
Guy MILLOT	Rapporteur
Philippe TAMARAT	Rapporteur
Jean-Claude WEEBER	

Table des matières

I Dossier administratif	5
Curriculum vitae	7
Encadrement de travaux de recherches	9
Animation et management de la recherche	11
Liste de travaux	13
II Projet de recherche : Plasmonique moléculaire	23
Introduction : parcours scientifique	25
1 Plasmons : définition et applications	27
1.1 Plasmon de volume	27
1.1.1 Plasma et modèle de Drude	27
1.1.2 Propagation d'une onde électromagnétique dans un plasma	28
1.2 Plasmon-polaritons de surface	29
1.2.1 Mode délocalisé	29
1.2.2 Modes localisés	30
1.3 Plasmonique moléculaire	31
1.3.1 Capteurs chimiques et biologiques	31
1.3.2 Thérapie anti-cancéreuse	32
1.3.3 Exaltation de courants photo-induits	32
1.3.4 Composants pour la photonique intégrée	32
2 Microscopie et spectroscopie optiques en champ proche	33
2.1 Fluorescence haute résolution dans une jonction pointe-surface	34
2.1.1 Sonde à ouverture triangulaire	34
2.1.2 Fluorescence de molécules individuelles	43
2.2 Modèle du dipole effectif	55
2.3 Equations de Bloch optiques en champ proche	65
2.4 Conclusion	73

3 Relaxation moléculaire par couplage aux plasmons	75
3.1 Règle d'or de Fermi	76
3.2 Imagerie de durée de vie de fluorescence (FLIM)	77
3.3 Transfert d'énergie en champ proche	89
3.4 Conclusion	105
4 Composants plasmoniques pour la photonique intégrée	107
4.1 Guide plasmonique confiné par un ruban diélectrique	108
4.2 Gain optique	121
4.3 Modélisation de la résonance	133
4.4 Conclusion	151
Conclusion et perspectives de recherches	153
III Annexes - Reproductions d'articles	163

Première partie

Dossier administratif

Curriculum vitae

Gérard COLAS DES FRANCS

Nationalité française

Né le 4 juillet 1973 à l'Union (31)

Marié, 2 enfants

ICB - Département Nanosciences
9, av. Savary, BP 47870
21078 Dijon Cedex
Tél : 03 80 39 90 67
Mél : gerard.colas-des-francs
@u-bourgogne.fr

Expérience professionnelle

Recherche

- depuis 2004 **Chargé de recherches** au CNRS (section 04), affecté à l'ICB,
équipe *Optique Submicronique et Nanocapteurs*
- 2002 - 2003 Séjour **post-doctoral** à l'Université de Münster (Allemagne, **bourse Marie Curie**)
Excitation localisée de films moléculaires dans une jonction pointe-surface

Enseignement et diffusion de la culture scientifique

- depuis 2008 Cours à l'ESEO Dijon (électrochimie L1 ou électromagnétisme L2 - 60h/an)
- 2003 - 2008 Interrogations de chimie en CPGE au lycée Carnot (L1 ou L2 - 70h/an)
- 2003 - 2004 **Professeur agrégé** au lycée Carnot, Dijon (2^{nde} et 1^{ère}S)
- 1999 - 2002 **Moniteur** à l'université Toulouse III (TP en DEUG - 96h/an)
- 2007 - 2008 Intervenant en classe de CM2 (programme **la main à la pâte**)

Formation et titres universitaires

- 2002 **doctorat** de l'Université de Toulouse III (directeur : C. Girard)
thèse soutenue le 3 octobre 2002, mention très honorable
Optique sublongueur d'onde et fluorescence moléculaire perturbée
- 1994 - 1999 Elève de l'**Ecole Normale Supérieure de Cachan**
Magistère de physico-chimie de l'université Paris XI
- 1997 **Aggrégation** de sciences-physiques, option chimie (47ème)

Encadrement de travaux de recherches

Accueil de post-doctorant

- Aurélien BRUYANT (2005-2006, financé par le projet européen ASPRINT) s'est occupé de la caractérisation expérimentale de pointes champ proche optique. Depuis septembre 2006, Aurélien Bruyant est maître de conférences à l'Université de Troyes.
- Guillaume LEGAY (2006-2007, financé à 50% par le projet européen ASPRINT) a réalisé des échantillons par lithographies de faisceau d'électrons pour les projets ASPRINT (sous ma direction) et PND (sous la direction de Alexandre Bouhelier). Il est ingénieur au CEA de Valduc depuis avril 2007.
- Sébastien MASSENOT (2007-2009, financé par le projet européen PLASMOCOM) a développé un code de simulations numériques pour la modélisation de guides plasmoniques. Il est maître de conférences à l'Ecole Supérieure d'Aréonautique de Toulouse depuis mars 2009.

Co-encadrement de thèses

- Jonathan GRANDIDIER (Fév. 07-déc. 09, financement projet européen PLASMOCOM, taux d'encadrement : 70 %)

Titre : "Guides plasmoniques hybrides : composants passifs et actifs pour la photonique intégrée".

Ce travail comporte à parts égales des réalisations expérimentales et des simulations numériques. Il s'agit de l'étude de guides plasmoniques formés de rubans de polymères déposés sur des films métalliques. Le dopage du polymère permet de réaliser des fonctions optiques. Récemment, Jonathan a réalisé une configuration type amplificateur optique en dopant le polymère avec des boîtes quantiques de PbS (émission vers $1,5 \mu\text{m}$). D'où une compensation partielle des pertes du plasmon lors de sa propagation (voir le chapitre 4).

La soutenance de thèse est prévue le 10 décembre 2009.

Jonathan Grandidier part ensuite en post-doctorat dans le groupe de Harry Atwater (Caltech, USA).

- Pierre BRAMANT (octobre 2008 -, bourse ministérielle, taux d'encadrement : 50 %)
Sujet : "Couplage de molécules fluorescentes avec des nanoparticules métalliques"
Il s'agit d'un travail principalement expérimental.

Animation et management de la recherche

Gestion de la recherche

- **2004-2007** : ASPRINT ("Advanced Scanning PRobes for Innovative Nanoscience and Technology", STREP européen, coordinateur Prof. Speller, Univ. Nijmegen)
Porteur local et co-animateur d'un axe du projet (WP2 : Nano optical probing) avec Alain Dereux. Collaboration avec Niek van Hulst (ICFO, Barcelone) et Ulrich Fischer (Univ. Münster).
- **2004-2008** : PND ("PlasmoNanoDevices", NoE européen, coordinateur Prof. Dereux, Univ. Bourgogne)
Collaboration avec Christian Girard (CEMES, Toulouse), Ulrich Fischer (Univ. Münster) et Niek van Hulst (ICFO, Barcelone).
- **2007-2010** : PLASMOCOM ("Polymer based nanoplasmonics components and devices", STREP européen, coordinateur Prof. Zayats, Univ. Belfast)
Porteur local avec Alain Dereux. Collaboration avec Sergey Bozhevolnyi (Univ. Aalborg) et Romain Quidant (ICFO, Barcelone).
- **2007-2010** : ANTARES - ("Arrangement of Nano Tunable Amplified REproducible Spot-light", ANR PNANO, coordinateur Prof. Finot, Univ. Bourgogne)
- **2009-2013** : PlasTips ("Plasmonics Tips for Near Field Optics, ANR Blanc)
Coordinateur. Collaboration avec Aurélien Drezet (Institut Néel, Grenoble) et Erik Du-jardin (CEMES, Toulouse).

J'anime le groupe de travail *modélisation* du réseau européen "COST plasmonic components and devices" coordonné par Olivier Marin (EPFL, Suisse, 2008-2012).
Par ailleurs, j'évalue régulièrement des projets de recherche pour d'autres Universités.

Organisation de conférences et workshops

J'ai organisé deux événements sur la période 2004-2009 :

- **SPP3** : Troisième *conférence internationale* Surface Plasmon Photonics, du 17 au 22 juin 2007 à l'Université de Dijon. 320 personnes ont participé à cette conférence au cours de laquelle il y a eu 10 conférences invitées, 100 conférences et environ 150 posters. Coor-

ganisateur avec Alain Dereux.

- **ASPRINT** : Organisation d'un *workshop avec mini-colloque* du projet européen AS-PRINT les 24 et 25 octobre 2005, Dijon, réunissant une trentaine de personnes dont 6 conférenciers invités extérieurs au projet.

D'autre part, je faisais partie du comité local d'organisation de COLOQ9 (9ème colloque sur les lasers et l'optique quantique), organisé par le professeur Guy Millot (Université de Bourgogne), qui s'est tenu à Dijon du 7 au 9 septembre 2005.

Participation à des comités de lecture

Je suis rapporteur pour

- Applied Physics Letters
- Journal of Microscopy
- The Journal of Physical Chemistry
- Optics Express
- Research Letters in Physics.

Liste de travaux

Revues à comité de lecture : 37 titres

Journal	Nombre d'articles
Physical Review Letters	3
Nano Letters	4
Applied Physics Letters	2
Physical Review A	1
Physical Review B	6
Physical Review E	3
Optics Letters	2
Optics Express	3
Journal of Chemical Physics	3
Chemical Physics Letters	2
Europhysics Letters	1
Autres journaux	7
Total	37

TAB. 1 – Répartition des publications de G. Colas des Francs

- (A1) Tuning of an optical dimer nano-antenna by electrically controlling its local impedance
J. Berthelot, A. Bouhelier, C. Huang, J. Margueritat, G. Colas des Francs, E. Finot, J.-C. Weeber, A. Dereux, S. Kostcheev, H. I. E. Ahrach, A.-L. Baudrion, J. Plain, R. Bachelot, P. Royer, and G. Wiederrecht, accepté pour publication (2009).
- (A2) Integrated plasmonic waveguides : a mode solver based on density of states (DOS) formulation
G. Colas des Francs, J. Grandidier, S. Massenot, A. Bouhelier, J. Weeber, and A. Dereux, accepté pour publication (2009).
- (A3) Molecule non–radiative coupling to a metallic nanosphere : an optical theorem treatment
G. Colas des Francs, International Journal of Molecular Science, **10**, pp. 3931–3936 (2009).

- (A4) Gain assisted propagation in a plasmonic nanowire at telecom wavelength
 J. Grandidier, G. Colas des Francs, S. Massenot, A. Bouhelier, L. Markey, J. Weeber, C. Finot, and A. Dereux, *Nano Letters* **9**, pp. 2935–2939 (2009).
- (A5) The single molecule probe : nanoscale vectorial mapping of photonic mode density in a metal nanocavity
 J. P. Hoogenboom, G. Sanchez-Mosteiro, G. Colas des Francs, D. Heinis, G. Legay, A. Dereux, and N. F. van Hulst, *Nano Letters* **9**, pp. 1189–1195 (2009).
- (A6) Dielectric-loaded surface plasmon polariton waveguides : figures of merit and mode characterization by image and Fourier plane leakage microscopy
 J. Grandidier, S. Massenot, G. Colas des Francs, A. Bouhelier, J.-C. Weeber, L. Markey, A. Dereux, J. Renger, M. U. González, and R. Quidant, *Physical Review B* **78**, p. 245419 (2008).
- (A7) Fluorescence relaxation in the near-field of a mesoscopic metallic particle : distance dependence and role of plasmon modes
G. Colas des Francs, A. Bouhelier, E. Finot, J.-C. Weeber, A. Dereux, C. Girard, and E. Dujardin, *Optics Express* **16**, pp. 17654– 17666 (2008).
- (A8) Differential method for modelling dielectric-loaded surface plasmon polariton waveguides
 S. Massenot, J.-C. Weeber, A. Bouhelier, G. Colas des Francs, J. Grandidier, L. Markey, and A. Dereux, *Optics Express* **16**, pp. 17599–17608 (2008).
- (A9) Gain, detuning and directivity of nanoparticles optical antennas
 C. Huang, A. Bouhelier, G. Colas des Francs, A. Bruyant, A. Guénot, E. Finot, J.-C. Weeber, and A. Dereux, *Physical Review B* **78**, p. 155407 (2008).
- (A10) Molecular quenching and relaxation in a plasmonic tunable nanogap
 G. Baffou, C. Girard, E. Dujardin, G. Colas des Francs, and O. Martin, *Physical Review B* **77**, p. 121101(R) (2008).
- (A11) Far-field imaging of the electromagnetic local density of optical states
 C. Huang, A. Bouhelier, G. Colas des Francs, G. Legay, J.-C. Weeber, and A. Dereux, *Optics Letters* **33**, pp. 300–302 (2008).
- (A12) Theory of molecular excitation and relaxation near a plasmonic device
G. Colas des Francs, C. Girard, T. Laroche, G. Lévéque, O. Martin, and A. Dereux, *Journal of Chemical Physics* **127**, p. 34701 (2007).
- (A13) Polymer-metal waveguides characterization by Fourier plane leakage radiation microscopy
 S. Massenot, J. Grandidier, A. Bouhelier, G. Colas des Francs, J.-C. Weeber, L. Markey,

and A. Dereux, Applied Physics Letters **91**, p. 243101 (2007).

- (A14) Surface plasmon hopping along coupled coplanar cavities
J.-C. Weeber, A. Bouhelier, G. Colas des Francs, S. Massenot, J. Grandidier, L. Markey, and A. Dereux, Physical Review B **76**, p. 113405 (2007).
- (A15) Surface plasmon interference excited by tightly focused laser beams
A. Bouhelier, F. Ignatovitch, A. Bruyant, C. Huang, G. Colas des Francs, J.-C. Weeber, A. Dereux, G. Wiederrecht, and L. Novotny, Optics Letters **32**, p. 2535 (2007).
- (A16) Submicrometer In-Plane Integrated Surface Plasmon Cavities
J.-C. Weeber, A. Bouhelier, G. Colas des Francs, L. Markey, and A. Dereux, Nanoletters **7**, p. 1352 (2007).
- (A17) Efficient surface plasmon field confinement in one dimensional crystal line-defect waveguides
J.-C. Weeber, A. Baudrion, A. Bouhelier, A. Bruyant, G. Colas des Francs, R. Zia, and A. Dereux, Applied Physics Letters **89**, p. 211109 (2006).
- (A18) Transmission of an obliquely incident beam of light through small apertures in a metal film
E. Bortchagovsky, G. Colas des Francs, D. Molenda, A. Naber, and U. Fischer, Applied Physics B **84**, p. 49 (2006).
- (A19) Generalized Bloch equations for optical interactions in confined geometries
C. Girard, O. Martin, G. Lévêque, G. Colas des Francs, and A. Dereux, Chemical Physics Letters **404**, p. 44 (2005).
- (A20) Enhanced light confinement in a triangular aperture : Experimental evidence and numerical calculations
G. Colas des Francs, D. Molenda, U. Fischer, and A. Naber, Physical Review B **72**, p. 165111 (2005).
- (A21) Energy transfer in near-field optics
G. Colas des Francs, C. Girard, M. Juan, and A. Dereux, Journal of Chemical Physics **123**, p. 174709 (2005).
- (A22) High-resolution mapping of the optical near-field components at a triangular nano-aperture
D. Molenda, G. Colas des Francs, U. Fischer, N. Rau, and A. Naber, Optics Express **13**, p. 10688 (2005).

Publications relatives aux travaux doctoraux

- (A23) Modelling resonant coupling between microring resonators addressed by optical evanescent waves
G. Lévéque, R. Mathevet, J. Weiner, G. Colas des Francs, C. Girard, R. Quidant, J.-C. Weeber, and A. Dereux, Nanotechnology **15**, pp. 1200–1210 (2004).
- (A24) Reply, Imaging the Local Density of States of Optical Corrals
C. Chicanne, T. David, R. Quidant, J.-C. Weeber, Y. Lacroute, E. Bourillot, A. Dereux, G. Colas des Francs, and C. Girard, Physical Review Letters **93**, p. 69702 (2004).
- (A25) Imaging surface photonic states with a circularly polarized tip
C. Girard, T. David, C. Chicanne, A. Mary, G. Colas des Francs, E. Bourillot, J.-C. Weeber, and A. Dereux, Europhysics Letters **68**, pp. 797–803 (2004).
- (A26) Fluorescent Resonant Energy Transfer in the Optical Near-Field,
G. Colas des Francs, C. Girard, and O. Martin, Physical Review A **67**, p. 53805 (2003).
- (A27) Subwavelength mapping of surface photonic states
A. Dereux, C. Girard, C. Chicanne, G. Colas des Francs, T. David, Y. Lacroute, and J.-C. Weeber, Nanotechnology **14**, p. 935 (2003).
- (A28) Polarization state of the optical near-field
G. Lévéque, G. Colas des Francs, C. Girard, J.-C. Weeber, C. Meier, C. Robilliard, R. Mathevet, and J. Weiner, Physical Review E **65**, p. 36701 (2002).
- (A29) Imaging the Local Density of States of Optical Corrals (Article commenté dans "news and views", Nature 416 du 21 mars 2002).
C. Chicanne, T. David, R. Quidant, J.-C. Weeber, Y. Lacroute, E. Bourillot, A. Dereux, G. Colas des Francs, and C. Girard, Physical Review Letters **88**, p. 97402 (2002).
- (A30) Subwavelength Optical Devices for Nanometer Scale Applications
C. Girard, A. Dereux, R. Quidant, G. Colas des Francs, and J.-C. Weeber, International Journal of Nanoscience **1**, pp. 63–78 (2002).
- (A31) Theory of near-field optical imaging with a single molecule as a light source
G. Colas des Francs, C. Girard, and A. Dereux, Journal of Chemical Physics **117**, pp. 4659–4666 (2002).
- (A32) Theory of near-field optical imaging with a single fluorescent molecule used as point-like detector
G. Colas des Francs and C. Girard, Chemical Physics **282**, pp. 277–287 (2002).

- (A33) Coplanar devices for the optical addressing of single molecules
G. Colas des Francs and C. Girard, Nanotechnology **12**, pp. 75–79 (2001).
- (A34) Optical Analogy to Electronic Quantum Corrals (Article commenté dans le Physical Review Focus du 22 mai 2001)
G. Colas des Francs, C. Girard, J.-C. Weeber, C. Chicanne, T. David, A. Dereux, and D. Peyrade, Physical Review Letters **86**, pp. 4950–4953 (2001).
- (A35) Addressing and imaging high optical index dielectric ridges in the optical near field
R. Quidant, J.-C. Weeber, A. Dereux, D. Peyrade, G. Colas des Francs, C. Girard, and Y. Chen, Physical Review E **64**, p. 66607 (2001).
- (A36) Relationship between scanning near-field optical images and local density of photonic states
G. Colas des Francs, C. Girard, J.-C. Weeber, and A. Dereux, Chemical Physics Letters **345**, pp. 512–516 (2001).
- (A37) Optical addressing at the subwavelength scale
J.-C. Weeber, A. Dereux, C. Girard, G. Colas des Francs, J. Krenn, and J. Goudonnet, Physical Review E **62**, pp. 7381–7388 (2000).

Actes de conférences à comité de lecture : 6 titres

- (AC1) SNOM signal near plasmonic nanostructures : an analogy with fluorescence decay channels
G. Colas des Francs, C. Girard, A. Bruyant, and A. Dereux, Journal of Microscopy (NFO9) **229**, pp. 302–306 (2008).
- (AC2) Single molecules probe local density of modes (LDOS) around photonic nanostructures
G. Colas des Francs, G. Sanchez-Mosteiro, M. Ujue-Gonzalez, L. Markey, N. van Hulst, and A. Dereux, Journal of Microscopy (NFO9) **229**, pp. 210–216 (2008).
- (AC3) On the optimum form of an aperture for a confinement of optically excited electric near-field
E. Bortchagovsky, G. Colas des Francs, D. Molenda, A. Naber, and U. Fischer, Journal of Microscopy (NFO9) **229**, p. 223 (2008).
- (AC4) Cartographie de la densité locale d'états photoniques de surface (résumé)
G. Colas des Francs, C. Girard, T. David, and A. Dereux, in *9^{eme} colloque sur les lasers et l'optique quantique (COLOQ9)* Dijon, 7-9 septembre, 2005.

- (AC5) Near-field optical addressing of single molecules in coplanar geometry : a theoretical study
G. Colas des Francs, C. Girard, J.-C. Weeber, and A. Dereux, Journal of Microscopy **202**, pp. 307–312 (2001).
- (AC6) Near-field optical probing of two-dimensional photonic crystals : theory and experiment
D. Mulin, C. Girard, G. Colas des Francs, M. Spajer, and D. Courjon, Journal of Microscopy **202**, pp. 110–116 (2001).

Conférences et séminaires invités : 6 titres

- (Inv1) Gain assisted propagation in a quantum dots doped plasmonic waveguide (invited conf.)
G. Colas des Francs, in SPIE, San Diego (U.S.A) August, 2009.
- (Inv2) Quantum emitter coupling to a plasmonic nanoparticle : models and numerical simulations (*Invited lecture*)
G. Colas des Francs, in HERODOT, Lille (France) 10-11 juin, 2009.
- (Inv3) Plasmonique moléculaire : modélisation et simulation numérique (conf. invitée)
G. Colas des Francs, in Forum des microscopies à sonde locale, Hardelot, France, 16-20 avril, 2009.
- (Inv4) Plasmonique moléculaire : matériaux hybrides pour la photonique intégrée (séminaire invitée)
G. Colas des Francs, in Institut Néel, Grenoble (France), 3 novembre, 2008.
- (Inv5) L'optique sub-longueur et ses applications en nanosciences (conf. invitée)
G. Colas des Francs and C. Girard, in Séminaire D. Dautreppe, Société Française de Physique, Grenoble, France, 22-26 Mars, 2001.
- (Inv6) Optical addressing and imaging with a single molecule (invited seminar)
G. Colas des Francs and C. Girard, in Research Conference within the EU projects "Bottom Up Nanomachines" and "Nanomol", Aspet, France, 3-6 Mai, 2001.

Actes de colloques sans comité : 6 titres

- (Proc1) Vers une nouvelle génération de microprocesseurs
G. Colas des Francs, in ICB News, 2009.

- (Proc2) Etude et caractérisation expérimentale de plasmons de surface confinés par des guides d'ondes diélectriques
 S. Massenot, J. Grandidier, A. Bouhelier, G. Colas des Francs, J.-C. Weeber, L. Markey, A. Dereux, in Journées Nationales de l'Optique Guidée (JNOG), 2008.
- (Proc3) Surface plasmon routing in dielectric-loaded surface plasmon polariton waveguides
 J. Grandidier, S. Massenot, A. Bouhelier, G. Colas des Francs, J.-C. Weeber, L. Markey and A. Dereux, in Proc. SPIE 7033, 70330S, 2008.
- (Proc4) Measuring the differential scattering cross-section* of gold nanoparticles
 C. Huang, A. Bouhelier, G. Colas des Francs, J.-C. Weeber, and A. Dereux, in Proc. SPIE 7032, 70321E, 2008.
- (Proc5) Single molecule imaging using a highly confined optical field at a triangular aperture
 D. Molenda, U. Fischer, G. Colas des Francs, and A. Naber, in Quantum Electronics and Laser Science Conference QELS (22-27 May 2005) Vol. 1, 368, 2005.
- (Proc6) Theory of near-field optical imaging with a single molecule as a light source
G. Colas des Francs, C. Girard, and A. Dereux, in Spring School on Single Molecules in Physics, Chemistry and Biology, Hofgeismar, Allemagne, 8-12 avril, 2002.

Communications orales dans des conférences : 8 titres

- (O1) La molécule unique comme sonde locale de la densité de modes électromagnétiques
 J. Hoogenboom, G. Colas des Francs, A. Dereux, and N. van Hulst, in Forum des microscopies à sonde locale, Hardelot, France, 16-20 avril, 2009.
- (O2) Fluorescence decay rate near a mesoscopic metallic particle : role of plasmon modes and distance dependence
G. Colas des Francs, in 10th International conference on near-field optics, nanophotonics and related techniques (NFO10), Buenos Aires (Argentine) 1-5 september, 2008.
- (O3) Couplage d'une molécule unique avec une nanoparticule métallique : contributions des modes plasmons
G. Colas des Francs, in Conférence C'NANO Grand-Est, 28-29 mai, 2008.
- (O4) Single-molecule emission control by coupling to photonic cavities
 G. Sanchez-Mosteiro, J.P. Hoogenboom, D. Heinis, G. Colas des Francs, A. Dereux, and N. van Hulst, in 3rd international conference on Surface Plasmon Photonics (SPP3), Dijon (France), 17-22 june, 2007.
- (O5) Molecular relaxation near complex plasmonic devices : radiative and non-radiative channels

C. Girard, E. Dujardin, and G. Colas des Francs, in 3rd international conference on Surface Plasmon Photonics (SPP3), Dijon (France) 17-22 june, 2007.

- (O6) SNOM signal near plasmonic nanostructures : an analogy with fluorescence decay channels
G. Colas des Francs, C. Girard, A. Bruyant, A. Bouhelier, and A. Dereux, in 9th International conference on near-field optics, nanophotonics and related techniques (NFO9), Lausanne (Suisse) 10-15 september, 2006.
- (O7) Single molecule fluorescence probes local density of states (LDOS) around photonic nanostructures
G. Colas des Francs, G. Sanchez-Mosteiro, N. Van Hulst, and A. Dereux, in EOS Topical Meeting on Molecular Plasmonic Devices, Engelberg (Suisse), 27-29 april, 2006.
- (O8) Imagerie optique en champ proche et transfert d' énergie avec une molécule unique
G. Colas des Francs and C. Girard, in Société Française de Microscopie-Toulouse, France, 2000.

Séminaires, *workshops* : 12 titres

- (S1) Challenges in modelling plasmonic structures
G. Colas des Francs, in workshop COST plasmonic components and devices, Lausanne (Suisse), 3-4 September, 2009.
- (S2) Couplage d'une molécule unique avec une nannoparticule métallique : contributions des modes plasmons
G. Colas des Francs, in workshop ANTARES (ANR PNANO), Grenoble (France), 4 juillet, 2008.
- (S3) Dielectric-loaded surface plasmon polariton waveguide : mode characterization
G. Colas des Francs, in Carnot Plasmonic Project Review, Grenoble, 17 june, 2008.
- (S4) Exaltation de fluorescence sur surface métallique
G. Colas des Francs, in workshop ANTARES (ANR PNANO), Marseille (France), septembre, 2007.
- (S5) Analysis of the angular emission of near-field optical probes
G. Colas des Francs, in workshop ASPIRENT, Nijmegen (Netherlands), 14-16 may, 2007.
- (S6) Angular Spectrum of Plane Waves Scattered by SNOM Probes : in situ Measurements
A. Bruyant and G. Colas des Francs, in ASPIRENT, Barcelone, Espagne, 16-18 mai, 2006.

- (S7) Résolution numérique des équations de Maxwell-Bloch pour l'étude des interactions optiques en géométrie confinée
G. Colas des Francs, in Fédération de recherche de l'Université de Bourgogne, Dijon (France), 4-5 décembre, 2006.
- (S8) Energy transfer in near-field optics
G. Colas des Francs, in workshop ASPRINT, Dijon, France, 24-25 octobre, 2005.
- (S9) Subwavelength mapping of surface photonic states
G. Colas des Francs, in workshop ASPRINT, Münster, Allemagne, 21-23 avril, 2005.
- (S10) Discrete Dipole Approximation (DDA) (practice)
G. Colas des Francs and C. Girard, in workshop PlasmoNanoDevices, Madrid, Espagne, 19-21 octobre, 2005.
- (S11) Optique en géométrie réduite
G. Colas des Francs and C. Girard, in Journée scientifique des utilisateurs du supercalculateur O2000 (CALMIP -CALcul en Midi-Pyrénées), 9 Mars, 2001.
- (S12) Adressage de molécules par un champ optique confiné
G. Colas des Francs and C. Girard, in Ecole thématique optique du champ proche, La Londe Les Maures-France.20-24 mars, 2000.

Chapitre d'ouvrage : 1 titre

- (S1) G. Colas des Francs and C. Girard, Le champ proche optique , D. Courjon et C. Bainier, 2001, ch. Fonction de Green en optique champ proche.

Deuxième partie

Projet de recherche

PLASMONIQUE MOLÉCULAIRE

SPECTROSCOPIE SUR SURFACE MÉTALLIQUE

ET

MATÉRIAUX HYBRIDES POUR LA PHOTONIQUE INTÉGRÉE

Introduction : parcours scientifique

Entre 1999 et 2002, j'ai préparé ma thèse sous la direction de Christian Girard au CEMES, à Toulouse. Je me suis alors intéressé à la fluorescence moléculaire en champ proche optique. Ce travail théorique a conduit à une meilleure compréhension des images obtenues par microscopie en champ proche optique (SNOM - Scanning Near-Field Optical Microscopy). En particulier, j'ai établi une analogie entre les images SNOM et le taux de relaxation de molécules fluorescentes. D'autre part, j'ai modélisé la fluorescence moléculaire dans une jonction pointe-surface à partir des équations de Bloch optiques, appliquées en champ proche.

Ensuite, j'ai effectué un séjour post-doctoral sous la responsabilité du professeur Ulrich Fischer à l'Université de Münster (Allemagne). J'ai étudié l'excitation localisée de molécules fluorescentes dans une jonction pointe-surface. J'ai principalement modélisé le confinement du champ proche optique à la sortie d'une sonde originale développée dans ce groupe (sonde à ouverture triangulaire).

Finalement, j'ai intégré l'équipe optique submicronique et nanocapteurs en octobre 2004 pour développer un axe plasmonique moléculaire qui présente des zones de contact avec deux activités déjà existantes : *la photonique intégrée* d'une part et les *capteurs chimiques* d'autre part. Il s'agit d'utiliser les propriétés de confinement et d'exaltation de modes supportés par des nanostructures métalliques : les *plasmon-polaritons de surface* (SPPs, surface plasmon polaritons). Ces modes résultent du couplage d'ondes électromagnétiques et de charges de surface. Ils sont caractérisés par un fort confinement les rendant prometteurs pour des applications optiques sous la limite de diffraction.

Ce document synthétise mes travaux de recherches sur la période 2002-2009. Le couplage de molécules avec des structures plasmoniques occupant une grande place dans mes travaux, je fais une brève présentation des plasmons de surface au chapitre 1. Les trois chapitres suivants présentent ensuite les axes majeurs de mon activité :

- Chapitre 2 : Microscopie et spectroscopie optiques en champ proche,
- Chapitre 3 : Relaxation moléculaire par couplage aux plasmons, en particulier, la possibilité de modifier les propriétés d'émission de molécules par couplage avec des structures métalliques,
- Chapitre 4 : Composants plasmoniques pour la photonique intégrée, où, à l'inverse, l'ingénierie de matériaux optiques (polymères dopés, non linéaire, ...) permet de contrôler la propagation de SPPs le long de films métalliques.

Finalement, je démontrerai que ces axes peuvent converger vers la notion d'antenne plasmonique, axe que je souhaite développer dans les prochaines années. A chaque fois que cela sera possible, je replacerai dans le contexte national ou international mon apport dans ces thématiques. Les principales publications sont placées directement dans le corps du mémoire, juste après une brève discussion qui met en lumière les principaux résultats.

Chapitre 1

Plasmons : définition et applications

Ce chapitre présente brièvement les différents types de plasmons-polaritons en s'appuyant sur des modèles simples pour mettre en évidence leurs principales caractéristiques. La lecture de ce chapitre est utile à la compréhension des chapitres 3 et 4 et, dans une moindre mesure du chapitre 2. Le lecteur un peu familier avec les plasmons de surface peut passer cette partie.

1.1 Plasmon de volume

1.1.1 Plasma et modèle de Drude

Nous nous intéressons aux propriétés optiques des métaux. Les électrons de conduction sont modélisés par un gaz d'électrons libres. Le mouvement des électrons soumis à un champ électrique $\mathbf{E}(t) = \Re[\mathbf{E}(\omega)e^{-i\omega t}]$ peut être décrit par le déplacement moyen \mathbf{r} des électrons par rapport à leur position d'équilibre. \mathbf{r} est régi par le principe fondamental de la dynamique, en tenant compte de la dissipation γ lors des collisions

$$\frac{d^2\mathbf{r}(t)}{dt^2} + \gamma \frac{d\mathbf{r}(t)}{dt} = \frac{e}{m_e} \mathbf{E}(\omega)e^{-i\omega t}. \quad (1.1)$$

Soit n_c la densité électronique, le vecteur polarisation de la matière par unité de volume se déduit aisément :

$$\mathbf{P}(\omega) = -n_c e \mathbf{r}(\omega) = -\frac{n_c e}{m_e} \frac{1}{\omega^2 + i\omega\gamma} \mathbf{E}(\omega). \quad (1.2)$$

La constante diélectrique du plasma apparaît alors facilement en écrivant le vecteur polarisation sous la forme :

$$\mathbf{P}(\omega) = \epsilon_0 [\epsilon_m(\omega) - 1] \mathbf{E}(\omega), \quad (1.3)$$

$$\epsilon_m(\omega) = 1 - \frac{\omega_p^2}{\omega^2 + i\omega\gamma}, \quad (1.4)$$

où $\omega_p = \sqrt{\frac{n_c e^2}{\epsilon_0 m_e}}$ est la pulsation propre du gaz d'électrons (fréquence de plasma). Par exemple, pour l'or et l'argent, on trouve respectivement $\omega_p^{Ag} = 5,8 \cdot 10^{15} s^{-1}$ ($\lambda_p^{Ag} = 324$ nm) et $\omega_p^{Au} = 8,3 \cdot 10^{15} s^{-1}$ ($\lambda_p^{Au} = 227$ nm). Le modèle de Drude, reproduit assez bien le comportement de la constante diélectrique de l'or et de l'argent dans le visible et le proche infra-rouge [1]. Pour des fréquences ultra-violettes, il faut ajouter des termes correctifs tenant compte des transitions

interbandes. Pour les simulations numériques présentées tout au long de ce mémoire, nous avons utilisé les valeurs expérimentales des matériaux massifs [2, 3]. Toutefois, dans ce chapitre, nous conservons la description par le modèle du plasma de Drude qui permet d'introduire plus simplement la notion de plasmon. De plus, en première approximation, nous négligerons la dissipation ($\gamma \ll \omega_p$), d'où $\epsilon_m(\omega) = 1 - \frac{\omega_p^2}{\omega^2}$. Les effets de la dissipation dans le métal seront discutés en détail au cours des chapitres suivants.

Dans le paragraphe suivant, nous analysons la propagation d'une onde électromagnétique dans ce plasma.

1.1.2 Propagation d'une onde électromagnétique dans un plasma

L'équation de propagation d'une onde plane $\mathbf{E}(\mathbf{r}, t) = \mathbf{E}_0 e^{i\mathbf{k}\cdot\mathbf{r}} e^{-i\omega t}$ dans le plasma s'écrit

$$\nabla^2 \mathbf{E}(\mathbf{r}, t) = \mu_0 \frac{\partial^2 \mathbf{D}(\mathbf{r}, t)}{\partial t^2}, \text{ avec} \quad (1.5)$$

$$\mathbf{D}(\mathbf{r}, \omega) = \epsilon_m(\omega) \mathbf{E}(\mathbf{r}, \omega). \quad (1.6)$$

Ce qui conduit à une condition d'existence sur vecteur d'onde \mathbf{k} :

$$\mathbf{k}(\mathbf{k} \cdot \mathbf{E}_0) - k^2 \mathbf{E}_0 = \frac{\epsilon_m(\omega)}{c^2} \mathbf{E}_0. \quad (1.7)$$

A ce stade, il convient de distinguer les ondes transverses et les ondes longitudinales.

- Pour une onde transverse, telle que $\mathbf{k} \cdot \mathbf{E}_0 = 0$, cette condition se réduit à la relation de dispersion usuelle $k^2 = \epsilon_m(\omega)/c^2$. Aux fréquences telles que $\epsilon_m(\omega) > 0$, le milieu est transparent et l'onde se propage. A contrario, aux fréquences telles que $\epsilon_m(\omega) < 0$, le milieu ne supporte pas d'onde propagative transverse. Il se comporte comme un miroir.
- Dans le cas d'une onde longitudinale, $\mathbf{k} \wedge \mathbf{E}_0 = 0$ d'où on tire $\epsilon_m(\omega) = 0$ puis $\omega = \omega_p$. Le plasma supporte une onde propagative longitudinale à sa seule fréquence propre. Nous discutons plus particulièrement la nature de cette onde ci-après.

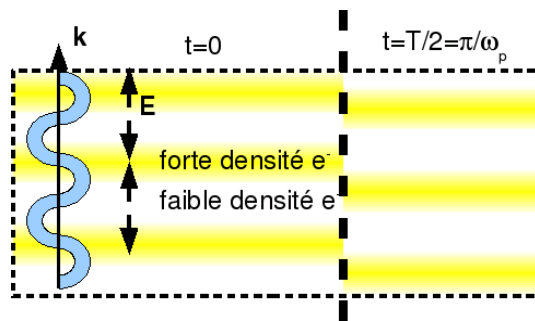


FIG. 1.1 – Perturbation du nuage électronique dans le plasma en présence d'un champ électrique longitudinal à $t = 0$ et après une demi-période ($\mathbf{E}(z, t) = E_0 \cos(kz - \omega_p t) \mathbf{u}_z$). L'amplitude du champ électrique à $t = 0$ le long du plasma est indiquée. Les électrons subissent une force $\mathbf{F} = -e\mathbf{E}$ conduisant à l'alternance de zones de fortes et faibles densités électroniques.

La figure (1.1) représente schématiquement le mouvement des électrons libres soumis au champ longitudinal. Il y a une oscillation collective des électrons libres, à la fréquence du plasma. Ce mode s'apparente donc à une quasi-particule de plasma, appelée *plasmon de volume*. Par

ailleurs, ce mode est couplé à une onde électromagnétique associée à la polarisation de matière, appelée *polariton*. Ainsi, ce mode couplant oscillation collective et onde électromagnétique est dénommé **plasmon-polariton de volume** [4]. La notion de plasmon-polariton étant maintenant clairement établie, nous considérons l'effet du confinement dans deux cas : une simple interface métal/diélectrique et une particule métallique. Cela nous amènera à définir différents types de plasmon-polaritons de *surface*, modes responsables du couplage de molécules fluorescentes avec des objets métalliques.

1.2 Plasmon-polaritons de surface

1.2.1 Mode délocalisé

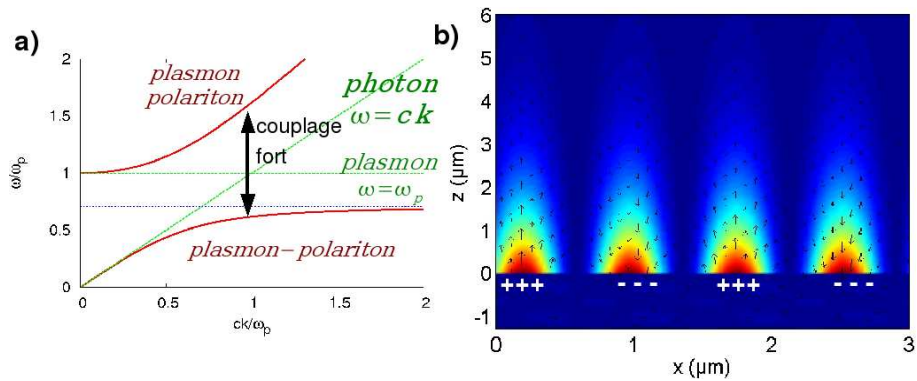


FIG. 1.2 – a) Relation de dispersion à l'interface métal/air. Le couplage entre le plasmon et le polariton conduit à la formation d'un plasmon-polariton de surface. b) Intensité électrique associée à $t = 0$ à l'interface or/air ($\lambda = 1,5\mu\text{m}$, $\epsilon_m = -131,95 + i12,65$ [3]). Le vecteur champ électrique est représenté par des flèches noires. Les signes "+" et "-" représentent les charges de surface déduites de la polarisation.

Dans un premier temps, considérons le cas d'une surface métallique semi-infinie. Comme nous nous intéressons aux phénomènes électromagnétiques à l'interface métal ($\epsilon_m(\omega)$)/diélectrique (ϵ_d), il est pratique d'étudier le comportement des coefficients de Fresnel. Ainsi, le coefficient de réflexion s'écrit-il, dans le cas d'une onde électromagnétique polarisée transverse-magnétique (TM) :

$$r_{TM} = \frac{\epsilon_d k_{zm} - \epsilon_m(\omega) k_{zd}}{\epsilon_d k_{zm} + \epsilon_m(\omega) k_{zd}}. \quad (1.8)$$

k_{zi} ($i = m, d$) est la composante du vecteur d'onde selon la normale à l'interface dans chaque milieu. Le coefficient de réflexion diverge lorsque son dénominateur s'annule ; $\epsilon_d k_{zm} + \epsilon_m(\omega) k_{zd} = 0$. Cela se produit lorsque la composante du vecteur d'onde parallèle à l'interface vaut [5]

$$k_x = \frac{\omega}{c} \sqrt{\frac{\epsilon_d \epsilon_m(\omega)}{\epsilon_d + \epsilon_m(\omega)}}, \quad (1.9)$$

qui devient avec le modèle de Drude $k_x = \frac{\omega}{c} \sqrt{\frac{\omega^2 - \omega_p^2}{2\omega^2 - \omega_p^2}}$ (avec $\gamma \ll \omega_p$ et $\epsilon_d = 1$). La figure 1.2a) représente cette relation de dispersion. Le mode correspondant est représenté sur la figure 1.2b).

Le mode correspond de nouveau à l'oscillation collective des électrons libres. Toutefois, il met en jeu des charges surfaciques, d'où l'appellation **plasmon-polariton de surface**.

1.2.2 Modes localisés

Terminons ce paragraphe en poussant un peu plus le confinement spatial du métal. Considérons le cas analytique d'une particule métallique sphérique de rayon a , dans un milieu homogène de constante ϵ_d . La réponse de cette particule à un champ électrique est exactement décrite par la théorie de Mie [6]. Dans l'approximation non-retardée ($\omega/c \rightarrow 0$), la réponse de la particule se simplifie et conduit à définir les polarisabilités quasi-statiques d'ordre n

$$\alpha_n = \frac{n(\epsilon_m - \epsilon_d)}{(n+1)\epsilon_d + n\epsilon_m} a^{(2n+1)}. \quad (1.10)$$

Physiquement, lorsque la particule métallique est illuminée avec un champ électrique non uniforme E , on peut décrire sa réponse électromagnétique sous la forme d'un développement multipolaire impliquant les moments d'ordre n :

$$\mathbf{p}^{(n)} = \frac{4\pi\epsilon_0\epsilon_d}{(2n-1)!!} \alpha_n \nabla^{n-1} \mathbf{E}. \quad (1.11)$$

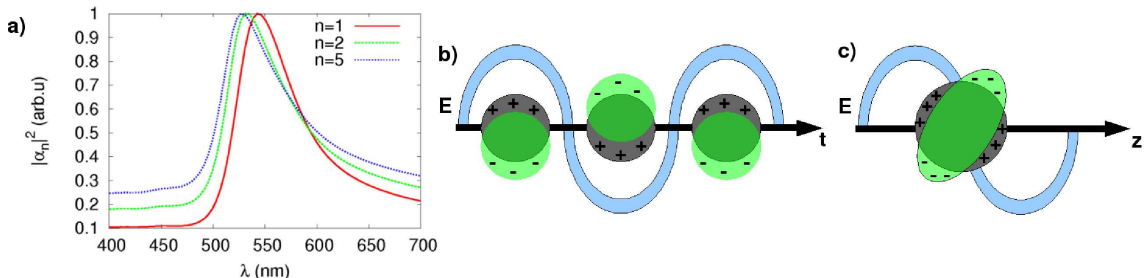


FIG. 1.3 – a) Spectres de polarisabilités quasi-statiques α_n . b) Mode dipolaire ($n=1$) : représentation schématique de l'oscillation *temporelle* du nuage électronique (en vert) dans une particule métallique (en gris) soumise à un champ électrique oscillant (le champ est supposé uniforme sur l'ensemble de la particule). c) Excitation du mode quadrupolaire ($n=2$) pour une particule de diamètre comparable à la longueur d'onde : le champ inhomogène induit une distribution quadrupolaire des charges. En b) l'axe représente le temps alors qu'en c), l'axe indique le sens de propagation.

Par exemple, seul le dipole $\mathbf{p}^{(1)} = 4\pi\epsilon_0\epsilon_d\alpha_1 \mathbf{E}$ subsiste pour un champ uniforme. Au contraire, nous verrons que les fortes variations spatiales du champ électrique émis dans le champ proche d'un émetteur quantique permettent d'exciter des modes d'ordres élevés (quadrupolaire $n=2$; octupolaire $n=3$; ... ; 2^n -polaire). Le mode d'ordre n est excité à la fréquence ω_n telle que $\epsilon_m(\omega_n) = -\frac{(n+1)}{n}\epsilon_d$ qui minimise le dénominateur de la polarisabilité α_n (éq. 1.10, et figure 1.3). Avec la constante diélectrique donnée par le modèle de Drude, il apparaît que ces fréquences de résonances sont comprises entre $\omega = \omega_p/\sqrt{3}$ ($n = 1$) et $\omega = \omega_p/\sqrt{2}$ ($n \rightarrow \infty$) dans l'air ($\epsilon_d = 1$). Ici de nouveau, ces résonances sont associées à l'oscillation collective des électrons libres dans la particule métallique (figure 1.3). Il s'agit de **plasmon-polaritons de surface localisés**, par opposition au plasmon-polariton de surface délocalisé vu précédemment.

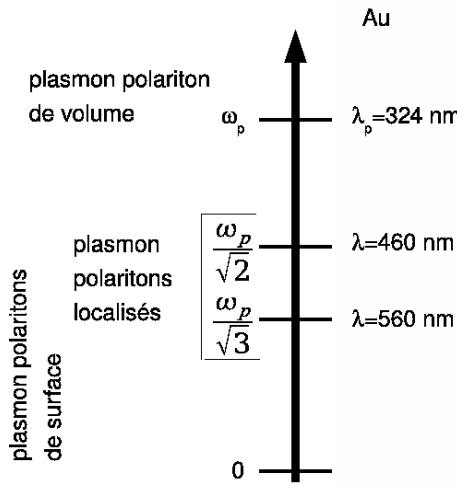


FIG. 1.4 – Domaines d’existence des différents types de plasmon-polaritons. La partie droite de la figure indique les valeurs de longueurs d’ondes correspondant au cas de l’or (pour le modèle de Drude).

Finalement, contrairement au plasmon-polariton de volume qui est supporté à l’unique fréquence plasma ω_p et est associé à une oscillation du nuage électronique dans le métal massif, les plasmon-polaritons de surface localisés et délocalisés sont associés à des oscillations de charges surfaciques et apparaissent dans un domaine énergétique ($0 < \hbar\omega < \hbar\omega_p\sqrt{2}$, mode délocalisé et $\hbar\omega_p/\sqrt{3} < \hbar\omega < \hbar\omega_p/\sqrt{2}$, modes localisés) comme résumé sur la figure 1.4. Il est important de noter que pour $\omega_p/\sqrt{3} < \omega < \omega_p/\sqrt{2}$, les modes de films et les modes localisés d’ordres élevés se confondent (modes quasi-statiques). Cet aspect nous conduira à la notion d’antenne optique, reposant sur le couplage de ces modes pour propager (mode délocalisé) et confiner (mode localisé) le champ électromagnétique.

1.3 Plasmonique moléculaire

La plasmonique moléculaire s’intéresse au couplage de molécules avec des structures métalliques [7]. Selon la forme et la nature de l’objet métallique et la fréquence d’émission des molécules, différents types de plasmon-polaritons de surface seront vecteurs de ce couplage. Par la suite, nous utiliserons le terme plasmon pour plasmon-polariton de surface par souci de brièveté. Nous décrivons ici très succinctement quelques applications et perspectives de la plasmonique moléculaire.

1.3.1 Capteurs chimiques et biologiques

Comme le démontrent les équations (1.9) et (1.10), les résonances plasmons sont très sensibles à l’environnement diélectrique (ϵ_d) à proximité du métal. Ceci est à l’origine de la détection très sensible de molécules. Par exemple, le système commercialisé par la société Biacore utilise la sensibilité de la résonance des plasmons de surface (délocalisés) de films métalliques pour détecter des molécules d’intérêt biologique [8]. De nombreux groupes ont proposé d’utiliser

le fort confinement des plasmons localisés de nanoparticules métalliques pour augmenter de plusieurs ordres de grandeurs la sensibilité des capteurs. Ceci est à l'origine de la spectroscopie exaltée sur surface métallique, et tout particulièrement de la diffusion Raman exaltée sur surface métallique (SERS - Surface Enhanced Raman Scattering). Cette dernière application fait l'objet d'un très important effort de recherche actuellement [9].

1.3.2 Thérapie anti-cancéreuse

La résonance des plasmons localisés s'accompagne d'un échauffement significatif à proximité de la particule métallique (~ 10 °C)[10, 11]. Très récemment, le groupe de Naomi Halas (Rice University, Houston) a démontré que ceci ouvre la voie à une méthode efficace de thérapie anti-cancéreuse. En injectant des nanoparticules d'or dans des souris atteintes de cancer, ils ont montré que ces particules se concentrent préférentiellement dans les tumeurs car leurs membranes sont très détendues. Ensuite, en illuminant dans le proche infra-rouge ces particules, l'élévation de température conduit à la destruction irréversible des cellules cancéreuses en environ une semaine [12, 13, 14]. Des essais cliniques sont en cours.

1.3.3 Exaltation de courants photo-induits

La figure 1.5 représente la diffusion par une particule métallique. Hors résonance, le champ électromagnétique semble éviter la particule alors qu'à la résonance, il converge vers celle-ci. Ceci se traduit par une forte augmentation de la section efficace d'absorption de la particule [6]. Ce phénomène pourrait être utilisé pour améliorer le rendement de cellules photovoltaïques [15].

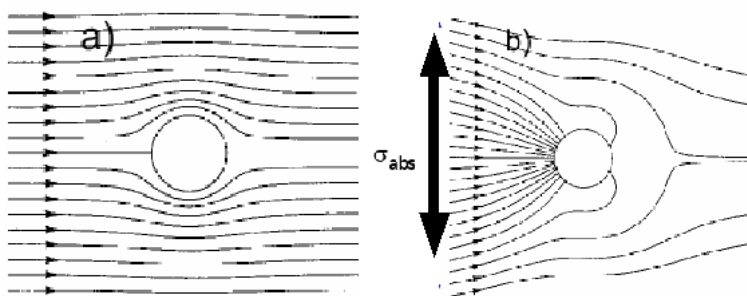


FIG. 1.5 – Lignes de champ associées au vecteur de Poynting. Contribution diffusée par une particule d'aluminium (a) hors résonance et (b) à la résonance plasmon. D'après [6].

1.3.4 Composants pour la photonique intégrée

A partir de la fin des années 1990, la plasmonique est apparue comme un moyen de concilier la miniaturisation de l'électronique avec la bande passante de l'optique guidée. Dans ce cas, le vecteur d'information est non plus l'électron (électronique) ou le photon (fibre optique) mais le plasmon-polariton de surface, délocalisé qui associe les deux [16, 17]. En fonctionnant le guide plasmonique avec des films moléculaires ou des boîtes quantiques, il est possible de réaliser différents types de composants actifs (commutateur, modulateur, transistor, ...) intégrés sur une surface [18, 19, 20].

Chapitre 2

Microscopie et spectroscopie optiques en champ proche

La microscopie en champ proche optique (SNOM, Scanning Near-field Optical Microscopy) s'est véritablement développée à la suite des deux autres grandes familles de microscopies à sondes locales : la microscopie à effet tunnel (STM) et la microscopie à force atomique (AFM). En particulier, ce développement s'est appuyé sur les méthodes d'asservissement de la distance pointe-échantillon. Après une longue période de développement de sondes optiques efficaces mais aussi de débat sur la nature du signal mesuré pendant les années 1990, cette technique a démontré son intérêt pour imager les ondes électromagnétiques de surface, notamment dans les dispositifs photoniques intégrés. Dans le même temps, de nombreux groupes se sont intéressés à la fluorescence dans une jonction pointe-surface. Deux applications majeures motivent ce type d'étude. Soit la sonde perturbe peu le système étudié et le SNOM est un dispositif imageur de la fluorescence, avec d'importantes perspectives pour l'étude de systèmes biologiques. Soit la sonde modifie considérablement l'émission de fluorescence. Dans ce cas, le SNOM constitue un système modèle et contrôlé pour l'étude de la fluorescence dans des géométries complexes. Une discussion générale et approfondie de la microscopie et de la spectroscopie en champ proche est donnée dans l'ouvrage *Principles of Nano-Optics* écrit par Lukas Novotny et Bert Hecht [1].

Ce chapitre rassemble les résultats que j'ai obtenus sur la fluorescence dans une jonction pointe-surface, en présence de structures métalliques dissipatives. Ils constituent un prolongement de mes travaux de thèse, qui concernaient le même type de configuration mais dans le cas de dissipation faible ou nulle. Bien que le formalisme utilisé soit très proche de celui mis en place pendant ma thèse, nous verrons que l'introduction de structures métalliques modifie considérablement la forme du signal détecté. Par ailleurs ce chapitre constitue une étape importante pour la caractérisation des processus de relaxation moléculaire par couplage aux modes plasmons auxquels nous nous intéresserons aux chapitres 3 et 4.

Le paragraphe 2.1 présente la formation d'un champ extrêmement confiné par une sonde optique métallisée à ouverture triangulaire et son utilisation pour l'excitation de molécules individuelles. Je discute ensuite de la forme du signal mesuré en champ proche optique au-dessus de nanostructures plasmoniques dans un modèle simplifié de sonde dipolaire (§2.2). Finalement, le paragraphe 2.3 présente la modélisation non-perturbative de la fluorescence dans un dispositif plasmonique à l'aide des équations de Bloch optiques.

2.1 Fluorescence haute résolution dans une jonction pointe-surface

2.1.1 Sonde à ouverture triangulaire

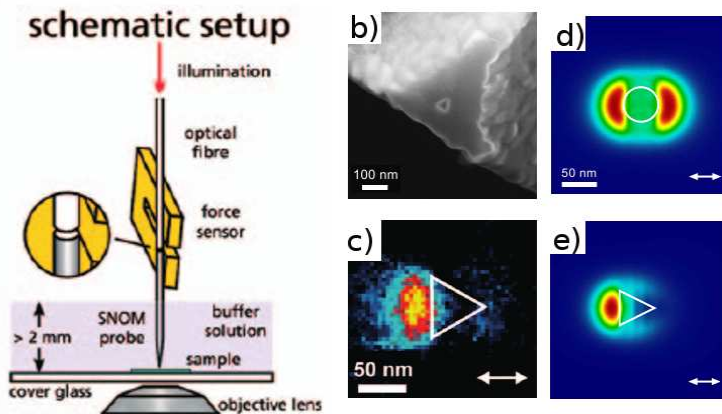


FIG. 2.1 – a) Description schématique du montage SNOM travaillant en milieu aqueux [21]. b) Sonde à ouverture triangulaire. c,e) Intensité du champ électrique mesurée (c) et calculée (e) à la sortie de la sonde. d) Intensité électrique calculée à la sortie d'une sonde à ouverture circulaire pour comparaison. La flèche blanche indique la polarisation de l'illumination ($\lambda = 488 \text{ nm}$).

Parmi la grande variété des sondes optiques en champ proche, les sondes dites à ouverture sont les plus couramment utilisées pour des applications de fluorescence hautement résolues. Ce type de sonde est généralement réalisé à partir d'une fibre optique très étirée puis métallisée avec de l'aluminium, opaque dans le visible. Seule l'extrémité de la fibre n'est pas métallisée, laissant ainsi une ouverture circulaire sub-longueur d'onde qui confine fortement le champ électrique (voir par exemple la figure 2.1d). Le diamètre de l'ouverture utilisée est souvent de l'ordre de 80 à 100 nm pour conserver une intensité électrique suffisante. Malheureusement, cela réduit considérablement la résolution puisque celle-ci est un peu supérieure au diamètre de l'ouverture, à cause de la présence des deux lobes (Fig. 2.1d). En 2002, Andreas Naber et Ulrich Fischer (Université de Münster) ont développé une sonde à ouverture triangulaire (figure 2.1b) [22]. Celle-ci est obtenue en déposant 100 nm d'aluminium sur un coin de verre. L'ouverture triangulaire est ensuite réalisée par exemple en coupant l'extrémité avec un faisceau d'électrons focalisés (Focus Ion Beam, FIB). Andreas Naber a démontré que cette géométrie conduit à une ouverture numérique élevée de la sonde d'où un pouvoir de transmission accru ($\sim 10^{-4}$ contre $\sim 10^{-6}$ pour une fibre optique effilée). Par ailleurs, la forme triangulaire de l'ouverture confine le champ électrique sur un seul côté, améliorant très nettement la résolution accessible ($\sim 30 \text{ nm}$, figure 2.1c).

Lors de mon séjour post-doctoral à l'Université de Münster (2002-2003), j'ai analysé le confinement du champ dans cette sonde [23]. La pointe est simplement modélisée par une ouverture triangulaire de 50 nm de côté dans un écran d'aluminium de 100 nm d'épaisseur. Pour être au plus près des conditions expérimentales, l'ouverture et le milieu incident sont du verre alors que le milieu extérieur est de l'air. La figure (Fig. 2.1e) représente l'intensité du champ électrique calculé à 10 nm de l'ouverture lorsque celle-ci est illuminée par une onde

plane. La forme et la position de l'intensité électrique reproduit correctement le signal champ proche optique mesuré en balayant la pointe au-dessus d'une bille de polystyrène dopée avec des molécules fluorescentes (Fig. 2.1c). Finalement, le champ électrique est confiné sur une ellipse de petit axe 30 nm et de grand axe 40 nm. Au cours de cette étude, nous avons aussi considéré d'autres métaux pour étudier les mécanismes de confinement. Nous avons montré que l'argent conduit à un signal plus intense, probablement grâce à la propagation de modes plasmons dans l'ouverture [24] mais au détriment du confinement du champ électrique [23].

A mon arrivée à Dijon, j'ai continué à collaborer avec ce groupe pour mieux comprendre la formation du confinement électrique à la sortie de l'ouverture. Nous avons donc étudié numériquement différentes formes d'ouvertures, et le rôle de l'angle d'incidence d'excitation [25, 26].

Publications correspondantes

Cette étude est discutée dans l'article suivant :

“Enhanced light confinement in a triangular aperture : Experimental evidence and numerical calculations”

G. Colas des Francs, D. Molenda, U. Fischer and A. Naber
Physical Review B **72**, 165111 (2005).

Deux autres articles discutent de différentes formes d'ouvertures et de l'excitation oblique de l'ouverture (non reproduits)

Transmission of an obliquely incident beam of light through small apertures in a metal film

E. Bortchagovsky, G. Colas des Francs, D. Molenda, A. Naber and U. Fischer
Applied Physics B **84**, 49 (2006).

On the optimum form of an aperture for a confinement of the optically excited electric near field

E. Bortchagovsky, G. Colas des Francs, A. Naber and U. Fischer
Journal of Microscopy **229**, 223 (2008).

Enhanced light confinement in a triangular aperture: Experimental evidence and numerical calculations

G. Colas des Francs

Laboratoire de Physique de Université de Bourgogne et CNRS, Optique Submicronique, 9 avenue A. Savary, F-21011 Dijon, France

D. Molenda and U. C. Fischer

Physikalisches Institut, Universität Münster, Wilhelm-Klemm Str. 10, D-48149 Münster, Germany

A. Naber*

Institut für Angewandte Physik, Universität Karlsruhe (TH), Wolfgang-Gaede-Str. 1, D-76131 Karlsruhe, Germany

(Received 30 July 2004; revised manuscript received 26 July 2005; published 24 October 2005)

We have recently demonstrated that the electric near-field emerging from a triangular aperture at the tip of a metal-coated tetrahedron of glass exhibits a highly confined and intense spot when the light incident from within the glass body is polarized perpendicularly to one edge of the aperture [Naber *et al.*, Phys. Rev. Lett. **89**, 210801 (2002)]. Here we present additional experimental material and a theoretical confirmation of this near-field optical effect. Based on the model of a triangular aperture in a planar metal film, we studied the influence of aperture size and film material on the field distribution. Even though our theoretical model is rather simplified as compared to the experimental setup, we find our numerical calculations to be in very good agreement to the experimental results. The simulation confirms that it is mainly the reduced symmetry of the triangular aperture as compared to a circular one which leads to the enhanced confinement and strongly increased transmission of the electric field.

DOI: 10.1103/PhysRevB.72.165111

PACS number(s): 78.67.-n, 78.20.Bh, 42.25.Gy, 07.79.Fc

I. INTRODUCTION

Aperture-probe scanning near-field optical microscopy (A-SNOM) relies on the extremely confined electric field that emerges from a subwavelength aperture in a metallic film to explore optical properties below the diffraction limit. The most common way of aperture probe fabrication is to coat a tapered optical fiber with metal in such a way that the very tip remains uncoated. Using this method one can obtain circular apertures of a diameter in the range of 100–50 nm or even less. By coupling light into the fiber, an electric field is created at the aperture which is confined to a subwavelength area of a size comparable to the one of the aperture.^{1–3} In practice, however, the diameter of the aperture and thus the optical resolution is commonly chosen >80 nm, because the transmitted intensity decreases overexponentially with decreasing size of the aperture. This severe drop in output intensity cannot simply be compensated by a higher input intensity, since the metal cladding is destroyed at input powers above a certain threshold (~ 10 –20 mW).⁴ Hosaka and Saiki succeeded to implement aperture probes with smaller apertures leading to SNOM imaging of single molecules at 15 nm in a selected example.⁵ An important advantage of these probes seems to be a larger taper angle leading to a higher transmission of light through the probe. Recently we introduced a kind of aperture probe (TA probe) featuring a full taper angle of 90° and a triangular aperture (TA) at the tip of a metal-coated tetrahedral glass body.⁶ We demonstrated that, in contrast to a circular aperture, an equilateral triangular aperture can concentrate the incident electric field with high intensity to an area considerably smaller than the aperture area if the polarization of the incident light is chosen to be

perpendicular to an edge of the aperture. Such a triangular aperture was proven to be useful for near-field fluorescence imaging at a resolution of 30–40 nm.⁶ Tanaka *et al.*⁷ and Tanaka and Tanaka⁸ numerically investigated different models of a triangular aperture in a metallic screen. Their results are in good qualitative agreement to the field patterns at a TA probe.

Here we present additional experimental data of the enhanced field confinement of a TA probe as well as a systematic study of the influence of aperture size and film material on the field distribution at a triangular aperture in a planar film. Though our theoretical model considerably deviates from the actual geometry of a TA probe, the numerical results turned out to be in very good agreement to the measurements. In preliminary calculations (not shown) for a more complex three-dimensional geometry we did not find a significant improvement. Our findings confirm the idea that it is mainly the reduced symmetry of the triangular aperture together with the boundary conditions of the electromagnetic field at the edges which lead to the confinement and strongly increased transmission of the electric field.

The paper is organized as follows: In Sec. II we briefly describe the fabrication of the TA probe and its characterization. A detailed account is given of the electric field distribution in the vicinity of the aperture as a function of the polarization of the incident beam. In Sec. III we give a short introduction to numerical simulations based on the field-susceptibility method. In Sec. IV this formalism is applied to a sub-wavelength triangular aperture in a planar metal film. We discuss the energy confinement properties in the near field of such an aperture irradiated by a plane wave at normal incidence. For comparison, we also apply this method to a

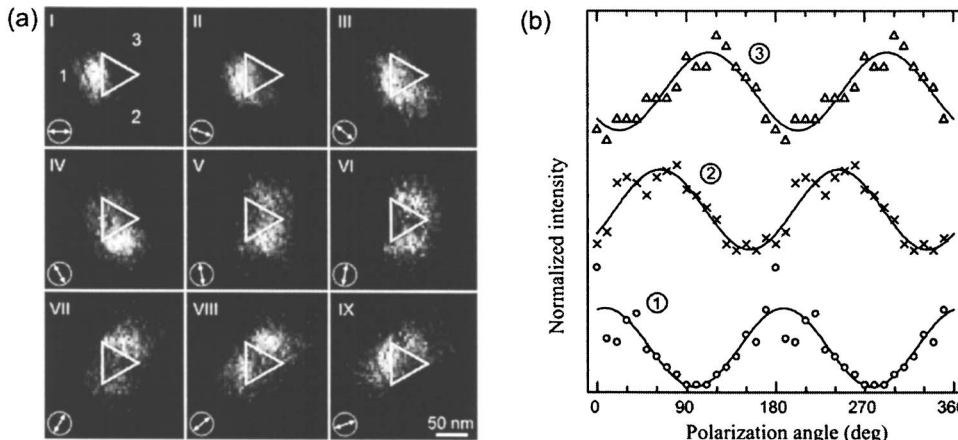


FIG. 1. (a) Measured field patterns (I-IX) at the triangular aperture (white line) of a TA probe for different polarization angles of the incident light. The double arrows indicate the respective polarization direction of the incident beam. (b) Plots of the averaged fluorescence intensity at the center of the aperture edges 1-3 as a function of the polarization angle ϕ . The solid curves fit the data with a $\cos^2\phi$ law. The respective plots for the sides 2 and 3 are both shifted by an arbitrary offset.

circular aperture. An interpretation of the numerical results based on the boundary conditions of the electric field allows us to discuss the enhanced light confinement in simple terms.

II. EXPERIMENTAL RESULTS

The fabrication of the TA probe is based on a glass body exhibiting a tetrahedron-shaped tip.^{6,9} After coating the glass body with an opaque aluminum layer, the probe is attached to a piezoelectric tuning fork serving as a force sensor for sample-distance control in the SNOM measurement.^{6,10} The triangular aperture is created by gently squeezing the metal-coated tip against a flat glass surface.^{6,11,12} The typical size of the resulting aperture is in the range of 30–60 nm.

For the characterization of the aperture, ~ 20 nm-sized dye-doped polystyrene spheres are imaged near-field optically.^{6,12} Due to the small size of the beads as compared to the aperture, probe and sample change their roles in the imaging process. The measured fluorescence intensity of the beads depends on the local excitation intensity at the aperture, so that the taken fluorescence image represents a highly resolved map of the electric field intensity at the probe.¹² In Fig. 1(a) the measured field distribution at the aperture of a TA probe is shown as a function of the polarization direction of the incident laser light. The size of the triangular aperture (indicated by a white line) has been mainly concluded from the distribution of the field intensity in the vicinity of the aperture⁶ and comparable studies of circular apertures.¹³

As in the case of circular apertures,^{1–3} a high field intensity arises at the metallic edges of the triangular aperture. For a direction of the polarization normal to one of the edges [Fig. 1(a): I, IV, and VII], we find a significant field intensity only at this edge, whereas the other two edges then exhibit only a comparatively weak field intensity. For other polarization directions, however, always two edges of the aperture are excited with varying intensity distribution [Fig. 1(a): II, III, V, VI, VIII, and IX]. In order to clarify the polarization dependent course of the field intensity, in Fig. 1(b) the averaged intensity at the center of each edge is plotted against the polarization angle of the incident light. For each edge, a simple sinusoidal function fitted to the respective data fairly reproduces the polarization dependent changes in intensity. The fitted curves are phase shifted $\sim 60^\circ$ to each other which

agrees well with the behavior expected for an aperture with a threefold symmetry.

III. THEORY

Several theoretical methods have been successfully applied to describe the near field of sub-wavelength apertures in metallic films. However, so far the only case that has been analytically solved is a circular hole in an infinitely thin and perfectly conducting metal.^{1,2} As far as only such idealized films are concerned, the application of the generalized Babinet's principles yields a simple and time saving numerical method for a characterization of arbitrarily shaped apertures.^{14,15} Nevertheless, as one is interested in the physical situation with an arbitrary aperture in a real metal film of finite thickness, more complex numerical methods become indispensable. Among them, the finite-difference time-domain (FDTD) method⁷ and the field-susceptibility technique (also called Green's dyadic)^{16,17} have been successfully applied to such systems. Here we use the field-susceptibility technique which has proven to be particularly well suited to near-field optics studies^{18,19} and investigations of single molecule interaction with a confined field.^{19,20} In the following, we briefly summarize the main steps of this formalism. More details can be found in Ref. 18. The geometry of the problem is schematically shown in Fig. 2. A ho-

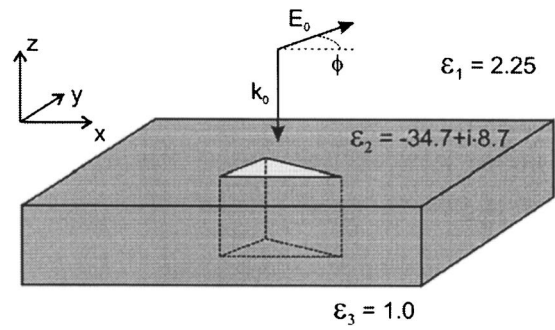


FIG. 2. Geometry of the model for the numerical calculations. An aperture of given shape in an aluminum film of 100 nm thickness is illuminated by a plane electromagnetic wave ($\lambda=488$ nm) at normal incidence. The polarization angle ϕ of the electric field E_0 is measured in respect to the x direction.

mogeneous electric field of vacuum-wavelength $\lambda=2\pi c/\omega=488$ nm illuminates the aperture in an aluminum film at normal incidence with a polarization angle Φ . The metal is described by its complex permittivity $\epsilon_2(\omega)=-34.7+i8.7$; the upper and lower media are glass ($\epsilon_1=2.25$) and air ($\epsilon_3=1$), respectively, to reproduce the probe characteristics.

An efficient way of using the field-susceptibility formalism is to consider first a reference system for which the associated field susceptibility is known. In our case this reference system is a plane metallic film of thickness d and infinite extension. The associated field-susceptibility $S_0(\mathbf{r}, \mathbf{r}', \omega)$ of such a system is straightforwardly deduced from a careful analysis of the electric field scattered by a dipole in a stratified media and can be found in the literature.^{17,21} Then we transform this reference system to the studied geometry, here a hole in the film which is simply modeled by adding N glass cubes of volume a^3 inside the film. The field susceptibility associated to the final system obeys the Dyson equation

$$\mathbf{S}(\mathbf{r}, \mathbf{r}', \omega) = \mathbf{S}_0(\mathbf{r}, \mathbf{r}', \omega) + a^3 \sum_{k=1,N} \mathbf{S}_0(\mathbf{r}, \mathbf{r}_k, \omega) \chi(\omega) \mathbf{S}(\mathbf{r}_k, \mathbf{r}', \omega),$$

$$\chi(\omega) = \frac{\epsilon_1 - \epsilon_2(\omega)}{4\pi}, \quad (1)$$

which is numerically solved.¹⁸ The electric field in the final system is then obtained from the Lippmann-Schwinger equation

$$\mathbf{E}(\mathbf{r}, \omega) = \mathbf{E}_0(\mathbf{r}, \omega) + a^3 \sum_{k=1,N} \mathbf{S}(\mathbf{r}, \mathbf{r}_k, \omega) \chi(\omega) \mathbf{E}_0(\mathbf{r}_k, \omega), \quad (2)$$

in which $\mathbf{E}_0(\mathbf{r}, \omega)$ represents the electric field of the reference system that can be found in textbooks.²² Let us point out that beginning with the aluminum film as the reference system instead of free-space as in Ref. 16, the sum runs over the aperture only. Nevertheless, a careful numerical evaluation is required for integrals that appear in the field-susceptibility expression of a stratified medium.²³

IV. NUMERICAL RESULTS AND DISCUSSION

We consider here two geometries: a circular aperture with a diameter of 50 nm and an equilateral triangular aperture with a side length of 50 nm. In both cases, the thickness of the metal film was chosen to be 100 nm. As illustrated in Fig. 2 the apertures are illuminated with polarized light at normal incidence. The electric field intensity is calculated 10 nm below the aperture which roughly corresponds to the mean distance of the aperture to the center of the fluorescing spheres in our experimental characterization. In all cases the calculated intensity is normalized to the incident beam intensity. As a reference we first simulated the field intensity at a circular aperture in a planar aluminum film [Fig. 3(a)]. As it is well-known from the solution of Bouwkamp² for an aperture in an infinitely thin, ideally conducting film, two maxima of equal intensity appear which are closely located below the metallic rim and are oriented along the direction of polarization. Due to the symmetry of the aperture the con-

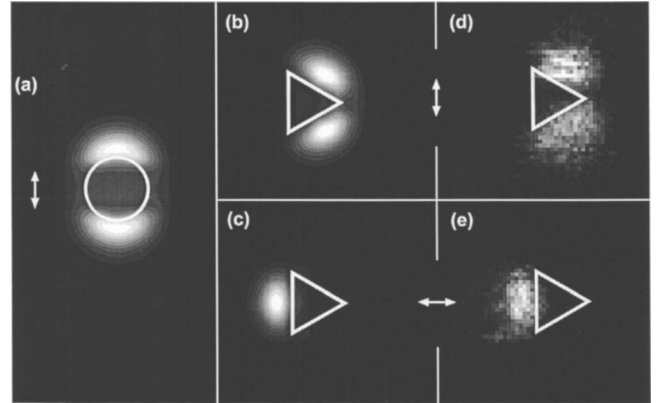


FIG. 3. Normalized electric field intensity computed at $z = -10$ nm for (a) a circular aperture and a polarization angle $\phi = 90^\circ$; (b),(c) the same for a triangular aperture with (b) $\phi = 90^\circ$ and (c) $\phi = 0^\circ$; (d),(e) measured field map of a TA probe at a distance of ~ 10 nm from the triangular aperture for (d) $\phi = 90^\circ$ and (e) $\phi = 0^\circ$. Location and shape of the respective apertures are marked by a white line; double arrows indicate the polarization direction of the incident light. Intensity scales linearly with grayscale; constant increments between successive contour lines in (a)–(c).

nnecting line of the spots is always parallel to the polarization direction and the shape of the pattern does not change with the polarization angle.

Figures 3(b) and 3(c) show the calculated field intensities at a triangular aperture for polarization directions parallel and perpendicular, respectively, to the left edge of the triangle. For comparison, the corresponding experimental field patterns for a TA probe⁶ are displayed in Figs. 3(d) and 3(e). The shape and intensity distribution of the calculated field patterns closely resemble the measured ones for both cases, the parallel as well as the perpendicular polarization direction. Even the initially unexpected location of the measured intensity maxima far outside the aperture is properly reproduced in the simulation. When the incident beam is perpendicular to one edge, the electric field emerging from the triangular aperture exhibits only one intense spot with a full width at half maximum (FWHM) of ~ 30 nm. This highly confined and intense electric field was shown to be useful for optical imaging with a resolution in the range of 30–40 nm.⁶ For similar dimensions the circular aperture creates a less intense and less confined near-field (FWHM ~ 100 nm). A comparison of the calculated intensity values of the triangular and the circular apertures shows that the suppression of one spot at the triangular aperture involves an at least three-fold higher intensity at the remaining spot.

Furthermore, we numerically investigated the effect of a continuous variation of the polarization of the incident beam on the aperture field and compared the calculation with our experimental data. Figure 4 shows the calculated intensity at the center of one edge as a function of the polarization angle ϕ of the incident beam. A fit of our numerical solution to a simple analytical function reveals that apart from a small offset the polarization-dependent intensity closely follows a $\cos^2\phi$ law. This finding is in good agreement with the respective experimental data of a TA probe shown in Fig. 1(b).

Figure 5 displays the normalized intensity of the E_z and the E_x component at the triangular aperture in case of a per-

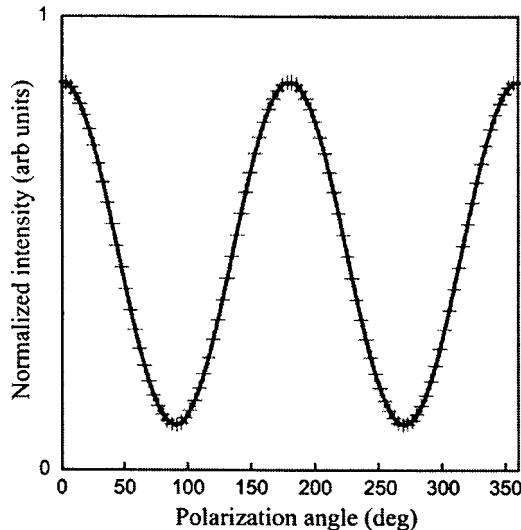


FIG. 4. Calculated intensity at the center of the bright spot of Fig. 3(c) as a function of the polarization angle ϕ (cross symbols). The solid line is a fit of the numerical data to a $\cos^2\phi$ function.

perpendicular polarization direction of the incident beam. The respective intensity of E_y is negligibly small and therefore not shown. From Fig. 5 it follows that the large shift of the confined spot seems mainly to be caused by a strong E_z component appearing on the metal film far outside the aperture. Owing to the well-known boundary conditions of electromagnetic fields at interfaces, the normal component E_z of the electric field is continuous at a surface of discontinuity and thus can take on large values even at a metal/air interface. However, it is surprising that the intensity maximum of $|E_z|^2$ is shifted ~ 25 nm away from the aperture while at the rim $|E_z|^2$ is almost vanishing. In particular, such a behavior

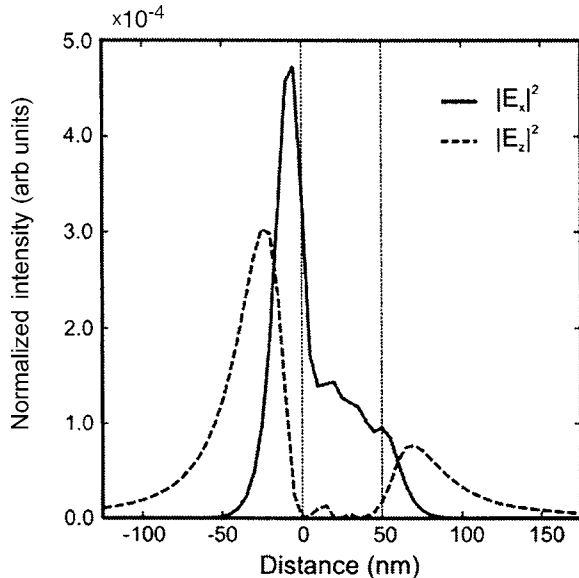


FIG. 5. Cross sections through the calculated field distributions of $|E_z|^2$ (dashed line) and $|E_x|^2$ along the y axis ($x=0$) at a distance of $z=-10$ nm behind a 50-nm-sized triangular aperture. The dotted lines indicate the position of the aperture [same orientation as in Fig. 3(c)].

does not seem to fit into a surface-plasmon-polariton (SPP) model recently proposed as a possible transmission mechanism through the aperture.⁸ A clue to the phenomenon of the displaced high electric field intensity may be found in the near-field distribution of the magnetic field. Preliminary calculations indeed indicate that magnetic fields penetrating the aperture might play an important role in shaping the spot; however, further theoretical studies are necessary to clarify this point. Here we want to focus mainly on a discussion of the field pattern in relation to the imposed boundary conditions and on the influence of material parameters on the shape of the spots.

The computational analysis presented so far clearly confirms our previous experimental result that the reduction of symmetry of the aperture shape can lead to an enhanced confinement of the electric near field. In the following we want to point out that the number and the positions of the bright spots are a direct manifestation of the boundary conditions at the film-air interface.^{7,17,24} When the incident beam is polarized along the x axis, the electric field is normal to the left edge of the triangular aperture depicted in Figs. 3(b)–3(e). The discontinuity of the field component normal to the metallic film implies a nonzero field at this edge. The other edges are inclined by 60° to the x axis and the amplitude of the component of the x -polarized incident field E_0 normal to these edges is $E_0 \cos(60^\circ) = \frac{1}{2}E_0$ and its intensity is $\frac{1}{4}E_0^2$. This simple argument thus explains almost quantitatively the result of the numerical calculations. The behavior of electromagnetic fields at metallic edges also explains that for a beam polarized in the y direction the intensity vanishes at the edge oriented along the y axis. Since the electric field component normal to the edge is proportional to $\cos\phi$, the boundary conditions predict the same polarization dependency for the intensity as observed in our simulation.

After this general discussion about the shape of the near-field pattern at the tip output we turn to the parameters governing the spot formation for an incident beam polarized normal to one edge. The major aim of this investigation is to find a way to further improve the performance of the TA probe for near-field optical applications. In particular, we are interested in parameters influencing spot confinement and location. At first, we calculated the electric intensity 10 nm below the aperture for several different sizes (see Fig. 6 and Table I). It turned out that spot shift and confinement normal to the edge are almost independent of the aperture size whereas the transmitted intensity and the extension of the spot along the edge increase with triangle length. Apparently, due to the almost constant width of the spot in the direction normal to the edge, no improved confinement can be expected by further decreasing the aperture size below a value of ~ 30 nm. This behavior is in good quantitative agreement to previous measurements with TA probes of largely different aperture size (Figs. 2(d) and 3(d) in Ref. 6).

As a consequence, further improvement can only be expected by changing other parameters. In the following we study the role of the metal properties in spot formation. Figure 7 represents the near-field intensity for a triangular aperture in silver as well as in a very good conductor at optical frequencies (VGC). The VGC is simulated by setting the imaginary part of the dielectric permittivity to zero and the

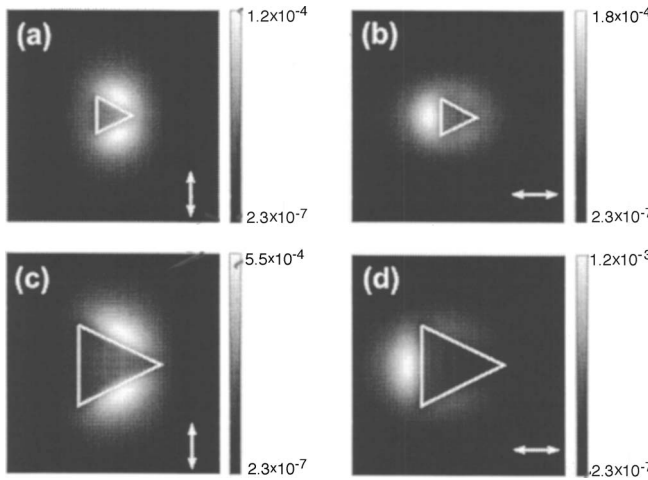


FIG. 6. Calculated intensity distributions at a distance of $z = -10$ nm behind a triangular aperture in a 100-nm-thick Al film for two different side lengths a of the triangle; (a), (b) $a=33$ nm, and (b), (c) $a=72$ nm. Double arrows indicate the polarization direction of illumination. Intensity values scale linearly with grayscale and are normalized to the incident intensity I_0 .

respective real part to a relatively large value.²⁵ For such an idealized metal, the transmitted intensity turned out to be very low as compared to a real metal. For a better comparison, the thickness of the VGC film was chosen such that the transmission of a plain film equals the transmission of a 100-nm-film of aluminum. The electric field intensity at a triangular aperture in a VGC film is clearly better confined (FWHM ~ 28 nm) and the intensity maximum is located much closer to the rim of the aperture. We assume therefore that for a perfect conductor and vanishing distance the peak intensity is located just below the rim of the aperture as it is the case in Bethe's model for a circular aperture. Using silver instead of aluminum as screen material, the transmitted intensity is much higher but the spot confinement is worse. Thus, we conclude that in the case of a triangular aperture the choice of the metal has a large influence on spot location as well as on field confinement. The peak intensity shift is probably a direct consequence of the finite field penetration

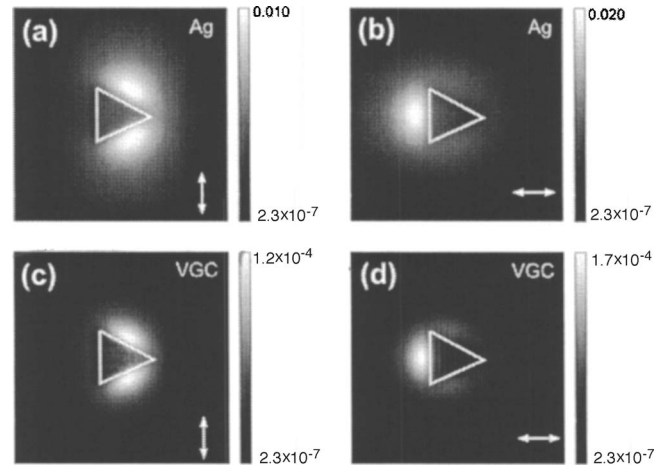


FIG. 7. Calculated intensity distributions at a distance of $z = -10$ nm behind a 50-nm-sized triangular aperture in a 100-nm-thick metal film for (a), (b) silver ($\epsilon = -7.9 + i \cdot 0.73$) and (b), (c) a very good conductor at optical frequencies (VGC, $\epsilon = -100.0 + i \cdot 0.0$) as film material. Double arrows indicate the polarization direction of illumination. Intensity values scale linearly with grayscale and are normalized to the incident intensity I_0 .

of the electric and magnetic fields into the metal film. We want to stress, however, that this shift depends on both metal properties and aperture shape. Though the skin depth of a silver film is about twice as large as the skin depth of an aluminum film [$\delta(\text{Ag}) \sim 28$ nm and $\delta(\text{Al}) \sim 13$ nm], the additional shift caused by the change in material ($\Delta = 1.6$ nm; Al and Ag for a 50-nm-sized triangular aperture) is smaller than the additional shift caused by the change in aperture shape ($\Delta = 2.8$ nm; 50-nm-sized Al-coated circular and triangular aperture).

In summary, we have shown in this study that the experimentally and theoretically obtained field distribution in a triangular aperture can be understood as a direct consequence of the boundary conditions of electromagnetic fields at metallic edges. An enhancement effect of the triangular aperture with respect to the circular aperture is explained by the numerical calculations. However, only a precise analysis of en-

TABLE I. (a) Spot characteristics for a triangular aperture in a plane aluminum film of thickness $d = 100$ nm as a function of aperture size. The incident field is polarized along the x axis and the excitation wavelength is $\lambda = 488$ nm. The side length a of the triangles ranges from 33 to 72 nm. The spot size (FWHM ~ 36 nm) as well as the peak shift ($\Delta x \sim 11$ nm) is almost independent of the aperture size. The maximum values of the transmitted light I_{\max} are given in relation to the incident intensity I_0 . (b) For comparison the respective values for a 50-nm-triangular aperture in silver ($d = 211$ nm, $\epsilon = -7.9 + i \cdot 0.73$) and a very good conductor (VGC, $d = 61$ nm, $\epsilon = -100.0 + i \cdot 0.0$) as well as for a circular aperture in aluminum (diameter $a = 50$ nm) are also shown. The film thicknesses are chosen such that the transmission without aperture is the same for all materials.

Aperture shape	Triangular						Circular	
	Al				VGC	Ag	Al	
Material								
a (nm)	33.3	50.0	55.6	61.1	66.7	72.2	50.0	50.0
FWHM (nm)	35	38	36	35	36	36	27	44
Δx (nm)	11	11	12	12	11	12	9	12
$I_{\max}/I_0 (\times 10^{-4})$	1.82	5.18	6.6	8.0	9.5	11.0	1.7	200

ergy transmission through the aperture can lead to a conclusive physical picture of the involved effects. We will investigate this in the near future.

Finally, we want to mention, that there are still open questions. We frequently observe in our experiments that by moving the normal polarization direction from one edge of the triangular aperture to another, the respective intensity ratios of the bright spot to the weak spots can considerably vary. In some cases this ratio is much larger than expected from calculations in which the illumination angle is allowed to deviate from normal incidence (not shown here). Though this effect is of great advantage for the use of a triangular aperture as probe in a SNOM measurement, because it results in a further field confinement, we did not yet find a conclusive explanation for it.

V. CONCLUSION

We have demonstrated experimentally and theoretically that at a nanometer scale the shape of an illuminated aperture in a metal film can have a large influence on both light confinement and transmission. On the basis of a simplified numerical model we investigated the influence of aperture size and film material on the field distribution at a triangular aperture. Compared to a circular aperture the reduced symmetry of a triangular aperture is accompanied by greatly enhanced and confined electric field intensities in the

immediate vicinity of the aperture when the incident beam is perpendicularly polarized to one edge of the triangle. The agreement between experiment and simulation turned out to be excellent, though our theoretical model of an aperture in a planar film considerably deviates from the actual geometry of the experimentally studied TA probe. This result can be largely understood by considering the behavior of electromagnetic fields at metallic edges. By applying the boundary conditions of electric fields to a triangular aperture in a metal film, we found the same angular dependence of the field pattern on the polarization state of the incident light as with our rigorous numerical solution based on Maxwell's equations.

ACKNOWLEDGMENTS

We thank H. Fuchs for continuous support of this work. G.C.F. benefits from the financial support of the European Community. D.M. was supported partly by the German Ministry of Research (BMBF 13N7641/4) and the Volkswagen foundation (VW1/75 098). A.N. gratefully acknowledges the generous support from the Deutsche Forschungsgemeinschaft (DFG, NA 382/1 and NA 382/2). U.C.F. also acknowledges support of the Deutsche Forschungsgemeinschaft (DFG Fi 608/5). The cooperation of the authors profits from the IST Network of excellence "plasmo-nano-devices" in the sixth Framework Programme of the European Community.

*Electronic Mail: andreas.naber@physik.uni-karlsruhe.de

- ¹H. A. Bethe, Phys. Rev. **66**, 163 (1944).
- ²C. J. Bouwkamp, Philips Res. Rep. **5**, 321 (1950); C. J. Bouwkamp, Rep. Prog. Phys. **XVII**, 35 (1954).
- ³E. Betzig and R. J. Chichester, Science **262**, 1422 (1993).
- ⁴B. Hecht, B. Sick, U. P. Wild, V. Deckert, R. Zenobi, O. J. F. Martin, and D. W. Pohl, J. Chem. Phys. **112**, 7761 (2000).
- ⁵N. Hosaka and T. Saiki, J. Microsc. **202**, 362 (2001).
- ⁶A. Naber, D. Molenda, U. C. Fischer, H.-J. Maas, C. Höppener, N. Lu, and H. Fuchs, Phys. Rev. Lett. **89**, 210801 (2002).
- ⁷K. Tanaka, M. Oumi, T. Niwa, S. Ichihara, Y. Mitsuoka, K. Nakajima, T. Ohkubo, H. Hosaka, and K. Itao, Jpn. J. Appl. Phys., Part 1 **42**, 1113 (2003).
- ⁸K. Tanaka and M. Tanaka, Appl. Opt. **43**, 1734 (2004).
- ⁹J. Koglin, U. C. Fischer, and H. Fuchs, Phys. Rev. B **55**, 7977 (1997).
- ¹⁰A. Naber, H.-J. Maas, K. Razavi, and U. C. Fischer, Rev. Sci. Instrum. **70**, 3955 (1999).
- ¹¹T. Saiki and K. Matsuda, Appl. Phys. Lett. **74**, 2773 (1999).
- ¹²C. Höppener, D. Molenda, H. Fuchs, and A. Naber, Appl. Phys. Lett. **80**, 1331 (2002).
- ¹³H. Gersen, M. F. García-Parajó, L. Novotny, J. A. Veerman, L. Kuipers, and N. F. vanHulst, Phys. Rev. Lett. **85**, 5312 (2000).
- ¹⁴J.-D. Jackson, *Classical Electrodynamics*, 3rd ed. (Wiley, New York, 1993).
- ¹⁵X. Shi, R. Thornton, and L. Hesselink, Proc. SPIE **4342**, 320 (2001).
- ¹⁶K. Tanaka and M. Tanaka, J. Microsc. **210**, 294 (2003).
- ¹⁷O. J. F. Martin and M. Paulus, J. Microsc. **205**, 147 (2001).
- ¹⁸C. Girard, A. Dereux, and O. J. F. Martin, "Theory of Near Field Optics" in *Photons and Local Probes*, edited by O. Marti and R. Möller, NATO Advanced Studies Institute, Series E: Applied Sciences (Kluwer Academic Publishers, Dordrecht, 1995), Vol. 300, pp. 1–20.
- ¹⁹A. Dereux, C. Girard, and J. C. Weeber, J. Chem. Phys. **112**, 7775 (2000).
- ²⁰C. Girard, O. J. F. Martin, G. Lévéque, G. Colas des Francs, and A. Dereux, Chem. Phys. Lett. **404**, 44 (2005).
- ²¹M. S. Tomás, Phys. Rev. A **51**, 2545 (1995).
- ²²M. Born and E. Wolf, *Principles of Optics*, 4th ed. (Pergamon Press, London, 1970).
- ²³M. Paulus, P. Gay-Balmaz, and O. J. F. Martin, Phys. Rev. E **62**, 5797 (2000).
- ²⁴J. Meixner, IEEE Trans. Antennas Propag. **AP-20**, 442 (1972).
- ²⁵Due to limitations in the accuracy of the used numerical method, the dielectric permittivity chosen for the "very good conductor" is limited to $\epsilon_2 = -100 + i \cdot 0$. Naturally, this is still far from representing a perfect conductor; however, due to the marked differences of the resulting field distribution as compared to that of a real metal, such a conductor can be used to extrapolate the results of a perfect conductor.

2.1.2 Fluorescence de molécules individuelles

Discussion

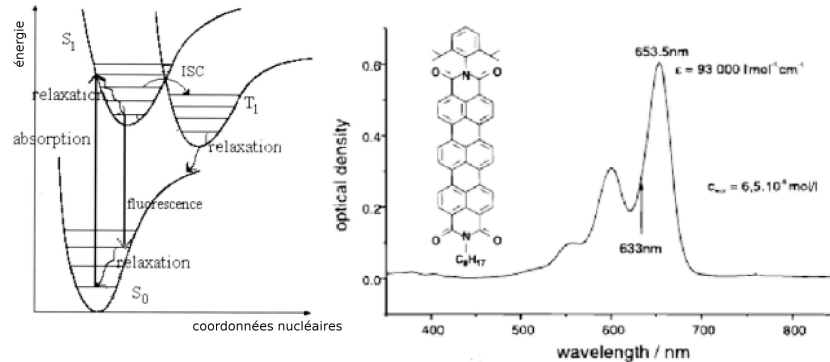


FIG. 2.2 – a) Représentation schématique des états électroniques (singulets S_0 , S_1 et triplet T_1) et vibrationnels (traits horizontaux) d'une molécule fluorescente (d'après [27]). b) Spectre d'absorption d'une solution de TDI (tiré de [28]).

L'objectif de cette discussion est de déterminer un ordre de grandeur du rapport signal sur bruit de fluorescence accessible avec la sonde à ouverture triangulaire caractérisée au paragraphe précédent. La figure 2.2 donne une représentation schématique des états moléculaires. Le cycle absorption-émission se produit entre les niveaux vibrationnels des deux états électroniques singulets S_0 et S_1 . Le croisement intersystème (ISC) vers l'état triplet T_1 correspond à une transition non radiative, interdite de spin, et diminue donc le nombre de photons de fluorescence. Le décalage Stokes entre les longueurs d'ondes d'absorption et d'émission est dû aux relaxations vibrationnelles, non radiatives aussi, au sein d'un même niveau électronique. Finalement, l'efficacité du processus absorption-fluorescence est quantifiée par le rendement quantique de fluorescence Φ_F , rapport du nombre de photons émis sur le nombre de photons absorbés par la molécule. Les molécules fluorescentes usuelles ont des Φ_F compris entre 0,1 et 1. Dans l'expérience qui suit, nous avons utilisé des molécules de terrylenediimide (TDI) qui présentent une bonne stabilité et une efficacité quantique élevée ($\Phi_F = 0,9$ - Fig. 2.2b).

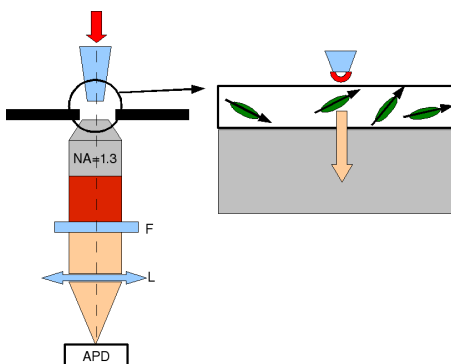


FIG. 2.3 – Représentation schématique du montage utilisé pour l'excitation localisée de molécules individuelles. Des molécules dispersées de manière aléatoire dans une matrice de polymère sont excitées localement avec une sonde SNOM. F : filtre bloquant le signal d'excitation transmis ($\lambda = 633 \text{ nm}$). L : lentille, APD : photodiode à avalanche.

Le rapport signal sur bruit de fluorescence d'une molécule unique est donné par [27]

$$SNR = \frac{\eta_{det} I_{fluo}}{\sqrt{\eta_{det} I_{fluo}(1 + k\sigma_{diff}nV/\sigma_{abs}) + N_{APD}T}}, \quad (2.1)$$

$$I_{fluo} = \sigma_{abs} \frac{P_{out}}{Ah\nu} \Phi_F T \quad (2.2)$$

Dans cette expression, $\eta_{det}\sigma_{abs}(P_{out}/Ah\nu)\Phi_F T$ est le signal de fluorescence détecté, avec η_{det} l'efficacité de la chaîne de détection (incluant l'objectif de collection, les filtres et l'efficacité de la photodiode, η_{det} est estimé à 6.10^{-3} dans notre montage), σ_{abs} la section efficace d'absorption ($\sigma_{abs} = 3,5.10^{-20} m^2$ pour le TDI), P_{out} la puissance d'excitation à la sortie de la sonde (en W), A l'aire de focalisation, $h\nu$ l'énergie d'un photon ($h\nu = 3,1.10^{-19} J$ pour $\lambda = 633 nm$) et T le temps d'acquisition.

Les termes au dénominateur déterminent le bruit de détection. $k\sigma_{diff}nV$ correspond à la diffusion Rayleigh, à la longueur d'onde d'excitation, par la matrice contenant les molécules fluorescentes. k est l'efficacité de la chaîne de détection à la longueur d'onde d'excitation ; $k \sim 10^{-7}$ pour un montage utilisant des filtres pour éliminer le signal d'illumination. σ_{diff} est la section de diffusion Rayleigh ($\sigma_{diff} \sim 10^{-24} m^2$) et n la densité de molécules de la matrice ($n \sim 10^{11} mol/\mu m^2$). V est le volume d'excitation. Enfin, $N_{APD}T$ représente le bruit de fond de la photodiode à avalanche ($N_{APD} \sim 100 coups/s$ dans l'expérience qui suit).

Finalement, l'intérêt de la microscopie en champ proche pour la spectroscopie de molécules uniques apparaît clairement. D'une part, la réduction de l'aire d'excitation A augmente considérablement le signal de fluorescence émis ($P_{out}/Ah\nu$). D'autre part, le bruit par diffusion Rayleigh est notablement diminué par réduction du volume V d'excitation. Ainsi, le rapport signal sur bruit se réduit alors à

$$SNR \approx \frac{\eta_{det}\sigma_{abs}(P_{out}/Ah\nu)\Phi_F T}{\sqrt{\eta_{det}\sigma_{abs}(P_{out}/Ah\nu)\Phi_F T + N_{APD}T}}. \quad (2.3)$$

En utilisant le confinement du champ électrique à la sortie de la sonde à ouverture triangulaire, on obtient $A = 9,4.10^{-16} m^2$. Ainsi l'utilisation du champ proche optique conduit-elle à une aire d'excitation supérieure à la section efficace d'absorption moléculaire de seulement quelques ordres de grandeurs ($\sigma_{abs} = 3,5.10^{-20} m^2$). Il serait aussi possible d'augmenter la section efficace d'absorption en travaillant à basse température. En effet, les couplages phonons de la molécule avec la matrice hôte sont fortement réduits à très basse température, ce qui permet de s'approcher de la valeur maximale de la section efficace d'absorption $3\lambda^2/2\pi$ (de l'ordre de $10^{-13} m^2$ dans le visible) [29]. Ces quelques ordres de grandeurs révèlent l'intérêt de la microscopie en champ proche, éventuellement combinée à la spectroscopie basse température, pour l'étude de molécules uniques.

Pour une excitation de 2 mW, la puissance à la sortie de la sonde est $P_{out} = 2.10^{-7} W$, ce qui conduit à un rapport signal sur bruit $SNR = 50$ pour un temps d'acquisition de 20 ms. Ce rapport peut encore être amélioré sensiblement en augmentant la puissance d'excitation.

Avant de discuter d'une telle expérience, il faut souligner que des techniques de champ lointain permettent d'obtenir des rapports similaires voire meilleurs. Signalons la microscopie confocale, avec des SNR de l'ordre de 100 mais une résolution (latérale et axiale) moindre (limitée par la diffraction). Enfin, il est apparu très récemment une nouvelle gamme de techniques de microscopie de champ lointain très haute résolution. Elles sont regroupées sous l'acronyme

RESOLFT (reversible saturable optically linear fluorescence) car elles jouent sur un effet de seuil entre un état sombre (saturable) et un état fluorescent pour activer séquentiellement les molécules sondes dispersées dans le système à étudier. Une discussion de l'évolution de la microscopie optique vers la très haute résolution est donnée dans la référence [30]. Ces techniques sont extrêmement prometteuses pour la caractérisation fine de systèmes biologiques.

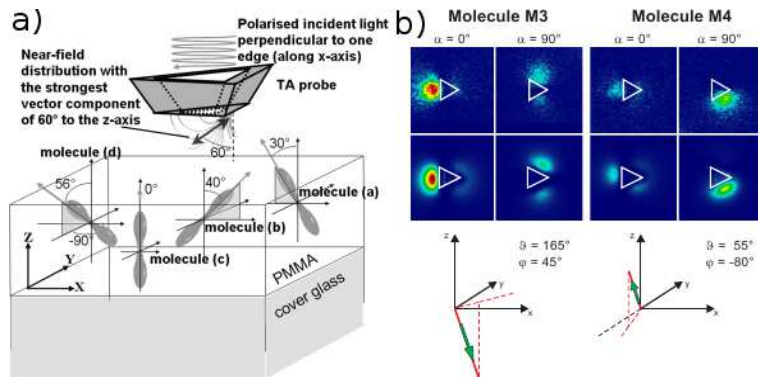


FIG. 2.4 – a) Excitation de molécules individuelles dispersées sur une surface. L'excitation est réalisée grâce à une pointe SNOM d'ouverture triangulaire (50 nm de côté) pour deux polarisations (parallèle - $\alpha = 0^\circ$, ou perpendiculaire - $\alpha = 90^\circ$, à une arête du triangle). b) Image de fluorescence mesurée (ligne du haut) et calculée (ligne du milieu) pour deux molécules différentes. L'orientation des molécules qui en est déduite est donnée sur la ligne du bas. La position latérale de l'ouverture triangulaire est reportée sur chaque image.

Nous avons vu que la sonde locale permet de détecter le signal de fluorescence de molécules uniques avec un rapport signal sur bruit satisfaisant. Des mesures ont été faites par Daniel Molenda lors de sa thèse à l'Université de Münster. Il a déposé un film de polyméthacrylate de méthyle (PMMA) dopé avec des molécules de TDI (concentration $10^{-8} mol.L^{-1}$) sur un substrat de verre. Il a ainsi obtenu des films de 10 à 20 nm d'épaisseur avec environ 10 molécules/ μm^2 . La sonde est ensuite balayée au-dessus des molécules. Le signal de fluorescence détecté dépend de l'orientation (aléatoire) des molécules sur la surface. Dans un modèle simple, la molécule est représentée par son moment dipolaire de transition \mathbf{p} . Le signal de fluorescence est proportionnel à la probabilité d'exciter la molécule par le champ électrique \mathbf{E} à la sortie de la sonde soit $|\mathbf{p} \cdot \mathbf{E}|^2$. En considérant plusieurs orientations possibles et en effectuant des simulations numériques, nous avons pu déterminer avec une grande précision l'orientation des molécules sur la surface (Fig. 2.4). Finalement, les images obtenues présentent une résolution d'environ 30 nm avec un rapport signal sur bruit de 20 en accord qualitatif avec l'ordre de grandeur obtenu précédemment.

Cette configuration de SNOM avec une sonde à ouverture triangulaire est désormais utilisée dans l'équipe d'Andreas Naber, maintenant en poste à l'Université de Karlsruhe, pour l'étude de membranes biologiques [31].

Publication correspondante

“High-resolution mapping of the optical near-field components at a triangular nano-aperture

D. Molenda, G. Colas des Francs, U. Fischer, N. Rau, and A. Naber

Optics Express **13**, 10688 (2005).

High-resolution mapping of the optical near-field components at a triangular nano-aperture

D. Molenda¹, G. Colas des Francs², U.C. Fischer¹,
N. Rau³, and A. Naber³

¹Physikalisches Institut,

Universität Münster, Wilhelm-Klemm-Str. 10, D-48149 Münster, Germany

²Laboratoire de Physique (LPUB-CNRS),

Université de Bourgogne, 9, av. A. Savary, BP 47870, F-21078 Dijon cedex, France

³Institut für Angewandte Physik,

Universität Karlsruhe (TH), Wolfgang-Gaede-Str. 1, D-76131 Karlsruhe, Germany

andreas.naber@physik.uni-karlsruhe.de

Abstract: A triangular nano-aperture in an aluminum film was used as a probe in a scanning near-field optical microscope (SNOM) to image single fluorescent molecules with an optical resolution down to 30 nm. The differently oriented molecules were employed as point detectors to map the vectorial components of the electric field distribution at the illuminated triangular aperture. The good agreement of the experimental results with numerical simulations enabled us to determine both the field map at a triangular aperture and the exact orientations of the probing molecules.

©2005 Optical Society of America

OCIS codes: (180.5810) Scanning microscopy; (180.2520) Fluorescence microscopy;
(050.1220) Apertures; (050.1960) Diffraction theory; (999.9999) Nano-optics

References and links

1. For a recent review, see B. Hecht, "Nano-optics with single quantum systems," *Phil. Trans. R. Soc. Lond. A* **362**, 881-899 (2004).
2. A. Dereux, C. Girard, and J.C. Weeber, "Theoretical principles of near-field optical microscopies and spectroscopies," *J. Chem. Phys.* **112**, 7775 (2000).
3. S. Linden, U. Neuberth, N. Rau, A. Naber, M. Wegener, S. Pereira, K. Busch, A. Christ, and J. Kuhl, "Near-field optical microscopy and spectroscopy of one-dimensional metallic photonic crystal slabs," *Phys. Rev. B* **71**, 245119 (2005).
4. E. Betzig and R. Chichester, "Single Molecules Observed by Near-Field Scanning Optical Microscopy," *Science* **262**, 1422 (1993).
5. J.A. Veerman, M.F. Garcia-Parajo, L. Kuipers, and N.F. van Hulst, "Single molecule mapping of the optical field distribution of probes for near-field microscopy," *J. Microsc.* **194**, 477 (1999).
6. H.G. Frey, S. Witt, K. Felderer, and R. Guckenberger, "High-Resolution Imaging of Single Fluorescent Molecules with the Optical Near-Field of a Metal Tip," *Phys. Rev. Lett.* **93**, 200801 (2004).
7. J. Koglin, U.C. Fischer, and H. Fuchs, "Material contrast in scanning near-field optical microscopy at 1–10 nm resolution," *Phys. Rev. B* **55**, 7977 (1997).
8. A. Naber, D. Molenda, U.C. Fischer, H.J. Maas, C. Höppener, N. Lu, and H. Fuchs, "Enhanced Light Confinement in a Near-Field Optical Probe with a Triangular Aperture," *Phys. Rev. Lett.* **89**, 210801 (2002).
9. J.A. Veerman, A.M. Otter, L. Kuipers, and N.F. van Hulst, "High definition aperture probes for near-field optical microscopy fabricated by focused ion beam milling," *Appl. Phys. Lett.* **72**, 3115 (1998).
10. G. Colas des Francs, D. Molenda, U.C. Fischer, and A. Naber, "Enhanced light confinement in a triangular aperture: Experimental evidence and numerical calculations," *Phys. Rev. B* **72**, 165111-6 (2005).
11. E. Bortchagovsky, G. Colas des Francs, D. Molenda, A. Naber, and U.C. Fischer, "On the confinement of the electric near field at optically excited triangular apertures in a metal film" (submitted).
12. K. Tanaka and M. Tanaka, "Analysis and numerical computation of diffraction of an optical field by a sub-wavelength-size aperture in a thick metallic screen by use of a volume integral equation," *Appl. Opt.* **43**, 1734 (2004).
13. F. de Lange, A. Cambi, R. Huijbens, B. de Bakker, W. Rensen, M. Garcia-Parajo, N.F. van Hulst, and C.G. Figdor, "Cell biology beyond the diffraction limit: near-field scanning optical microscopy," *J. Cell Science* **114**, 4153-60 (2001).

14. M. Koopman, A. Cambi, B.I. de Bakker, B. Joosten, C.G. Figdor, N.F. van Hulst, and M.F. Garcia-Parajo, "Near-field scanning optical microscopy in liquid for high resolution single molecule detection on dendritic cells," *FEBS Lett.* **573**, 6-10 (2004).
 15. C. Höppener, J.P. Siebrasse, R. Peters, U. Kubitscheck, and A. Naber, "High-Resolution Near-Field Optical Imaging of Single Nuclear Pore Complexes under Physiological Conditions," *Biophys. J.* **88**, 3681-8 (2005).
-

1. Introduction

Optical properties of single metallic or non-metallic nanostructures are still mainly investigated by classical methods like absorption and transmission measurements of light. Spatial information on a scale larger than half the wavelength of light ($\lambda/2$) can be easily obtained using conventional far-field optical microscopy techniques. The intensity distribution of the electromagnetic fields in the immediate vicinity of nanostructures, however, can only be deduced from near-field optical methods since the information contained in the evanescent fields around such structures are not transferred to the far-field [1].

The usual way to measure an optical near-field is to scan a submicroscopic detector several nanometers over the sample such that probe and sample can interact with each other via evanescent fields. The achievable optical resolution is mainly limited by the size of the detector and its distance to the sample. In a photon scanning tunneling microscope (PSTM), for example, the sharp tip of a tapered optical glass fiber or a submicroscopic aperture at the very end of a metal-coated glass fiber are employed as detectors for the near-field. The interpretation of a PSTM measurement, however, can be rather complicated because the influence of the probe on the field map as well as the special characteristics of the probe as detector for different electric and magnetic field components have to be taken into account [2,3].

A very effective method to determine the field map of an illuminated metallic nanostructure with molecular resolution was found by Betzig and Chichester in the context of the first single molecule fluorescence measurements at room temperature [4]. The fluorescence of single molecules embedded in a thin film of polymer was locally excited through a circular, 100-nm-sized aperture of a near-field probe and collected by an optical microscope. By scanning the aperture at a distance of 10 nm over a molecule, the intensity of the resulting fluorescence was modulated according to the varying local electric field intensity of the extended field distribution around the aperture. Thus, the measured fluorescence image corresponded to an intensity map of the electric field in the fixed direction of the molecular dipole transition 10 nm below the aperture. By comparing the field map with results of a well known theoretical model it was possible to roughly determine the orientation of a molecule within the polymer film. So far, similar measurements could be accomplished only for apertures sizes $d > 70$ nm and were carried out exclusively with circular apertures [4,5]. Recently, such a method was also used to characterize the electric field emitted by a *tip-on-aperture* [6].

In this paper, the electric field map at a 50-nm-sized triangular aperture (TA) in a metallic film is revealed using single molecule fluorescence measurements in combination with a numerical model. The excellent agreement of experimentally obtained field maps with results of the numerical simulation allowed us to determine with high accuracy the vectorial field components at a triangular aperture as well as the orientation of the measured molecules. Vice versa, we are able to demonstrate that a triangular aperture as near-field optical probe (TA probe) makes it possible to detect single fluorescent molecules with an optical resolution down to 30 nm. The high signal-to-noise ratio enabled us to localize a molecule within a few nanometers on a time scale of 20 ms.

2. Background and experimental details

Our method to form a triangular nano-aperture is based on a tetrahedral glass body which is simply fabricated by scratching and cleaving of a cover glass [7]. The common tip of three

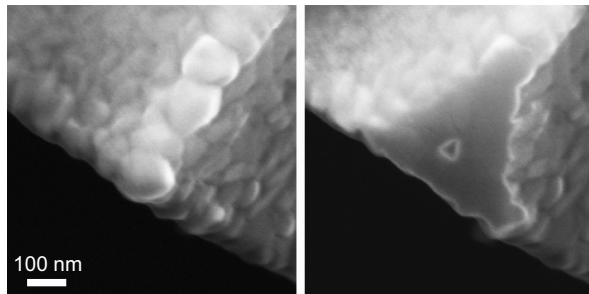


Fig. 1. Electron micrographs of an aluminum-coated tetrahedral glass tip before (left) and after (right) focused ion beam milling. Cutting off the metal-coated, ultra-sharp glass tip routinely results in a well-shaped triangular nano-aperture embedded in a flat aluminum end face.

orthogonal cleavage edges is known to be extraordinarily sharp which enables us to create TAs with sizes in the 10-nm-regime. After coating the glass tip with an opaque film of aluminum, an almost equilateral TA was formed either by gently squeezing the metal-coated tetrahedral tip against a flat glass surface [8] or by side-milling using a focused ion beam [9] (Fig. 1). The aperture is illuminated through the glass body along the direction of symmetry by means of a focused laser beam (wavelength $\lambda=633$ nm). Recently, such a TA was used as near-field probe for imaging quantum dot aggregates with an optical resolution of 30-40 nm [8]. Owing to the large opening angle of the glass tip, a TA probe proved to have an optical transmission coefficient several orders higher than conventional SNOM aperture probes based on thermally pulled fiber tips.

Previously, we have used single 20-nm-sized polystyrene beads doped with a large number of differently oriented fluorescent molecules to map the optical near-field of a TA probe [8]. Due to the isotropic absorption properties of such beads, however, only the scalar intensity distribution could be measured. The results of a numerical simulation based on the field susceptibility technique were shown to be in good agreement to the experimental results though only a simplified model of an aperture in a planar film was used for the calculations [10].

To illuminate the unique electromagnetic properties of a TA, the calculated field maps of a circular aperture and a TA are compared in Fig. 2. Instead of two intensity maxima as in the case of a circular aperture, the electric field distribution at a TA is mainly confined to one side if the TA is illuminated with light of a polarization directed perpendicular to one of the three edges. For a polarization direction parallel to an edge, however, a field map is created which corresponds qualitatively to the one of a circular aperture (not shown) [8,10].

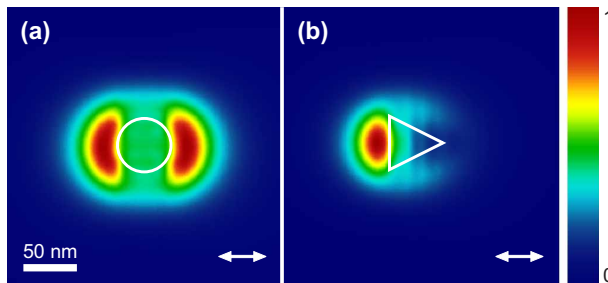


Fig. 2. Scalar electric field intensity calculated near a circular (a) and a triangular nano-aperture (b). The aluminum slab (thickness $d=100$ nm) separates a glass and an air half-space; the aperture is filled with glass. For the simulation, the aperture is assumed to be illuminated from the glass side by a monochromatic plane wave ($\lambda=633$ nm) which is linearly polarized parallel to the slab (white arrows). The intensity map is calculated at the air side in a plane 10 nm below the film (see also Fig. 5(a)). Intensities are normalized to the respective maximum values.

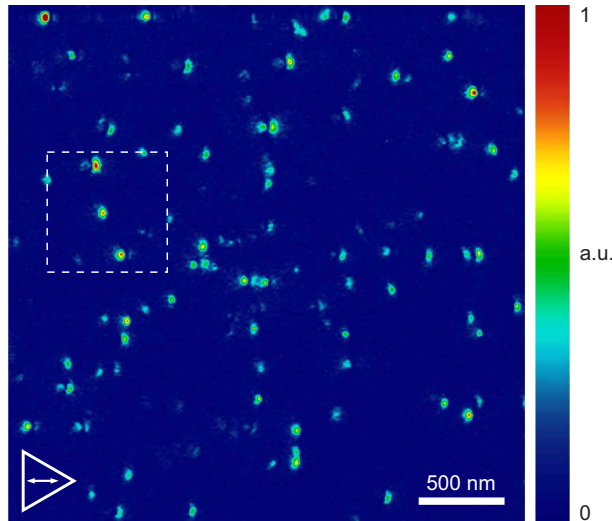


Fig. 3. Near-field optical fluorescence image of randomly oriented TDI molecules embedded in a 10-nm-thin PMMA film. The molecules are excited by means of a triangular aperture probe. The aperture is aligned relative to the sample as indicated by the white triangle. The white double-arrow represents the incident beam polarization. For an enlarged view of the framed area, see Fig. 4.

The major aim of this work was to measure the vectorial components of the electric field map at a TA by making use of differently oriented single molecules as detectors and to compare the experimental results with numerical calculations from our theoretical model. For this purpose, terrylenediimide (TDI) molecules were embedded in a 10-nm-film of polymethylmethacrylate (PMMA) by spin-coating an appropriate solution of TDI/PMMA/toluol on a clean cover slide. Our measurements described below indicate that under ambient conditions the spatial orientation of the TDI molecules in the PMMA film seems to be frozen to an arbitrary direction. Mainly as a result of the finite thickness of the PMMA film, the distance of the molecules to the TA ranges from 10 nm to 20 nm.

Fluorescence excitation of the molecules occurred through the near-field of the aperture which was illuminated by focused laser light ($\lambda=633$ nm) with a typical power of 1 mW. The fluorescence light was collected by a 1.3-numerical-aperture oil-immersion-objective and was detected by an avalanche photo diode after passing a filter combination to suppress the excitation light (for more details, see Ref. 8).

3. Experimental results

Figure 3 displays a fluorescence image of TDI molecules in PMMA taken by a TA probe with a 50-nm-sized optical aperture. The image covers an area of $3\mu\text{m} \times 3\mu\text{m}$ in which ~ 100 fluorescence spots of varying shape and intensity appear. Each of these patterns is interpreted as near-field map of a triangular aperture probed by a single, arbitrarily oriented molecule. The signal-to-noise (S/N) ratio of the intense spots is in the range of 20-30 (pixel time of 20 ms) and thus clearly higher than in comparable studies using fiber probes with larger apertures. Since the TA probe turned out to withstand laser intensities of > 50 mW, the S/N ratio may even be further improved easily. The distinct improvement of S/N ratio originates from the special geometry of a TA probe: first, the large taper angle of $\sim 90^\circ$ provides a relatively high transmission of light; and second, the excitation light is focused directly to the aperture through an only 0.5 mm long piece of glass thus avoiding unwanted background, for example, from a light-guiding fiber.

The fluorescence spots appearing in the image can be roughly classified in two categories: about half of the spots are composed of two sub-spots of different shape and intensity with a

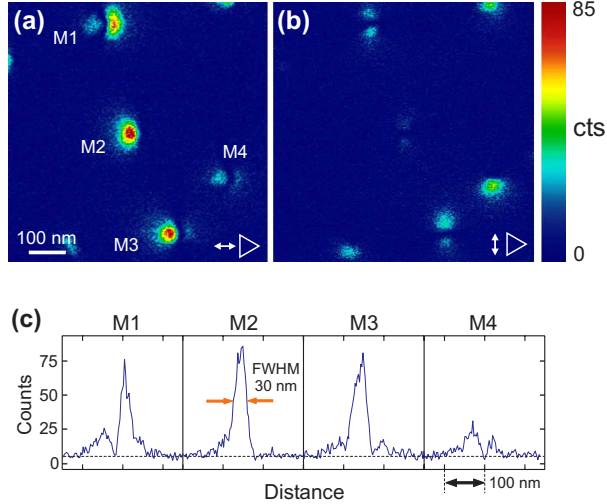


Fig. 4. (a,b) Enlarged view of the framed sample area in Fig. 3 for two different polarization directions of the incident light (indicated by double-arrows). As a result of the polarization rotation the intensity maximum and distribution of the fluorescence spots drastically changed. The different shape of the spots within an image is caused by different orientations of single molecules and represents a map of the electric field component at the triangular aperture in direction of the molecular dipole. Integration time per pixel was 20 ms. (c) Cross-sections along polarization direction through the center of the fluorescence spots M1-M4 in (a).

total extension of > 50 nm whereas the other half are mainly bright single spots with a size of 30-40 nm. A more detailed view of several different field maps produced by differently oriented molecules is presented in Fig. 4. The images Fig. 4(a) and 4(b) display exactly the same area of the sample, only the polarization direction of the incident light was rotated from $\alpha=0^\circ$ (normal to left side, Fig. 4(a)) to $\alpha=90^\circ$ (parallel to left side, Fig. 4(b)). Nonetheless, the appearance of the fluorescence spots completely changed with polarization direction in shape as well as in intensity. Sections along the x-direction through the center of the spots of the left image are presented in Fig. 4(c). Interestingly, the emission intensities between the sub-spots of M1, M2 and M3 decrease within 20-25 nm to the background level indicating that the continuously varying electric field changes its polarity between the sub-spots.

4. Comparison with numerical simulations

In order to determine the orientation of the molecules as well as the different field components at a TA, the measured field patterns are compared to numerical simulations of an aperture in a planar aluminum film of 100 nm thickness. At first, we calculated the electric field distribution $\mathbf{E}(x,y)$ at a distance of 10 nm behind a 50-nm-sized aperture for two different polarization directions of the incident light. The shape of the aperture has been chosen not exactly equilateral for reasons of numerical discretization (cell size is $5.8 \times 5.8 \times 5.8$ nm 3 ; for more details, see Ref. 10). The excitation intensity $I(x,y)$, which depends on the location (x,y) of the aperture with regard to the probing dipole, is then calculated for many different dipole orientations \mathbf{p} using the relation $I(x,y)=|\mathbf{p} \cdot \mathbf{E}(x,y)|^2$. Note that the simulation does not include fluorescence quenching caused by the metallic end face which can occur for a probe-molecule distance smaller than a few nanometers [1,6].

In Fig. 5(b), a limited number of field maps calculated for several different polar angles θ and azimuth angles φ (cf. Fig. 5(a)) are organized in two panels for two different polarization directions of illumination. In case of a polarization normal to an edge (table on the left), three sub-spots of different intensity generally appear at the aperture. The intensity ratios of the sub-spots strongly vary with dipole orientation so that most orientations create an almost

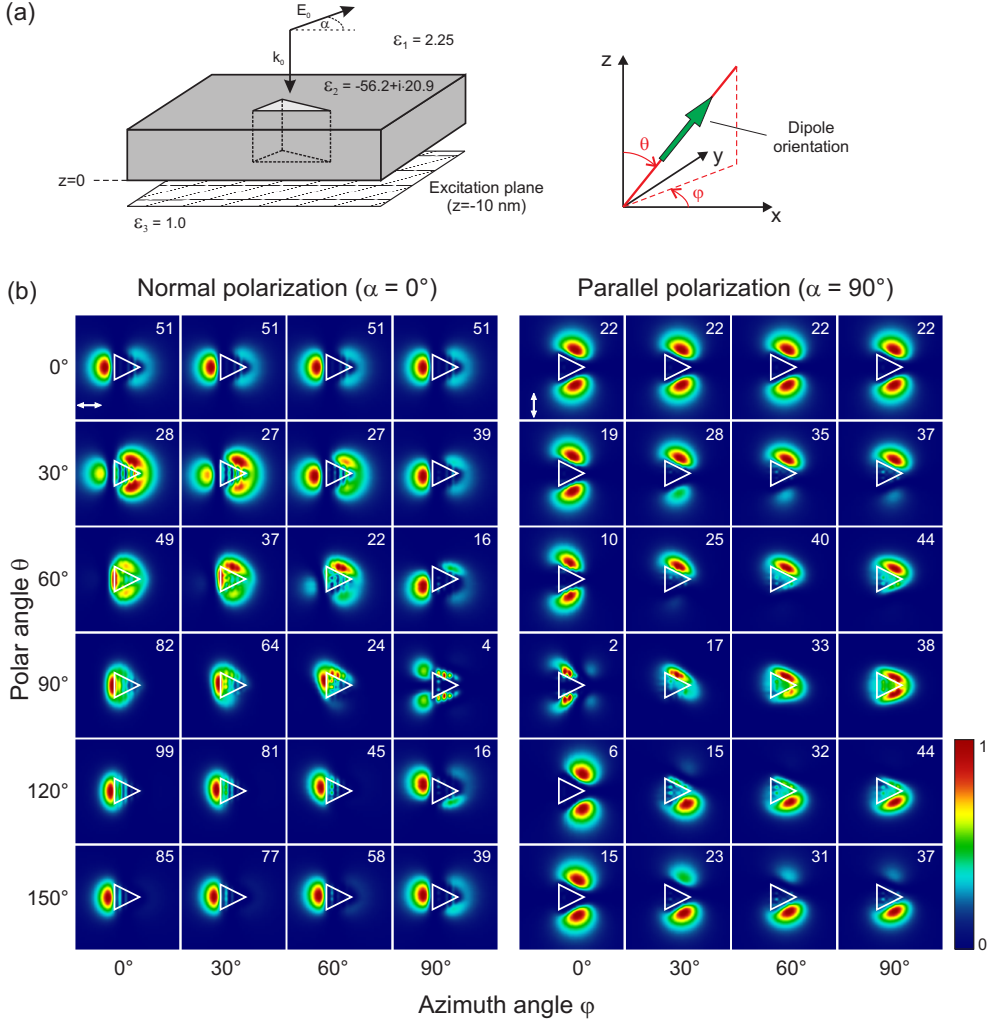


Fig. 5. (a) Numerical model for the simulation of fluorescence patterns caused by single molecules excited through a triangular aperture. The triangular aperture is illuminated at normal incidence with a plane wave which is linearly polarized either perpendicular ($\alpha=0^\circ$) or parallel ($\alpha=90^\circ$) to the left aperture edge. The orientation of the absorption dipole moment is represented by the two spherical angles θ and φ . (b) Calculated fluorescence maps for various dipole moment orientations organized in two panels for the two polarization directions $\alpha=0^\circ$ and $\alpha=90^\circ$. The color scale of each image has been normalized with respect to its maximum intensity value. The number in the upper right corner displays the relative normalization value in percent.

individual pattern. Only for polar angles $\theta>120^\circ$, the patterns are less characteristic because two of the three spots are almost fully suppressed. For this range of polar angles, however, the patterns produced by an illumination polarization direction parallel to an edge (table on the right) are much more sensitive to a change in dipole orientation. Thus for a particular dipole orientation a pair of fluorescence patterns taken from the two panels indeed provides a unique fingerprint.

In order to identify the orientation of a particular molecule, the two measured fluorescence patterns are compared to the calculated field maps of Fig. 5 regarding shape as well as relative intensities of the two maps and the sub-spots. The precision of the orientation determination is then further optimized by gradually changing the angles φ and θ in steps of 1° . As an

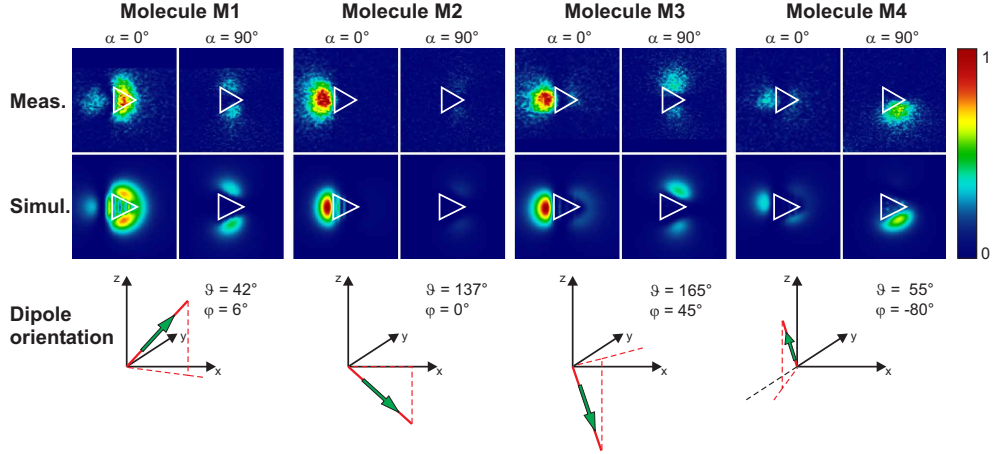


Fig. 6. Comparison of the measured fluorescence patterns (upper row) to the simulated intensity maps $I(x,y)$ (lower row) for the molecules M1 to M4 in Fig. 4(a). For each molecule the maximum intensity of the simulated maps was fitted to the experimental ones without changing the intensity ratio of the two maps for $\alpha=0^\circ$ and $\alpha=90^\circ$. The deduced dipole moment orientation of each molecule is shown below the images.

example, the measured patterns M1-M4 of Fig. 4 are compared in Fig. 6 to the respective field maps selected in this way.

The agreement between experiment and simulated field maps turned out to be excellent. Not only shape and extension of the patterns but also relative intensities of the fluorescence maxima for both polarizations are reproduced properly. Since molecule-metal interactions were neglected in the simulation, quenching thus seems to have only a minor location-dependent effect on the fluorescence of a fixed molecule in front of a small TA, which is possibly a result of the relatively large probe-molecule distance of >10 nm. Small differences in the near-field distributions of experiment and theory can be attributed to a real molecule-aperture distance deviating from the assumption made in the simulation. In the case of molecule M1, for example, the maximum intensity for $\alpha=0^\circ$ occurs near the center of the aperture whereas in the simulation the maxima are located at the rim. Such a movement of the field maximum to the center is well known to occur with increasing distance to the aperture. The good agreement of theory and experiment together with the high S/N ratio of the data allowed us to determine the orientation angles of a molecule with an uncertainty clearly below 10° . The lateral position of a molecule could be localized with a precision down to a few nanometers (at a pixel time of 20 ms).

Regarding the relative intensities of two differently oriented molecules the agreement between measurement and simulation turned out to be less convincing though the qualitative behavior is similar. Considering the experimental conditions, however, a better agreement could not be expected for at least three reasons: first, the distance of two different molecules to the aperture may differ up to 10 nm (the sample thickness) resulting in a markedly different excitation intensity because the near-field decreases exponentially with distance to the aperture; second, differently oriented molecules have different angular radiation characteristics so that their fluorescence is generally collected with different efficiency (finite numerical aperture of the objective); and third, it is well known, that a metal film near a molecule has a considerable distance- and orientation-dependent influence on the quenching rate and the fluorescence yield of the molecule [1].

From the successful simulation of the experimental fluorescence patterns of single molecules, we can conclude that the simple model of a TA in a planar film is perfectly adequate to describe the near-field optical properties of a real TA probe. A preliminary simulation of a more complex, three-dimensional model of the TA probe confirmed this conclusion, since it produced almost the same results as the simple model. The tetrahedral

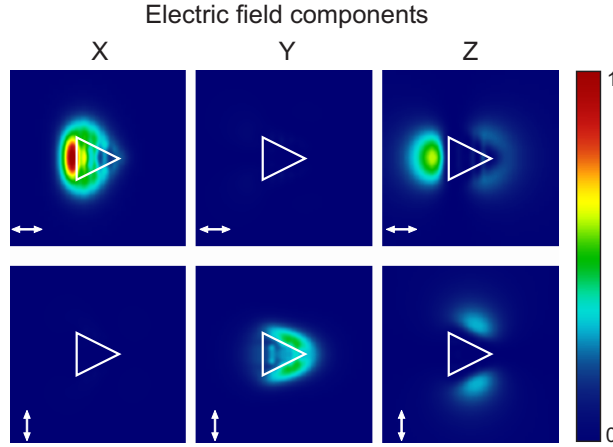


Fig. 7. Square of the electric field components in x-, y- and z-direction at a 50-nm-sized triangular aperture for an illuminating beam polarized normal (upper row) or parallel (lower row) to the left edge. The intensities are normalized to the maximum intensity of the upper left image.

form of the waveguide thus seems to have only a minor influence on the performance of a TA as near-field probe. The spatial distribution of the near-field is mainly shaped by the physical transmission mechanism of electromagnetic fields through the triangular aperture and is much less dependent on the particular way of illumination. In numerical simulations published elsewhere, we could show, for example, that the field distribution is almost independent of the direction of the illuminating beam as long as the film is sufficiently thick and the size of the aperture is much smaller than the wavelength [11]. This is also consistent to our recent result that the general shape of the field pattern at small apertures can be simply deduced from the boundary conditions of electromagnetic fields within the aperture [10].

The experimentally confirmed validity of our numerical model allows us to report the vectorial electric field maps at a real TA probe. These maps are identical with the respective field patterns in Fig. 5 produced by a dipole transition with an orientation in x-direction ($\theta=90^\circ$, $\varphi=0^\circ$), y-direction ($\theta=90^\circ$, $\varphi=90^\circ$), and z-direction ($\theta=0^\circ$). For a better comparison, the vectorial components of a TA are compiled without normalization in Fig. 7. For both illumination conditions the field component along the direction of the incident electric field is the strongest whereas the respective perpendicular component along the x-axis or y-axis is negligible. In both cases the strength of the z-component is around 60% of the most intense component. Recently, Tanaka and Tanaka discussed the enhanced intensity of the z-component in terms of a surface plasmon polariton excitation on the sidewalls of the aperture [12]. For the field maps resulting from our study, however, it is striking that the intensity maxima are clearly outside the aperture; for the z-components the maxima are even ~ 25 nm away from the edges. We think that this behavior may be readily explained by considering also the magnetic near-fields at the aperture; related numerical calculations are currently carried out.

5. Conclusion

So far, a triangular nano-aperture was primarily used as ultra-local light source in SNOM measurements. The detailed understanding of the behavior of electromagnetic fields at a triangular aperture described in this paper thus enables a far better interpretation of near-field optical images taken with such a probe. We have demonstrated that the relatively high transmission of triangular nano-apertures together with the enhanced field confinement at only one edge makes it possible to image single fluorescent molecules with high S/N ratio at high optical resolution. Today, most studies employing single molecule detection are based on con-

focal or wide-field optical microscopy. Owing to the diffraction-limited resolution, however, these approaches require the concentration of fluorescent particles to be largely diluted. In a natural surrounding, e.g. for a biological membrane in its native environment, this is not always possible, so that ultra-sensitive imaging at high optical resolution again becomes desirable [13-15]. Especially in applications where the molecular dipole is free to rotate (e.g., biomolecules in solution), an optical resolution down to 30 nm is readily feasible using a TA probe since on time average the electric field component at the distinguished edge will always be dominant. For molecules with a fixed orientation (e.g., in a lipid membrane) the overall optical spot size may be much less confined so that the optical resolution will be accordingly lower. In this case, however, shape and relative intensities of the measured patterns can be analyzed to figure out the molecular orientation with an accuracy of better than 10°.

Acknowledgments

We thank H. Fuchs for continuous support. The help of F. Pérez-Willard (Laboratorium für Elektronenmikroskopie, University of Karlsruhe) regarding the preparation of FIB-milled apertures is gratefully acknowledged. This work was supported by the Volkswagen foundation within the research program “Physics, chemistry and biology of single molecules”, by the German Science Foundation (FI 608 and NA 382/2), and by the network of excellence “Plasmo-Nano-Devices” of the European community.

2.2 Modèle du dipôle effectif

Idealement, la sonde champ proche optique se comporte comme un dipôle ponctuel. Quelques configurations s'approchent de ce cas idéal. Citons le cas d'une seule molécule fluorescente [32] ou d'une nanoparticule métallique [33, 34] attachée à l'extrémité d'une fibre optique effilée. Plus généralement, les sondes de microscopes optiques sont souvent modélisées par un dipôle effectif pour obtenir une analyse simple du signal. Lors de ma thèse, cela nous avait conduit à interpréter les images de SNOM en mode illumination en terme de densité locale d'états photoniques (LDOS), en analogie directe avec la microscopie par effet tunnel électronique (STM). J'ai poursuivi ce travail en arrivant à Dijon, pour établir la forme du signal mesuré en présence de nanostructures métalliques supportant des modes plasmons [35, 36]. Le groupe de H. Okamoto (Japon) s'est inspiré de ces travaux pour établir expérimentalement la relation de dispersion de barreaux métalliques [37].

Lors de ce travail, j'ai cherché à préciser les différents mécanismes intervenant dans le transfert d'énergie en champ proche. Plus précisément, j'ai quantifié les contributions de la dissipation et de la diffusion dans la formation d'images en champ proche en présence de structures plasmoniques [35].

L'analogie entre l'émission (quantique) spontanée et le rayonnement (classique) dipolaire de la pointe nous a conduit à démontrer que le signal mesuré par un microscope optique en champ proche est similaire au taux de relaxation moléculaire. Cela démontre l'intérêt de cette configuration comme système expérimental modèle de la fluorescence en géométrie complexe. Et m'a naturellement conduit à m'intéresser précisément aux processus de relaxation moléculaire en présence de structures métalliques. Je discute ce point en détail au chapitre 3.

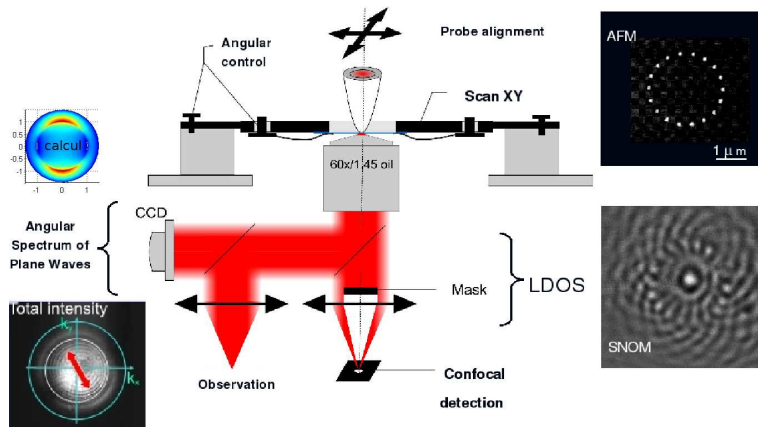


FIG. 2.5 – Caractérisation du comportement dipolaire d'une sonde SNOM. L'émission est mesurée dans le plan image et dans le plan de Fourier. Le comportement dipolaire conduit à imager la LDOS de l'échantillon dans le plan image et une émission avec 2 lobes dans le plan de Fourier, semblable à l'émission d'un dipôle sur une surface (calcul). La flèche rouge indique la polarisation de l'excitation de la sonde. L'image de LDOS a été obtenue avec une sonde sans ouverture (fibre optique étirée métallisée avec de l'or) et l'image dans le plan de Fourier avec une sonde à ouverture circulaire ($\Phi = 100 \text{ nm}$) commercialisée par la société JASCO. La longueur d'onde d'excitation est $\lambda = 633 \text{ nm}$.

En parallèle de ce travail théorique, nous avons cherché à caractériser expérimentalement le comportement dipolaire de pointes SNOM ou de structures déposées sur une surface. A cette fin,

Aurélien Bruyant a développé pendant son séjour post-doctoral un montage pour caractériser l'émission de sondes dans le plan de Fourier. Il a comparé la forme du signal à l'émission d'un dipôle sur une surface (non publié). Le montage est décrit sur la figure 2.5. Le comportement dipolaire de la sonde est révélé par la mesure de la LDOS dans le plan image et par une émission angulaire caractéristique d'un dipôle (magnétique pour une sonde à ouverture et électrique pour une sonde diffusante) dans le plan de Fourier [38]. La présence d'une émission sous l'angle critique dans le plan de Fourier est due aux fuites dans le corps de la pointe SNOM. Ces ondes radiatives sont éliminées lors de l'imagerie dans le plan direct avec un masque, assurant que seules les ondes évanescentes participent à la formation de l'image LDOS.

Nous avons ensuite utilisé ce montage pour caractériser l'émission de nanoparticules d'or couplées. Nous avons ainsi pu caractériser la formation progressive de zones de champs confinés par couplage de plusieurs nanoparticules [39] puis mesurer le diagramme d'émission d'un dimère [40]. En particulier, il apparaît des zones de fortes exaltations du champ électromagnétique entre les deux particules. Ce type de configuration fait l'objet d'une recherche intense pour des applications de Spectroscopie Raman Exaltée en Surface (SERS) avec des applications pour améliorer la sensibilité de capteurs chimiques [9]. Cette étude, menée principalement par Alexandre Bouhelier, est reproduite en annexe.

Publications associées

“Energy transfer in near-field optics”

G. Colas des Francs, C. Girard, M. Juan and A. Dereux
Journal of Chemical Physics **123**, 174709 (2005).

L'équation (13) comporte une erreur. Le terme de diffusion I_{scatt} ne doit pas apparaître car il est pris en compte implicitement. Cette erreur provient d'une mauvaise interprétation des effets de taille finie et sera discutée en détail au chapitre suivant. Toutefois, l'expression approchée de la diffusion reste valable et cet article quantifie les contributions de la diffusion et de la dissipation dans le signal (figure 3).

L'analogie avec l'émission de fluorescence est discutée dans l'article suivant reproduit en annexe.

“SNOM signal near plasmonic nanostructures : an analogy with fluorescence decay channels”

G. Colas des Francs, C. Girard, A. Bruyant and A. Dereux
Journal of Microscopy **229**, 302-306 (2008).

Dans deux autres articles, nous avons caractérisé en champ lointain le couplage de nanoparticules d'or (le premier est reproduit en annexe).

“Gain, detuning and directivity of nanoparticles optical antennas”

C. Huang, A. Bouhelier, G. Colas des Francs, A. Bruyant, A. Guénot, E. Finot, J.-C. Weeber and A. Dereux
Physical Review B **78** 155407 (2008).

“Far-field imaging of the electromagnetic local density of optical states”

C. Huang, A. Bouhelier, G. Colas des Francs, G. Legay, J.-C. Weeber and A. Dereux
Optics Letters **33**, 300-302 (2008).

Energy transfer in near-field optics

Gérard Colas des Francs^{a)}

Equipe Optique Submicronique, Laboratoire de Physique Université de Bourgogne/Centre National de la Recherche Scientifique (LPUB/CNRS), 9 Avenue Alain Savary, F-21078 Dijon, France

Christian Girard and Mathieu Juan

NanoSciences Group Centre d'Elaboration des Matériaux et d'Etudes Structurales/Centre National de la Recherche Scientifique (CEMES/CNRS), 29 rue Jeanne Marvig, BP 4347, F-31055 Toulouse, France

Alain Dereux

Equipe Optique Submicronique, Laboratoire de Physique Université de Bourgogne/Centre National de la Recherche Scientifique (LPUB/CNRS), 9 Avenue Alain Savary, F-21078 Dijon, France

(Received 15 June 2005; accepted 7 September 2005; published online 3 November 2005)

When the probe tip of a near-field optical microscope illuminates nanoparticles with marked absorption bands, a large number of photons are absorbed before reaching the detector. These energy losses enhance the dark contrast usually observed in the vicinity of metallic nanoparticles. We demonstrate theoretically that this phenomenon can be exploited to image, in the optical frequency range, dissipative domains with a nanometer scale resolution. Simulations performed with noble-metal particles indicate that the detected signal significantly drops down when the excitation frequency is approaching the plasmon resonance of the particles. © 2005 American Institute of Physics. [DOI: [10.1063/1.2101567](https://doi.org/10.1063/1.2101567)]

I. INTRODUCTION

Over the two last decades the extensive exploitation of all different kinds of near fields existing spontaneously or artificially at the immediate proximity of the surface of materials has generated a considerable amount of new exciting developments. Behind the average properties of these near fields (usually generated or detected by a local probe technique), it is important to emphasize that the associated particles (photons or electrons) are randomly exchanged through the gap lying between the probe tip and the surface of the material. Consequently, it becomes possible to both trigger and analyze, with a nanometer scale resolution, a large class of dissipative phenomena by controlling these different near fields.

We can first mention the scanning tunneling microscope (STM), where the introduction of some material in the gap between the source and the detector leads to well-identified dissipative phenomena. For example, tunneling electrons can be coupled to some vibration modes of the material confined inside the tunnel barrier. This gives the opportunity to perform inelastic electron tunneling spectroscopy (IETS).¹ In such experiments, the insulator embedded in the planar junction contains specified molecules. The transferred electrons are inelastically coupled to the vibration levels of these molecules.¹ We had to wait several years before the first actual experimental evidence of this effect was observed at a single molecule scale. Such observations were reported very recently² with C₂H₂ and C₂D₂ molecules and with CO molecules.³

In van der Waals force microscopy, the discrete ex-

change of virtual photons cannot be directly observed.⁴ Although, their role could be very important in determining the noise level in the van der Waals dispersion force measurements, the virtual nature of the particles exchanged precludes a direct measure in the very near-field zone.

In near-field optics, the transfer process involves individual photonic particles as well. However, when working with standard light sources (laser) the pure quantum aspect of photon is masked by the fact that the observable electromagnetic field is an average on many photon states. With such classical waves a local density of photonic states (photonic LDOS) can be defined from Maxwell's equations.⁵ In strong analogy with STM that maps the electronic LDOS of dense metallic surfaces, the scanning near-field optical microscopy (SNOM) can reveal the photonic LDOS variation sculpted by the nanostructures themselves.^{6–8} Because photonic LDOS is an important parameter for the interpretation of light-matter interaction, SNOM images measuring this quantity were recorded near several systems, including semiconductor,^{7,9,10} photonic crystals,¹¹ designed structures for light localization,^{5,8,12} and plasmonic nanostructures.¹³ Plasmonic nanostructures present resonant effects at visible wavelengths^{14–16} generally accompanied by a significant amount of energy dissipated by Joule effect. As analyzed in the following sections, these losses can affect the imaging process in near-field optics.

Although the evanescent electromagnetic field displays imaginary wave-vector components, it may be considered as a classical quantity that will enter the coupling Hamiltonian (between electric near field and nanostructures) with the status of a parameter. Consequently, in near-field optics, a realistic description of dissipation effects is directly related to a proper description of the imaginary parts of either the dy-

^{a)}Electronic mail: gerard.colas-des-francs@u-bourgogne.fr

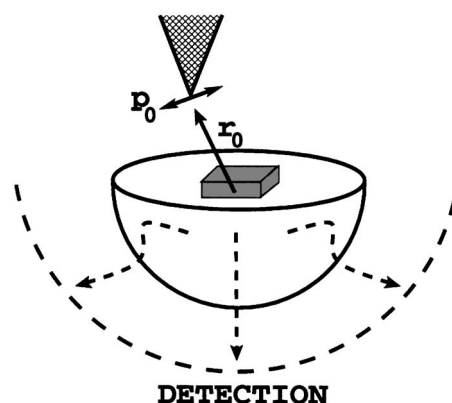


FIG. 1. Schematic representation of a SNOM setup. The active part of the probe is represented by an ideal pointlike dipolar light source \mathbf{p}_0 that illuminates nano-objects supported by a transparent surface. The signal transmitted below the surface is recorded in far field when the probe tip is scanned over the sample. \mathbf{r}_0 indicates the tip position.

nanical response functions of the nanostructures or the dynamical polarizabilities of molecules adsorbed on the surface sample.

In this article, we demonstrate theoretically that the SNOM can provide a unique opportunity to image, in the optical frequency range, *dissipative regions* with a nanometer scale resolution. In particular, in the vicinity of nanoparticles with marked absorption bands, we will show that the detected signal can reveal the dissipation properties of the sample at the nanometer scale. Simulations and experiments performed with noble-metal particles indicate dramatic change of the SNOM images when working near the plasmon resonance of the particles while we observe the photon-unoccupied states maps tailored by the nanostructures when working far from these resonances.¹⁶ As an alternative to the photothermal imaging method¹⁷ or confocal microscopy,¹⁸ we show how these features can be recorded with a SNOM working with a pointlike dipolar tip design.

II. SNOM SIGNAL AND ENERGY LOSSES

Figure 1 represents schematically the transmission SNOM setup considered throughout this article. A probe tip illuminates in the near-field nanostructures lithographed on a glass substrate and the energy transmitted below the surface is detected in the far-field zone with a high numerical aperture objective. Several other configurations exist. They are generally classified in two families: illuminating and collecting mode devices. The setup described in Fig. 1 belongs to the first family but, with the help of the reciprocity theorem, a strict equivalence between these two families has been demonstrated.¹⁹ Actually, as we will see below, the main point is the high numerical aperture of the system. Therefore, SNOMs working either in collecting or emitting configuration, in which a specific direction for detection or injection is used, are not considered in this paper. Nevertheless, our formalism can be generalized to these configurations.^{15,16}

In SNOM instrumentation, the optimization of local probe design can lead to efficient tips that behave like ideal emitting dipoles.^{8,20–23} The signal recorded by a SNOM setup (Fig. 1) below the sample can be computed by using

the Green dyadic tensor formalism.^{24–26} Nevertheless, in this section, we have adopted a more pedagogical method that will enlighten on the elementary mechanisms of the energy transfer in near-field optics.²⁷ Furthermore, to simplify the discussion, we will assume that the intensity scattered in the whole space approximates the experimental signal usually recorded after a large detection angle below the surface.

The detected signal is then obtained in two independent steps:

- (i) First, we determine the amount of light that can be emitted by the source dipole when it interacts with the sample.
- (ii) In a second stage, we analyze what portion of this emitted light can really reach a far-field detector after absorption and scattering by the sample.

In the Appendix, we give a direct derivation of the signal for a simplified configuration. This leads to an original interpretation in strong analogy with the optical theorem.

A. Light emission by the probe tip

The flux of radiation emitted by a small dipolar light source is significantly modified when the dipole is brought close to an object. To introduce this basic issue, we apply the laws of electrodynamics to the geometry of Fig. 1. By applying Poynting's theorem, the power that can be delivered by the dipole source is a linear function of the current density $\mathbf{j}(\mathbf{r}, t)$ associated with the fluctuating dipole (cgs units).²⁸

$$I_{\text{emitted}} = - \left\langle \int_{V_0} d\mathbf{r} \mathbf{j}(\mathbf{r}, t) \cdot \mathbf{E}(\mathbf{r}, t) \right\rangle, \quad (1)$$

where $\mathbf{E}(\mathbf{r}, t)$ defines the local electric field and V_0 is a small volume including the emitting dipole.²⁹ In addition, we assume that the probing dipole of magnitude p_0 oscillates according to the simple sinusoidal law $\mathbf{p}_0(t) = \mathbf{n} p_0 \cos(\omega_0 t)$ along a direction \mathbf{n} located in the surface plane. The associated current density is therefore proportional to a Dirac δ function centered on the dipole position \mathbf{r}_0 :

$$\mathbf{j}(\mathbf{r}, t) = \frac{\partial \mathbf{p}_0(t)}{\partial t} \delta(\mathbf{r} - \mathbf{r}_0) = - \mathbf{n} p_0 \omega_0 \sin(\omega_0 t) \delta(\mathbf{r} - \mathbf{r}_0). \quad (2)$$

At this point of the demonstration, we introduce the relationship between the local electric field and its local source. That leads to a simple constitutive relation

$$\mathbf{E}(\mathbf{r}, t) = \int_{-\infty}^{+\infty} dt' \mathbf{S}(\mathbf{r}, \mathbf{r}_0, t - t') \cdot \mathbf{p}_0(t'), \quad (3)$$

which introduces the so-called *field-susceptibility* $\mathbf{S}(\mathbf{r}, \mathbf{r}_0, t - t')$ of the optical surroundings seen by the source dipole. This dyadic tensor describes how an electric field appears in \mathbf{r} when a dipole is placed in \mathbf{r}_0 . This scattering contribution to the detected signal turns out to be proportional to the imaginary part $\text{Im } \mathbf{S}(\mathbf{r}, \mathbf{r}_0, \omega)$ of the Fourier transform of the various components of \mathbf{S} . Indeed, with α and β labeling the Cartesian components x , y , and z of vectors, elementary algebra based on substituting relations (2) and (3) into Eq. (1) leads to²⁶

$$\begin{aligned} I_{\text{emitted}} &= - \left\langle \int_{V_0} d\mathbf{r} \mathbf{j}(\mathbf{r}, t) \cdot \mathbf{E}(\mathbf{r}, t) \right\rangle \\ &= \frac{\omega_0 p_0^2}{2} \sum_{\alpha, \beta} n_\alpha n_\beta \operatorname{Im} S_{\alpha, \beta}(\mathbf{r}_0, \mathbf{r}_0, \omega_0), \end{aligned} \quad (4)$$

where we defined the Fourier transform by ($\tau = t - t'$)

$$\mathbf{S}(\mathbf{r}, \mathbf{r}_0, \omega_0) = \int_{-\infty}^{+\infty} d\tau \mathbf{S}(\mathbf{r}, \mathbf{r}_0, \tau) e^{i\omega_0 \tau}. \quad (5)$$

Now, to enhance the physical meaning of relation (4), it is worthwhile to introduce the concept of photonic LDOS $\rho(\mathbf{r}_0, \omega_0)$. This scalar function represents the probability to detect a photon of angular frequency ω_0 at a given position \mathbf{r}_0 . From the scattering theory of scalar waves, it is well known that any LDOS can be formulated as a function of the imaginary part of the Fourier transform of the field susceptibility.^{5,30} Here, due to the vector character of light fields, this function appears as the sum of three partial LDOS $\rho_\alpha(\mathbf{r}_0, \omega_0)$, each of them being related to each Cartesian direction

$$\rho(\mathbf{r}_0, \omega_0) = \sum_{\alpha=x, y, z} \rho_\alpha(\mathbf{r}_0, \omega_0), \quad (6)$$

where

$$\rho_\alpha(\mathbf{r}_0, \omega_0) = \frac{1}{2\pi^2 \omega_0} \operatorname{Im} S_{\alpha\alpha}(\mathbf{r}_0, \mathbf{r}_0, \omega_0). \quad (7)$$

At this point, it is instructive to fix a specific orientation α of the dipolar source \mathbf{p}_0 along anyone of the Cartesian axis. In this case, it is possible to establish a relation between the scattered signal and one of the partial LDOS

$$I_{\text{emitted}} = \omega_0^2 \pi^2 p_0^2 \rho_\alpha(\mathbf{r}_0, \omega_0). \quad (8)$$

B. Energy dissipation into the sample

Some part of the light delivered by the source dipole is absorbed by the sample. This dissipative term²⁸ represents the power dissipated by the system by Joule effect. It is proportional to the imaginary part $\operatorname{Im}[\epsilon(\mathbf{r}, \omega_0)]$ of the dielectric permittivity of the nanostructures:

$$Q_{\text{diss}} = \frac{\omega_0}{8\pi} \int_{\text{object}} \operatorname{Im}[\epsilon(\mathbf{r}, \omega_0)] |\mathbf{E}(\mathbf{r}, \omega_0)|^2 d\mathbf{r}, \quad (9)$$

where $\mathbf{E}(\mathbf{r}, \omega_0)$ defines the local electric field inside the materials. This local field, that is directly produced by the tip, can be expressed with the field-susceptibility tensor \mathbf{S} [see Eq. (3) and below].

C. Light scattered by the nanostructures

Another part of the light emitted by the dipole source is scattered by the sample. This contribution is proportional to the square modulus of the dipolar polarization $\mathbf{P}(\mathbf{r}, \omega_0)$ inside the volume of the nanostructure. Indeed, each elementary volume $d\mathbf{r}$ scatters an energy:

$$\frac{\omega_0^4}{3c^3} |\mathbf{P}(\mathbf{r}, \omega_0)|^2 d\mathbf{r} \quad (10)$$

per time unit, and the total power scattered by the nanostructure is given by

$$I_{\text{scatt}} = \frac{\omega_0^4}{3c^3} \int_{\text{object}} |\mathbf{P}(\mathbf{r}, \omega_0)|^2 d\mathbf{r}. \quad (11)$$

In this last expression, the dipolar polarization $\mathbf{P}(\mathbf{r}, \omega_0)$ is induced by the SNOM tip. Consequently, it is directly proportional to the local field $\mathbf{E}(\mathbf{r}, \omega_0)$

$$\mathbf{P}(\mathbf{r}, \omega_0) = \chi(\omega_0) \mathbf{E}(\mathbf{r}, \omega_0) = \frac{\epsilon(\omega_0) - 1}{4\pi} \mathbf{E}(\mathbf{r}, \omega_0). \quad (12)$$

Let us note that expression (10) has been established from the formula of the radiative power of a dipole in vacuum. In the vicinity of a plane surface of low optical index this approximation is justified by the weakness of the LDOS variation. Furthermore, due to its induced character, contribution (11) is expected to be much weaker than the two other contributions (8) and (9) and generally appears as a small correction to the total signal.

D. Far-field detection

An expression of SNOM signal including radiative and nonradiative losses can be deduced from the previous subsections. That leads to

$$I(\mathbf{r}_0, \omega_0) = I_{\text{emitted}} + I_{\text{scatt}} - Q_{\text{diss}}, \quad (13)$$

where, with Eqs. (8), (9), and (11), we have gathered all the ingredients needed to investigate SNOM signal behavior in the presence of dissipative materials. In the following, we will discuss this problem with a single spherical nanoparticle lying at the location \mathbf{r}_s on the substrate, and the emitting source dipole will be aligned along the x axis. In this case, the linear response of the nanoparticle is completely characterized by its polarizability α :

$$\chi(\mathbf{r}, \omega) = \alpha(\omega) \delta(\mathbf{r} - \mathbf{r}_s) \quad \text{with } \alpha(\omega) = \alpha'(\omega) + i\alpha''(\omega). \quad (14)$$

This particle modifies the field-susceptibility $\mathbf{S}_0(\mathbf{r}, \mathbf{r}', \omega_0)$ associated with the bare sample. At the first Born approximation, we can write

$$\begin{aligned} \mathbf{S}(\mathbf{r}, \mathbf{r}', \omega_0) &= \mathbf{S}_0(\mathbf{r}, \mathbf{r}', \omega_0) \\ &+ \mathbf{S}_0(\mathbf{r}, \mathbf{r}_s, \omega_0) \cdot \alpha(\omega_0) \cdot \mathbf{S}_0(\mathbf{r}_s, \mathbf{r}', \omega_0). \end{aligned} \quad (15)$$

Finally, after straightforward algebra, the various contributions to the signal simplify to (for the sake of clarity, we have introduced the notation $\mathbf{S}_0(\mathbf{r}_s, \mathbf{r}_0, \omega_0) = \mathbf{S}'_0 + i\mathbf{S}''_0$)

$$I(\mathbf{r}_0, \omega_0) = \frac{ck_0^4 p_0^2}{3} \left[1 + \frac{|\mathbf{p}_s|^2}{|\mathbf{p}_0|^2} + \overline{\Delta\rho_x}(\mathbf{r}_0, \omega_0) - \overline{Q_{\text{diss}}}(\mathbf{r}_0, \omega_0) \right], \quad (16)$$

with

$$\mathbf{p}_s = \alpha(\omega_0) \mathbf{S}_0(\mathbf{r}_s, \mathbf{r}_0, \omega_0) \cdot \mathbf{p}_0, \quad (17)$$

$$\overline{\Delta\rho_x}(\mathbf{r}_0, \omega_0) = (\rho_x(\mathbf{r}_0, \omega_0) - \rho_x^0(\mathbf{r}_0, \omega_0))/I_0 \quad (18)$$

$$\begin{aligned} &= \frac{3}{k_0^3} \alpha'(\omega_0) \sum_{\beta=x,y,z} S'_{0\beta,x} S''_{0\beta,x} \\ &+ \frac{3}{2k_0^3} \alpha''(\omega_0) \sum_{\beta=x,y,z} (S'^2_{0\beta,x} - S''^2_{0\beta,x}), \end{aligned} \quad (19)$$

and

$$\overline{Q}_{\text{diss}}(\mathbf{r}_0, \omega_0) = \frac{3}{2k_0^3} \alpha''(\omega_0) \sum_{\beta=x,y,z} (S'^2_{0\beta,x} + S''^2_{0\beta,x}). \quad (20)$$

The overline indicates that the parameter is normalized with respect to the free-space signal $I_0 = ck_0^4 p_0^2 / 3$ ($k_0 = \omega_0/c$). The physical meaning of expression (16) appears clearly:

- (i) the first two terms represent the scattering of both source \mathbf{p}_0 and induced dipoles \mathbf{p}_s , respectively.
- (ii) the x -LDOS $\Delta\rho_x$ variation describes how the nanoparticle modifies the emission process of the source dipole.
- (iii) the last term accounts for the energy dissipation inside the nanoparticle.

Let us remember that this expression is not rigorously exact because the induced dipole scattering term includes an approximation [cf. previous remark concerning Eq. (11)]. However, it compares rigorously with the direct calculation exposed in the Appendix where we have removed the bearing surface. For more complex geometry, the emitted and the dissipative contributions to the signal are treated exactly in Eq. (16). Finally, a detailed comparison between the different terms of expressions (19) and (20) shows that a part of photons emitted by the tip dipole is then immediately reabsorbed by the particle (term $3/2k_0^3 \alpha''(\omega_0) \sum S'^2_{0\beta,x}$). After combining the different relations [(16)–(20)], the SNOM signal reduces to

$$\begin{aligned} I(\mathbf{r}_0, \omega_0) = & \frac{ck_0^4 p_0^2}{3} \left\{ 1 + |\alpha(\omega_0)|^2 \sum_{\beta=x,y,z} S''^2_{0\beta,x} \right. \\ & + \frac{3}{k_0^3} \left[\alpha'(\omega_0) \sum_{\beta=x,y,z} S'_{0\beta,x} S''_{0\beta,x} \right. \\ & \left. \left. - \alpha''(\omega_0) \sum_{\beta=x,y,z} S''^2_{0\beta,x} \right] \right\}. \end{aligned} \quad (21)$$

This last expression is reminiscent from the *inelastic tunneling current* measured and described in Ref. 31. It shows precisely the balance between scattering and dissipation when the nanoparticle is locally excited [see also relation (A6) in the Appendix]. Apart from the scattered part (term in $|\alpha|^2$), the major contribution of the signal depends on the third power of the particle radius a . It is of great interest for optical characterization of very small particles. Similar expression has been derived for confocal microscopy.¹⁸

III. NUMERICAL RESULTS

From the dielectric data of Ref. 32, we have applied our formalism to a single silver particle (cf. Fig. 2). In the vicin-

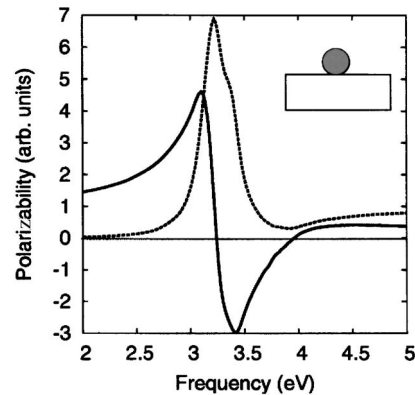


FIG. 2. Numerical simulation performed with a single silver particle [including the surface coupling (Ref. 24)]. Plot of the spectral variation of the dipolar polarizability (solid line: real part, dashed line: imaginary part).

ity of $\omega_0 = \omega_p = 3.2$ eV, the dipolar polarizability is greatly enhanced revealing the excitation of a localized plasmon mode. As expected, this resonance corresponds to a sign change of the real part of the polarizability. Far away from this resonance, we have plotted in Fig. 3(a) the individual variations of the LDOS [Eq. (19)], dissipative [Eq. (20)], and induced dipole scattering [Eq. (17)] contributions to the total signal. In this off-resonance regime, we note that the main contribution to the signal is produced by the lateral variation

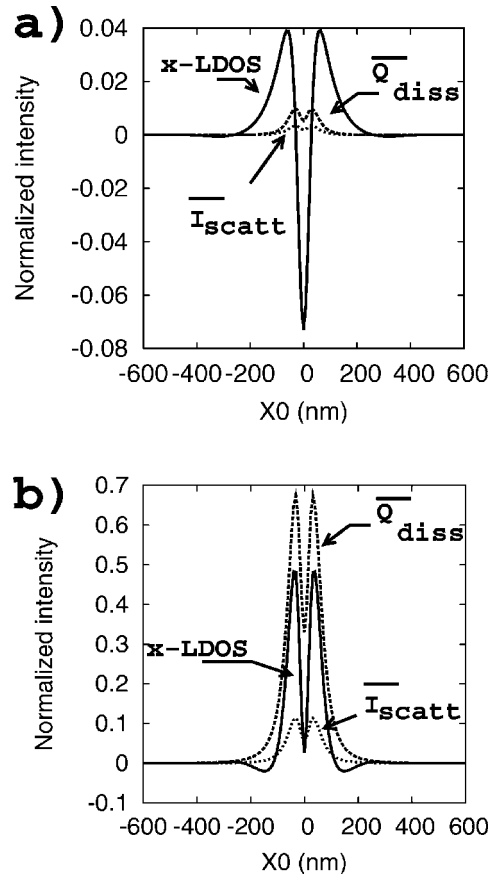


FIG. 3. Numerical simulation of the contributions to the total signal detected when a dipole is scanned over a single silver nanoparticle supported by a transparent surface. (a) Off-resonant wavelength ($\omega_0 = 2$ eV). (b) Resonant wavelength ($\omega_0 = 3.2$ eV). All the signals are normalized with respect to their value without the silver particle.

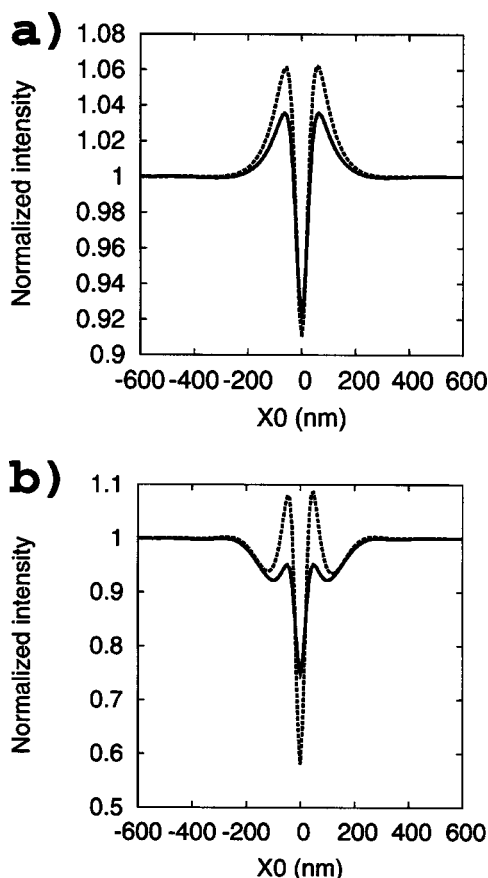


FIG. 4. Direct numerical integration of the signal transmitted below the surface (dashed curve) and signal obtained from the approximated expression (21) (solid curve) at $\omega_0=2$ eV (c) and $\omega_0=3.2$ eV (d). All the signals are normalized with respect to their value without the silver particle.

of the x -LDOS. Both induced scattering and dissipative contributions remain weak. Recently, SNOM experimental signals have been recorded near both metal particles⁸ and metallic patterned structures²¹ by working far from any localized resonances. These data display similar contrast reversal when the tip scans above the structures.

Let us see what happens when the excitation frequency comes closer and closer to ω_p [see Figs. 3(b) and 4(b)]. According to the polarizability variations, we observe a neat enhancement of the so-called *dissipative signal*. As discussed above, a large amount of photons does not reach the detector because of the absorption process (Q_{diss}). Consequently, this effect tends to reinforce and enlarge the depression of the scan line around the metal particle. In conclusion, an increasing of the dark contrast areas is associated with some absorption phenomena [Fig. 4(b)].^{13,33}

We have also computed the SNOM signal by applying a numerical integration of the electric intensity transmitted below the surface (see Ref. 26 for details). Far from the resonance, the analytical expression (21) reproduces satisfactorily the exact calculation [Fig. 4(a)]. These two numerical simulations reveal that the small difference is not related to the evaluation of the scattered contribution in (21), but it rather originates from the 4π sr solid angle integration used to obtain the analytical expression (21).³⁴ At the plasmon resonance, the divergence between analytical and numerical

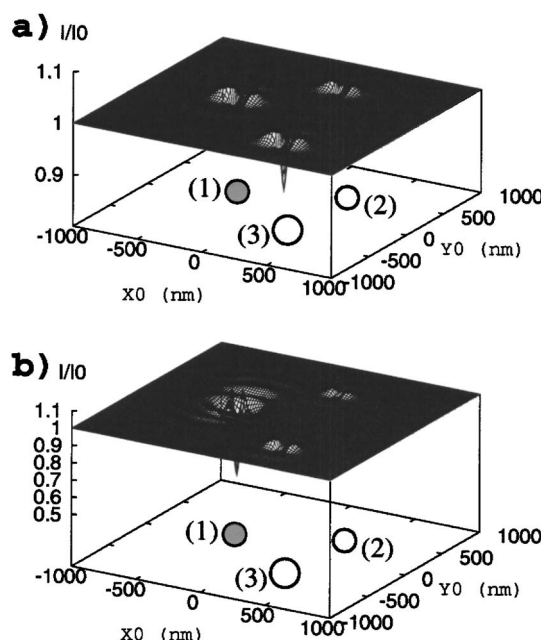


FIG. 5. SNOM images computed in the vicinity of nanometer-sized metal particles among dielectric scatterers. The tip dipole is oriented along the x axis and scans the sample at a constant distance $Z_d=80$ nm from the surface. (1) is a 20-nm-radius silver nanoparticle, while (2) and (3) designate, respectively, two 20-nm-radius and 25-nm-radius dielectric particles (optical index of 2.2). (a) frequency $\omega_0=2$ eV and (b) $\omega_0=3.2$ eV. The calculated signal is obtained by the numerical integration of the signal transmitted below the surface.

approaches increases [Fig. 4(b)]. Nevertheless, even in this particular case, our analytical expression remains precious for the understanding of elementary mechanisms of the energy transport from probe tips towards detectors.

To get more insight on the transition between scattering and dissipation regimes, we have simulated in Fig. 5 two SNOM images with a single nanometer scale Ag particle located among two other optically inactive particles of different sizes. Far away from the plasmon resonance, the Ag particle [labeled (1)] behaves like the two other ones with the usual image shape that is associated with a polarized x -LDOS change.^{8,26} Near the resonance frequency of the silver particle, the image displays profound changes. The dark contrast observed around the silver particle increases dramatically and tends to weaken the visibility of the other non-dissipative particles. In this case, the SNOM maps look different from the usual partial LDOS maps observed in the off-resonant regime.

IV. CONCLUSION

To conclude, we have presented calculations of the influence of dissipation effects on the SNOM image formation. We have shown that the position of the excitation frequency with respect to the resonance frequencies of the object can lead to drastic changes of the expected contrast. The results are in overall good agreement with previous experiments performed in the off-resonant regime in the vicinity of metallic posts and could be a useful guide to extract the dissipa-

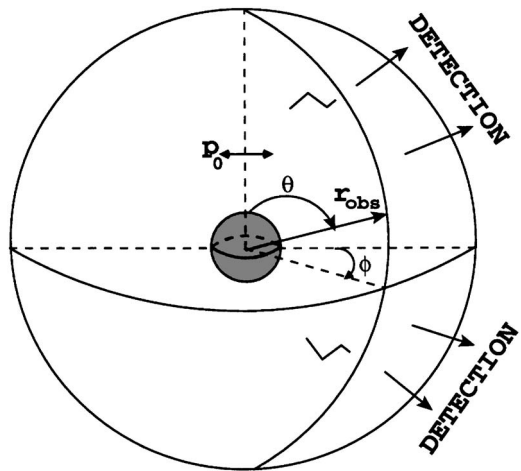


FIG. 6. Configuration used for a direct calculation of the SNOM signal. An ideal pointlike dipolar light source illuminates a nanoparticle. The scattered light is collected in the whole space.

pation map from SNOM signal near the resonance. This could also be an interesting alternative to the photothermal imaging method described recently.^{17,35}

ACKNOWLEDGMENTS

The cooperation of the authors profits from the European Network of Excellence (NoE) Plasmo-Nano-Devices (Contract No. FP6 2002-IST-1-507879) and the Specific Target Research Project (STRP) ASPIRENT (Contract No. NMP-CT-2003-001601) in the sixth Framework Program of the European Community.

APPENDIX: DIRECT CALCULATION OF THE SNOM SIGNAL

When considering the simple configuration of Fig. 6, from the first principles of electrodynamics, one can elaborate a rigorous analytical expression of the scattered signal without splitting the total power in three parts (emitted, scattered, and absorbed). This second approach will be used to compare with the results obtained in Sec. II.

The dipole source is moved in front of a spherical nanoparticle of radius a , located at $\mathbf{r}_s = (0, 0, 0)$. For simplicity, we restrict our demonstration to a dipole source aligned along the x axis $\mathbf{p}_0 = p_0 \mathbf{e}_x$ and moving vertically [$\mathbf{r}_0 = (0, 0, z_0)$]. The complete demonstration can easily be generalized to arbitrary configuration.

The ω -Fourier transform of the fluctuating dipole $\mathbf{p}_s(\omega)$ induced in the particle by the source dipole $\mathbf{p}_0(\omega)$ is proportional to the dipolar polarizability $\alpha(\omega)$ of the particle. One has then

$$\mathbf{p}_s(\omega) = \alpha(\omega) \mathbf{E}(\mathbf{r}_s, \omega) = \alpha(\omega) \left[\frac{k_0^2}{z_0} + i \frac{k_0}{z_0^2} - \frac{1}{z_0^3} \right] e^{ik_0 z_0} p_0 \mathbf{e}_x. \quad (\text{A1})$$

The electric field emitted by these two dipoles at a point \mathbf{r}_{obs} located in the far-field zone is given by

$$\mathbf{E}(\mathbf{r}_{\text{obs}}, \omega) = \mathbf{S}_\infty(\mathbf{r}_{\text{obs}}, \mathbf{r}_0, \omega) \cdot \mathbf{p}_0 + \mathbf{S}_\infty(\mathbf{r}_{\text{obs}}, \mathbf{r}_s, \omega) \cdot \mathbf{p}_s, \quad (\text{A2})$$

where

$$\begin{aligned} \mathbf{S}_\infty(\mathbf{r}_{\text{obs}}, \mathbf{r}_i, \omega) \cdot \mathbf{e}_x &= k_0^2 \frac{e^{ik_0 r_{\text{obs}}}}{r_{\text{obs}}} e^{ik_0 z_i \cos \theta} \\ &\times [1 - \sin^2 \theta \cos^2 \phi] \mathbf{e}_x \\ &- \sin^2 \theta \cos \phi \sin \phi \mathbf{e}_y \\ &- \sin \theta \cos \theta \cos \phi \mathbf{e}_z \end{aligned} \quad (\text{A3})$$

is the field radiated by a unit dipole oriented along the x axis. r_{obs} , θ , and ϕ are the three spherical coordinates used to locate the observation point. If one assumes an energy collection over a solid angle of 4π sr, the recorded signal is

$$I(z_0) = \frac{c}{8\pi} \int_0^\pi d\theta \int_0^{2\pi} d\phi \mathbf{r}_{\text{obs}}^2 |\mathbf{E}(\mathbf{r}_{\text{obs}}, \omega)|^2 \sin \theta. \quad (\text{A4})$$

After introducing expression (A2) in this equation, we can distinguish several contributions to the signal:

$$\begin{aligned} I(z_0) &= \frac{ck_0^4 p_0^2}{8\pi} \int_0^\pi d\theta \int_0^{2\pi} d\phi [1 + |\alpha(\omega_0)|^2 |s_1|^2 \\ &+ 2\alpha'(\omega_0) \text{Re}(s_1 e^{ik_0 z_0 \cos \theta}) \\ &- 2\alpha''(\omega_0) \text{Im}(s_1 e^{ik_0 z_0 \cos \theta})] (1 - \sin^2 \theta \cos^2 \phi) \end{aligned} \quad (\text{A5})$$

with $s_1 = [(k_0^2/z_0) + i(k_0/z_0^2) - (1/z_0^3)] e^{ik_0 z_0}$. After evaluation of the angular integrals, we obtain

$$\begin{aligned} I(z_0) &= \frac{ck_0^4 p_0^2}{3} \left[1 + |\alpha(\omega_0)|^2 \left(\frac{1}{z_0^6} - \frac{k_0^2}{z_0^4} + \frac{k_0^4}{z_0^2} \right) \right. \\ &+ \frac{3}{2} \alpha'(\omega_0) \sin(2k_0 z_0) \left(\frac{k_0}{z_0^2} - \frac{3}{k_0 z_0^4} + \frac{1}{k_0^3 z_0^6} \right) \\ &+ \frac{3}{2} \alpha'(\omega_0) \cos(2k_0 z_0) \left(\frac{2}{z_0^3} - \frac{2}{k_0^2 z_0^5} \right) \\ &- \frac{3}{2} \alpha''(\omega_0) \sin(2k_0 z_0) \left(\frac{2}{z_0^3} - \frac{2}{k_0^2 z_0^5} \right) \\ &- \frac{3}{2} \alpha''(\omega_0) \cos(2k_0 z_0) \left(\frac{3}{k_0 z_0^4} - \frac{k_0^2}{z_0^2} - \frac{1}{k_0^3 z_0^6} \right) \\ &\left. - \frac{3}{2} \alpha''(\omega_0) \left(\frac{1}{k_0^3 z_0^6} - \frac{1}{k_0 z_0^4} + \frac{k_0}{z_0^2} \right) \right]. \end{aligned} \quad (\text{A6})$$

The physical meaning of the first and last lines of this expression is straightforward using relation (A1).

- The first term is the signal scattered by the dipole source.
- The second term can be rewritten in the form $|\alpha(\omega_0)|^2 (1/z_0^6 - k_0^2/z_0^4 + k_0^4/z_0^2) = |\mathbf{p}_s|^2/|\mathbf{p}_0|^2$ so that it clearly represents the induced dipole scattering.
- Similarly, the last term is rewritten as $3/2\alpha''(\omega_0) \times (1/k_0^3 z_0^6 - 1/k_0 z_0^4 + k_0/z_0^2) = 3/2k_0^3 \alpha''(\omega_0) |\mathbf{E}(\mathbf{r}_s)|^2/|\mathbf{p}_0|^2$ which is the energy dissipated inside the nanoparticle [see Eq. (9)].

The other terms describe an interferential term between the light emitted by the source and induced dipole. Finally, after introducing the vacuum field-susceptibility expression in relation (21), we recover the result (A6) of this Appendix. In strong analogy with the *optical theorem*,^{28,36} the interferences between the light emitted directly by the dipole source and the light scattered by the nanoparticle are responsible for the source emission modification described by the LDOS [see Eq. (8)].

- ¹P. K. Hansma, *Tunneling Spectroscopy* (Plenum, New York, 1982).
- ²B. Stipe, M. Rezaei, and W. Ho, *Science* **279**, 1907 (1998).
- ³L. Lauhon and W. Ho, *Phys. Rev. B* **60**, R8525 (1999).
- ⁴U. Hartmann, *Phys. Rev. B* **42**, 1541 (1990).
- ⁵P. de Vries, D. V. van Coeverden, and A. Lagendijk, *Rev. Mod. Phys.* **70**, 447 (1998).
- ⁶R. Carminati and J. J. Sáenz, *Phys. Rev. Lett.* **84**, 5156 (2000).
- ⁷J. Guest, T. Stievater, G. Chen, E. Tabak, B. Orr, D. Steel, D. Gammon, and D. Katzer, *Science* **293**, 2224 (2001).
- ⁸C. Chicanne, T. David, R. Quidant, J. C. Weeber, Y. Lacroute, E. Bourillot, A. Dereux, G. Colas des Francs, and C. Girard, *Phys. Rev. Lett.* **88**, 097402 (2002).
- ⁹K. Matsuda, T. Saiki, S. Nomura, M. Mihara, Y. Aoyagi, S. Nair, and T. Takagahara, *Phys. Rev. Lett.* **91**, 177401 (2003).
- ¹⁰O. D. Stefano, S. Savasta, G. Pistone, G. Martino, and R. Girlanda, *Phys. Rev. B* **68**, 165329 (2003).
- ¹¹E. Flück, N. van Hulst, W. Vos, and L. Kuipers, *Phys. Rev. E* **68**, 015601(R) (2003).
- ¹²C. Girard, T. David, C. Chicanne, A. Mary, G. Colas des Francs, E. Bourillot, J. Weeber, and A. Dereux, *Europhys. Lett.* **68**, 797 (2004).
- ¹³K. Imura, T. Nagahara, and H. Okamoto, *J. Chem. Phys.* **122**, 154701 (2005).
- ¹⁴J. P. Kottmann, O. J. F. Martin, D. R. Smith, and S. Schultz, *Phys. Rev. B* **64**, 235402 (2001).
- ¹⁵G. Wurtz, J. Hranisavljevic, and G. Wiederrecht, *Nano Lett.* **3**, 1511 (2003).
- ¹⁶G. Wiederrecht, *Eur. Phys. J.: Appl. Phys.* **28**, 3 (2004).
- ¹⁷D. Boyer, P. Tamarat, A. Maali, M. Orrit, and B. Lounis, *Science* **297**, 1160 (2002).
- ¹⁸K. Lindfors, T. Kalkbrenner, P. Stoller, and V. Sandoghdar, *Phys. Rev. Lett.* **93**, 037401 (2004).
- ¹⁹E. R. Méndez, J.-J. Greffet, and R. Carminati, *Opt. Commun.* **142**, 7 (1997).
- ²⁰K. Lieberman, S. Harush, A. Lewis, and R. Kopelman, *Science* **247**, 59 (1990).
- ²¹J. Michaelis, J. M. C. Hettich, and V. Sandoghdar, *Nature (London)* **405**, 325 (2000).
- ²²U. C. Fischer, A. Dereux, and J. C. Weeber, in *Near Field Optics and Surface Plasmon Polaritons*, edited by S. Kawata (Springer, Berlin, 2001), chap. 4, pp. 49–69.
- ²³N. Chevalier, M. J. Nasse, J. C. Woehl, P. Reiss, J. Bleuse, F. Chandeson, and S. Huant, *Nanotechnology* **16**, 613 (2005).
- ²⁴H. Metiu, *Prog. Surf. Sci.* **17**, 153 (1984).
- ²⁵L. Novotny, *J. Opt. Soc. Am. A* **14**, 105 (1997).
- ²⁶G. Colas des Francs, C. Girard, and A. Dereux, *J. Chem. Phys.* **117**, 4659 (2002).
- ²⁷P. Das and H. Metiu, *J. Phys. Chem.* **89**, 4680 (1985).
- ²⁸J. Jackson, *Classical Electrodynamics*, 3rd ed. (Wiley, Hoboken, 1998).
- ²⁹In previous papers, we consider a volume large enough to include the sample, this leads to neglect both the scattering and dissipation by the sample term, approximation which is no more valuable here; see also S. Savasta, O. D. Stefano, R. Girlanda, and M. Pieruccini, *Phys. Rev. Lett.* **93**, 069701 (2004); C. Chicanne, T. David, R. Quidant, J. C. Weeber, Y. Lacroute, E. Bourillot, A. Dereux, G. Colas des Francs, and C. Gerard, *ibid.* **93**, 069702 (2004).
- ³⁰E. N. Economou, *Green's Functions in Quantum Physics*, Springer Series in Solid-State Science, Vol. 7, 2nd ed. (Springer, Berlin, 1983).
- ³¹N. Lorente and M. Persson, *Phys. Rev. Lett.* **85**, 2997 (2000).
- ³²Z. Palik, *Handbook of Optical Constants of Solids* (Academic, San Diego, CA, 1985).
- ³³C. Hubert, A. Rumyantseva, G. Lerondel *et al.*, *Nano Lett.* **5**, 615 (2005).
- ³⁴G. Colas des Francs, C. Girard, J. C. Weeber, and A. Dereux, *Chem. Phys. Lett.* **345**, 512 (2001).
- ³⁵A. Arbouet, D. Christofilos, N. D. Fatti, F. Valle, J. R. Huntzinger, L. Arnaud, P. Billaud, and M. Broyer, *Phys. Rev. Lett.* **93**, 127401 (2004).
- ³⁶H. van de Hulst, *Light Scattering by Small Particles*, 1st ed. (Dover, New York, 1981).

2.3 Equations de Bloch optiques en champ proche

Emission et relaxation en présence de structures plasmoniques

Lors de ma thèse, défendue à l'Université de Toulouse en 2001, j'ai démontré l'intérêt des équations de Bloch optiques pour modéliser la fluorescence moléculaire en présence de nanostructures non dissipatives. Ce travail reposait sur la généralisation des équations de Bloch optiques en champ proche. Depuis mon arrivée à Dijon, je me suis appliqué à adapter cette méthode en présence de structures plasmoniques (films étendus et nanoparticules métalliques).

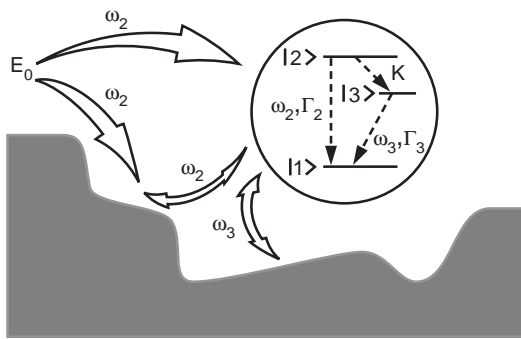


FIG. 2.6 – Représentation schématique d'une molécule fluorescente en interaction avec un environnement complexe. L'excitation à ω_2 pompe la molécule dans un état vibrationnel excité $|2\rangle$. Après relaxation vibrationnelle vers le niveau $|3\rangle$, il y a émission de fluorescence à ω_3 . Γ_i ($i=1,2$) est le taux de relaxation du niveau $|i\rangle$. K est le taux de relaxation vibrationnelle.

La figure 2.6 donne une représentation simplifiée d'une molécule en interaction avec un environnement quelconque. Seuls les niveaux vibrationnels sont représentés. On peut facilement introduire un état triplet non radiatif si nécessaire (voir la fig. 2.2). Les équations de Bloch optiques traitent la molécule de manière quantique et le rayonnement électromagnétique de manière classique. Cela conduit à faire apparaître deux paramètres importants : i) *la fréquence de Rabi* $\Omega(\mathbf{r}_m) = -\mathbf{p} \cdot \mathbf{E}(\mathbf{r}_m)/\hbar$, décrit le couplage avec le champ d'excitation, et ii) *les taux d'émission* $\Gamma(\mathbf{r}_m)$.

J'ai indiqué la dépendance de ces grandeurs avec la position \mathbf{r}_m de la molécule dans son environnement dont il faut tenir compte dans les systèmes étudiés. En particulier, le taux d'émission spontanée vérifie la règle d'or de Fermi

$$\Gamma(\mathbf{r}_m) = \frac{\pi\omega^3}{\hbar\epsilon_0c^2}(1 + \coth\frac{\hbar\omega}{2kT})|\mu_0|^2\rho_{\mathbf{u}}(\mathbf{r}_m, \omega), \quad (2.4)$$

où $\rho_{\mathbf{u}}$ décrit la densité locale de modes électromagnétiques (LDOS), tenant compte de l'orientation \mathbf{u} du moment dipolaire de transition \mathbf{p} et de la contribution électrique uniquement (unité de la LDOS en $s.m^{-3}$). Ce terme inclut l'ensemble des modes électromagnétiques disponibles pour que le niveau moléculaire excité se relaxe soit en émettant un photon, soit par couplage non radiatif avec le métal. Ce point sera discuté en détail au chapitre suivant.

Dans le cas d'un système à deux niveaux, le signal de fluorescence s'écrit en régime stationnaire (le cas d'un système à 3 niveaux est traité dans la référence [41])

$$I_{fluo}(\mathbf{r}_m) = \hbar\omega_2\Gamma_2(\mathbf{r}_m)\frac{\Omega^2(\mathbf{r}_m)/4}{\Gamma_2(\mathbf{r}_m)^2/4 + \Omega^2(\mathbf{r}_m)/2} \quad (2.5)$$

Il est important de traiter le couplage d'une molécule à un mode plasmon de façon non perturbative car le champ électrique d'excitation peut-être fortement exalté à la résonance plasmon. La Fig. 2.7 décrit l'évolution du signal de fluorescence en fonction de l'intensité du laser incident. La fluorescence est d'abord contrôlée par le champ électrique d'excitation (Fig. 2.7A) puis par la LDOS (Fig. 2.7F) lorsque la saturation est atteinte [42]. Cette description nous a permis d'homogénéiser l'interprétation d'expériences récentes d'excitation de molécules fluorescentes en champ proche optique [41].

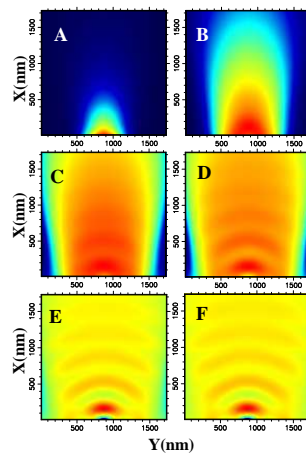


FIG. 2.7 – Cartographie de l'émission de fluorescence d'une molécule excitée par couplage avec des nanostructures métalliques. Le passage du régime non saturé (A, $\Omega = 100MHz$) au régime saturé (F, $\Omega = 2,5GHz$) est visible. Les oscillations d'interférences qui apparaissent progressivement indiquent que la molécule émet ou non un photon par couplage avec les modes supportés par le système. En régime de saturation, le signal de fluorescence reproduit donc la densité de modes (LDOS).

A court terme, je souhaite appliquer ce formalisme à l'analyse de la diffusion Raman exaltée en surface. Cette description fine des processus d'interactions de molécules avec des nanostructures plasmoniques est particulièrement adaptée aux spectroscopies exaltées en surface telle que le SERS [43]. Une description plus aboutie du couplage molécule-plasmon passera aussi par l'écriture des équations de Maxwell-Bloch qui tiennent compte de la perturbation du champ par la molécule [44]. Par la suite, je souhaite aussi m'intéresser à la statistique de comptage de photons d'un émetteur quantique couplé à des structures plasmoniques. De telles configurations sont prometteuses pour optimiser par exemple le rendement de sources de photons uniques [45].

Publication associée

”Theory of molecular excitation and relaxation near a plasmonic device“

G. Colas des Francs, C. Girard, T. Laroche, G. Lévêque, O. Martin and A. Dereux

Journal of Chemical Physics **127**, 34701 (2007).

La lettre suivante, reproduite en annexe, décrit de manière plus approfondie l'écriture des équations de Bloch en champ proche optique

”Generalized Bloch equations for optical interactions in confined geometries“

C. Girard, O. Martin, G. Lévêque, G. Colas des Francs and A. Dereux

Chemical Physics Letters **44**, 204 (2005).

Theory of molecular excitation and relaxation near a plasmonic device

Gérard Colas des Francs^{a)}

Institut Carnot de Bourgogne, CNRS UMR5209, Université de Bourgogne, 9 Avenue A. Savary, F-21078 Dijon, France

Christian Girard and Thierry Laroche^{b)}

Centre d'Elaboration de Matériaux et Etudes Structurales (CNRS), Nanoscience Group, 29 rue J. Marvig, F-31055 Toulouse, France

Gaëtan Lévèque and Olivier J. F. Martin

Nanophotonics and Metrology Laboratory, Swiss Federal Institute of Technology Lausanne (EPFL), CH-1015 Lausanne, Switzerland

(Received 23 February 2007; accepted 18 May 2007; published online 16 July 2007)

The new optical concepts currently developed in the research field of *plasmonics* can have significant practical applications for integrated optical device miniaturization as well as for molecular sensing applications. Particularly, these new devices can offer interesting opportunities for optical addressing of quantum systems. In this article, we develop a realistic model able to explore the various functionalities of a plasmon device connected to a single fluorescing molecule. We show that this theoretical method provides a useful framework to understand how quantum and plasmonic entities interact in a small area. Thus, the fluorescence signal evolution from excitation control to relaxation control depending on the incident light power is clearly observed. © 2007 American Institute of Physics. [DOI: [10.1063/1.2748753](https://doi.org/10.1063/1.2748753)]

I. INTRODUCTION

The current research stream towards optical system miniaturization is motivated by a need for (i) higher density of integrated photonic components, (ii) low threshold biological and chemical sensors, and (iii) molecular scale characterization of complex biomolecules. In the rapidly growing field of the *nanophotonics*, systems consisting of isolated molecules in interaction with noble metal nanostructures^{1,2} are used as prototype models to test and validate new proposal of active plasmonic devices.

In the early stage of the surface molecular spectroscopy, the unusual optical properties of plasmonic materials were already invoked as possible mechanisms for the surface enhanced Raman spectroscopy.³ Very recently, with the demonstration of the control of fluorescent resonant energy transfer⁴ through thin layers of plasmonic materials, a new step towards the *molecular plasmonics* has been achieved.^{4–7} These new experiments use the excitation of surface plasmons to enhance and control the efficiency of the light transfer between two remote molecular sites. This control of light transfer in ultrareduced geometry^{8,9} could have a positive impact on a future optical technology scalable to molecular dimension.¹⁰ In a closely related context involving the spatial control of sharp metal tips or the effective realization of nanoparticle plasmon waveguides, single molecules are often used as efficient local sensors of the plasmonic near-field intensity.

To support the development of these molecular plas-

monic devices, specific theoretical frameworks must be imagined. They should be able to include the complex physics we have to deal with when we couple quantum systems with plasmonic environments. For example, from numerous models, it is well known^{11–13} that nanostructured surface samples can dramatically modify the fluorescence lifetime of molecules. However, such information is not sufficient to predict the complete photophysical behavior of the molecule and to determine the amount of energy released by the molecule as a function of both *excitation energy* and the *excitation frequency*. Especially in the presence of plasmonic devices that sustain localized plasmon modes, such an analysis requires a special attention to properly include local field enhancements, Ohmic losses, and radiative decay rates. In this article, we show that all these characteristics can be included by applying a combination of the *field-susceptibility technique*¹³ together with the formalism of the *optical Bloch equations*.^{14–17} This self-consistent version of *Maxwell Bloch equation* approach relies on the fact that quantum-mechanical calculations can be restricted to the molecular system,¹⁸ while the complex optical environment can be treated classically using the field-susceptibility technique.

II. LIGHT GUIDING AND CONFINEMENT

To illustrate our technique, we have chosen a system of experimental interest (cf. Fig. 1). In this example, the sample consists of metallic nanoparticles arranged to form plasmonic chain waveguides.¹⁹ Three years ago, direct experimental evidence of short range coupling has been reported by measuring electromagnetic energy transport along silver nanoparticle plasmon waveguides.¹⁹ As described in this reference, the simplest optical method aimed at addressing sur-

^{a)}Electronic mail: gerard.colas-des-francs@u-bourgogne.fr

^{b)}Present address: LNIO-Université Technologique de Troyes—12, rue Marie Curie BP2060, F10010 Troyes, Cedex, France.

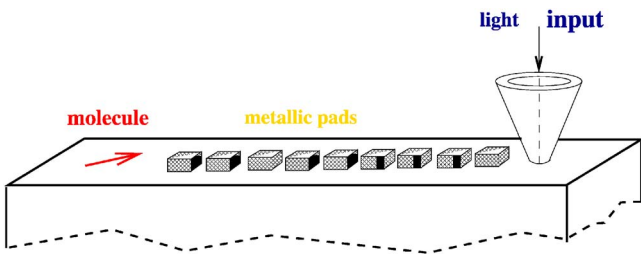


FIG. 1. (Color online) Perspective view of a periodic linear chain of metal particles deposited on a dielectric surface. The chain is optically addressed by the extremity of a SNOM tip. Fluorescent molecules are located at the chain exit.

face nanostructures consists in using and controlling the light polarization state of the electromagnetic field generated at the apex of the probe tip of a scanning near field optical microscope (SNOM).²⁰ To describe the excitation electric field, we can assume that the effective tip dipole $\mathbf{m}(t)$, located at \mathbf{r}_{tip} , is driven by an external monochromatic excitation of angular frequency ω_0 and polarized in a direction \mathbf{a} parallel to the surface. It thus oscillates according to the simple cosine law

$$\mathbf{m}(t) = \mathbf{a}m \cos(\omega_0 t). \quad (1)$$

The total near-field distribution $\mathcal{E}(\mathbf{r}, t)$ generated by the SNOM tip around the plasmonic device can be easily obtained by solving a dyadic integral equation

$$\mathcal{E}(\mathbf{r}, t) = \frac{1}{2}\{\mathcal{E}(\mathbf{r}, \omega_0)\exp(i\omega_0 t) + \text{c.c.}\} \quad (2)$$

with

$$\mathcal{E}(\mathbf{r}, \omega_0) = \mathcal{S}(\mathbf{r}, \mathbf{r}_{\text{tip}}, \omega_0) \cdot \mathbf{a}m \quad (3)$$

where \mathcal{S} is the total field-susceptibility dyadic tensor of the plasmonic device. This tensor obeys Dyson's equation

$$\begin{aligned} \mathcal{S}(\mathbf{r}, \mathbf{r}_{\text{tip}}, \omega_0) &= \mathbf{S}(\mathbf{r}, \mathbf{r}_{\text{tip}}, \omega_0) + \int_{\text{metal}} \mathcal{S}(\mathbf{r}, \mathbf{r}', \omega_0) \cdot \chi(\omega_0) \cdot \mathbf{S}(\mathbf{r}', \mathbf{r}, \omega_0) d\mathbf{r}'. \end{aligned} \quad (4)$$

In this relation, \mathbf{S} is the field-susceptibility associated with the bare dielectric surface and $\chi(\omega_0)$ represents the susceptibility of the metal. Equation (4) can be solved numerically by using an algorithm based on a three-dimensional meshing of the metal chain.¹³ The electric field around the system is then used to compute at the chain exit (i.e., in a predefined location \mathbf{R}_m) near-field transmission spectra

$$I_{\text{chain}}(\mathbf{R}_m, \omega_0) = |\mathcal{E}(\mathbf{R}_m, \omega_0)|^2. \quad (5)$$

When the SNOM tip optically addresses one of the extremities of the chain, the evanescent electric field that tails off the very tip couples with the closest metal post so that significant energy transfer can be triggered along the chain. In Fig. 2, we present transmittance spectra of a gold nanoparticle chain. The transmittance bands correspond to the coupling of localized plasmon modes sustained by each gold pad (located around 620 nm for an isolated gold pad). More precisely, they result from the superimposition of these individual resonances that are redshifted by their mutual interactions. To complete our analysis, we present in Fig. 3 two electric intensity field maps computed around the chain for two wavelengths corresponding to the two maxima of Fig. 2. The guiding efficiency is significantly improved when the extremity of the chain is excited by a transverse electric field [see map (A) of Fig. 3]. Furthermore, in this case the transmittance band (see Fig. 2) is sufficiently broad to address a large family of dye molecules with excitation spectra ranging from 680 to 750 nm. Consequently, in the following of this paper we will use this polarization mode.

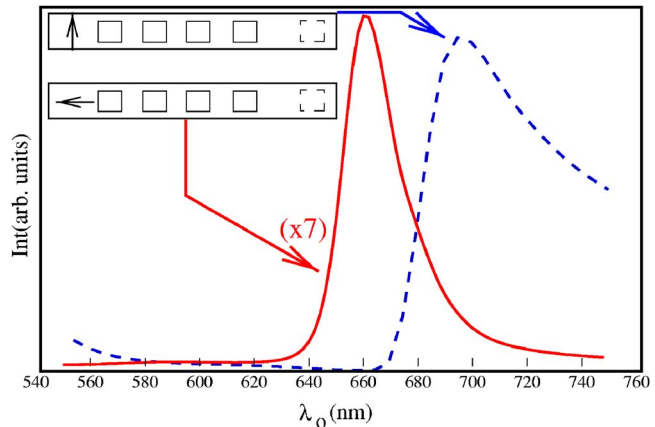


FIG. 2. (Color online) Optical transmittance of a metal particle chain composed of 15 square shaped gold nanoparticles ($100 \times 100 \times 40 \times \text{nm}^3$) spaced by 100 nm. The arrow inside the inset frame schematizes the SNOM tip dipole orientation: (in blue) the tip dipole is along the longitudinal axis; (in red) the tip dipole is perpendicular to the chain.

vidual resonances that are redshifted by their mutual interactions. To complete our analysis, we present in Fig. 3 two electric intensity field maps computed around the chain for two wavelengths corresponding to the two maxima of Fig. 2. The guiding efficiency is significantly improved when the extremity of the chain is excited by a transverse electric field [see map (A) of Fig. 3]. Furthermore, in this case the transmittance band (see Fig. 2) is sufficiently broad to address a large family of dye molecules with excitation spectra ranging from 680 to 750 nm. Consequently, in the following of this paper we will use this polarization mode.

III. MOLECULAR FLUORESCENCE

Let us consider a molecular system located at the position \mathbf{R}_m of the chain exit [Fig. 4(a)]. In order to simplify the description, the fluorescing molecule will be schematized by a two-level quantum system characterized by its ground state $|g\rangle$ and its excited state $|e\rangle$ so that $\delta_L = \omega_0 - \omega_e$ is the detuning factor between the laser frequency ω_0 and the resonant molecular absorption frequency ω_e .

The matrix density operator ρ is introduced to describe the molecule dynamics. We define $u = \text{Re}(\rho_{ge} e^{-i\omega_0 t})$, $v = \text{Im}(\rho_{ge} e^{-i\omega_0 t})$, and $w = (\rho_{ee} - \rho_{gg})/2$ the usual Bloch vector. The optical Bloch equations are then written in the rotating wave approximation

$$\dot{u} = \delta_L v - \Gamma_e(\mathbf{R}_m) u/2, \quad (6)$$

$$\dot{v} = -\delta_L u - \Omega(\mathbf{R}_m) w - \Gamma_e(\mathbf{R}_m) v/2, \quad (7)$$

$$\dot{w} = \Omega(\mathbf{R}_m) v - \Gamma_e(\mathbf{R}_m) w - \Gamma_e(\mathbf{R}_m)/2, \quad (8)$$

where we have introduced the Rabi frequency $\Omega(\mathbf{R}_m) = -|\mathbf{P}_{eg} \cdot \mathcal{E}(\mathbf{R}_m, \omega_0)|/\hbar$ and the decay rate $\Gamma_e(\mathbf{R}_m)$, which both depend on the molecule position near the metallic structures. According to Fermi's golden rule and applying the fluctuation-dissipation theorem, this total decay rate is known to depend on the orientation \mathbf{b} of the transition moment P_{eg} of the molecule with the relation¹⁴

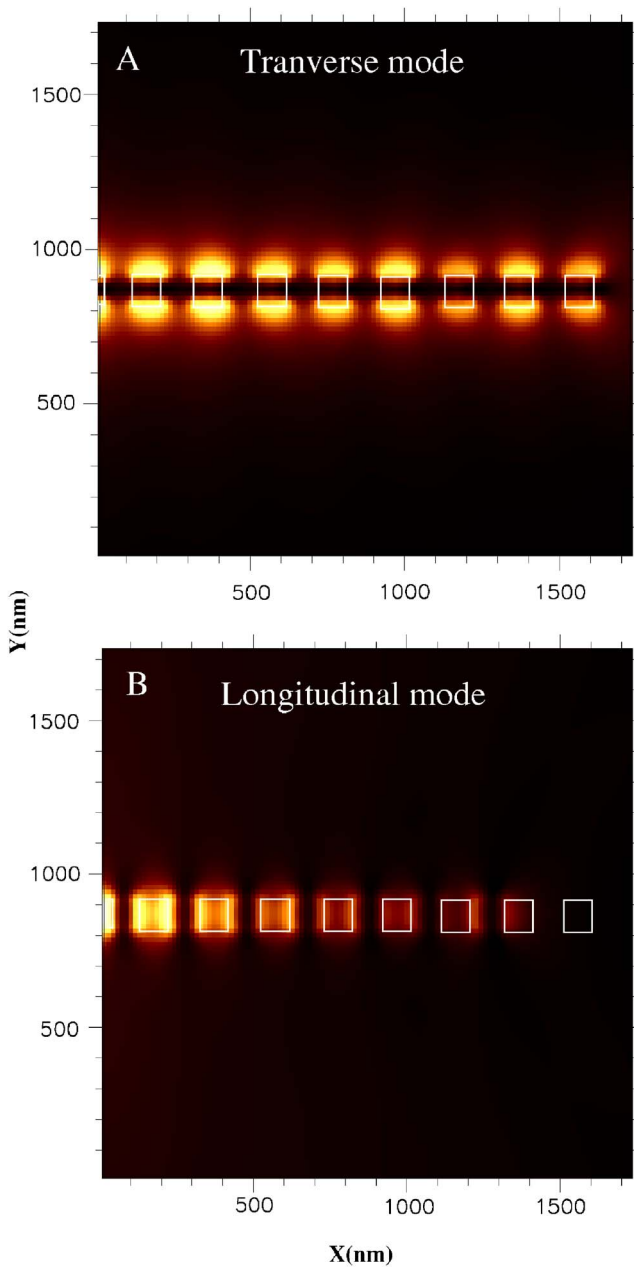


FIG. 3. (Color online) Two near-field optical images along the gold particle chain. The images have been calculated for two polarization modes: (A) transverse mode ($\lambda=690$ nm) and (B) longitudinal mode ($\lambda=668$ nm). Color scale increasing from dark brown to bright yellow.

$$\Gamma_e(\mathbf{R}_m) = \Gamma_e^{(0)} + \frac{2P_{eg}^2}{\hbar} \operatorname{Im}\{\mathcal{S}(\mathbf{R}_m, \mathbf{R}_m, \omega_e)\} : \mathbf{b}\mathbf{b}. \quad (9)$$

Note that the field susceptibility that enters the decay rate is nothing but the tensor already introduced to define the electric field in Eqs. (2)–(4). Within this numerical scheme, the fluorescence rate and the excitation field are simultaneously obtained by solving the same Dyson equation (4). Additionally, the complex polarization of the electric near field responsible for the molecular excitation is naturally introduced in the Rabi frequency through the \mathcal{S} dyadic tensor. Finally, it is worthwhile to note that both dissipation and radiative fluorescence relaxation channels are included in the decay rate expression.²¹ Figures 4(b) and 5 represent, respectively, the

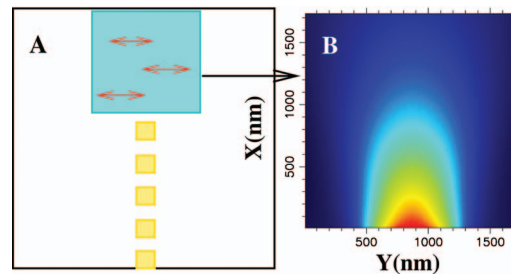


FIG. 4. (Color) (A) Geometry of the molecular addressing area. The molecules deposited in this area lie at 1 nm from the dielectric surface supporting the gold structures. (B) Map of the square modulus of the Rabi frequency $|\Omega(\mathbf{R}_m)|^2$ computed in the addressing area defined in (A). The used wavelength $\lambda_0=690$ nm corresponds to the peak of the transverse mode and the transition dipolar moment of the molecule is perpendicular to the chain (see orientation of the red arrows). Rainbow color scale increasing from blue to red.

square modulus of the Rabi frequency Ω^2 and the molecular decay rate Γ_e computed when the molecule is successively oriented along (OX) and (OY) directions. A close look at these three maps indicates the striking difference between excitation light distribution and decay rate topography. For instance, typical local density of states (LDOS) oscillations are observed when moving away from the plasmonic waveguide. These are attributed to the interferences between the fields emitted by the source and reflected by the structure in the classical driven dipole model of the decay rate. In quantum description, node(antinode) of LDOS simply reveals no(good) coupling of the emitted photon to the electromagnetic modes supported by the sample.

The stationary population of the molecule levels can be deduced from the three equations [Eqs. (6)–(8)]. For the excited state we obtain

$$\rho_{ee}(\mathbf{R}_m) = \frac{\Omega^2(\mathbf{R}_m)/4}{\delta_L^2 + \Gamma_e(\mathbf{R}_m)^2/4 + \Omega^2(\mathbf{R}_m)/2}. \quad (10)$$

As indicated by Eq. (10), the molecular population rate ρ_{ee} intricately depends on both Rabi frequency and excited state decay rate. This population coefficient enters the effective signal delivered by the molecule (expressed in energy per time unit) as follows:

$$I_{\text{mol}}(\mathbf{R}_m) = \rho_{ee}(\mathbf{R}_m) \hbar \omega_e \Gamma_e(\mathbf{R}_m). \quad (11)$$

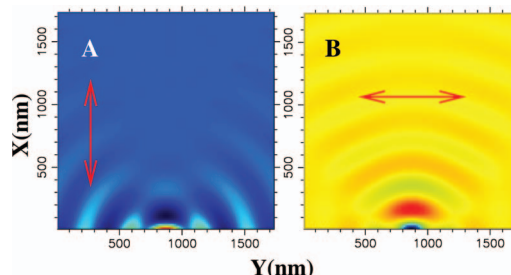


FIG. 5. (Color) Sequence of two maps of molecular decay rate (fluorescing wavelength $\lambda_e=690$ nm) computed in the green area depicted in the device of Fig. 4(a). In these simulations this quantity has been normalized with respect to the natural linewidth $\Gamma_e^{(0)}$. (A) The molecule is aligned along the (OX) direction; (B) same as (A) along the (OY) direction. Rainbow color scale increasing from blue to red.

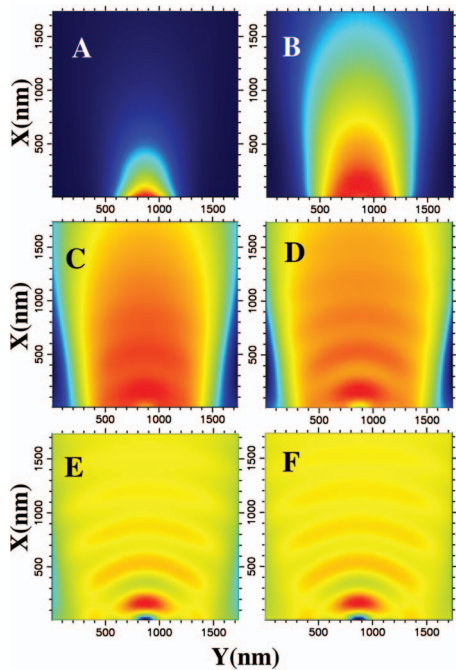


FIG. 6. (Color) Sequence of six maps that describe the evolution of the expected molecule signal when increasing gradually the laser intensity used to address the plasmonic waveguide (fluorescing wavelength $\lambda_e=690$ nm). These signals have been computed in the green area depicted in the device of Fig. 4(a). (A) Off-saturation absorption regime: Rabi frequency $|\Omega|=100$ MHz; (B) $|\Omega|=500$ MHz; (C) $|\Omega|=1$ GHz; (D) $|\Omega|=1.5$ GHz; (E) $|\Omega|=2$ GHz; (F) $|\Omega|=2.5$ GHz. Rainbow color scale increasing from blue to red.

- (i) In the limit case, where we work at low Rabi frequency, these relations clearly indicate that the molecule probes the local near-field intensity $|\mathcal{E}_b(\mathbf{R}_m, \omega_0)|^2$ in the direction (**b**) of its transition dipole moment.
- (ii) In the general case described by Eqs. (10) and (11), the saturated absorption regime occurs when increasing the square modulus of the Rabi frequency beyond the magnitude of $\Gamma_e(\mathbf{R}_m)^2$. The appearance of this phenomenon has been simulated in Fig. 6 by gradually increasing the applied field amplitude. These simulations of the power delivered by the molecule are based on the complete numerical implementation of the *Maxwell-Bloch equations* [Eqs. (2), (4), and (9)–(11)]. The detuning factor has been put to zero and we have fixed the linewidth Γ_0 at 1 GHz. In Fig. 6, we begin the sequence with two maps labeled (A) and (B) in which the Rabi frequency is weaker than the linewidth. In this regime, the molecule essentially responds to the optical near-field intensity that exits the plasmon device. A profound change of the molecule signal occurs when the Rabi frequency range goes beyond the critical value $|\Omega|=1$ GHz. In this case, the molecule tends progressively to deliver a signal proportional to the LDOS tailored by the plasmonic device itself. For example, in maps (E) and (F) of Fig. 6, the saturation regime is reached and the molecule analyzes the *partial LDOS* (Ref. 22) along the (*OY*) axis [see the comparison between Figs. 5(b)

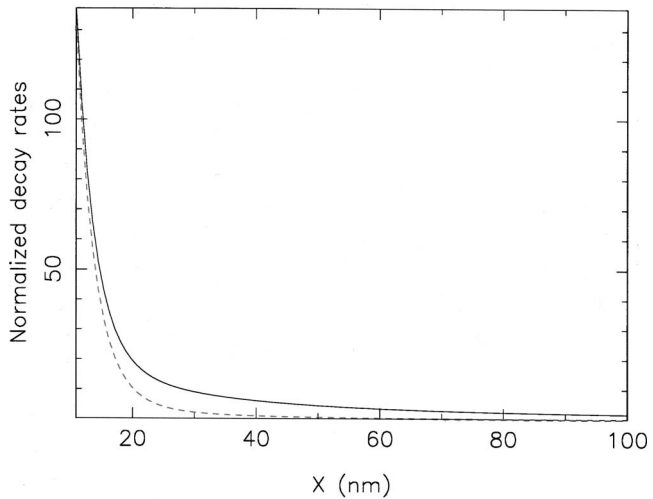


FIG. 7. Normalized total Γ_e (solid line) and nonradiative Γ_{NR} (dashed line) decay rate for molecule at distance X from the last gold pad. The molecule is oriented along the Y axis and is located 1 nm above the substrate.

and 6(f)]. In this case, the molecule loses the history of the successive absorption events and emits fluorescence photons that probe the *partial LDOS* associated with the environment. Such experimental conditions can be obtained by working at low temperature in order to minimize the absorption linewidth Γ_e of the molecular probe. Very recently, Michaelis *et al.* succeeded in operating a low temperature SNOM configuration where the source of light was reduced to a single fluorescing terrylene molecule embedded in a paraterphenyl microcrystal, which itself was glued on the apex of a sharpened optical fiber.²³ These authors have recorded signals related to the variation of the local density of photon states tailored by aluminum surface patterns. The fluorescence signal actually detected is the emitted signal [Eq. (11)] minus the power dissipated inside the metallic particles. The dissipated rate is also easily obtained within the field-susceptibility formalism as²⁴

$$\Gamma_{NR}(\mathbf{R}_m) = \frac{8}{\hbar} \text{Im} \chi \int_{\text{metal}} |\mathcal{S}(\mathbf{R}_m, \mathbf{R}_m, \omega_e) \cdot P_{eg}|^2. \quad (12)$$

This nonradiative contribution to the total decay rate is represented on Fig. 7. Near the metal, the decay rate is dominated by Joule losses responsible for quenching but the dissipation becomes negligible above 40 nm. In the case of low temperature conditions as discussed above, this term remains small even at short distances so that the evolution described on Fig. 6 remains valid for the recorded signal.

IV. CONCLUSION

In conclusion, we have developed a unified formalism to describe molecular photophysical processes triggered by complex plasmonic devices. This approach includes a non-perturbative treatment of the excitation field so that large

field enhancement of plasmonic system is naturally taken into account. The generalization to a many level molecular system can be made without any formal difficulty and the method can be easily adapted to other experimental configurations of the nano-optics world (metal tips, apertures, multilayer environment, etc.). Finally, photon counting statistics might be properly treated by applying the generalization of optical Bloch equations recently proposed by Zheng and Brown.¹⁷

ACKNOWLEDGMENTS

One of the authors (G.C.d.F.) acknowledges support of the Regional Council of Burgundy and another author (O.J.F.M.) gratefully acknowledges support from the Swiss National Science Foundation.. This work was supported in part by the European Network of Excellence (NoE) *Plasmo-Nano-Devices* (Contract No. 507879).

- ¹P. Anger, P. Bharadwaj, and L. Novotny, Phys. Rev. Lett. **96**, 113002 (2006).
²S. Kühn, U. Hakanson, L. Rogobete, and V. Sandoghdar, Phys. Rev. Lett. **97**, 017402 (2006).
³H. Metiu, Prog. Surf. Sci. **17**, 153 (1984).
⁴P. Andrew and W. Barnes, Science **306**, 1002 (2004).
⁵R. V. Duyne, Science **306**, 985 (2004).
⁶A. V. Krasavina and N. I. Zheludev, Appl. Phys. Lett. **84**, 1416 (2004).
⁷P. Mühlischlegel, H.-J. Eisler, O. J. F. Martin, B. Hecht, and D. W. Pohl,

Science **308**, 1607 (2005).

- ⁸H. Ditlbacher, A. Hohenau, D. Wagner, U. Kreibig, M. Rogers, F. Hofer, F. R. Aussenegg, and J. R. Krenn, Phys. Rev. Lett. **95**, 257403 (2005).
⁹C. Girard, E. Dujaudin, M. Li, and S. Mann, Phys. Rev. Lett. **97**, 100801 (2006).
¹⁰M. Sukharev and T. Seideman, J. Chem. Phys. **124**, 144207 (2006).
¹¹G. S. Agarwal, Phys. Rev. A **12**, 1475 (1975).
¹²C. Henkel and V. Sandoghdar, Opt. Commun. **158**, 250 (1998).
¹³C. Girard, O. J. F. Martin, G. Lévéque, G. Colas des Francs, and A. Dereux, Chem. Phys. Lett. **404**, 44 (2005).
¹⁴C. Cohen-Tannoudji, J. Dupont-Roc, and G. Grynberg, *Processus d'Interaction entre Photons et Atomes* (InterEditions, Paris, 1988).
¹⁵C. M. Bowden and J. P. Dowling, Phys. Rev. A **47**, 1247 (1993).
¹⁶J. Weiner and P. T. Ho, *Light-Matter Interaction: Fundamentals and Applications*, 1st ed. (Wiley, Hoboken, NJ, 2003), Vol. 1.
¹⁷Y. Zheng and F. Brown, Phys. Rev. Lett. **90**, 238305 (2003).
¹⁸D. E. Chang, A. S. Sørensen, P. R. Hemmer, and M. D. Lukin, Phys. Rev. Lett. **97**, 053002 (2006).
¹⁹S. A. Maier, P. G. Kik, H. A. Atwater, S. Meltzer, E. Harel, B. E. Koel, and A. A. G. Requicha, Nat. Mater. **2**, 229 (2003).
²⁰M. Brun, A. Drezet, H. Mariette, N. Chevalier, J. C. Woehl, and S. Huant, Europhys. Lett. **64**, 634 (2003).
²¹P. de Vries, D. V. van Coeverden, and A. Lagendijk, Rev. Mod. Phys. **70**, 447 (1998).
²²Definition and measurement of *partial LDOS* are discussed in A. Dereux, C. Girard, C. Chicanne, G. Colas des Francs, T. David, E. Bourillot, Y. Lacroute, and J.-C. Weeber, Nanotechnology **14**, 935 (2003).
²³J. Michaelis, J. M. C. Hettich, and V. Sandoghdar, Nature (London) **405**, 325 (2000).
²⁴G. Colas des Francs, C. Girard, M. Juan, and A. Dereux, J. Chem. Phys. **123**, 174709 (2005).

2.4 Conclusion

Dans ce chapitre, nous avons établi des outils utiles pour étudier la fluorescence moléculaire dans une jonction pointe-surface, en mettant l'accent sur la présence de structures plasmoniques.

Ces outils, expérimentaux (SNOM) et théoriques (équations de Bloch en champ proche optique), ouvrent la voie à de nouveaux concepts. En particulier, il a récemment été proposé de réaliser des expériences d'*optique quantique sans cavité* en profitant du confinement modal intrinsèque des plasmon-polaritons de surface [45]. De récentes expériences ont démontré que le couplage d'un émetteur quantique individuel à une particule plasmonique exalte les taux d'excitation et d'émission, tout en conservant les propriétés de source de photons uniques [46, 47, 48]. Cet axe de recherches est particulièrement actif aujourd'hui. Le chapitre suivant, qui décrit les processus de relaxation moléculaire par couplage aux plasmons, s'inscrit dans cette démarche.

Chapitre 3

Relaxation moléculaire par couplage aux plasmons

L'étude de l'interaction d'une molécule avec des nanostructures métalliques est fondamentale pour interpréter les mesures de spectroscopie exaltée sur surface métallique, telle que le SERS. J'ai rappelé au chapitre 1 les principales propriétés des plasmon-polaritons de surface et les applications de la plasmonique moléculaire. Brièvement, il existe deux types de plasmons de surface : les plasmons localisés supportés par des nanoparticules métalliques et les plasmons délocalisés supportés par des structures métalliques étendues (films, fil, ...). Les deux formes présentent une forte exaltation du champ électromagnétique. De plus les plasmons localisés présentent un volume modal effectif extrêmement faible, assurant un excellent couplage avec des molécules fluorescentes ou Raman actives, à l'origine du SERS par exemple [49]. Les plasmons délocalisés sont des ondes se propageant à la surface du métal et sont activement étudiés en vue d'applications pour la photonique intégrée, comme nous le verrons au chapitre 4.

Nous avons montré au chapitre 1 qu'il existe un domaine d'existence commun pour les deux types de plasmons de surface (Fig. 1.4). Ce domaine, qui correspond à la limite quasi-statique (donc non propagative), assure la possibilité de coupler des plasmons propagatifs avec des plasmons localisés, par exemple avec une structure métallique passant adiabatiquement d'une forme étendue à une forme nanostructurée telle qu'une pointe [50]. Ce point est important car il assure un bon couplage entre une onde propagative et une zone de fort confinement du champ électromagnétique, dans le visible ou proche du visible. Cette propriété est à la base du nouveau concept d'**antenne optique** [51]. Au-delà d'une simple relecture de la microscopie en champ proche optique, la notion d'antenne optique conduit à s'inspirer de l'ingénierie développée dans le domaine des antennes radio-électriques et à l'adapter au domaine visible (voir la figure 3.1) [52, 53, 54]. Les applications sont nombreuses, citons l'imagerie de systèmes biologiques [55] et l'optimisation de cellules photovoltaïques [56].

Finalement, l'étude du couplage d'une molécule avec une structure plasmonique nécessite de bien comprendre les processus de relaxation en présence de systèmes métalliques. En particulier, le rôle et la contribution des différents types de plasmons qui interviennent. De plus, à température ambiante, la dissipation par effet Joule dans le métal implique de perdre une partie du signal émis par la molécule. Il est donc très important de contrôler et mesurer la part de dissipation, de diffusion et éventuellement de propagation d'un plasmon dans le processus de relaxation d'une molécule couplée à une structure métallique.

J'ai abordé ce problème de deux façons. Premièrement, en collaboration avec le groupe

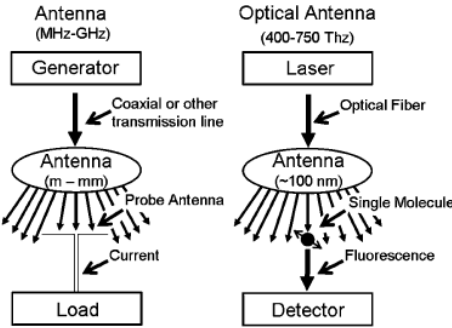


FIG. 3.1 – Analogie entre l’antenne radio-électrique et l’antenne optique, reproduit de Taminiau *et al* [57].

de Niek van Hulst (ICFO, Barcelone), nous avons mesuré les taux de fluorescence dans des géométries simples, permettant des comparaisons avec des simulations numériques (§3.2). D’autre part, j’ai développé un modèle analytique dont l’étude approfondie conduit à une interprétation simple des processus de transferts d’énergie en champ proche (§3.3).

3.1 Règle d’or de Fermi

Le taux de relaxation spontanée d’une molécule fluorescente, inverse de la durée de vie de fluorescence τ , est donné par la règle d’or de Fermi, introduite au §2.3. A température ambiante, celle-ci devient

$$\Gamma(\mathbf{r}_m) = \frac{1}{\tau} = \frac{2\pi\omega^3}{\hbar\epsilon_0c^2}|\mathbf{p}|^2\rho_{\mathbf{u}}(\mathbf{r}_m, \omega), \quad (3.1)$$

où $\rho_{\mathbf{u}}$ est la densité de modes électromagnétiques (LDOS) partielle, selon l’orientation du moment dipolaire de transition \mathbf{p} de la molécule. En particulier les modes plasmons sont inclus dans cette définition. Bien que la présence de dissipation élevée rende abusif le terme de densité de modes (durée de vie très faible), nous continuerons à utiliser le terme de LDOS, couramment accepté par la communauté internationale. Finalement, cette grandeur gouverne la relaxation moléculaire et doit être caractérisée dans toute étude impliquant le couplage molécule-plasmon.

Plusieurs solutions apparaissent pour établir une cartographie de la LDOS en surface :

- Mesure de la durée de vie de fluorescence, inverse du taux de relaxation. Bien que seule mesure exacte (non perturbative) de la LDOS, cela pose la difficulté de connaître avec précision la position de la sonde fluorescente dans le système. De plus, la longueur d’onde de mesure est imposée par le spectre d’émission de l’émetteur. Cette approche est discutée dans le paragraphe 3.2 : *Imagerie de la durée de vie de Fluorescence - (FLIM)*.
- *Dès 2001, nous avons proposé une méthode originale pour cartographier la LDOS dans le domaine optique.* L’idée repose sur le comportement dipolaire d’une pointe SNOM (Scanning Near-field Optical Microscope). Cette approche a été discutée au §2.2 du chapitre 2.
- En analogie directe avec le rayonnement du corps noir, Yannick de Wilde (ESPCI Paris) et Jean-Jacques Greffet (ECP Paris) se sont intéressés au transfert d’énergie en champ proche. Cela a conduit Y. de Wilde à réaliser en 2005 un ThSNOM (Thermal Scanning

Optical Microscope) [58]. L'intérêt de ce montage pour étudier localement les échauffements dans des circuits électroniques est évident. Par contre, la loi de Planck implique que la LDOS soit mesurée dans l'infra-rouge ($\lambda \approx 10\mu\text{m}$) pour des températures proches de la température ambiante. Les applications dans le domaine optique (exaltation de la fluorescence) ne sont donc pas accessibles avec ce montage.

3.2 Imagerie de durée de vie de fluorescence (FLIM)

L'imagerie de la durée de vie de fluorescence - (FLIM - Fluorescence lifetime imaging) est très utilisée pour caractériser *in situ* des systèmes biologiques. Dès mon intégration au CNRS, j'ai suivi une formation pour me familiariser avec cette technique¹. J'ai ensuite proposé de l'utiliser pour caractériser les canaux de relaxation à proximité de structures plasmoniques, en collaboration avec l'équipe de Niek van Hulst (ICFO- Barcelone).

Dans un premier temps, nous avons mesuré les durées de vie τ de molécules dispersées dans un corral optique (constitué de nanoparticules d'or disposées en cercle) [59]. En effet, nous avions déjà cartographié la LDOS dans ce type d'échantillon. Nous espérions comparer les mesures de LDOS faites par microscopie en champ proche SNOM avec les mesures de taux de fluorescence de molécules, en lien avec la règle d'or de Fermi (éq. 3.1). Des molécules de colorants ont été dispersées dans un film de PMMA d'environ 50 nm, déposé sur l'échantillon. La fluorescence des molécules individuelles est ensuite mesurée à l'aide d'un microscope confocal. La difficulté pour comparer ces données avec les mesures SNOM était de placer suffisamment de molécules pour sonder tout le système mais suffisamment espacées pour faire des mesures individuelles et éviter tout couplage entre les molécules. Nous avons pu démontrer des variations de durée de vie mais très faibles.

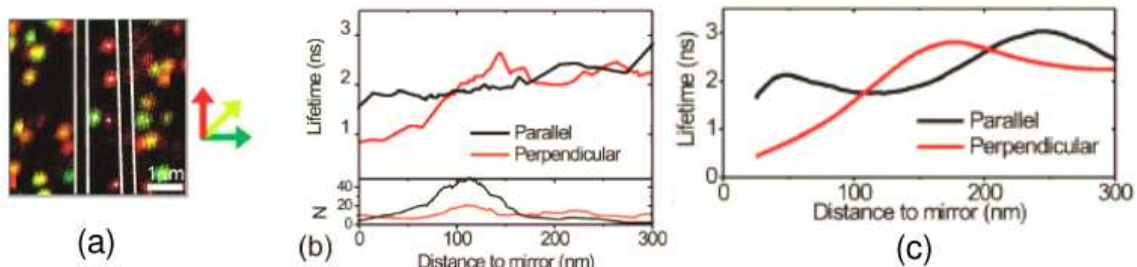


FIG. 3.2 – a) Image de fluorescence ($\lambda \approx 665\text{nm}$) de molécules individuelles dispersées sur une surface de verre entre deux miroirs d'or (indiqués en blanc). Chaque point correspond à une unique molécule. La couleur indique l'orientation de la molécule dans le plan. b) Durée de vie mesurée pour deux orientations en fonction de la distance au miroir le plus proche. c) Durée de vie calculée.

Nous avons alors décidé de considérer une géométrie plus simple : une cavité ouverte constituée de deux rubans d'or déposés sur un substrat de verre (Fig. 3.2) [60]. La distance entre les miroirs varie de 250 nm à 2 μm . Un point important du montage développé à l'ICFO est qu'il permet de déterminer l'orientation des molécules dans le plan en mesurant l'émission dans le

¹Impact des microscopies photoniques pour l'étude des surfaces et des systèmes auto-assemblés, Université Paris Sud, novembre 2005.

substrat selon deux plans orthogonaux (Fig. 3.2a) [61]. D'autre part, les molécules étant suffisamment espacées, il est possible de déterminer leur position avec une grande précision. Il suffit de prendre le centre du signal de fluorescence mesuré en microscopie confocale. La résolution n'est limitée que par le nombre de photons détectés. Les mesures réalisées ont été faites avec une résolution de l'ordre de 30 nm. Ainsi, nous avons pu mesurer les taux de fluorescence pour chaque molécule en fonction de la taille de la cavité, la distance de la molécule aux miroirs, et l'orientation de la molécule. Les valeurs obtenues sont en excellent accord avec les simulations numériques faites avec un modèle simplifié (Fig. 3.2). Il est à noter que le seul paramètre libre du calcul est la durée de vie de la molécule isolée. Cette valeur a été fixée à une valeur moyenne obtenue lors d'une précédente expérience. Nous avons finalement établi les différents modes de la cavité responsable de la relaxation moléculaire (Fig. 3.3).

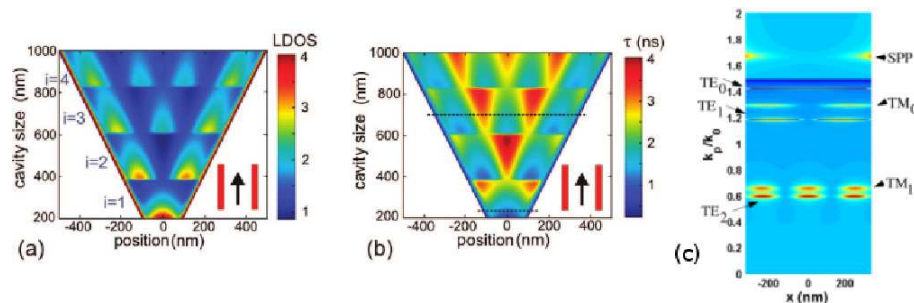


FIG. 3.3 – a) LDOS partielle calculée dans la cavité pour une orientation parallèle aux miroirs. b) Durée de vie correspondante ($\tau \propto 1/LDOS$). c) Contribution des modes de la cavité à la relaxation moléculaire en fonction de la position de la molécule dans la cavité. La distance entre les miroirs est fixée à 670 nm.

Publication correspondante

“The single molecule probe : nanoscale vectorial mapping of photonic mode density in a metal nanocavity”

J. Hoogenboom, G. Sanchez-Mosteiro, G. Colas des Francs, D. Heinis, G. Legay, A. Dereux and N. van Hulst
Nano Letters **9**, 1189-1195 (2009).

L'article présentant les mesures de durée de vie dans un corral optique est reproduit en annexe.

“Single molecules probe local density of modes (LDOS) around photonic nanostructures”

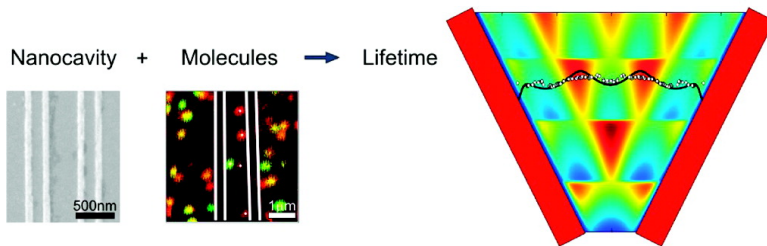
G. Colas des Francs, G. Sanchez-Mosteiro, M. Ujue-Gonzalez, L. Markey, N. van Hulst and A. Dereux
Journal of Microscopy **229**, 210-216 (2008).

The Single Molecule Probe: Nanoscale Vectorial Mapping of Photonic Mode Density in a Metal Nanocavity

Jacob P. Hoogenboom, Gabriel Sanchez-Mosteo, Gerard Colas des Francs, Dominique Heinis, Guillaume Legay, Alain Dereux, and Niek F. van Hulst

Nano Lett., 2009, 9 (3), 1189-1195 • DOI: 10.1021/nl803865a • Publication Date (Web): 16 February 2009

Downloaded from <http://pubs.acs.org> on March 12, 2009



More About This Article

Additional resources and features associated with this article are available within the HTML version:

- Supporting Information
- Access to high resolution figures
- Links to articles and content related to this article
- Copyright permission to reproduce figures and/or text from this article

[View the Full Text HTML](#)



ACS Publications

High quality. High impact.

Nano Letters is published by the American Chemical Society. 1155 Sixteenth Street N.W., Washington, DC 20036

The Single Molecule Probe: Nanoscale Vectorial Mapping of Photonic Mode Density in a Metal Nanocavity

Jacob P. Hoogenboom,^{*,†,‡} Gabriel Sanchez-Mosteiro,[†] Gerard Colas des Francs,[§] Dominique Heinis,[†] Guillaume Legay,[§] Alain Dereux,[§] and Niek F. van Hulst^{†,||}

ICFO—Institut de Ciències Fotòniques, Av. Canal Olímpic s/n, E-08860 Castelldefels (Barcelona), Spain, Soft Condensed Matter, Debye Institute for Nanomaterials Research, Utrecht University, Utrecht, The Netherlands, Institut Carnot de Bourgogne, CNRS UMR 5209—Université de Bourgogne, 9 avenue A. Savary, F-21078 Dijon, France, ICREA—Institució Catalana de Recerca i Estudis Avançats, E-08015 Barcelona, Spain

Received December 22, 2008; Revised Manuscript Received February 4, 2009

ABSTRACT

We use superresolution single-molecule polarization and lifetime imaging to probe the local density of states (LDOS) in a metal nanocavity. Determination of the orientation of the molecular transition dipole allows us to retrieve the different LDOS behavior for parallel and perpendicular orientations with respect to the metal interfaces. For the perpendicular orientation, a strong lifetime reduction is observed for distances up to 150 nm from the cavity edge due to coupling to surface plasmon polariton modes in the metal. Contrarily, for the parallel orientation we observe lifetime variations resulting from coupling to characteristic $\lambda/2$ cavity modes. Our results are in good agreement with calculations of the nanoscale variations of the projected LDOS, which demonstrates the potential of single molecules as nonperturbative, nanoscale vectorial point probes in photonic and biological nanostructures.

Recent advances in high-resolution optical microscopy have highlighted the possibility of truly nanoscopic, subdiffraction limited, far-field imaging using single fluorescent probes.¹ Novel modalities like photoactivated localization microscopy (PALM)² and stochastic optical reconstruction microscopy (STORM)^{3,4} rely on confinement of the fluorescence emission down to the level of a single molecule. By collection of a statistically sound number of photons from each single emitter sequentially, their individual positions can be retrieved resulting in a spatial resolution on the order of 20 nm.^{5,6} While the possibility to image spatial structure with nanoscopic resolution already presents an important breakthrough, the intrinsic multiparameter character of fluorescence emission provides a means to also acquire functional information with nanometer-scale precision. For instance, using different labeling strategies for spectrally shifted fluorophores, biological functionality can be mapped onto spatial structure.^{7,8} So far, however, the *intrinsic* variations in single-molecule fluorescence properties due to variations

in the local nanoenvironment of the emitters have been only sparsely exploited in combination with high-resolution spatial imaging.⁹ As we will demonstrate in this Letter, this scheme provides a means to acquire detailed spatial, and in addition vectorial, functional information, in our case on the mode density in photonic nanostructures.

The fluorescence characteristics of a molecule are determined by both the internal energy level diagram and the external photonic local density of states (LDOS), as expressed by the well-known Fermi golden rule.¹⁰ Since the pioneering work of Drexhage¹¹ the distance-dependent lifetime variations near mirror and grating planes have been investigated by positioning a bulk amount of europium fluorophores at fixed distances using nanometric polymer Langmuir–Blodgett multilayers.^{12,13} In recent years, the ability to create photonic structures with nanometric position control has led to a renewed interest in fluorescence lifetime and spectra control through tailored modification of the LDOS. Controlled emission in systems like nanoantennas, cavities, photonic bandgap materials, and plasmon nanostructures holds promise for applications in sensing, light harvesting and energy conversion, photon sources, and quantum computation. Indeed, modification of lifetime,^{14–23} spectra,^{17,24,25} emission directivity,²⁶ and intersystem crossing

* Corresponding author. j.p.hoogenboom@tudelft.nl. Present address: Department of Imaging Science and Technology, Faculty of Applied Physics, Delft University of Technology, Delft, The Netherlands.

† ICFO.

‡ Debye Institute.

§ Institut Carnot de Bourgogne.

|| ICREA.

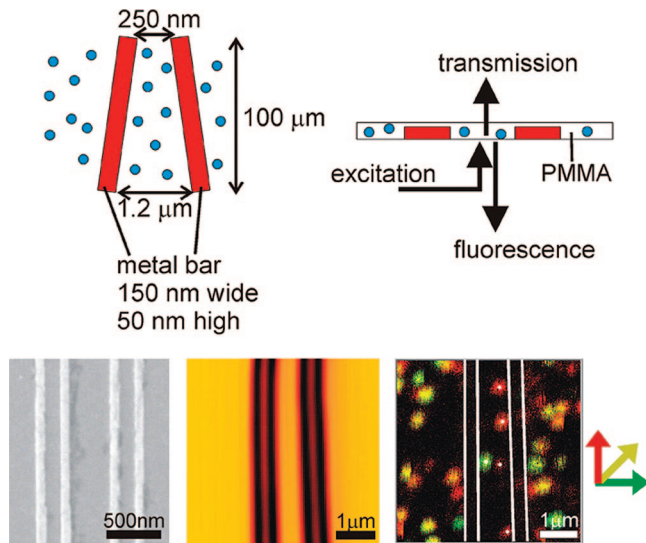


Figure 1. Schematic indication of the cavity design and relevant experimental parameters. Upper left part of the figure shows a top view of the cavity structure where red stripes indicate the gold bars and blue dots the randomly positioned molecules. Upper right part shows a side view with the relevant excitation and detection light paths indicated. Bottom left shows a SEM image of the metal mirror cavity prior to deposition of the polymer and molecules. Three cavity structures were fabricated next to each other: spacing between first and second and third and fourth metal bar was kept constant at 250 nm, the spacing between the second and third bar was gradually increased as indicated in the upper left image. The 150 nm width of the gold bars prevents long-range interactions between molecules located in adjacent cavities. The cavity structure is imaged in transmission mode (middle image) while DiD molecules are simultaneously imaged in fluorescence mode (bottom right). Retrieved positions of mirror planes and molecules are indicated with white stripes and dots. Red and green color coding in the fluorescence image refers to orthogonal emission polarization directions as indicated by the arrows.

rates²⁷ has recently been explored. However, while experiments on single fluorophores positioned in a cavity have recently been reported,^{17,23,24,28,29} the high-resolution single-molecule spatial accuracy has not yet been used in combination with retrieval of such functional information. While several alternative techniques to probe the LDOS in photonic nanostructures have been proposed,^{30,31} direct measurement using fluorophores³² ultimately yields nanoscopic spatial resolution. Embedding the nanoscopic molecular probe in the cavity structure, bears the further advantage that the probe itself does not in turn perturbate the LDOS.³³ In addition, the fixed transition dipole moment of an immobilized molecule holds the clear advantage of probing the LDOS in a vectorial fashion.

Here, we use high-resolution single-molecule fluorescence lifetime imaging to spatially and vectorially probe the LDOS in a metallic nanocavity. This provides us with a full vectorial lifetime-LDOS map throughout the nanocavity. Our results are compared to the expected behavior based on direct calculations of the projected LDOS inside the cavity.

The two-dimensional nanocavity we investigated consists of two gold bars, each of 150 nm width and 50 nm height, fabricated by electron-beam lithography on an indium tin oxide substrate using a standard lift-off procedure. On the

samples, three nanocavities were fabricated next to each other, the outer with a fixed width of 250 nm, the middle one with width varying between 250 nm and 1.2 μm . The layout is schematically indicated in Figure 1. By spin coating from a toluene solution, the structure was embedded in a 60 nm high poly(methyl methacrylate) (PMMA) film containing about 10^{-8} M of fluorescent 1,1'-dioctadecyl-3,3',3'-tetramethylindocyanine perchlorate (DiD, Invitrogen) molecules. The thickness of the PMMA film was chosen to be larger than the height of the mirror bars in order to minimize curvature of the polymer–air interface in the cavity, while still maintaining a sufficiently thin film to avoid focal overlap of molecules located at different heights in the film. The quantum yield of DiD is 1, which means that unless additional nonradiative decay channels are opened such as quenching in very close proximity (<10 nm) to the metal surface, lifetime changes are reminiscent of changes in the radiative decay rate. The structure was imaged in optical transmission and fluorescence simultaneously (as indicated in Figure 1) using a home-built confocal microscope. Excitation was performed using a 635 nm diode laser (Picoquant LDH-635, 90 ps fwhm, 20 MHz). Fluorescence light was separated from reflected excitation light using a dichroic mirror (Omega 650DRPLP) and a 665 nm long pass filter (Omega 665ALP), split by a polarization cube and collected on two avalanche photodiodes (APD, EG&G Electro Optics SPCM-AQ-14) connected to a time-correlated single photon counting card (TCSPC, Picoquant Timeharp 200). Images were acquired using a reduced power density of 0.11 kW/cm^2 to avoid rapid photobleaching, with a pixel size of $39 \times 39 \text{ nm}^2$ and a 1 ms dwell time. After image scanning, fluorescence from selected single-molecule locations was collected by continuous excitation at 3 kW/cm^2 . Single-molecule positions were extracted from the fluorescence image by applying a Gaussian filter followed by calculation of the center-of-mass for selected molecular intensity profiles (see Figure 1). The fluorescence lifetime was calculated from the intensity time trace recorded for a specific molecule by constructing the histogram of photon arrival times and fitting to a single-exponential decay. Both positional⁵ and lifetime accuracy³⁴ are dependent on the number of detected photons. For the highly photostable DiD molecule (typically 10^4 – 10^5 detected photon counts), we have molecular positional accuracy ~ 30 nm, and lifetime accuracy ~ 0.1 ns. Positions of the metal mirror bars were retrieved from the transmission image. In addition to the high-resolution determination of dipole position and lifetime, the polarization-sensitive detection of emission light allows us to also determine the orientation of the dipole emitter.

Measured position- and orientation-dependent fluorescence lifetimes are compared to the outcome of LDOS calculations. For an emitter with a fixed transition dipole moment, like our immobilized DiD molecules, the fluorescence decay rate Γ —the inverse of the lifetime—is related to the projected LDOS (pLDOS) through Fermi's golden rule¹⁰

$$\Gamma(\mathbf{r}) = \frac{\pi\omega}{\hbar\varepsilon_0} |\mu|^2 \rho_u(\mathbf{r}, \omega)$$

where r is the position of the emitter, ω its resonance frequency, μ the transition dipole moment, and ρ_u the pLDOS along the direction \mathbf{u} of the transition dipole moment $\mu = \mu\mathbf{u}$. The pLDOS is determined using Green's dyad formulation.³⁵ In order to take into account the unknown transition dipole moment in Fermi's golden rule, the decay rate relative to a reference decay rate is calculated. As a reference we take the average decay rate for DiD molecules in a thin PMMA film. We will see below that this reference also allows us to take into account the intrinsic heterogeneity in the experimental single-molecule lifetime distribution.

In total, we extracted positions and lifetimes inside the cavity for 880 DiD molecules. The position in the cavity was defined as the distance to the nearest cavity edge. In Figure 2a the single-molecule lifetime as a function of position inside cavity is given. As can be seen, the distribution of lifetimes broadens and shifts to lower values with decreasing distance to a mirror. In addition to the cavity molecules, we measured 158 DiD molecules at a macroscopic distance from the mirror cavities to extract the reference. This reference distribution, yielding an averaged DiD lifetime of 2.6 ns, is indicated in Figure 2b together with the full distribution for the cavity molecules. Here, we note a clear shift of the distribution average to lower lifetime values as well as a broadening toward even lower, sub-1-ns lifetimes

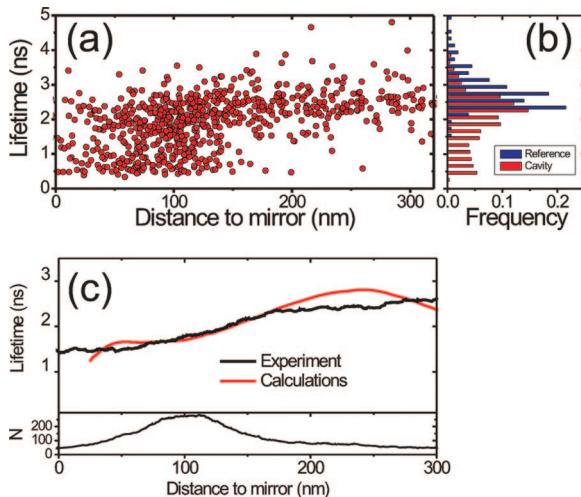


Figure 2. (a) Lifetime as a function of distance to the nearest mirror bar for all 880 molecules measured inside the mirror cavity. (b) Distribution of fluorescence lifetimes for all these cavity molecules (in red), compared to the reference histogram of 158 molecules measured far away from the cavity structure. The reference histogram shows the effects of intrinsic molecular variations in the lifetime due to, e.g., variations in the local nanoenvironment of the molecules, and the finite size of the PMMA film and the proximity of the glass plate. Compared to the reference distribution, the distribution of lifetimes in the cavity is markedly shifted to lower values, with a tail extending to sub-1-ns values. (c) Average lifetime as a function of distance to the nearest mirror (black line) compared to the expected lifetime behavior based on LDOS calculations (red line). Both experimental and calculated curves have been retrieved by applying a 50 nm averaging window and are averaged over all orientations and cavity sizes. The lower panel indicates the number of experimental data points (i.e., molecules) in the averaging window as a function of distance.

for the cavity molecules. This result along with Figure 2a strongly indicates position-dependent lifetime modifications for molecules located inside the cavity.

A second point to note here is that the reference distribution of “free” molecules already shows broadening and thus lifetime variations from molecule to molecule. This broadening is predominantly caused by the proximity of polymer–air and polymer–glass interfaces due to the finite size of the PMMA film. These interfaces lead to modifications in the LDOS and thus in fluorescence lifetimes for molecules at different heights in the film and with different out-of-plane orientations³⁶ (note that in the polarization-sensitive fluorescence image in Figure 1, we measure the molecular orientation projected onto the substrate). In addition, small variations in lifetime from molecule to molecule may be caused by variations in the local nanoenvironment.³⁷ Thus, in order to extract position-dependent information on molecular lifetime variations, one has to either measure the same molecule in different conditions, which is rather cumbersome but could in principle be performed with a scanning probe microscope^{18,19,26} or an ion trap,²⁸ or one has to explicitly take into account the distributed lifetimes, as we will do in the following.

First, we construct a position-dependent average lifetime, by averaging the data in Figure 2a with a 50 nm window. The result is indicated in Figure 2c, together with the expected lifetime behavior based on LDOS calculations. In the calculations, we consider a 1D cavity, neglecting the finite height of the cavity. Note that refractive indices of substrate and polymer film are very similar (around 1.5) and that molecular lifetime variation due to the finite polymer thickness will be accounted for in the experimental results by comparison to the reference distribution. In Figure 2c, we observe a good agreement between the experimental and calculated results, indicating that the observed modifications in molecular lifetime distributions are indeed due to the modified LDOS inside the cavity. At this point, however, we have to bear in mind that data are averaged over all molecular orientations and all cavity widths. These two points will be disentangled consecutively.

Now, we note that a different lifetime behavior may be expected for molecules with a transition dipole moment located parallel and perpendicular to the mirrors (indicated in Figure 3a). The molecular dipole orientation can be evaluated from the measured fluorescence polarization by defining the degree of polarization $P = (I_r - I_g)/(I_r + I_g)$, where I_r and I_g denote detected intensity on red and green APD channels, respectively (see also lower right image in Figure 1). Figure 3a depicts the histogram of degree of polarization for all cavity molecules. Now, we define the subsets of parallel and perpendicular oriented molecules as indicated in Figure 3a. For both these subsets we apply the same procedure with a 50 nm integration window as above to plot the molecular lifetime as a function of distance to the mirror (Figure 3b). A clearly different behavior for parallel compared to perpendicular molecules can be observed. Most notably, the strong decrease in lifetime for distances < 100 nm to the mirror is mostly due to perpen-

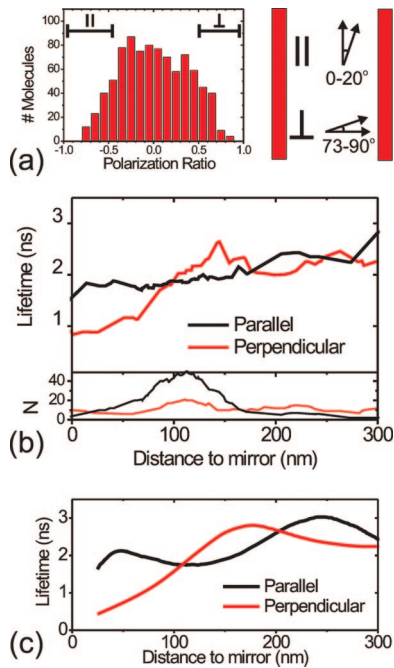


Figure 3. (a) Histogram of the degree of polarization of all 880 molecules inside the cavity structure. For vectorial probing the cavity LDOS, we look at two subdistributions, which are defined by their relative orientation with respect to the cavity design, as indicated in the drawing. For selecting both parallel and perpendicular sets of molecules, the outmost 12.5% of molecules on both sides of the distribution were taken (102 parallel, 85 perpendicular). (b) Measured fluorescence lifetime as a function of distance to the nearest mirror for both distributions of molecules oriented parallel and perpendicular to the mirror. The lower panel indicates the number of molecules within the 50 nm averaging window as a function of distance. (c) Calculated dependence of the lifetime on distance to the mirror for both orientations. There is a good agreement between experimental and calculated results in terms of the strong reduction of lifetime for perpendicular orientation for distances below 100 nm, the more gradual increase of lifetime away from the mirror for the parallel orientation, and the crossover between parallel and perpendicular curves at ~ 100 nm and ~ 190 nm.

dicular oriented molecules, while the parallel molecules display a more gradual decrease with decreasing distance to one of the mirrors. In addition, comparing both curves to the results based on LDOS calculations (given in Figure 3c), we see that the relative behavior of both curves is in correspondence with the theoretical predictions. Thus, the fixed transition dipole moment of an immobilized molecule is found to reproduce LDOS variations in a *vectorial* fashion; i.e., it probes the *projected* LDOS (pLDOS).

Next, we turn to the behavior for both orientations for different cavity sizes. We note that different behavior may be expected for cavities that differ in size by integer times half the effective wavelength, $i\lambda/2n = i223$ nm, with $\lambda = 665$ nm and $n = 1.49$. In Figure 4 the calculated pLDOS and corresponding lifetimes for all cavity sizes and all positions within the cavity are shown. A clear difference for dipoles oriented parallel with respect to the axis compared to those with a perpendicular orientation can be observed over the full range of cavity widths. This difference originates from coupling to two different types of modes in the

nanocavity. For a parallel orientation, the pLDOS, depicted in Figure 4a, is dominated by Fabry–Perot type cavity modes (see Supporting Information). Here, the number of maxima increases with i as expected. Thus, for $i = 1$, i.e., cavity size $\lambda/2n < d < \lambda/n$, we observe a single maximum in the pLDOS at the cavity center. For very small distances (< 10 nm) to the metal edge, strong nonradiative decay due to quenching to the metal takes place leading to a steep increase of the pLDOS. At positions equal to 0.25 and 0.75 of the size of the $i = 1$ cavity, pLDOS is at a minimum. For $i = 2$, $\lambda/n < d < 3\lambda/2n$, two maxima in the pLDOS are observed, and so on for increasing i . Note that the actual values are slightly smaller than $i\lambda/2n$ due to the penetration depth in the metal.³⁸ The pLDOS translates into inverse behavior for the fluorescence lifetime as indicated in Figure 4b for a parallel oriented dipole.

For the perpendicular orientation, given in panels c and d of Figure 4, an entirely different behavior is observed. In this case the pLDOS is dominated by surface plasmon polariton (SPP) modes in the metal edges^{35,39} (see Supporting Information), which, for distances < 150 nm from the edge, leads to a gradual decrease in lifetime when approaching one of the edges. At distances > 150 nm, the fluorescence lifetime is basically unaffected by the presence of the metallic nanocavity.

We compare the pLDOS calculations with our experimental data for two different cavity types, namely, the smallest one ($i = 1$) and the $i = 3$ cavity. These are indicated with dashed lines in Figure 4. In the experimental data we collect all molecules in cavity size range supporting these mode types, i.e., $0.45\lambda/n < d < 0.67\lambda/n$ for the $i = 1$ cavity and $1.40\lambda/n < d < 1.90\lambda/n$ for the $i = 3$ cavity. These values deviate slightly from integer times $\lambda/2n$ due to the penetration depth in the metal and the fact that we exclude the region close to the mode cutoff. For the $i = 3$ cavity, the criteria for parallel and perpendicular molecules was increased to respectively $P < -0.05$ and $P > 0.05$ to have sufficient molecules in each subset (66 and 93, respectively, compared to 115 and 48, respectively, for the (shorter) $i = 1$ cavity), where we verified that applying these criteria to the entire set of molecules in Figure 3 remained unchanged.

The experimental data for the lifetime as a function of distance to the nearest mirror is given in Figure 5, together with the theoretical results for cavity sizes of $d = 225$ and 670 nm, respectively, which correspond to the positions indicated by dashed lines in Figure 4. For the $i = 1$ cavity, it can be seen that the lifetime at every position in the cavity for both orientations is reduced compared to the average lifetime in the reference distribution (indicated by the dashed line) in correspondence with the lifetime calculations and the strong increase in pLDOS in Figure 4c. Moreover, we see that while for the parallel orientation the lifetime only shows small variations between $\tau = 1.5$ ns and $\tau = 2$ ns, the perpendicular orientation displays even lower lifetime values which gradually decrease below 1 ns upon approaching the mirror. As the response time of the APD is of the order of 200–400 ps, the few molecules in the 50 nm averaging window with relatively longer lifetimes dominate

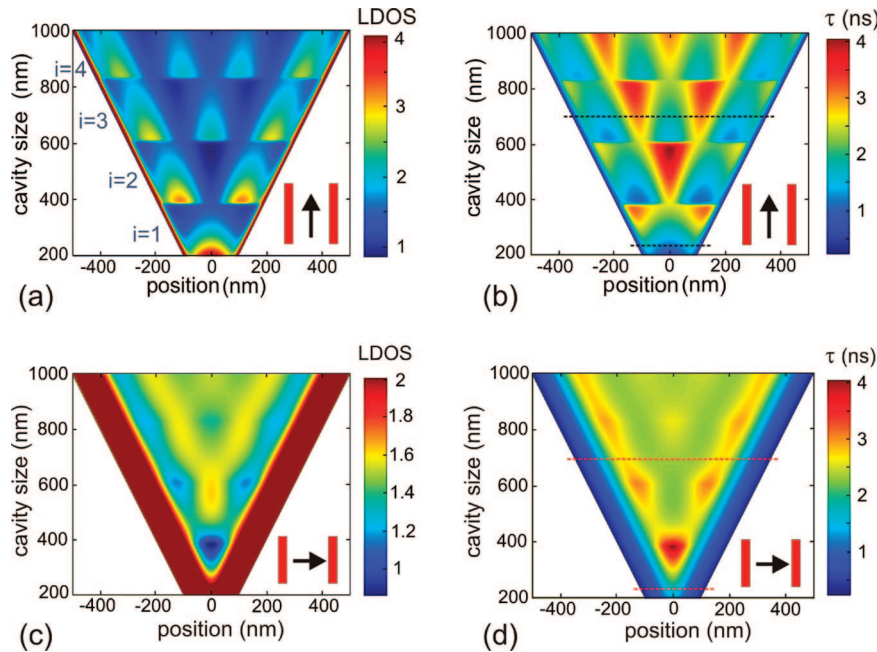


Figure 4. (a) Calculated pLDOS in the direction parallel to the cavity interfaces, as a function of both position in the cavity and cavity size. (b) Corresponding fluorescence lifetime for a DiD fluorescent molecule oriented parallel with respect to the cavity. (c) pLDOS and (d) DiD lifetime for a perpendicular orientation. The pLDOS is normalized with respect to the free space value, its color scale is saturated with maxima reaching 15 for parallel (top left) and 35 for perpendicular orientation (bottom left). Indicated in the top left image are the cavity types i that group cavity sizes based on the number of sustained modes. A clear difference between both dipole orientations can be seen, which results from predominant coupling to cavity modes for a parallel orientation compared to coupling to SPP modes for the perpendicular orientation. Dashed lines indicate the location of the curves shown in Figure 5.

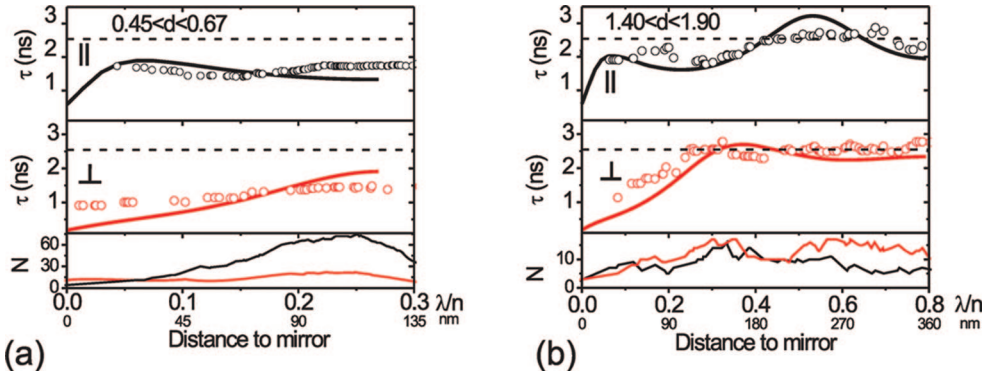


Figure 5. Average lifetime as a function of position to the nearest metal mirror plane for the two cavity sizes indicated in Figure 4. Cavity size is indicated in reduced units (relative to the effective wavelength in the PMMA matrix), which corresponds to (a) cavity type $i = 1$ (interval of $200 < d < 300$ nm), and (b) cavity type $i = 3$ ($625 < d < 850$ nm). Open dots refer to the molecular lifetime, averaged over the indicated range of cavity sizes and a 50 nm window in position; the solid lines refer to the calculated lifetime for a cavity size halfway the experimental interval. Top panels (black curves and dots) are for a dipole orientated parallel to the mirror, middle panels (red curves and dots) for a perpendicular dipole orientation. The lower panels indicate the number of molecules in the averaging. The dashed lines indicate the average fluorescence lifetime without cavity structure. For both cavity sizes a clear difference between the two dipole orientations can be observed, closely following the expected behavior based on the LDOS calculations.

the averaging. Thus our averaged experimental lifetime data has a lower limit of ~ 1 ns, while the calculated result decays toward zero.

For the $i = 3$ cavity, we observe a different behavior with smaller reduction of fluorescence lifetime due to smaller LDOS variations in line with the results from the calculations. At comparatively larger distance from the mirror, the lifetime is about equal to its reference value with, for the parallel case, a reduction to 2 ns for distances smaller than about 200 nm ($0.45\lambda/n$) as well as very close

to the cavity center. For the perpendicular orientation, fluorescence lifetime is only modified from the reference value for distances smaller than 110 nm ($0.25\lambda/n$), where it steadily decreases to zero due to coupling to the SPP mode in the metal like for the $i = 1$ cavity. All in all, we observe clearly different behavior for both cavity sizes and for both orientations, in all cases in line with the expected lifetime behavior based on pLDOS calculations. Thus we conclude that our single-molecule lifetime

measurements map the LDOS with vectorial sensitivity at nanometer-scale, single-molecule spatial resolution.

The approach presented here, relying on superresolution, single-molecule, spatial imaging of fluorescence lifetime and polarization anisotropy, can be highly relevant for biological systems, extending the possibilities of novel nanoscopy techniques¹ like PALM² and STORM.^{3,4} While polarization-sensitive superresolution microscopy, based on fluorescence photoactivation (P-FPALM),⁴⁰ has very recently been demonstrated, the inclusion of fluorescence lifetime measurements⁴¹ truly exploits the multiparameter character of molecular fluorescence for unraveling biological structure and functionality at the nanoscale. The vectorial information gives access to (locally restricted) rotational diffusion, and thus viscosity, and to emerging orientational and positional ordering. Note that this holds both for situations where the molecular transition dipole moment is fixed, like in our study, and those situations where it is not. The latter case also allows a single molecule to probe part of the orientation and position phase space; however, it should be noted that this comes at the expense of position accuracy, which directly depends on the number of detected photon counts. Adding to the vectorial information, molecular fluorescence lifetime variations may be related to differences in the biochemical environment of the probe or to binding or energy transfer events. Moreover, fluorescence lifetime is an important discriminator between different fluorophores and can thus be used to map functionality using different labeling strategies. Clearly, correlating lifetime and orientation data, like in our nanophotonics structure, extends these capabilities, for instance revealing orientation-dependent interactions and transfer processes in biomolecular machinery.

In our study, we have an estimated average accuracy of ~ 30 nm in position and ~ 0.1 ns in lifetime. For localization microscopy using photoactivated fluorophores, position resolution of ~ 20 nm has been reported. Both position and lifetime resolution are dependent on the number of detected photon counts^{5,34} and thus mostly limited by photobleaching. The use of photobleaching-resistant quantum dots, or anisotropic quantum rods, would allow for detection of a fixed, aimed number of photon counts, and could push this resolution to 10 nm, if photoblinking⁴² can be substantially prevented. With respect to lifetime, we currently encounter a lower limit of ~ 0.5 ns, set by a detector response time of 200–400 ps, compared to an average molecular fluorescence lifetime of 2.6 ns. Here, the tens of nanoseconds or larger lifetime of quantum dots would considerably increase the dynamic range, which would for instance be important in probing strong quenching close to the metal interface. However, care should be taken to properly analyze and interpret the multiexponential decay of single quantum dots.^{43,44}

In summary, we have presented the use of single fluorescent molecules as local nanoscopic probes for the LDOS in a metallic nanocavity, mapping the full position- and cavity-size-dependent lifetime LDOS curve. The single-molecule probe holds the demonstrated advantages of vectorial sensitivity and ultimate nanometer-scale spatial resolution; i.e.,

it is a vectorial point-probe. In addition, probing is performed in a nonperturbative fashion. Thus, this approach has the promising perspective of probing functional nanophotonic structures like nanoantennas, photonic crystals, high-Q resonators, and sensors based on near-field enhancement. In addition, the methodology can be relatively straightforwardly extended to the probing of nanofocusing effects, local field enhancement, and enhanced quantum efficiency in such structures. Finally, as discussed, the concept of superresolution single-molecule fluorescence lifetime, and polarization imaging has great prospects for nanoscopy of biological systems.

Acknowledgment. The authors thank Aude Lereu for assistance with the sample preparation. This work was supported in part by the European Network of Excellence (NoE) Plasmonanodevices, the Stichting voor Fundamenteel Onderzoek der Materie (FOM), and the STREP ASPIRE in the EU 6th framework.

Supporting Information Available: Results of a plane wave expansion of the emitted power of a dipole in relation to its position and orientation in the nanocavity, which reveals the magnitude of coupling to cavity and SPP modes. This material is available free of charge via the Internet at <http://pubs.acs.org>.

References

- (1) Hell, S. W. *Science* **2007**, *316* (5828), 1153–1158.
- (2) Betzig, E.; Patterson, G. H.; Sougrat, R.; Lindwasser, O. W.; Olenych, S.; Bonifacino, J. S.; Davidson, M. W.; Lippincott-Schwartz, J.; Hess, H. F. *Science* **2006**, *313* (5793), 1642–1645.
- (3) Huang, B.; Wang, W. Q.; Bates, M.; Zhuang, X. W. *Science* **2008**, *319* (5864), 810–813.
- (4) Bates, M.; Huang, B.; Dempsey, G. T.; Zhuang, X. W. *Science* **2007**, *317* (5845), 1749–1753.
- (5) Thompson, R. E.; Larson, D. R.; Webb, W. W. *Biophys. J.* **2002**, *82* (5), 2775–2783.
- (6) Qu, X. H.; Wu, D.; Mets, L.; Scherer, N. F. *Proc. Natl. Acad. Sci. U.S.A.* **2004**, *101* (31), 11298–11303.
- (7) Churchman, L. S.; Okten, Z.; Rock, R. S.; Dawson, J. F.; Spudich, J. A. *Proc. Natl. Acad. Sci. U.S.A.* **2005**, *102* (5), 1419–1423.
- (8) Bossi, M.; Fölling, J.; Belov, V. N.; Boyarskiy, V. P.; Medda, R.; Egner, A.; Eggeling, C.; Schönle, A.; Hell, S. W. *Nano Lett.* **2008**, *8* (8), 2463–2468.
- (9) van Oijen, A. M.; Kohler, J.; Schmidt, J.; Muller, M.; Brakenhoff, G. J. *J. Opt. Soc. Am. A* **1999**, *16* (4), 909–915.
- (10) Fermi, E. *Rev. Mod. Phys.* **1932**, *4*, 87.
- (11) Drexhage, K. *J. Lumin.* **1970**, *1*, 2, 693–701.
- (12) Amos, R. M.; Barnes, W. L. *Phys. Rev. B* **1997**, *55* (11), 7249–7254.
- (13) Andrew, P.; Barnes, W. L. *Phys. Rev. B* **2001**, *64* (12), 125405.
- (14) Kleppner, D. *Phys. Rev. Lett.* **1981**, *47* (4), 233–236.
- (15) Goy, P.; Raimond, J. M.; Gross, M.; Haroche, S. *Phys. Rev. Lett.* **1983**, *50* (24), 1903–1906.
- (16) Lodahl, P.; van Driel, A. F.; Nikolaei, I. S.; Irman, A.; Overgaag, K.; Vanmaekelbergh, D.; Vos, W. L. *Nature* **2004**, *430* (7000), 654–657.
- (17) Steiner, M.; Schleifenbaum, F.; Stupperich, C.; Failla, A. V.; Hartschuh, A.; Meixner, A. J. *ChemPhysChem* **2005**, *6*, 2190–2196.
- (18) Kuhn, S.; Hakanson, U.; Rogobete, L.; Sandoghdar, V. *Phys. Rev. Lett.* **2006**, *97*, 017402.
- (19) Anger, P.; Bharadwaj, P.; Novotny, L. *Phys. Rev. Lett.* **2006**, *96* (11), 113002.
- (20) Tam, F.; Goodrich, G. P.; Johnson, B. R.; Halas, N. J. *Nano Lett.* **2007**, *7* (2), 496–501.
- (21) Muskens, O. L.; Giannini, V.; Sánchez-Gil, J. A.; Gómez-Rivas, J. *Nano Lett.* **2007**, *7* (9), 2871–2875.
- (22) Buchler, B. C.; Kalkbrenner, T.; Hettich, C.; Sandoghdar, V. *Phys. Rev. Lett.* **2005**, *95* (6), 4.
- (23) Lund-Hansen, T.; Stobbe, S.; Julsgaard, B.; Thyrrstrup, H.; Sunner, T.; Kamp, M.; Forchel, A.; Lodahl, P. *Phys. Rev. Lett.* **2008**, *101*, 113903.

- (24) Barth, M.; Schuster, M.; Gruber, A.; Cichos, F. *Phys. Rev. Lett.* **2006**, *96*, 243902.
- (25) Ringler, M.; Schwemer, A.; Wunderlich, M.; Nichtl, A.; Kurzinger, K.; Klar, T. A.; Feldmann, J. *Phys. Rev. Lett.* **2008**, *100*, 203002.
- (26) Taminiua, T. H.; Stefani, F. D.; Segerink, F. B.; Van Hulst, N. F. *Nat. Photonics* **2008**, *2* (4), 234–237.
- (27) Stefani, F. D.; Vasilev, K.; Bocchio, N.; Gaul, F.; Pomozi, A.; Kreiter, M. *New J. Phys.* **2007**, *9*, 21.
- (28) Guthohrlein, G. R.; Keller, M.; Hayasaka, K.; Lange, W.; Walther, H. *Nature* **2001**, *414* (6859), 49–51.
- (29) Steiner, M.; Failla, A. V.; Hartschuh, A.; Schleifenbaum, F.; Stupperich, C.; Meixner, A. J. *New J. Phys.* **2008**, *10*, 123017.
- (30) Chicanne, C.; David, T.; Quidant, R.; Weeber, J.-C.; Lacroute, Y.; Bourillot, E.; Dereux, A.; Colas des Francs, G.; Girard, C. *Phys. Rev. Lett.* **2002**, *88*, 097402.
- (31) Huang, C.; Bouhelier, A.; Colas des Francs, G.; Legay, G.; Weeber, J.-C.; Dereux, A. *Opt. Lett.* **2008**, *33* (4), 300–302.
- (32) Koenderink, A. F.; Kafesaki, M.; Soukoulis, C. M.; Sandoghdar, V. *Opt. Lett.* **2005**, *30* (23), 3210–3212.
- (33) Mujumdar, S.; Koenderink, A. F.; Sunner, T.; Buchler, B. C.; Kamp, M.; Forchel, A.; Sandoghdar, V. *Opt. Express* **2007**, *15* (25), 17214–17220.
- (34) Köllner, M.; Wolfrum, J. *Chem. Phys. Lett.* **1992**, *200* (1–2), 199–204.
- (35) Barnes, W. L. *J. Mod. Opt.* **1998**, *45* (4), 661–699.
- (36) Vallee, R.; Tomczak, N.; Gersen, H.; van Dijk, E.; Garcia-Parajo, M. F.; Vancso, G. J.; van Hulst, N. F. *Chem. Phys. Lett.* **2001**, *348* (3–4), 161–167.
- (37) Vallee, R. A. L.; Tomczak, N.; Kuipers, L.; Vancso, G. J.; van Hulst, N. F. *Phys. Rev. Lett.* **2003**, *91* (3), 038301.
- (38) Ram, R. J.; Babic, D. I.; York, R. A.; Bowers, J. E. *IEEE J. Quantum Electron.* **1995**, *31* (2), 399–410.
- (39) Weber, W. H.; Eagen, C. F. *Opt. Lett.* **1979**, *4* (8), 236.
- (40) Gould, T. J.; Gunewardene, M. S.; Gudheti, M. V.; Verkhusha, V. V.; Yin, S.-R.; Gosse, J. A.; Hess, S. T. *Nat. Methods* **2008**, *5* (12), 1027–1030.
- (41) Clayton, A. H. A.; Hanley, Q. S.; Arndt-Jovin, D. J.; Subramaniam, V.; Jovin, T. M. *Biophys. J.* **2002**, *83*, 1631–1649.
- (42) Stefani, F. D.; Hoogenboom, J. P.; Barkai, E. *Phys. Today* **2009**, *2*, 34–39.
- (43) Fisher, B. R.; Eisler, H. J.; Stott, N. E.; Bawendi, M. G. *J. Phys. Chem. B* **2004**, *108* (1), 143–148.
- (44) van Driel, A. F.; Nikolaev, I. S.; Vergeer, P.; Lodahl, P.; Vanmaekelbergh, D.; Vos, W. L. *Phys. Rev. B* **2007**, *75*, 035329.

NL803865A

Supplementary information for the manuscript “*The single molecule probe: nanoscale vectorial mapping of photonic mode density in a metal nanocavity*”
by J. P. Hoogenboom, G. Sanchez-Mosteiro, G. Colas des Francs, D. Heinis, G. Legay, A. Dereux,
and N. F. van Hulst

In the pLDOS calculations described in the manuscript, we can determine the contribution of each of the modes in the cavity to the total pLDOS by applying the formalism described in ref. 33 (Barnes, W. L. *Journal of Modern Optics* **1998**, 45 (4), 661-699). In the following figure, the emitted power as a function of molecular position x (with respect to the center of the cavity), and in-plane wave vector k_p (normalized with respect to free-space wave vector k_0) is given for both dipole orientations for an $i = 3$ cavity ($d = 670\text{nm}$). Figure (a) depicts the emitted power for a dipole with an orientation parallel to the cavity interfaces, figure (b) the same information for a perpendicular oriented dipole. We observe clear, distinct cavity modes for values $k_p/k_0 < 1.49$ ($= n_{PMMA}$) and a surface plasmon polariton (SPP) mode for $k_p/k_0 = 1.66$. The cavity modes can be assigned as TE and TM modes depending on their mode profile (figure (c)). For the parallel oriented dipole, we see that the emission is dominated by coupling to the TE, and slightly weaker the TM, cavity modes, with a noticeable coupling to the SPP mode only for very short distances from the metal interface. Contrarily, for the perpendicular oriented dipole, excitation of the SPP mode is dominant over distances up to 150nm from the metal cavity interface. In addition, closer to the cavity center, emission into TM_0 and, very weakly, TM_1 modes occurs. For the perpendicular oriented dipole, TE modes are forbidden. As expected, the dipole-mode coupling strength is proportional to $|\mathbf{u} \cdot \mathbf{E}(x)|^2$, where, as in the main text, \mathbf{u} is the dipole transition moment.

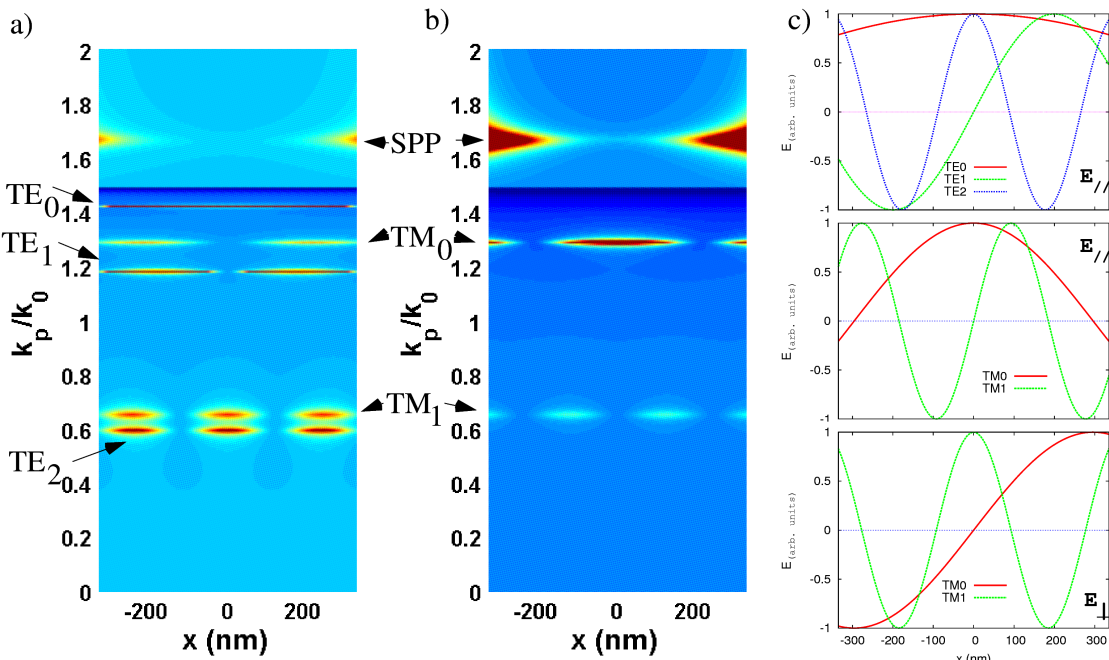


Figure: (a) Emitted power as a function of both molecule position and in-plane wave vector (relative to free-space wave vector) for a dipole parallel to the cavity interface. (b) Same information for perpendicular orientation. (c) Cavity modes profiles. The modes effective indices are $n_{\text{eff}}(\text{TE}_0)=1.42$, $n_{\text{eff}}(\text{TE}_1)=1.18$, $n_{\text{eff}}(\text{TE}_2)=0.59$ for TE polarization and $n_{\text{eff}}(\text{TM}_0)=1.29$, $n_{\text{eff}}(\text{TM}_1)=0.65$ for TM polarization, and $n_{\text{eff}}(\text{SPP})=1.66$.

3.3 Transfert d'énergie en champ proche

Ces dernières années, plusieurs expériences ont démontré la possibilité de mesurer précisément l'interaction de molécules uniques avec des nanostructures plasmoniques. Le point crucial est le contrôle de la distance entre la molécule et l'objet métallique. Cela peut se faire en attachant une unique molécule à l'extrémité d'un brin d'ADN dont l'autre extrémité est attachée à la particule métallique [62, 63]. Une autre configuration repose sur l'utilisation d'un microscope à sonde locale. La nanostructure est accrochée à l'extrémité de la sonde qui est approchée de manière très contrôlée de molécules individuelles déposées sur un substrat [64, 65]. La plupart des études ont considéré des particules d'or sphériques qui permettent des comparaisons avec un modèle analytique exact. En particulier, les taux de relaxation radiatifs et non radiatifs d'une molécule en interaction avec une bille métallique peuvent s'écrire sous un développement de Mie faisant apparaître explicitement les ordres des modes impliqués. Cela a permis de déterminer simplement les modes intervenant dans le processus de relaxation par couplage aux plasmons [66]. Ainsi, la modification du taux radiatif est principalement issue du couplage avec le mode dipolaire de la particule alors que le taux non radiatif résulte du couplage avec les modes d'ordres élevés [67] (voir la figure 3.4). En effet, l'émission de fluorescence, de nature dipolaire, génère des gradients de champs suffisants pour exciter efficacement l'ensemble des modes de la particule (voir par exemple l'équation 1.11 du chapitre 1).

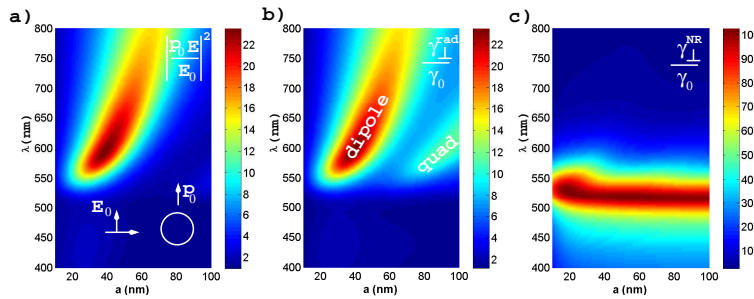


FIG. 3.4 – a) Intensité du champ électrique, b) taux radiatif, et c) taux non radiatif calculés à 10 nm de la surface d'une particule sphérique d'or en fonction du rayon a de la particule et de la longueur d'onde. Le champ électrique d'excitation de la molécule suit la relation de dispersion du mode dipolaire (Fig. 3.4a) alors que le taux radiatif résulte d'un couplage avec le mode dipolaire puis quadrupolaire de la particule lorsque la taille de celle-ci augmente (Fig. 3.4b). Enfin, la faible dispersion du taux non radiatif est caractéristique du couplage avec le mode plasmon d'interface du système.

Dans ce contexte, je me suis intéressé à la compréhension fine du transfert d'énergie entre la molécule et la bille métallique, notamment en lien avec la conservation de l'énergie [67, 68]. Par exemple, aux très courtes distances de séparation z_0 , le transfert non radiatif prend la forme approchée suivante (les polarisabilités quasi-statiques α_n sont données par l'équation 1.10 du chapitre 1)

$$\begin{aligned} \frac{\gamma_{\perp}^{\text{NR}}}{\gamma_0} &\approx \frac{3}{2} n_B \frac{1}{(k z_0)^3} \sum_{n=1}^{\infty} \frac{(n+1)^2}{z_0^{(2n+1)}} \\ &\left[\text{Im}(\alpha_n^{\text{eff}}) - \frac{(n+1)k^{2n+1}}{n(2n-1)!!(2n+1)!!} |\alpha_n^{\text{eff}}|^2 \right], \text{avec} \end{aligned} \quad (3.2)$$

$$\alpha_n^{eff} = \left[1 - i \frac{(n+1)k^{2n+1}}{n(2n-1)!!(2n+1)!!} \alpha_n \right]^{-1} \alpha_n. \quad (3.3)$$

Cette expression montre que le transfert non radiatif se fait par couplage aux modes plasmons. De plus, pour chaque mode n , le terme proportionnel à $Im(\alpha_n^{eff})$ décrit l'extinction du signal émis par la molécule, soit par absorption, soit par diffusion par la particule. En soustrayant la contribution de la diffusion (terme proportionnel à $|\alpha_n^{eff}|^2$), on obtient la contribution non radiative. Toutefois, il faut signaler que la conservation de l'énergie n'est assurée dans cette forme approchée que si on tient compte de la taille finie de la particule [68]. Cela conduit à introduire les polarisabilités effectives définies par la relation 3.3. L'interprétation microscopique du terme correctif $-i \frac{(n+1)k^{2n+1}}{n(2n-1)!!(2n+1)!!} \alpha_n$ est une force de friction, appelée réaction de rayonnement, qui décrit la perte d'énergie par rayonnement des électrons en mouvement [69].

Publications correspondantes

“Fluorescence relaxation in the near-field of a mesoscopic metallic particle : distance dependence and role of plasmon modes”

G. Colas des Francs, A. Bouhelier, E. Finot, J.-C. Weeber, A. Dereux, C. Girard and E. Dujardin
Optics Express **16**, 17654-17666 (2008).

Les effets de taille finie sont discutés dans la Communication suivante (disponible en accès libre à <http://www.mdpi.com/1422-0067/10/9/3931>)

“Molecule non-radiative coupling to a metallic nanosphere : an optical theorem treatment”

G. Colas des Francs
International Journal of Molecular Science, **10**, 3931-3936 (2009).

Enfin, la relaxation moléculaire dans une jonction-pointe surface de géométrie complexe est analysée dans l'article reproduit en annexe

“Molecular quenching and relaxation in a plasmonic tunable system”

G. Baffou, C. Girard, E. Dujardin, G. Colas des Francs and O. Martin
Physical Review B, **77**, 122101(R) (2008).

Fluorescence relaxation in the near-field of a mesoscopic metallic particle: distance dependence and role of plasmon modes

G. Colas des Francs¹, A. Bouhelier¹, E. Finot¹, J. C. Weeber¹, A. Dereux¹, C. Girard² and E. Dujardin²

¹Institut Carnot de Bourgogne, UMR 5209 CNRS - Université de Bourgogne,
9 Av. A. Savary, BP 47 870, 21078 Dijon, FRANCE

²Centre d'Elaboration de Matériaux et d'Etudes Structurales (CNRS)
29, rue Jeanne Marvig BP 4347, F-31055 Toulouse, FRANCE
**Corresponding author: gerard.colas-des-francs@u-bourgogne.fr*

Abstract: We analytically and numerically analyze the fluorescence decay rate of a quantum emitter placed in the vicinity of a spherical metallic particle of mesoscopic size (*i.e.* with dimensions comparable to the emission wavelength). We discuss the efficiency of the radiative decay rate and non-radiative coupling to the particle as well as their distance dependence. The electromagnetic coupling mechanisms between the emitter and the particle are investigated by analyzing the role of the plasmon modes and their nature (dipole, multipole or interface mode). We demonstrate that near-field coupling can be expressed in a simple form verifying the optical theorem for each particle modes.

© 2008 Optical Society of America

OCIS codes: (260.2510) Fluorescence;(260.2160) Energy transfer;(240.6680) Surface plasmons

References and links

1. R. P. Van Duyne, Molecular plasmonics, *Science* **306**, 985 (2004).
2. D. W. Pohl, "Near-field optics seen as an antenna problem," in *Near-field Optics, Principles and Applications*, X. Zhu and M. Ohtsu, eds., pp. 9–21. (World Scientific, Singapore, 2000).
3. P. Mühlischlegel, H.-J. Eisler, O. J. F. Martin, B. Hecht, and D. W. Pohl, "Resonant Optical Antennas," *Science* **308**, 1607 – 1609 (2005).
4. T. H. Taminiua, R. J. Moerland, F. B. Segerink, L. Kuipers, and N. F. van Hulst, " $\lambda/4$ resonance of an optical monopole antenna probed by single molecule fluorescence," *Nano Lett.* **7**, 28–33 (2007).
5. D. Chang, A. Sørensen, P. Hemmer, and M. Lukin, "Quantum Optics with Surface Plasmons," *Phys. Rev. Lett.* **97**, 053002 (2006).
6. L. A. Blanco and F. J. G. de Abajo, "Spontaneous light emission in complex nanostructures," *Phys. Rev. B* **69**, 205414 (2004).
7. P. Anger, P. Bharadwaj, and L. Novotny, "Enhancement and quenching of single molecule fluorescence," *Phys. Rev. Lett.* **96**, 113002 (2006).
8. T. Härtling, P. Reichenbach, and L. M. Eng, "Near-field coupling of a single fluorescent molecule and a spherical gold nanoparticle," *Opt. Express* **15**, 12806–12817 (2007).
9. L. Rogobete, F. Kaminski, M. Agio, and V. Sandoghdar, "Design of nanoantennae for the enhancement of spontaneous emission," *Opt. Lett.* **32**, 1623–1625 (2007).
10. G. Baffou, C. Girard, E. Dujardin, G. Colas des Francs, and O. Martin, "Molecular quenching and relaxation in a plasmonic tunable nanogap," *Phys. Rev. B* **77**, 121101(R) (2008).

11. E. Dulkeith, A. C. Morteani, T. Niedereichholz, T. A. Klar, J. Feldmann, S. A. Levi, F. C. J. M. van Veggel, D. N. Reinhoudt and M. Möller, and D. I. Gittins, "Fluorescence Quenching of Dye Molecules near Gold Nanoparticles: Radiative and Nonradiative Effects," *Phys. Rev. Lett.* **89**, 203002 (2002).
12. S. Kühn, U. Hakanson, L. Rogobete, and V. Sandoghdar, "Enhancement of single molecule fluorescence using a gold nanoparticle as an optical nano-antenna," *Phys. Rev. Lett.* **97**, 017402 (2006).
13. P. Bharadwaj and L. Novotny, "Spectral dependence of single molecule fluorescence enhancement," *Opt. Express* **15**, 14266–14274 (2007).
14. H. Mertens, A. Koenderink, and A. Polman, "Plasmon-enhanced luminescence near noble-metal nanospheres: Comparison of exact theory and an improved Gersten and Nitzan model," *Phys. Rev. B* **76**, 115123 (2007).
15. V. Klimov, M. Ducloy, and V. S. Letokhov, "Radiative Frequency Shift and Line Width of an Atom Dipole in the Vicinity of a Dielectric Microsphere," *J. Mod. Opt.* **43**, 2251 (1996).
16. P. T. Leung, "Decay of molecules at spherical surfaces: Nonlocal effects," *Phys. Rev. B* **42**, 7622 (1990).
17. C. Girard, S. Maghezzi, and F. Hache, "Multipolar propagators near a small metallic sphere : A self consistent calculation," *J. Chem. Phys.* **91**, 5509–5517 (1989).
18. C. Bohren and D. Huffman, *Absorption and scattering of light by small particles* (1983).
19. Y. S. Kim, P. T. Leung, and T. F. George, "Classical Decay Rates for Molecules in the Presence of a Spherical Surface: a Complete Treatment," *Surf. Sci.* **195**, 1–14 (1988).
20. H. Chew, "Transitions rates of atoms near spherical surfaces," *J. Chem. Phys.* **87**, 1355–1360 (1987).
21. M. Abramowitz and I. Stegun, *Handbook of mathematical functions* (Dover Publications, 1972).
22. G. Colas des Francs, C. Girard, M. Juan, and A. Dereux, "Energy transfer in near-field optics," *J. Chem. Phys.* **123**, 174709 (2005).
23. R. Carminati, J. Greffet, C. Henkel, and J. Vigoureux, "Radiative and non-radiative decay of a single molecule close to a metallic nanoparticle," *Opt. Commun.* **261**, 368–375 (2006).
24. R. R. Chance, A. Prock, and R. Silbey, "Molecular fluorescence and energy transfer near interfaces," *Adv. Chem. Phys.* **37**, 1–65 (1978).
25. M. Meier and A. Wokaun, "Enhanced fields on large metal particles: dynamic depolarization," *Opt. Lett.* **8**, 581 (1983).
26. G. Colas des Francs, C. Girard, A. Bruyant, and A. Dereux, "SNOM signal near plasmonic nanostructures: an analogy with fluorescence decay channels," *J. Microsc. (NFO9)* **229**, 302–306 (2008).
27. A. Trügler and U. Hohenester, "Strong coupling between a metallic nanoparticle and a single molecule," *Phys. Rev. B* **77**, 115403 (2008).
28. W. Barnes, "Fluorescence near interfaces: the role of photonic mode density," *J. Mod. Opt.* **45**, 661–699 (1998).
29. C. S. Yun, A. Javier, T. Jennings, M. Fisher, S. Hira, S. Peterson, B. Hopkins, N. O. Reich, G. F. Strouse Nanometal Surface Energy Transfer in Optical Rulers, Breaking the FRET Barrier, *J. Am. Chem. Soc.* **127** (2005) 3115–3119.

1. Introduction

The precise control of the coupling efficiency between a quantum emitter (fluorescent molecule, quantum dot...) and a metallic nanoparticle is at the origin of the new field of *molecular plasmonics* [1]. In these composite systems, coupling with the molecule is mainly of electromagnetic origin, principally mediated by plasmon resonances. The optical properties of metallic nanoparticles are strongly relying on different plasmon–polaritons modes with specific properties. For instance, an elongated metallic particle can support both a dipolar (localised) plasmon mode characterized by high electromagnetic field confinement and an interface (propagating) plasmon mode able to guide electromagnetic energy along the particle surface. The strong confinement of the localised plasmon mode leads to a very efficient coupling with a nearby emitter. This coupling strength is at the origin of surface–enhanced spectroscopy. In addition, the excitation of the interface mode of the particle is responsible for transferring luminous energy away from the source of emission. By controlling the electromagnetic confinement at a nanorod extremity and understanding the propagation of the optical mode along its surface, it was recently proposed to realize an antenna in the optical domain [2, 3, 4]. Optical antennas are fundamental devices for interfacing light with nano-objects and could be used for instance to efficiently couple a single photon source to an optical fiber [4, 5]. Optimization of an optical antenna is a difficult problem since its spectroscopic response strongly depends on the shape, the chemical nature of the materials, and the surrounding environment. Among several methods available to describe the electromagnetic response of metallic particle of arbitrary shape, boundary element

method [6], multiple multipole technique [7, 8], finite-difference time-domain simulations [9], and Green dyadic formalism [10] have been used to analyze the coupling between a fluorescent molecule and an optical antenna.

All these purely numerical studies however, can be supplemented by analytical approaches for which mathematical solutions exist. Indeed, an analytical study of simplified geometries can facilitate the description of the elementary processes involved in these coupled systems. Despite restricted shapes, *e.g.* spheres or ellipsoids, some important behaviors and trends can be identified [7, 8, 11, 12, 13, 14]. In a recent work, using a quasi-static model, Bharadwaj and Novotny discussed the optimal fluorescence wavelength and found that it should be red-shifted from the interface plasmon resonance of the particle [13]. In the same time, Mertens *et al* compared full electrodynamical theory to a corrected quasi-static model and demonstrated a trade-off between emitter-particle coupling, efficient for small spheres, and signal scattering, efficient for large particles [14]. They obtained an optimal sphere diameter around 50–100 nm, in the optical domain.

In this article, we address, from analytical arguments, the problem of optical near-field coupling processes governing the fluorescence of a molecule placed in the vicinity of a mesoscopic spherical metallic particle, *i.e.* a nanoparticle with characteristic dimensions that are not very small compared to the emission wavelength. In particular, we precisely distinguish the radiative and non-radiative channels and clearly identify different coupling mechanisms. In section 2, we describe the asymptotic behavior of the decay rates in the very near-field of a metallic particle. The coupling of the emitter to the different plasmon modes is demonstrated from detailed analysis of the analytical expressions. The distance dependence of the decay rates is then investigated in section 3. Finally, we discuss in section 4 the fluorescence enhancement optimization.

2. Near-field behavior

Figure 1 describes the model we consider. A single emitter is placed at a distance z_0 from a spherical particle of radius a . The surrounding medium optical index is n_B . In the following, we adopt the classical point of view for the description of the decay rate. This model assumes that the fluorescent emission can be identified to the power emitted by a dipole \mathbf{p}_0 oscillating at the fluorescent frequency $\omega_0 = 2\pi c/\lambda_0$ in vacuum. Here the classical dipole represents twice the quantum transition dipole moment of the emitter. As demonstrated in [15], this model is appropriate for describing weak coupling regime. In this article, we also assume that the electromagnetic properties of the metallic particle are described by a bulk optical index n_S . For molecule–particle distance below one nanometer, non-local description of the optical index should be taken into account [16, 17].

2.1. Analytical formulation based on Mie's expansion

The decay rates of a molecule in presence of a spherical particle can be solved by using well-known Mie formalism [18, 19]. When they are normalized with respect to the decay rate γ_0 of the free molecule, total decay rates write [19]:

$$\frac{\gamma_{\perp}}{\gamma_0} = n_B \left\{ 1 + \frac{3}{2} Re \sum_{n=1}^{\infty} n(n+1)(2n+1) B_n \left[\frac{h_n^{(1)}(u)}{u} \right]^2 \right\}, \quad (1)$$

$$\frac{\gamma_{\parallel}}{\gamma_0} = n_B \left\{ 1 + \frac{3}{2} Re \sum_{n=1}^{\infty} (n+\frac{1}{2}) \left[B_n \left[\frac{\zeta'_n(u)}{u} \right]^2 + A_n [h_n^{(1)}(u)]^2 \right] \right\}, \quad (2)$$

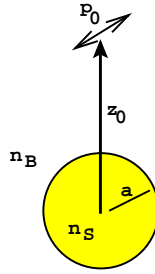


Fig. 1. Model used to study the molecule-particle coupling.

where the subscript \perp (\parallel) indicates a dipole perpendicular (parallel) to the particle surface and $u = k_B z_0 = 2\pi n_B z_0 / \lambda_0$. For the sake of clarity, the analytical expressions of the Mie coefficients A_n and B_n will be detailed in the appendix. The two special functions $h_n^{(1)}$ and ζ_n that enter Eq. (1) and (2) represent the spherical Hankel and Riccati–Bessel functions, respectively. Prime stands for differentiation with respect to u .

The radiative decay rates can be written as follows [19]:

$$\frac{\gamma_{\perp}^{\text{rad}}}{\gamma_0} = \frac{3n_B}{2} \sum_{n=1}^{\infty} n(n+1)(2n+1) \left| \frac{j_n(u) + B_n h_n^{(1)}(u)}{u} \right|^2, \quad (3)$$

$$\frac{\gamma_{\parallel}^{\text{rad}}}{\gamma_0} = \frac{3n_B}{4} \sum_{n=1}^{\infty} (2n+1) \left[|j_n(u) + A_n h_n^{(1)}(u)|^2 + \left| \frac{\psi'_n(u) + B_n \zeta'_n(u)}{u} \right|^2 \right], \quad (4)$$

where j_n is the spherical Bessel function and $\psi_n(u) = u j_n(u)$. From these four relations, the non–radiative decay rate can be obtained by computing the difference between total and radiative decay rates. Since we are interested in describing analytically the coupling process, we had to express this difference. Applying the procedure described in [20] in the presence of dielectric sphere to the present case of a metallic particle, we first develop the expressions (3) and (4) of radiative contributions to the relaxation rate. After some algebra, this leads to

$$\frac{\gamma_{\perp}^{\text{rad}}}{\gamma_0} = n_B + \frac{3n_B}{2} \sum_{n=1}^{\infty} n(n+1)(2n+1) \frac{|B_n h_n^{(1)}(u)|^2 + 2j_n(u) \text{Re}[B_n h_n^{(1)}(u)]}{u^2}, \quad (5)$$

$$\begin{aligned} \frac{\gamma_{\parallel}^{\text{rad}}}{\gamma_0} &= n_B + \frac{3n_B}{4} \sum_{n=1}^{\infty} (2n+1) \\ &\quad \left[|A_n h_n^{(1)}(u)|^2 + 2j_n(u) \text{Re}[A_n h_n^{(1)}(u)] + \frac{|B_n \zeta_n^{(1)}(u)|^2 + 2\psi'_n(u) \text{Re}[B_n \zeta_n^{(1)}(u)]}{u^2} \right]. \end{aligned} \quad (6)$$

The non-radiative decay rates are now easily expressed as the difference between the total and

radiative rates. After a few manipulations, we obtain

$$\begin{aligned}\frac{\gamma_{\perp}^{NR}}{\gamma_0} &= \frac{\gamma_{\perp}}{\gamma_0} - \frac{\gamma_{\perp}^{rad}}{\gamma_0} = \frac{3n_B}{2} \sum_{n=1}^{\infty} n(n+1)(2n+1) \left| \frac{h_n^{(1)}(u)}{u} \right|^2 [-Re(B_n) - |B_n|^2], \quad (7) \\ \frac{\gamma_{\parallel}^{NR}}{\gamma_0} &= \frac{\gamma_{\parallel}}{\gamma_0} - \frac{\gamma_{\parallel}^{rad}}{\gamma_0} \\ &= \frac{3n_B}{2} \sum_{n=1}^{\infty} \left(n + \frac{1}{2} \right) \left[\left| \frac{\zeta_n^{(1)}(u)}{u} \right|^2 [-Re(B_n) - |B_n|^2] + |h_n^{(1)}(u)|^2 [-Re(A_n) - |A_n|^2] \right]. \quad (8)\end{aligned}$$

Let us note that the difference between the two terms proportional to $[-Re(B_n)]$ or $[-Re(A_n)]$ (extinction) and to $|B_n|^2$ or $|A_n|^2$ (scattering) directly relates to the energy conservation as discussed in section 2.2.1 [18]. Up to now, no assumption has been made on either the emitter-particle distance or the particle size. In the following section, we show how the expressions (1-8) simplify for short coupling distance regime.

2.2. Relaxation channels at very short distances

As recently discussed by Bharadwaj and Novotny [13], the non-radiative decay rate of a molecule is mainly dictated by an efficient coupling to the interface plasmon mode of the antenna whereas the radiative decay rate is associated to the excitation of a dipolar mode of the metallic particle. Indeed, in the very near-field, fluorescence relaxation processes are dominated by non-radiative transfer to the metal. It should be noted that for an emitter located at very short distance from the particle, the otherwise curved surface can be approximated by a flat interface. We therefore define the very near-field as the distance range such that $(z_0 - a) \ll a$. This criterion will be refined in section 3 devoted to the study of distance dependence of the decay rates.

The radiative channel, however, has other characteristics because it describes the power radiated in far-field zone by the whole *molecule plus particle* system. Since the particle dipolar mode presents the highest scattering cross-section, the radiative emission rate of the system may be similar to that of a molecule placed in the presence of a simple dipolar particle.

In the following, we will focus on the study of radiative and non-radiative contributions in the domain of the very short emitter-particle distances.

2.2.1. Nonradiative channel

At very short distances, the emitter-particle coupling relies mainly on the non-radiative channel. Using the asymptotic behavior of the spherical Bessel functions near zero [21], we can write from Eq. (7) and (8) respectively

$$\begin{aligned}\frac{\gamma_{\perp}^{NR}}{\gamma_0} \underset{u \rightarrow 0}{\sim} & \frac{3n_B}{2u^3} \sum_{n=1}^{\infty} \frac{(n+1)^2}{u^{(2n+1)}} k_B^{2n+1} \\ & \left[Im(\alpha_n) - \frac{n+1}{n(2n-1)!!(2n+1)!!} k_B^{2n+1} |\alpha_n|^2 \right], \text{ and} \quad (9)\end{aligned}$$

$$\begin{aligned}\frac{\gamma_{\parallel}^{NR}}{\gamma_0} \underset{u \rightarrow 0}{\sim} & \frac{3n_B}{2u^3} \sum_{n=1}^{\infty} \frac{n(n+1)(n+1/2)}{(2n+1)u^{(2n+1)}} k_B^{2n+1} \\ & \left[Im(\alpha_n) - \frac{n+1}{n(2n-1)!!(2n+1)!!} k_B^{2n+1} |\alpha_n|^2 \right], \quad (10)\end{aligned}$$

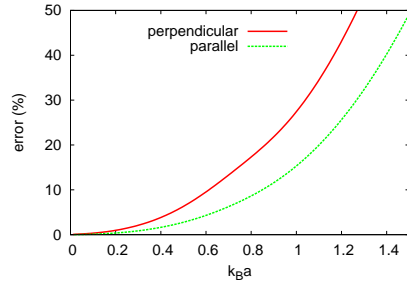


Fig. 2. Error done on the non radiative decay rate when approximated by Eq. (9) or (10) for a perpendicular or parallel orientation, respectively. The molecule is located 1 nm from a gold particle in air. The emission wavelength is $\lambda_0 = 580$ nm.

where $(2n+1)!! = 1 \times 3 \times 5 \dots \times (2n+1)$ and we introduce the n^{th} order polarizability of the sphere

$$\alpha_n = \frac{n(\epsilon_S - \epsilon_B)}{(n+1)\epsilon_B + n\epsilon_S} a^{(2n+1)}. \quad (11)$$

Figure 2 represents the error done using the approximated expressions (9) or (10). The error is less than 10 % for $k_Ba < 0.5$ and is around 20 % for mesoscopic particles ($k_Ba \sim 1$).

Eq. (9) and (10) are an important result of this paper, since the non-radiative rate appears in a form that generalizes the expressions obtained previously with a purely dipolar sphere [22, 23], by including in a similar way all the particle modes. Moreover, within this formulation, the non radiative decay rate respects the optical theorem for each mode. More precisely, the first term in Eq. (9) or (10), proportional to $\text{Im}(\alpha_n)$, encodes the whole emission extinction, due to both absorption into the metallic particle and scattering in the far-field. The second term, proportional to $|\alpha_n|^2$ gives the fraction of power scattered by the particle itself. Hence, the non-radiated decay contribution is given by the difference between this two terms, as a direct consequence of the optical theorem [18, 22]. Finally, considering Eq. (9) and (10), it clearly appears that when the molecule approaches the metallic particle, it couples first to the dipole mode, then to multipole modes and finally to the interface plasmon mode for very short distances. This directly originates from the highest confinement of high order modes.

Terms $k_B^{2n+1} \alpha_n / u^{(2n+1)}$ are proportional to $(a/z_0)^{2n+1}$, therefore, when the emitter is placed in close vicinity to the particle ($z_0 \rightarrow a$), the high order terms [$\propto n^2(a/z_0)^{2n+1}$] dominate the expressions of the non-radiative decay rates. Under these conditions, Eq. (9) and Eq. (10) can be approximated by

$$\frac{\gamma_{\perp}^{NR}}{\gamma_0} \underset{z_0 \rightarrow a}{\sim} \frac{3n_B}{2u^3} \frac{a}{z_0} \text{Im} \left(\frac{\epsilon_S - \epsilon_B}{\epsilon_S + \epsilon_B} \right) \sum_{n>>1} n^2 \left(\frac{a}{z_0} \right)^{2n}, \quad (12)$$

$$\underset{z_0 \rightarrow a}{\sim} \frac{3n_B}{8k_B^3} \text{Im} \left(\frac{\epsilon_S - \epsilon_B}{\epsilon_S + \epsilon_B} \right) \frac{1}{(z_0 - a)^3} \quad (13)$$

$$\frac{\gamma_{\parallel}^{NR}}{\gamma_0} \underset{z_0 \rightarrow a}{\sim} \frac{3n_B}{4u^3} \frac{a}{z_0} \text{Im} \left(\frac{\epsilon_S - \epsilon_B}{\epsilon_S + \epsilon_B} \right) \sum_{n>>1} n^2 \left(\frac{a}{z_0} \right)^{2n}, \quad (14)$$

$$\underset{z_0 \rightarrow a}{\sim} \frac{3n_B}{16k_B^3} \text{Im} \left(\frac{\epsilon_S - \epsilon_B}{\epsilon_S + \epsilon_B} \right) \frac{1}{(z_0 - a)^3}. \quad (15)$$

Note that we used the fact that the serie diverges for $z_0 \simeq a$, so that the infinite serie sum reduces to its highest order term and can be compared to the serie expansion of $(1 - a/z_0)^{-3}$ (see also

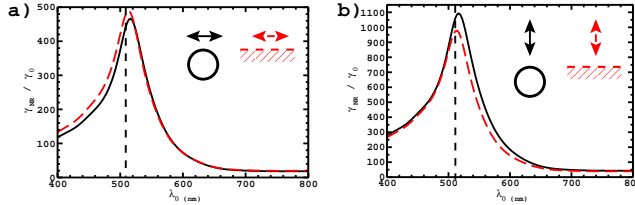


Fig. 3. Non radiative decay rate dependence for an emitter placed 5 nm above a gold nanoparticle (80 nm diameter) embedded in a PMMA matrix (solid line) or above a flat gold/PMMA interface film (dashed line, quasi-static approximation). (a) Dipole parallel to the surface. (b) Dipole perpendicular to the surface. Vertical lines indicate the Au/PMMA interface plasmon mode resonance.

[15]). Expressions (13) and (15) exactly reproduce the short range (quasi-static) behavior of non-radiative decay rate near a flat metal surface [24].

As a concrete example, we now consider a fluorescent molecule in presence of a 80 nm diameter gold nanoparticle ($a = 40$ nm) since similar systems were the topic of recent experimental [7, 11, 12] and theoretical works [8, 14]. The surrounding medium index is $n_B = 1.5$ corresponding to both PMMA (polymethylmethacrylate) and glass indices since molecule are generally dispersed into a PMMA matrix deposited on a glass substrate. Note that in this case, $k_B a \approx 0.3$ for emission wavelength in the visible range, corresponding to a particle of mesoscopic size. Figure 3 represents the wavelength dependence of the non radiative decay rate in the very near-field of a gold particle or a flat film. As expected, the non-radiative coupling to a spherical metallic particle is very well reproduced by assuming the quasi-static approximations (13) or (15). In both cases, a resonance occurs at $\lambda \simeq 515$ nm indicating a coupling to the interface plasmon mode.

2.2.2. Radiative channel

We apply a similar procedure to the radiative contribution. Taking the limit $u \rightarrow 0$ in expression (5), the radiative decay rate for a dipole perpendicular to the particle surface is given by

$$\begin{aligned} \frac{\gamma_{\perp}^{rad}}{\gamma_0} \underset{u \rightarrow 0}{\sim} n_B + \frac{3}{2u^2} \sum_{n=1}^{\infty} n(n+1)^2(2n+1) & \left\{ \frac{n+1}{[(2n+1)!!]^2 u^{2n+2}} k_B^{4n+2} |\alpha_n|^2 \right. \\ & + \frac{2}{[(2n+1)!!]^2 u} k_B^{2n+1} \operatorname{Re}(\alpha_n) \\ & \left. - \frac{2}{(2n-1)!! [(2n+1)!!]^3} u^{2n} k_B^{2n+1} \operatorname{Im}(\alpha_n) \right\}. \quad (16) \end{aligned}$$

Numerical simulations (not shown) reveal an error up to 50 % for mesoscopic particles. The behavior of the radiative decay rate is drastically different from the non-radiative contributions in the very near-field of the particle. Having in mind that the polarizability depends on the sphere radius as a^{2n+1} , we note that the series converges to zero in the near-field range for small particle sizes. Therefore, the radiative decay rate can be reduced to the first terms only. Neglecting the last term in Eq. (16) compared to the two others, the radiative decay rate for a vertical dipole simplifies to

$$\frac{\gamma_{\perp}^{rad}}{\gamma_0} \underset{z_0 \rightarrow a}{\sim} n_B \left\{ 1 + \frac{4}{z_0^3} \operatorname{Re}(\alpha_1) + \frac{4}{z_0^6} |\alpha_1|^2 \right\} \quad (17)$$

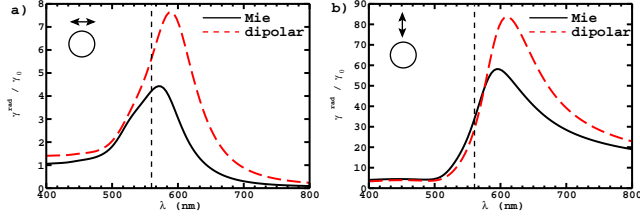


Fig. 4. Radiative decay rate for an emitter placed 5 nm above a gold nanoparticle (80 nm in diameter). (a) Dipole parallel to the surface. (b) Dipole perpendicular to the surface. The solid curves are calculated from Mie formalism (Eq. 3,4). The dashed curves assume a dipolar response of the particle, including finite size effects [Eq. 28] and (29) in appendix (6.2)]. Vertical lines indicate the sphere dipolar resonance.

which exactly reproduces the radiative contribution at small distance assuming a dipolar response of the metallic sphere (see *e.g* [23]). In case of a dipole parallel to the sphere surface, we obtain the following relation:

$$\frac{\gamma_{\parallel}^{rad}}{\gamma_0} \underset{z_0 \rightarrow a}{\sim} n_B \left\{ 1 - \frac{2}{z_0^3} \text{Re}(\alpha_1) + \frac{1}{z_0^6} |\alpha_1|^2 \right\}, \quad (18)$$

that is once again in agreement with a dipolar response of the metallic sphere. Note that these expressions slightly differ from the equation given in [23] by the absence of the radiation reaction term in the polarizability α_1 . This term, which comes from the finite size of the particle, is necessary in order to satisfy the optical theorem. In a more critical way, a correct description of scattering resonances requires to include simultaneously both the radiation reaction term *and* a dynamic polarization term [25]. This can be easily achieved within the volume integral methods and leads to the following polarizability [26]

$$\alpha_{eff} = [1 - M_B \frac{\alpha_1}{a^3}]^{-1} \alpha_1 \quad (19)$$

$$M_B = 2[(1 - ik_B a)e^{ik_B a} - 1] \quad (20)$$

where α_1 is the static polarizability as defined in Eq. (11) and the dipolar response \mathbf{p} of the particle to an external electric field \mathbf{E}_0 obeys $\mathbf{p} = 4\pi\epsilon_0\epsilon_B\alpha_{eff}\mathbf{E}_0$.

As shown on Fig. 4, the dipolar model qualitatively reproduces the wavelength dependence of the radiative decay rates. Clearly, the resonances are red-shifted compared to the dipolar mode frequency ω_1 ($\lambda_1 = 2\pi c/\omega_1 = 560$ nm). More precisely, the resonance is only slightly red-shifted in case of a dipole parallel to the particle surface ($\lambda = 570$ nm instead of $\lambda_1 = 560$ nm), whereas a stronger deviation is observed for a dipole perpendicular to the surface of the metallic particle ($\lambda = 595$ nm). This red-shift is due to a more important dipole-dipole coupling between the molecule and the gold particle for this dipole orientation. The efficiency of dipole-dipole coupling also explains the higher decay rate obtained when considering dipolar response of the particle compared to Mie description in which the energy is dispersed on all modes. Let us also note that the distance dependence of the radiative decay rate should strongly depends on the emission wavelength. Far from any resonance, the amplitude of the particle dipole is proportional to the field emitted by the emitter. Consequently, a z_0^{-3} dependence is expected for a particle in the near-field of the quantum emitter. As already discussed in [23], an additional Förster-type dependence contribution (z_0^{-6}) is expected close to the particle resonance because a strong dipole-dipole coupling dominates between the particle and the emitter. Note that in this case, a corrective term should be added to properly describe the whole decay rate [15, 27].

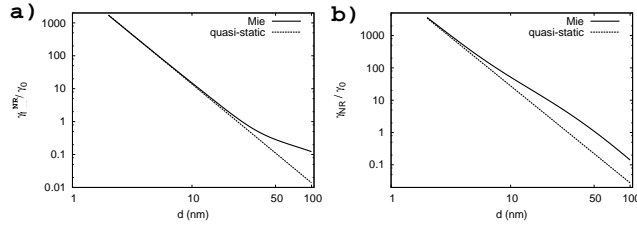


Fig. 5. Non radiative decay rates as a function of the distance $d = (z_0 - a)$ to the particle surface (solid lines) or gold flat film (dashed lines, quasi-static approximation) for a parallel (a) and perpendicular (b) dipole. The emission wavelength is $\lambda_0 = 580$ nm.

3. Distance dependence

In this section, we have chosen the emission wavelength $\lambda_0 = 580$ nm of the terrylene molecule. This molecule is widely used in single molecule spectroscopy experiments and the position of emission wavelength ensures that both the parallel and perpendicular radiative channels should be strongly enhanced. The embedding medium is again PMMA. We compare the distance dependence to the two limiting cases (quasi-static flat surface and dipolar particle) introduced in the previous section. Exact expressions of the different decay rates are given in the appendix.

Figure 5 represents the non radiative decay rate variation when increasing the particle-molecule distance. The quasi-static approximation remains satisfying only below 10 nm, corresponding to $d/a < 0.2$ as the range where the spherical surface can be approximated by a flat interface. As expected, a d^{-3} law is observed for these very short distance corresponding to the creation of an exciton in the bulk of the metal [28]. Note that a d^{-4} law can be expected for even shorter distances, due to the creation of an exciton at the metal surface [29]. Such a description needs to properly describe the metal/dielectric interface and to take into account the nonlocals effect into the metal dielectric constant [28].

We now consider the radiative contribution to the decay rate, and compare it to a dipolar response of the particle (Fig. 6). In order to improve the comparison accuracy, we include finite size effects into the polarizability. The dipolar model only qualitatively reproduces the radiative decay rate behavior, indicating that higher plasmonic modes are involved in the radiative process [14]. At large distances, however, the dipolar mode is sufficient to describe the radiative emission evolution, as far as finite size effects are properly included. Finally, we do not observe simple distance dependence law for small separation distance since the two z_0^{-3} and z_0^{-6} processes compete [23].

4. Fluorescence enhancement and particle size effect

In this last section, we discuss the influence of the particle size on the fluorescent enhancement for a molecule coupled to a gold particle. The fluorescence intensity enhancement is given by

$$\eta_{\text{fluo}}(\mathbf{r}_0) = |\mathbf{u} \cdot \mathbf{E}(\lambda_{\text{exc}}, \mathbf{r}_0)|^2 \frac{\gamma^{\text{rad}}(\mathbf{r}_0)}{\gamma(\mathbf{r}_0)}, \quad (21)$$

where \mathbf{E} is the normalized electric field computed at the molecule location \mathbf{r}_0 from Mie theory [18] at the excitation wavelength λ_{exc} and $\gamma^{\text{rad}}/\gamma$ represents the quantum efficiency. \mathbf{u} indicates the orientation of the molecule transition dipole moment.

A critical parameter for fluorescence enhancement is position of both the excitation and emission wavelengths compared to the plasmon modes resonances [8, 13]. Indeed, the excited field mainly couples to the dipolar mode and therefore strongly depends on the particle size, as

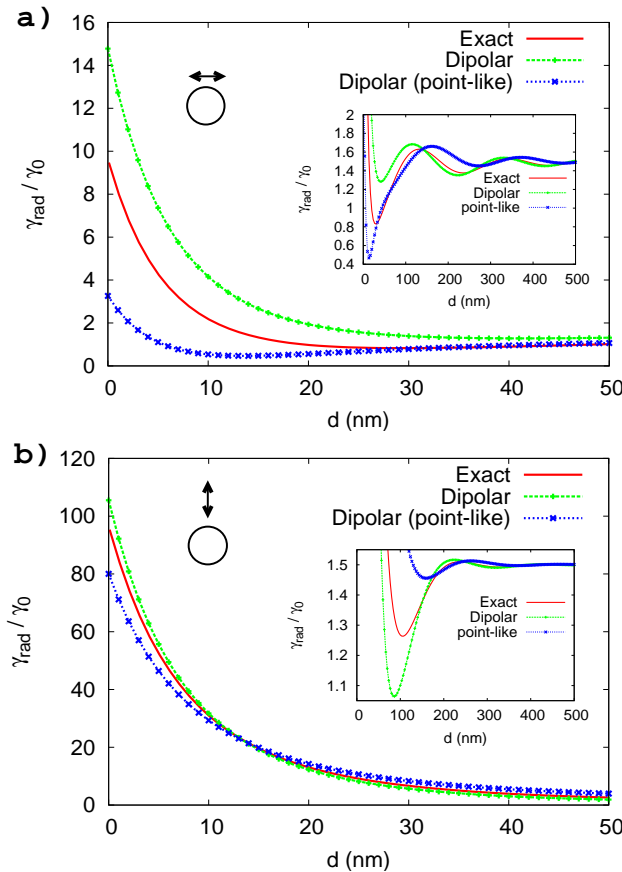


Fig. 6. Radiative decay rate dependence with respect to the distance d between the particle and the molecule: for a dipole (a) parallel or (b) perpendicular to the particle surface. ‘Exact’ curves refers to Mie formalism (Eq. 3,4), ‘dipolar’ corresponds to a dipolar model, including finite size effects [Eq. 28] and (29) in appendix (6.2)] and ‘dipolar (point-like)’ assumes a point-like dipolar response of the particle to an external field [(Eq. 28) and (29) where α_{eff} is approximated by α_1]. The insets show far-field behaviours. The emission wavelength is $\lambda_0 = 580$ nm.

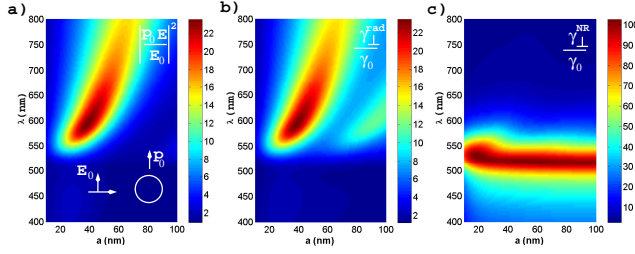


Fig. 7. Normalized electric-field intensity (a), decay rate (b) and non-radiative rate (c) calculated 10 nm away the particle surface as a function of both wavelength and particle radius. The system is shown in the inset of Fig. 7(a). The molecule is oriented perpendicularly to the sphere surface.

shown by Eq. (19). Moreover, as discussed above, the radiative decay rate also mainly originates from coupling to the dipolar mode. However, due to dipole-dipole coupling, an additional redshift occurs, particularly for dipole perpendicular to the particle surface (see Fig. 4). On the contrary, the non-radiative rate is governed by interface mode so that it does almost not depend on the particle size for small emitter-particle coupling distances.

We consider again a gold nanoparticle embedded in PMMA coupled to a fluorescent molecule. The molecule is perpendicular to the particle surface since strongest effects are expected in this case. Figure 7(a) represents the excitation field intensity near the particle in function of both the particle size and the excitation wavelength. Figures 7(b) and 7(c) show respectively the radiative (Eq. 5) and non-radiative (Eq. 7) decay rates when varying emission wavelength and also the particle radius. Independent of the particle size, the non radiative channel is resonantly opened for emission wavelengths around $\lambda_0 = 515$ nm (see Fig. 7(c)) due to coupling to the interface mode. As expected, the excitation intensity (Fig. 7(a)) and the radiative decay rate (Fig. 7(b)) present very similar behaviors, closely related to the dipolar mode of the metallic particle. Let us note, however, that for particle radius above $a \approx 80$ nm, the radiative channel also couples to quadrupolar mode as can be seen on Fig. 7(b) [14].

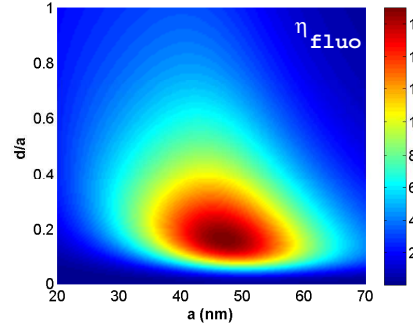


Fig. 8. Fluorescent enhancement for 'DiD-gold particle' coupled system embedded in PMMA.

Therefore, strong fluorescent enhancement can be expected for a molecule–particle coupled system such that: i) the absorption wavelength is close to the particle dipolar resonance to enhance the excitation field, ii) the emission wavelength is far from the interface mode resonance to reduce ohmic losses and iii) the particle is small enough to avoid molecule coupling to the quadrupolar mode resonance and strongly enhance the radiative channel. Finally, we consider

a specific dye molecule, namely DiD which presents absorption and emission peaks around $\lambda_{exc} = 635$ nm and $\lambda = 665$ nm respectively. Figure 8 presents the fluorescent enhancement for several particle radius, in function of the emitter-particle distance. A strong 17 fold enhancement is observed for radius $40nm < a < 50nm$ at separation distance around $d \approx 8$ nm ($d/a \approx 0.2$). It is worthwhile to note here that matching the excitation and detection wavelengths to the molecule absorption and emission peaks respectively, we profit from both the molecule absorption and fluorescence cross-sections and also fluorescence enhancement due to coupling to the metallic particle.

5. Conclusion

In summary, we have theoretically and numerically investigated the decay rate of an emitter coupled to a mesoscopic metallic particle. By starting from an asymptotic expansion of the different decay rate contributions in the very near-field of a spherical metallic particle, we demonstrated that the non-radiative channel process is associated with a coupling to the interface plasmon mode of the particle whereas the radiative decay rate process involves a transfer to dipolar plasmon mode. We have examined the extent of these couplings and compared it with two asymptotic models: a flat metal surface and a dipolar response of the particle. We found a red-shift of the radiative decay rate due to dipole-dipole coupling between the molecule and the particle. We also demonstrated that near-field coupling can be expressed in a simple form that obeys optical theorem for each particle mode. These results show that a deep understanding of the complex fluorescence decay mechanisms can be obtained from a simple and analytical model. Finally, it provides some guidelines for optimizing the particle size to enhance the molecular fluorescence.

Acknowledgements

This work is partially supported by the Agence Nationale de la Recherche (ANR) (project ANTARES, PNANO07-51) and the European Network of Excellence PlasmoNanoDevices (contract No 507879).

6. Appendix

To facilitate the reading of this article, we reproduce in this appendix the various expressions of the decay rates assuming a dipolar response of the spherical particle. These expressions can be easily deduced from the classical description of the spontaneous emission rates and can be found in the literature.

6.1. Mie coefficients

An exact description of the particle electromagnetic response to an external field needs to properly describe all the particle modes. The n^{th} mode contribution depends on the two Mie scattering coefficients A_n and B_n [18, 19] ($k_B = 2\pi n_B/\lambda_0$ and $k_S = 2\pi n_S/\lambda_0$ are the wavenumbers into the embedding medium and the sphere, respectively)

$$A_n = \frac{j_n(k_B a)\psi'_n(k_S a) - j_n(k_S a)\psi'_n(k_B a)}{j_n(k_S a)\zeta'_n(k_B a) - h_n^{(1)}(k_B a)\psi'_n(k_S a)}, \quad (22)$$

$$B_n = \frac{\epsilon_B j_n(k_B a)\psi'_n(k_S a) - \epsilon_S j_n(k_S a)\psi'_n(k_B a)}{\epsilon_S j_n(k_S a)\zeta'_n(k_B a) - \epsilon_B h_n^{(1)}(k_B a)\psi'_n(k_S a)}. \quad (23)$$

where j_n and $h_n^{(1)}$ are the usual spherical Bessel and Hankel functions, and $\psi_n(z) = z j_n(z)$ and $\zeta_n(z) = z h_n^{(1)}(z)$ the Riccati-Bessel functions [18, 21].

6.2. Dipolar spherical particle

The total decay rates write [22, 23, 26]

$$\frac{\gamma_{\parallel}}{\gamma_0} = n_B \left\{ 1 + \frac{3k_B^3}{2} \text{Im} \left[\alpha_{eff} e^{2iu} \left(\frac{1}{u} + \frac{i}{u^2} - \frac{1}{u^3} \right)^2 \right] \right\}, \quad (24)$$

$$\frac{\gamma_{\perp}}{\gamma_0} = n_B \left\{ 1 + 6k_B^3 \text{Im} \left[\alpha_{eff} e^{2iu} \left(\frac{1}{u^3} - \frac{i}{u^3} \right)^2 \right] \right\}, \quad (25)$$

where α_{eff} is the particle effective polarizability associated to the dipolar mode, including finite size effects as expressed by Eq. (19). The non radiative decay rates write

$$\frac{\gamma_{\parallel}^{NR}}{\gamma_0} = \frac{3n_B}{2} k_B^3 \left[\text{Im}(\alpha_{eff}) - \frac{2k_B^3}{3} |\alpha_{eff}|^2 \right] \left[\frac{1}{u^2} - \frac{1}{u^4} + \frac{1}{u^6} \right], \quad (26)$$

$$\frac{\gamma_{\perp}^{NR}}{\gamma_0} = 6k_B^3 n_B \left[\text{Im}(\alpha_{eff}) - \frac{2k_B^3}{3} |\alpha_{eff}|^2 \right] \left[\frac{1}{u^4} + \frac{1}{u^6} \right]. \quad (27)$$

Then the radiative decay rates are calculated as the difference between the total and the non radiative decay rates:

$$\frac{\gamma_{\perp}^{rad}}{\gamma_0} = \frac{\gamma_{\perp}}{\gamma_0} - \frac{\gamma_{\perp}^{NR}}{\gamma_0} \quad (28)$$

$$\frac{\gamma_{\parallel}^{rad}}{\gamma_0} = \frac{\gamma_{\parallel}}{\gamma_0} - \frac{\gamma_{\parallel}^{NR}}{\gamma_0}. \quad (29)$$

3.4 Conclusion

En analysant finement les processus de couplage de molécules avec des structures plasmoniques, nous avons pu établir quelques propriétés simples. En particulier, une meilleure compréhension de ces phénomènes de couplage est une étape cruciale pour déterminer grossièrement les géométries et matériaux les plus aptes à la réalisation, par exemple, d'antennes optiques. Bien entendu, les paramètres peuvent ensuite être précisés en s'appuyant sur des méthodes de simulations numériques dédiées [70].

D'autre part, je souhaite attirer l'attention sur le pont que la règle d'or de Fermi fait avec la quantification du plasmon. En effet, l'émission spontanée résulte du couplage de l'état excité de la molécule avec les modes électromagnétiques de son environnement [71]. La généralisation de la règle d'or de Fermi en présence de structures métalliques pose la difficulté de la quantification du champ en présence de dissipation [72, 73]. Par contre, elle peut être facilement obtenue à partir de la description dipolaire classique de l'émission de fluorescence, démarche adoptée dans ce chapitre. Toutefois, de récents travaux proposent de réaliser des expériences d'optique quantique à partir de structures plasmoniques [45]. Une description rigoureuse de ces expériences impose de traiter correctement la seconde quantification du champ.

Enfin, puisque le couplage d'un émetteur quantique avec des particules métalliques conduit à l'émission spontanée de plasmon-polaritons de surface, il est naturel de s'intéresser à l'émission stimulée de plasmons, phénomène purement quantique. Cela a conduit Bergman et Stockman à proposer en 2003 l'analogue plasmonique du laser : le SPASER (Surface Plasmon Amplification by Stimulated Emission of Radiation) [74]. Dans la configuration proposée, un milieu à gain est couplé à une particule plasmonique supportant des modes plasmons *localisés*, qui remplace la cavité laser. Le fort confinement des modes plasmons permet de réaliser des sources cohérentes de plasmons de très petites dimensions [75]. Dans le chapitre suivant, nous discuterons de l'émission stimulée de plasmons par couplage à des modes *délocalisés*, en analogie avec les amplificateurs optiques.

Finalement, l'étude de la relaxation moléculaire par couplage aux plasmons, ou plus généralement la notion d'antenne optique, ouvre de nouveaux champs de recherche. Je reviendrai sur ce point lors de ma conclusion générale.

Chapitre 4

Composants plasmoniques pour la photonique intégrée

Dès 1965, Gordon Moore, cofondateur d'INTEL, constata que la complexité des circuits électroniques intégrés doublait chaque année, à coût constant. Cette observation, d'autant plus spectaculaire que les circuits électroniques venaient d'être inventés, le conduira à énoncer peu après la fameuse loi de Moore : «le nombre de transistors intégrés sur une puce de silicium double tous les 2 ans». Cette prédiction s'est avérée étonnamment juste jusqu'à aujourd'hui. Toutefois, cette progression ne pourra se poursuivre qu'au prix de nouvelles technologies. En effet, la miniaturisation des transistors ne pourra sans doute pas aller en-deçà d'environ 20 nm, taille à laquelle apparaissent des courants de fuites, et qui devrait être atteinte vers 2015. Une alternative est donc d'augmenter la bande passante des composants intégrés pour faire transiter une grande quantité d'informations par le même canal. L'optique guidée est une technologie parfaitement adaptée à ce besoin comme l'atteste le fort débit permis par les fibres optiques. Malheureusement, cette technologie est peu compatible avec la miniaturisation car celle-ci s'accompagne d'une forte dégradation du signal par diffraction.

C'est dans ce contexte que nous nous intéressons aux guides plasmoniques. En particulier, un guide métallique peut transporter simultanément une onde électrique et une onde électromagnétique et apporte donc une solution élégante pour l'opto-électronique. Nous espérons ainsi combiner la miniaturisation de l'électronique et la large de bande passante de l'optique pour aller au-delà de l'état de l'art.

Il existe de nombreuses configurations de guides plasmoniques. Dès 1997, Takahara a proposé d'utiliser des nanocylindres métalliques pour guider un plasmon avec d'excellents confinements [76]. Cette proposition a rapidement été suivie de démonstrations expérimentales sur des fils d'argent [77, 78]. Cependant, ces structures imposent d'avoir une cristallinité du métal bien contrôlée, faute de quoi la longueur de propagation chute considérablement [79]. Seules les méthodes de synthèse et dépôt par voie chimique permettent d'obtenir des fils de bonne cristallinité, limitant les formes accessibles. La plupart des autres configurations de guides plasmoniques implique des formes réalisables par lithographie (UV, par faisceau d'électrons ou par faisceau d'ions). Dans ce cas le métal, est évaporé, donc dans une phase amorphe, ce qui implique des pertes importantes lors de la propagation du mode. La réalisation de guides métalliques de formes bien contrôlées et de haute cristallinité est sans aucun doute un défi majeur. Toutefois, de nombreuses démonstrations de guidages par modes plasmons ont été réalisées ces 10 dernières années. Les références [16, 17] donne un bon aperçu de l'état de

l'art. De nombreux composants passifs (guide, miroir semi-réfléchissant, coupleur directionnel, interféromètre, ...) ont été réalisés. Il a été récemment proposé d'établir une loi de Moore pour les circuits photoniques intégrés passifs, selon différents critères [80]. Lorsque l'on considère la densité d'intégration des filtres optiques (réseau, interféromètre Mach Zehnder, ...), la plus forte densité d'intégration est obtenue avec un composant plasmonique.

L'étape suivante consiste à réaliser des composants plasmoniques actifs (commutateur, modulateur, transistor, ...) indispensables pour envisager de véritables applications pour l'opto-électronique. Quelques réalisations de principe récentes existent, généralement impliquant des modes plasmons de films métalliques étendus [18, 20, 19]. Dans ce chapitre, nous nous étudions des guides plasmoniques confinés par un ruban diélectrique. Le ruban diélectrique assure un bon confinement du mode plasmon. De plus, l'utilisation de différents matériaux diélectriques permet de réaliser des fonctions optiques variées. Le paragraphe 4.1 présente les propriétés de guidage et de confinement de ces guides. Nous considérons ensuite la propagation du mode plasmon assistée par émission stimulée de puits quantiques dispersés dans le ruban diélectrique (§4.2). Le paragraphe 4.3 discute finalement de la forme de la résonance du mode guidé, en particulier en présence d'émission spontanée.

4.1 Guide plasmonique confiné par un ruban diélectrique

La figure 4.1a) présente un guide planaire confiné par un diélectrique (“dielectric loaded waveguide”). Cette configuration est très utilisée pour des applications de photonique intégrée. En effet, le mode est confiné latéralement sans être en contact avec le ruban diélectrique, d'où une réduction des pertes par diffusion sur les bords du guide [81]. Une autre configuration, appropriée pour l'opto-électronique, confine le mode planaire entre deux électrodes métalliques (Fig. 4.1b). Le projet PLASMOCOM (Polymer based nanoplasmatics components and de-

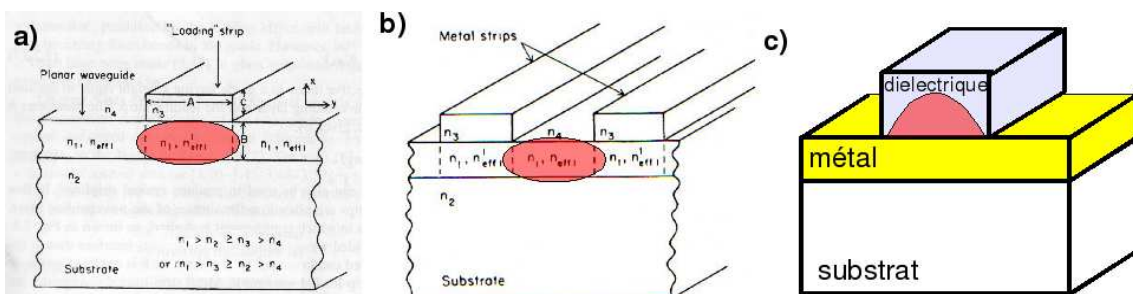


FIG. 4.1 – a) Guide planaire confiné par (a) un ruban diélectrique ou (b) des électrodes métalliques (D'après [81]). (c) Guide plasmonique confiné par un ruban diélectrique (DLSPPW). Le confinement modal est schématisé en rouge.

vices) étend ce concept au mode plasmon. La configuration obtenue (dielectric loaded surface plasmon polariton waveguide - DLSPPW) est schématisée sur la figure 4.1c. Un ruban diélectrique, par exemple un polymère, est lithographié sur un film métallique (de l'or ou de l'argent, généralement). Le système repose sur un substrat de verre. Sous certaines conditions un mode plasmon-polariton de surface se propage à l'interface métal-diélectrique. Il est utile de noter que le mode étant confiné à cette interface, l'influence du polymère est sans doute plus forte que dans un guide usuel chargé par diélectrique où le mode est confiné à l'intérieur

du guide planaire (Fig. 4.1a). La propagation du mode dans de tels guides peut ensuite être contrôlée en utilisant des matériaux non-linéaires ou des polymères dopés par exemple.

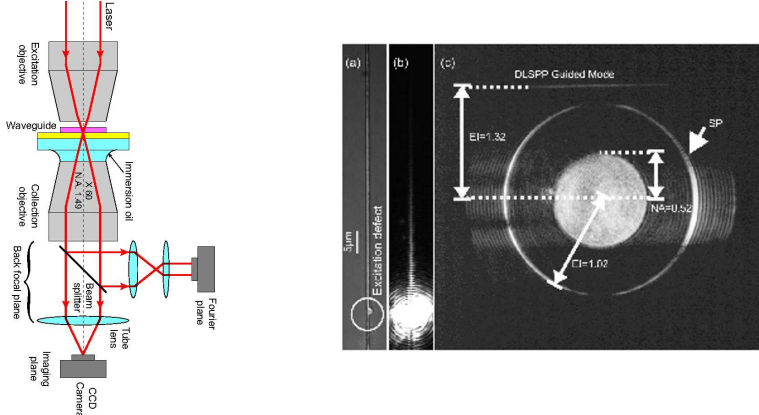


FIG. 4.2 – Gauche : LRM - (leakage radiation microscopy). Montage diascopique. Le mode du guide d'onde est excité grâce à la diffusion du laser focalisé sur un défaut du guide (entouré sur en a). Les fuites du mode dans le substrat sont imitées simultanément dans le plan image et dans le plan de Fourier. a) Image optique du guide de PMMA ($w=350\text{ nm}$, $t=300\text{ nm}$) lithographié sur un film d'or (épaisseur 50 nm). b,c) Images mesurées dans le plan image (b) et dans le plan de Fourier (c).

Dans ce projet, je **co-encadre la thèse de Jonathan Grandidier** depuis février 2007. Dans un premier temps, nous avons déterminé les dimensions optimales du ruban de polymère pour confiner le mode avec un modèle simple (approximation de l'indice effectif) et des simulations numériques (méthode différentielle [82], codes développés par Jean-Claude Weeber et Sébastien Massenot - post-doctorant, ou méthode de Green [83] que je développe). Le facteur de confinement est défini par la proportion de l'intensité du mode dans le polymère (Fig. 4.3). C'est un paramètre qu'il faut maximiser pour optimiser l'interaction du mode guidé avec le polymère, en vue de la réalisation de composants actifs via le dopage du polymère (§4.2).

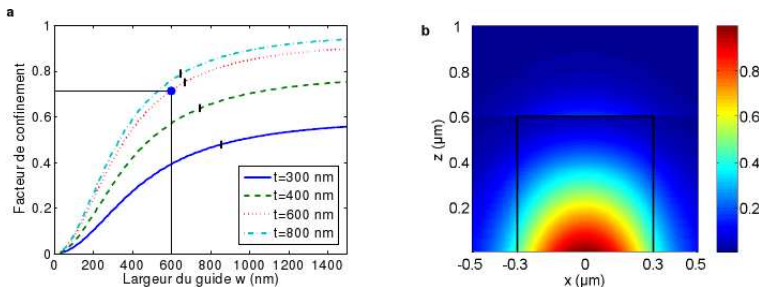


FIG. 4.3 – (a) Facteur de confinement en fonction de la largeur du guide w pour quatre épaisseurs t de PMMA. Sur chaque courbe, le trait vertical indique la fin du régime monomodal ($\lambda = 1.55\text{ }\mu\text{m}$). (b) Intensité électrique du mode calculée pour des dimensions optimales ($t = 600\text{ nm}$ et $w = 600\text{ nm}$). Le facteur de confinement calculé est de 71%.

Les guides sont caractérisés expérimentalement par microscopie des fuites radiatives (LRM - leakage radiation microscopy), à la fois dans le plan image et dans le plan de Fourier (voir la Fig. 4.2). C'est le même type de montage que celui utilisé pour étudier le comportement

dipolaire de nanostructures au chapitre 2 (§2.2). Ainsi pouvons-nous déterminer à la fois la constante de propagation et la longueur de propagation du mode guidé [84]. La figure 4.1 donne un exemple. L'intensité mesurée dans le plan image (b) donne une longueur de propagation de $4,8 \pm 0,5\mu\text{m}$ en accord avec la valeur calculée ($5,2\mu\text{m}$). Dans le plan de Fourier (c), le mode plasmon polariton à l'interface Au/air conduit à la formation de deux arcs de cercles, qui suivent la polarisation TM. La constante de propagation du mode dans le guide apparaît comme un segment de droite tel que sa projection sur l'axe du guide est constante $k_y/k_0 = (1,08 \pm 0,003)$, proche de la valeur théorique ($k_y/k_0 = 1,09$).

Nous avons étudié les propriétés de guidage et de confinement pour différents paramètres (dimensions du guide, longueur d'onde d'excitation, largeur du film d'or) dans le proche infrarouge [82, 85]. Tout particulièrement, nous avons établi que l'amélioration du confinement modal se fait au détriment de la longueur de propagation. Cela constitue une limitation fondamentale pour des applications intégrées. L'utilisation d'un matériau à gain comme diélectrique, discutée au prochain paragraphe, est une réponse à ce problème.

Publications correspondantes

Cette étude est présentée dans l'article suivant :

“Dielectric-loaded surface plasmon polariton waveguides : figures of merit and mode characterization by image and Fourier plane leakage microscopy”

J. Grandidier, S. Massenot, G. Colas des Francs, A. Bouhelier, J.-C. Weeber, L. Markey, A. Dereux, J. Renger, M. U. González and R. Quidant

Physical Review B **78**, 245419 (2008).

Les autres articles associés sont reproduits en annexe

- La caractérisation de modes guidés par microscopie des fuites radiatives est discutée sur un cas simple la lettre suivante

“Polymer-metal waveguides characterization by Fourier plane leakage radiation microscopy”

S. Massenot, J. Grandidier, A. Bouhelier, Colas des Francs, J.-C. Weeber, L. Markey and A. Dereux

Applied Physics Letters **91**, 243101 (2007).

- Enfin, les méthodes numériques développées dans l'équipe pour modéliser les DLSPPW sont détaillées dans deux articles (le second est présenté au §4.3)

“Differential method for modelling dielectric-loaded surface plasmon polariton waveguides”

S. Massenot, J.-C. Weeber, A. Bouhelier, Colas des Francs, J. Grandidier, L. Markey and A. Dereux

Optics Express **16**, 17599-17608 (2008).

“Integrated plasmonic waveguides : a mode solver based on density of states (DOS) formulation”

G. Colas des Francs, J. Grandidier, S. Massenot, A. Bouhelier, J.-C. Weeber and Alain Dereux

Physical Review B, accepté pour publication (2009).

Dielectric-loaded surface plasmon polariton waveguides: Figures of merit and mode characterization by image and Fourier plane leakage microscopy

J. Grandidier,* S. Massenot, G. Colas des Francs, A. Bouhelier, J.-C. Weeber, L. Markey, and A. Dereux

Institut Carnot de Bourgogne, UMR 5209, CNRS, Université de Bourgogne, 9 Avenue A. Savary, BP 47 870, 21078 Dijon, France

J. Renger, M. U. González, and R. Quidant[†]

Institut de Ciències Fotoniques (ICFO), Mediterranean Technology Park, 08860 Castelldefels (Barcelona), Spain

(Received 24 June 2008; revised manuscript received 25 September 2008; published 19 December 2008)

Waveguiding of surface plasmon polaritons by dielectric-loaded metal structures is studied in detail by combining numerical simulations and leakage radiation microscopy. These types of waveguides are first numerically investigated using the effective index model and the differential method. We analyzed systematically the influence of the ridge width and thickness of the waveguide on the properties of the surface plasmon guided modes. In particular we investigated the confinement factor of the modes and their associated propagation lengths. These two parameters can be optimized by adjusting the thickness of the dielectric layer. Waveguides loaded with thick and thin dielectric ridges are then optically characterized by leakage radiation microscopy. The mode propagation distance is measured by direct-space imaging and the propagation constants are evaluated by Fourier imaging and analysis. Good agreements are found between theoretical and experimental data.

DOI: 10.1103/PhysRevB.78.245419

PACS number(s): 73.20.Mf, 71.36.+c, 42.79.Gn, 42.82.Gw

I. INTRODUCTION

Surface plasmon polaritons (SPPs), originating from the coupling of an electromagnetic wave to the free electrons of a metal, open new perspectives in optoelectronics.^{1,2} In the last years there has been an increased effort toward the development of surface plasmon-based devices, and the design of appropriate SPP waveguides constitutes a key element in this route. Different configurations have been already proposed and validated, and their degree of applicability analyzed.^{2–8}

One of the considered configurations relies on the extension of the concept of dielectric-loaded waveguides to plasmon polariton mode and consists on the deposition of a dielectric stripe atop a metallic surface. This approach has been experimentally demonstrated recently,⁹ and the theoretical analysis of the properties of these dielectric-loaded SPP waveguides (DLSPPWs) shows their high potential in integrated photonics.^{10,11} In fact, bends, splitters, and couplers based on these DLSPPW have already been experimentally proved.^{12,13} Moreover, the dielectric layer can be artificially doped by suitable materials so that its optical properties could be externally modified to actively control the SPP mode. This configuration opens then an interesting way for active plasmonics (e.g., electrically or optically controlled plasmonics).

Taking into account the perspectives offered by this kind of waveguides, a detailed analysis of their performance is needed. This study can be done in terms of appropriate figures of merit defined to describe the suitability of a given configuration to a particular application.¹⁴ In this paper, we provide an extensive study of the dielectric-loaded surface plasmon polaritons waveguides by means of two different figures of merit: one that takes into account the aptness of the DLSPPW to transport information over relatively long distances and the other that evaluates the confinement of the waveguide mode. Based on these figures of merit, we iden-

tify two regimes of interest for DLSPPW: thick (thickness $\approx \lambda/2$) and thin (thickness $\ll \lambda/2$) dielectric loads. Thick dielectric loads provide a strong-mode confinement within the dielectric stripe, making them suitable for the development of bends, splitters, and active devices. Thin dielectric loads offer longer propagation distances, allowing their use as simply connecting waveguides.

Once these two regimes have been identified (Sec. II), we have calculated numerically the more appropriate sets of dimensions for each case to highlight their characteristics. These dimensions were used to design and fabricate dielectric structures on thin-metal films. Section III presents the experimental characterization carried out on the fabricated structure to confirm and further analyze their behavior. This experimental study has been done by means of leakage radiation microscopy (LRM).^{15–17} LRM is a highly appropriate technique to perform this study since it is possible to image both the direct and Fourier planes. These two operation modes provide information about the intensity distribution and propagation length of the guided modes as well as their effective indices. In a previous letter, we assessed this method by characterizing a rectangular dielectric waveguide used as a reference.¹⁸ We now use it to fully understand mode construction in DLSPPW.

II. FIGURE OF MERIT AND CONFINEMENT FACTOR OF DLSPPW

Figure 1 schematically describes the DLSPPW geometry considered in the following. A dielectric ridge of thickness t and width w is deposited on a gold film of thickness d covering a glass substrate. For the calculations, the gold thickness and the incident wavelength are fixed to $d=50$ nm and $\lambda_0=780$ nm [$n_{\text{Au}}=0.18+i4.92$ (Ref. 19)], respectively. To evaluate the performance of a waveguide we introduce a set of parameters that can be optimized. These parameters are the confinement factor R , the mode area A_e (Ref. 14), and its

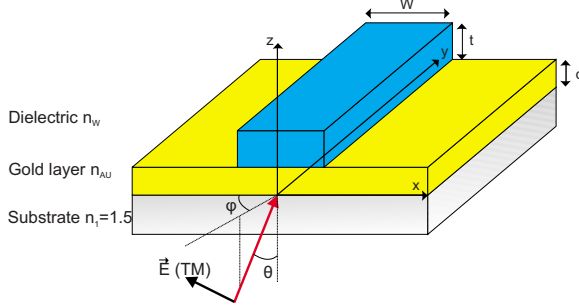


FIG. 1. (Color online) DLSPPW configuration. The guided mode is excited by a TM-polarized wave incident in total internal reflection.

propagation length L_{SPP} . In this section we systematically study the influence of the ridge thickness and width on these parameters.

Recently, Berini¹⁴ proposed the concept of figures of merit for determining optimized dimensions of surface plasmon polariton waveguides. For SPP waveguides consisting of metal stripes, small sizes and limited losses are prerequisites. The figure of merit for these parameters can be defined as^{14,20}

$$M_1^{2D} = \sqrt{\frac{\pi}{A_e}}(2 \times L_{\text{SPP}}). \quad (1)$$

Adapted for propagation length and mode area, this figure of merit lacks information on the mode confinement which is of great importance for applications in active plasmonics. If the dielectric layer is doped to introduce an external control of the guided SPP mode, the amount of mode sustained inside the dielectric stripe determines how strong the influence of the changes would be in the whole mode. The confinement factor measures the proportion of the mode energy inside the waveguide. A high degree of confinement would ensure a stronger interaction between the SPPs and an active material. We compute the confinement factor R as

$$R = \frac{\iint_{\text{guide}} \vec{P} \cdot d\vec{S}}{\int_{-\infty}^{+\infty} \int_{z>0} \vec{P} \cdot d\vec{S}}, \quad (2)$$

where \vec{P} is the Poynting vector. Note that in the regime of thin-metal film ($d < 60$ nm), the modes studied here are intrinsically leaky through the substrate. Consequently, we limit the integration above the substrate for the normalization.

Considering the application range of dielectric-loaded SPP waveguides, we have evaluated their performance based on both the figure of merit and the confinement factor. The mode properties are calculated using the effective index model (EIM) (Refs. 10 and 21) and the differential method.^{18,22} In general an excellent agreement between the effective index model and the differential method is found except for the propagation length which is often overestimated in the EIM. This discrepancy is attributed to the limi-

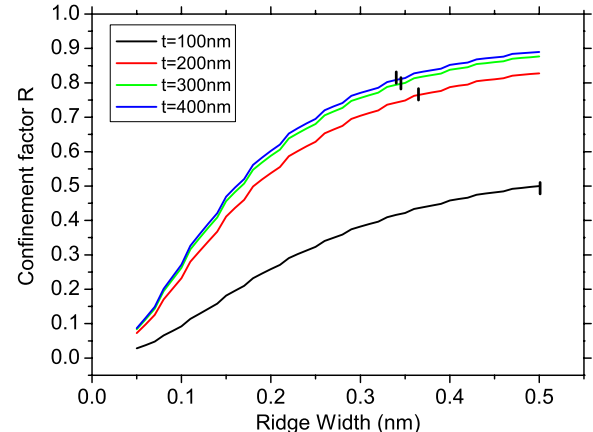


FIG. 2. (Color online) Confinement factor calculated using EIM for several PMMA film thicknesses as a function of ridge width. The crosses indicate the TM_{01} cut-off width. The PMMA optical index is $n_w = 1.49$.

tation of the EIM in taking into account the corners of the dielectric stripe, which therefore disregards the mode scattering along these corners. Therefore, the DLSPPW properties accessible from the effective index model (number of modes, effective index values, cut-off conditions, mode expansion, and confinement) are determined first. The intensity distribution of the modes is then calculated using the differential method which is more time consuming compared to EIM.

A. Thick dielectric load

We first consider the case of a thick dielectric load, i.e., with a thickness around $\lambda/2n_w = 260$ nm. The dielectric stripe consists of poly-methyl-methacrylate (PMMA) since it is an electron-sensitive resist that can be structured by electron-beam (*e*-beam) lithography and it can be readily doped with different active substances. Using the effective index model, as described in detail in Ref. 10, we determine the confinement [Eq. (2)] of the mode supported by the DLSPPW. The values for the mode confinement as a function of the width of ridge w and for different PMMA thicknesses t are presented in Fig. 2. The field confinement increases with PMMA thicknesses and tends to saturate for thicknesses larger than 300 nm. Moreover, increasing the dielectric ridge width allows the excitation of higher-order modes in the waveguide.¹⁰ In order to maximize the interaction between the mode and the polymer, we impose monomodal conditions, corresponding to ridge widths below 350 nm. Finally, a set of parameters (t, w) that combines good confinement and monomodal waveguide is around $t = 350$ nm and $w = 300$ nm.

Having determined an optimized set of parameters for the PMMA ridge, we investigate the mode characteristics using the differential method.^{18,22} A detailed description of the differential method applied to DLSPPW analysis has been published elsewhere.²³

Following the discussion above, we realized a sample with the following parameters (see Sec. III A): the gold film thickness is $d = 50$ nm, the PMMA ridge width $w = 240$ nm,

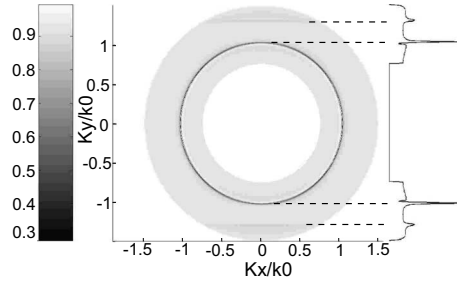


FIG. 3. Reflectivity map with varied incident angles θ and φ (see Fig. 1). The DLSPPW is made of a PMMA ridge of width $w=240$ nm and thickness $t=330$ nm. The incident wave-vector components along the x and y axes are $k_x/k_0=n_1 \sin \theta \cos \varphi$ and $k_y/k_0=n_1 \sin \theta \sin \varphi$, respectively.

and thickness $t=330$ nm. The incident wavelength is $\lambda=780$ nm. Note that by using the differential method, we obtain a mode propagation length in the range of $L_{\text{SPP}}=6.5 \pm 0.5 \mu\text{m}$ for a ridge width varying from 150 to 500 nm. This justifies *a posteriori* that we only focused on the confinement properties when optimizing the ridge dimensions.

Figure 3 shows the reflectivity diagram calculated with the differential method when the DLSPPW is illuminated with a plane wave from below the substrate at different angles of incidence.¹⁸ A low reflectivity circle is clearly visible at $n_{\text{eff}}=k_{\parallel}/k_0=1.02$ where $k_{\parallel}=(k_x^2+k_y^2)^{1/2}$ is the wave-vector component parallel to the gold surface. This is the signature of the excitation of the Au/air surface plasmon polariton mode. Two absorption lines also appear at $n_{\text{eff}}=|k_y/k_0|=1.30$. These two bands originate from light coupling to DLSPPW modes which propagate toward increasing y direction ($k_y/k_0>0$) or decreasing y direction ($k_y/k_0<0$) inside the guide.¹⁸ Note that the same value for the effective index of the mode ($n_{\text{eff}}=1.30$) is obtained using effective index model.

Figures 4(a) and 4(b) show the electric-field intensity distribution of the mode across a section of the waveguide and its evolution along the propagation direction, respectively. The profiles are calculated using a TM-polarized incident beam oriented along the waveguide ($\varphi=90^\circ$) and matched to the mode momentum [$\theta=\arcsin(n_{\text{eff}}/n_1)=60^\circ$]. The calculations show that the mode is well confined by the dielectric structure and has its maximum at the Au/PMMA interface as expected from a SPP wave. The decay along the propagation is exponential. We deduce from Fig. 4(a) the confinement factor $R=69\%$ and from Fig. 4(b) a propagation length at $1/e$ attenuation of $L_{\text{SPP}}=6.1 \mu\text{m}$. R is in excellent agreement with the confinement calculated using the effective index model (see Fig. 2).

B. Thin dielectric load

While optimized mode confinement can be achieved by nearly squared waveguide sections (e.g., $w=350$ nm \times $t=300$ nm), DLSPPWs formed by thinner loads offer a different range of guiding properties.¹⁵ In this section, we focus our attention on a 70-nm-thick dielectric. For this range of

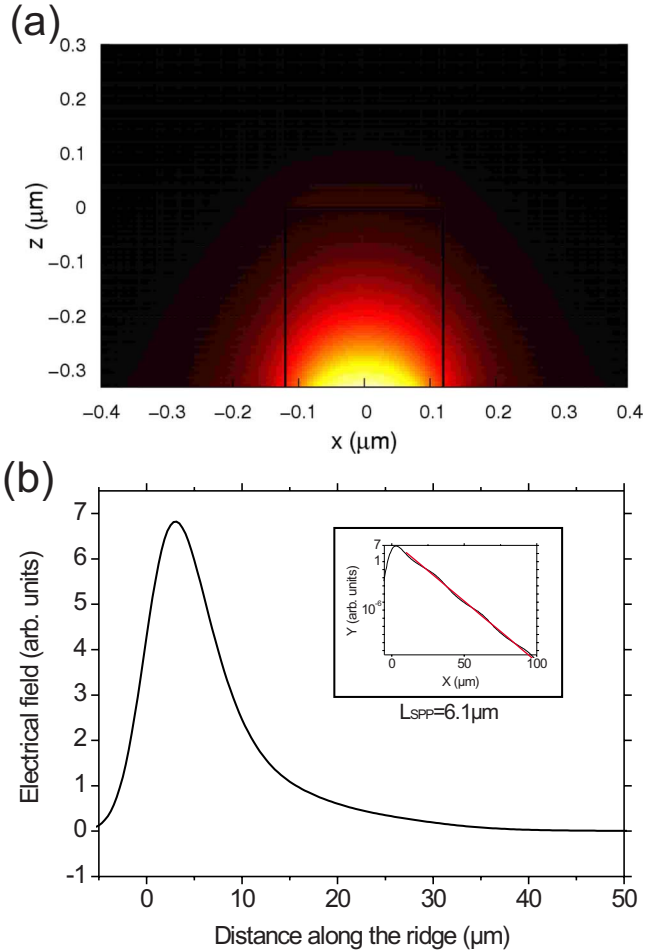


FIG. 4. (Color online) (a) Electrical-field intensity distribution inside the guide. The mode is excited using an incident wave at $\theta=60^\circ$. (b) Cross section along the ridge center. The inset shows a linear fit in semilogarithmic scale.

thickness, the confinement R is small (see Fig. 2) and the mode substantially extends out of the dielectric structure. Nonetheless, these types of waveguides benefit from longer propagation length as compared with thick dielectric. Thin DLSPPW can therefore provide the basic units for designing more complex SPP routing (mode couplers, filters, etc.). In this respect, the figure of merit M_1^{2D} defined in Eq. (1) is the critical parameter.

On the basis of the effective index model, we first determine the modes supported by a 70 nm thin SiO₂ DLSPPW. The choice of SiO₂ over PMMA is dictated by its compatibility with current microelectronic technology (of interest if this kind of DLSPPW is useful in SPP routing systems) and do not change the general conclusions drawn so far.

Figure 5 shows the effective indices for the different TM modes supported by the DLSPPW. The effective index of the fundamental mode TM₀₀ increases with w from the Au/air effective index ($n_{\text{eff}}=1.02$) up to that of a Au/SiO₂(70 nm)/air system ($n_{\text{eff}}=1.15$). Higher-order modes are populated when the ridge width increases. As an example, the TM₀₁ and TM₀₂ modes have a cut-off width at, respectively, 700 nm and 1.5 μm .

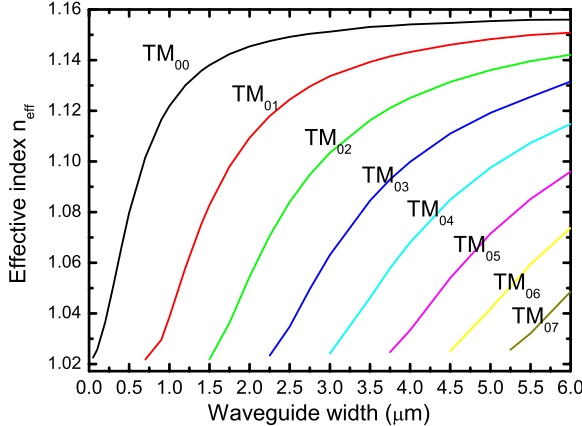


FIG. 5. (Color online) Effective indices of the fundamental and higher-order modes associated with a 70-nm-SiO₂ ($n_w=1.453$) DLSPPW as a function of the waveguide's width.

Figure 6 shows the calculated mode intensity pattern across the DLSPPW for several ridge widths. For very narrow waveguides only the fundamental mode TM₀₀ is present. For the narrowest waveguide shown $w=100$ nm, the field intensity is spread across the dielectric loading (indicated by a blue rectangle in the figure) and the surrounding air media. Thus, the n_{eff} of the guided mode is comparable to that of the gold-air SPP mode. As the waveguide width increases, the TM₀₀ mode becomes more confined in the SiO₂ loading as well as above the structure [see Figs. 6(b)–6(d)] and its effective index increases accordingly. Note that the dielectric load thickness is below TE₀ mode cutoff so that no TE-polarized mode is supported.¹⁰

It can be seen in Fig. 5 that the 70 nm SiO₂ DLSPPW becomes multimodal for a width larger than 700 nm. Note that the first higher-order appearing mode TM₀₁ shows an odd field distribution (not shown here) and therefore cannot be excited by a plane wave impinging along the waveguide direction. On the contrary, even modes can be easily excited and their corresponding field patterns for a width $w=4$ μm are shown in Figs. 6(e) and 6(f).

Figure 7 represents the figure of merit M_1^{2D} associated to the fundamental mode TM₀₀ calculated from Eq. (1) using

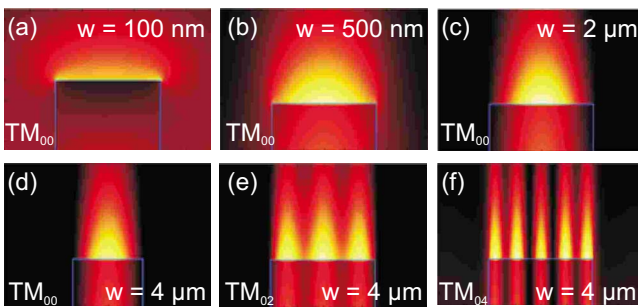


FIG. 6. (Color online) Calculated mode intensity distribution across the DLSPPW in the air half space. [(a)–(c)] TM₀₀ patterns for waveguide widths $w=0.1$, 0.5, and 2 μm , respectively. The dielectric waveguide is indicated by the blue rectangle. [(d)–(f)] Pattern for the even modes TM₀₀, TM₀₂, and TM₀₄ for a waveguide of $w=4$ μm . The aspect ratios are different for the sake of visibility.

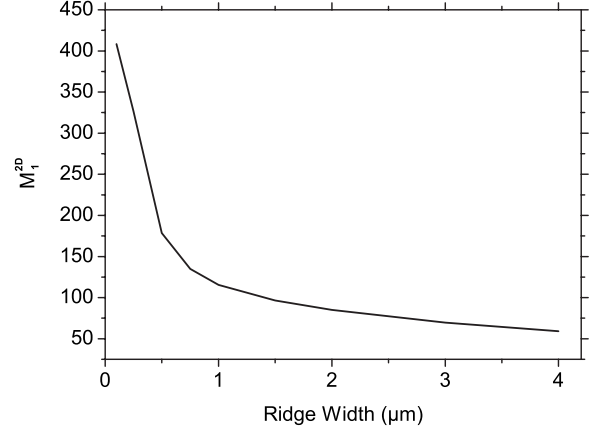


FIG. 7. Figure of merit obtained from differential method for the fundamental TM₀₀ mode for a 70-nm-thin SiO₂ ridge loaded on a 62-nm-gold film.

the differential method. Thin ridges are characterized by a better figure of merit than thick ones (not shown). In spite of the spreading of the mode outside the dielectric ridge, the longer propagation distances of the mode in this case lead to a large value for M_1^{2D} ; mainly for narrow waveguides. Note also that the values of the M_1^{2D} obtained for the thin SiO₂ DLSPPW are high despite the large ohmic losses of gold at the frequency we consider.²⁰

III. EXPERIMENTS

A. Thick dielectric load

With the aim of controlling the numerical results, a sample was prepared according to the following procedure: a gold layer with a thickness of 50 nm was first evaporated on a glass substrate. A 330-nm-thick electron-sensitive PMMA layer was then spin coated onto the gold film. The PMMA was then exposed by standard *e*-beam lithography to form a ridge of 240 nm width. The surface plasmon modes supported by the waveguide can be excited following different diascopic or episcopic excitation schemes. A schematic of the setup in diascopic configuration is shown in Fig. 8. A 0.52 numerical aperture (NA) objective incident from the air side focuses a collimated laser beam onto the ridge structure. The polarization state was controlled by inserting a retarder in the optical path. Momentum transfer through scattering on the ridge or on a defect ensured that part of the incident energy was coupled in the SPP mode. To investigate the characteristics of the guided modes, we collected the intrinsic radiation leaking through the gold film by using a high numerical aperture oil immersion objective (Nikon 60× and NA=1.49). The intensity of the leakage radiation emitted at the substrate/gold interface is directly related to the intensity distribution of the SPP mode and provides therefore a unique mean to easily assess SPP properties.

1. Measurement at $\lambda_0=780$ nm

A typical DLSPPW structure of the sample is shown in the bright-field optical micrograph of Fig. 9(a). A defect,

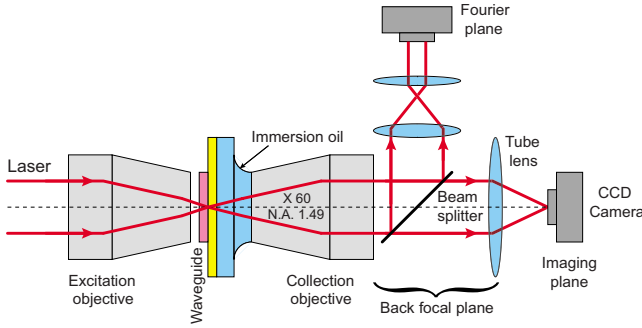


FIG. 8. (Color online) Sketch of the leakage radiation microscopy setup. A 0.52 NA objective focuses the incident light onto the structure or a defect. The modes are excited through scattering and momentum transfer. Leakage radiation of the guided modes is collected with a 1.49 NA objective and recorded either in the image plane or in the Fourier plane.

helping to convert part of the incident energy into the SPP mode, is indicated by the white circle. Figure 9(b) shows the spatial intensity distribution of the radiation leakage as recorded in the image plane. The focalization of the incident light by the 0.52 objective is readily visible in the bottom part of the image as a bright overexposed spot. The SPP guided mode is recognized as the confined streak of light propagating from the bottom to the top of the image. An exponential fit of the decaying intensity gives a propagation length of $5.5 \mu\text{m}$, in very good agreement with the calculated value [$6.1 \mu\text{m}$; see Fig. 4(b)].

Figure 9(c) shows the leakage radiation recorded in the Fourier plane of the microscope. The bright central disk corresponds to the numerical aperture ($\text{NA}=0.52$) of the top illuminating objective and is used for calibration of the Fourier plane.¹⁸ The two symmetric half moons that appear at $n_{\text{eff}}=1.02 \pm 0.03$ correspond to leakage radiation coming from the Au/air SPP mode. The NA of the objective limits the upper value of the mode index, which is 1.49 in our

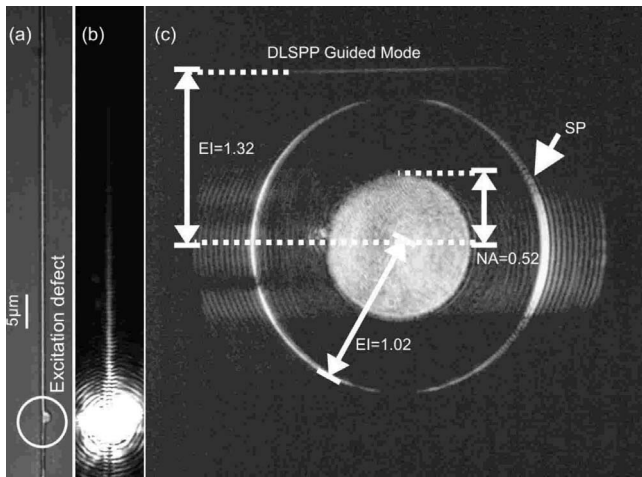


FIG. 9. (a) Optical micrograph of a typical PMMA waveguide fabricated on a gold substrate. The DLSPPW modes are excited by focusing a TM-polarized beam on the defect marked in (a). LRM observation of the propagation along the waveguide: in the (b) image plane and in the (c) Fourier plane.

TABLE I. Experimental and theoretical values (calculated using differential method and effective index model) of the mode effective index.

λ_0 (nm)	Effective index		
	Differential method	EIM	Experiment
750	1.32	1.31	1.28
760	1.32	1.31	1.28
770	1.31	1.30	1.26
780	1.30	1.30	1.26
790	1.29	1.29	1.26
800	1.28	1.28	1.26
810	1.28	1.28	1.25
820	1.27	1.27	1.24
830	1.26	1.27	1.24
840	1.26	1.26	1.23
850	1.25	1.26	1.23
860	1.24	1.26	NA
870	1.24	1.25	NA
880	1.23	1.25	NA
890	1.23	1.24	NA
900	1.22	1.24	NA

experiment. The signature of the guided mode inside the DL-SPPW appears as a horizontal line in the Fourier plane. This line corresponds to the value of the propagation constant and has a measured effective index of $n_{\text{eff}}=1.32 \pm 0.04$, in fair agreement with the theoretical reflectivity measurement shown in Fig. 3. Note however that only the mode that propagates in the forward direction appears in Fig. 9(c) because the waveguide is not well defined below the defect used for the excitation. Additionally, the intensity of the DL-SPP mode is significantly weaker than the other features on Fig. 9(c) because of the SPPs coupling efficiency of our excitation scheme.

2. Measurements at different wavelengths

Wavelength influence on the mode properties is now considered. Table I and Fig. 10 present the effective indices and propagation lengths measured and calculated for $750 \text{ nm} \leq \lambda_0 \leq 900 \text{ nm}$. Despite a few atypical points, the L_{SPP} evolution is quite monotonous with increasing wavelength since the imaginary part of the gold refractive index decreases in the infrared domain. A fair agreement is obtained between experimental data and numerical simulations. Note that effective indices for $\lambda_0 \geq 860 \text{ nm}$ were not measured experimentally since low radiative losses at these wavelengths lead to poor signal-to-noise ratios in the LRM images.

B. Thin dielectric load

The fabrication procedure for thin SiO_2 loads also relies on standard e -beam lithography followed by thermal deposition of SiO_2 layer and a liftoff of the resist. Thin DLSPPWs were also characterized by leakage radiation microscopy.

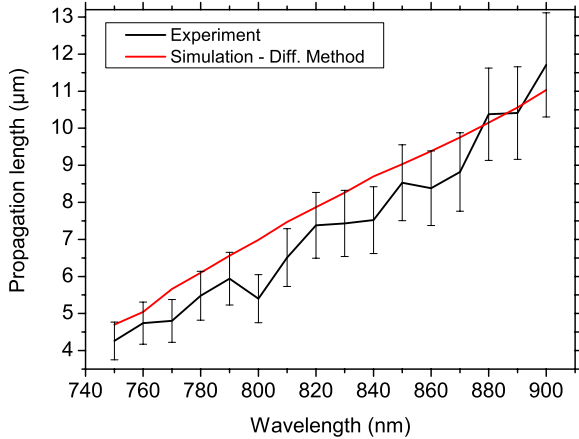


FIG. 10. (Color online) Experimental and theoretical values (calculated using differential method) of the propagation length as a function of the wavelength for a $330 \text{ nm} \times 240 \text{ nm}$ PMMA DLSPPW.

Figure 11 shows the experimental images for thin waveguides with several ridge widths. Instead of exciting the DLSPPW mode by focusing onto a defect,²⁴ SPPs on the bare 62-nm-thick Au film were excited using a total internal reflection (TIR) illumination scheme.^{15,25} Therefore, the in-

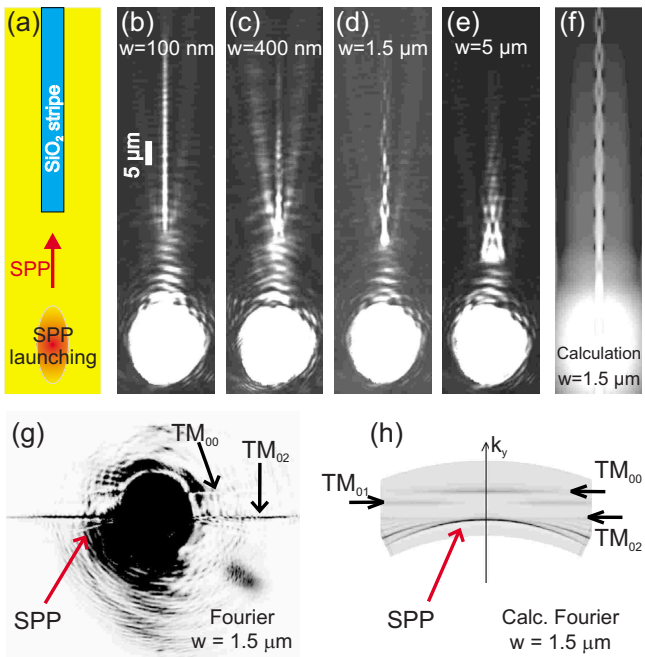


FIG. 11. (Color online) LRM images of light propagating through a thin SiO_2 ridge ($t=70 \text{ nm}$) waveguide for different widths w at $\lambda_0=800 \text{ nm}$. (a) Sketch of the excitation configuration. The SPPs are launched on the gold film by TIR illumination and hit the end face of the DLSPPW, thereby exciting the waveguide modes. [(b)–(e)] Direct-space LRM images of the waveguides. (f) Calculated (differential method) field intensity for light propagating along a DLSPPW of width $1.5 \mu\text{m}$ excited by a Gaussian beam impinging on the waveguide. (g) Fourier plane image corresponding to the waveguide of $w=1.5 \mu\text{m}$. (h) Calculated reflectivity map in a portion of the reciprocal space for a waveguide of $w=1.5 \mu\text{m}$. The excited modes are indicated by arrows in the image.

cident TM-polarized light having a wavelength $\lambda_0=800 \text{ nm}$ was displaced from the optical axis and slightly focused onto the back focal plane of the immersion-oil objective (Olympus $60\times$ and $\text{NA}=1.45$). This results in illuminated areas of $10 \mu\text{m}$ by $15 \mu\text{m}$ that appear as white distorted ellipses in Figs. 11(b)–11(e). The back-reflected field saturates the charge-coupled device (CCD) camera. We focus the beam several microns before the entrance of the dielectric stripe, as sketched in Fig. 11(a). The light matching k_{SPP} excites the SPPs having most of its energy at the gold/air interface. The SPPs propagate a few tens of micrometers toward the DLSPPW as indicated by the red arrow. During propagation, the SPPs produce the leakage radiation visible in Figs. 11(b)–11(e) in between the incidence spot and the dielectric stripe. The modes existing in the DLSPPW are leaky because of the finite gold layer thickness of 62 nm and can be easily imaged by LRM.

The LRM images for DLSPPW of different widths are displayed in Figs. 11(b)–11(e). The images clearly reveal the strong dependence of the mode characteristics on the width of the dielectric loading. For a $5\text{-}\mu\text{m}$ -wide SiO_2 stripe [Fig. 11(e)], which has nearly the same width as the incident SPPs, most of the SPPs are converted into the DLSPPW modes. The intensity along the waveguide decays much more rapidly compared to SPPs on the unloaded gold-air interface. For narrower DLSPPWs, the section of the DLSPPW does not fully overlap the width of the incident SPPs and three distinct regions can be distinguished. The first one corresponds to leakage radiation along the waveguide and originates from the coupling of the incident SPPs into the guiding structure. The second region corresponds to the portion of the incident SPPs not coupled into the waveguide. This uncoupled part propagates sidewise the guides along both edges and is readily visible in Figs. 11(b)–11(d). Finally, the third region is associated with incident SPP which is backreflected and/or scattered by the DLSPPW edge. This latter portion is dominantly emitted into the air space.

From the LRM images, we can determine the characteristic properties of the waveguides, namely, the effective refractive index n_{eff} and the propagation length L_{SPP} . The latter was determined by fitting the intensity decay along the waveguides for a variety of widths and is displayed in Fig. 12. In the case of a multimodal waveguide, the measured L_{SPP} represents an average decay length considering all the excited modes.

The upper limit for L_{SPP} is given by the unloaded gold surface and is indicated by the horizontal red dashed line in Fig. 12 (theory $L_{\text{SPP}}=35.3 \mu\text{m}$). The experimentally determined decay value for our gold films is $L_{\text{SPP}}=33.6 \mu\text{m}$, in very good agreement with this theoretical value. The green dashed line at $L_{\text{SPP}}=9 \mu\text{m}$ corresponds to a complete $70\text{-nm-}\text{SiO}_2$ dielectric film and provides a lower bound for L_{SPP} . This lower limit is reached for DLSPPW width greater than approximately $2 \mu\text{m}$. For narrower waveguides, the value of L_{SPP} increases significantly toward the upper limit. This general behavior is in good agreement with the figure of merit M_1^{2D} shown in Fig. 7: for narrow waveguides M_1^{2D} strongly increases as a consequence of the higher propagation length.

The experimental effective indices of the DLSPPW modes inside the waveguides were assessed from LRM Fou-

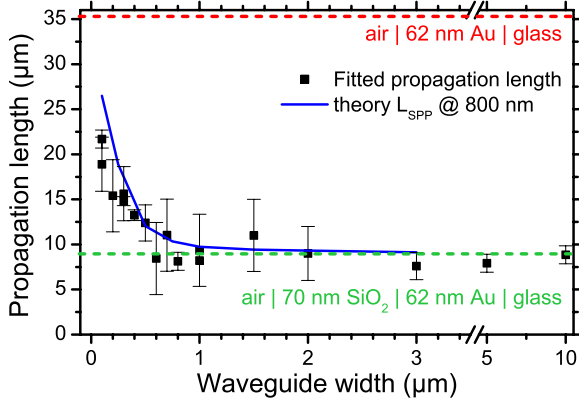


FIG. 12. (Color online) Evolution of the propagation length L_{SPP} with the width w of a thin SiO_2 ridge ($t=70$ nm) waveguide (TM polarization and $\lambda_0=800$ nm). The red and green dashed lines correspond to the upper and lower limits of this propagation length, respectively: the plasmon of the interface air/Au and that of the interface air/70-nm- SiO_2 /Au. The blue line shows the theoretical values for L_{SPP} , corresponding to TM_{00} mode only, calculated with the differential method.

rier images, as the one shown in Fig. 11(g). In contrast to Fig. 9(c) where the waveguided mode was excited by the use of a local defect, here the TIR configuration outlined above was used. Figure 11(g) is the Fourier plane image of a DL-SPPW with $w=1.5$ μm [Fig. 11(d)]. The excitation geometry gives rise to a strong reflection spot in the Fourier image. The size of the spot is a measure of the distribution of incident wave vectors. To efficiently couple the SPPs, the location of the spot in the reciprocal space is adjusted to coincide with the SPP resonant wave vectors. The coupling to the SPP mode is detected by the presence of a dip within the distribution. This dip is however not clearly visible in the image since the saturation of the detector was adjusted to enhance the weak signature of the waveguided modes. Note that outside the incident distribution of wave vectors, the SPP coupling at the Au/air interface can be recognized as a small crescent (indicated with an arrow in the figure). It originates from SPPs propagating in directions diverging from the incident excitation. More importantly, the signature of the DL-SPPW modes also marked with arrows appears as straight bright lines extending out of the incident wave-vector distribution. For this particular width, two modes are observed in the Fourier plane image of Fig. 11(g). The n_{eff} of the various modes appearing for each waveguide was measured using the k_{SPP} position of SPPs propagating at the bare gold/air interface as a reference. The results are gathered in Fig. 13.

As expected, the effective indices of the DL-SPPW modes are within the limits given by the bare gold surface ($n_{\text{eff}}=1.02$, dashed red line) and a gold surface completely loaded with 70 nm SiO_2 ($n_{\text{eff}}=1.15$, dashed green line). In order to identify the order of the modes associated for each value, we have also plotted the n_{eff} values obtained from the EIM calculations presented in Fig. 5. The experimental results for n_{eff} are in good agreement with the predictions and the small differences originate from experimental uncertainties such as the exact shape of the dielectric loading, the surface rough-

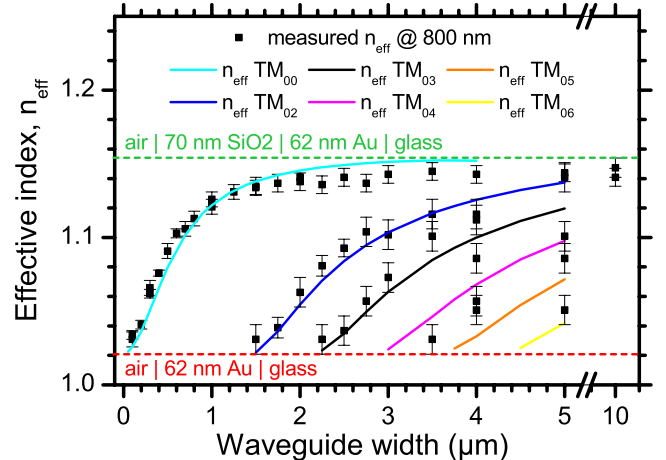


FIG. 13. (Color online) Evolution of the mode effective index n_{eff} with the width w of a thin SiO_2 ridge ($t=70$ nm) waveguide (TM polarization and $\lambda_0=800$ nm). The values of n_{eff} should be comprised within those of the plasmon in an air/Au interface (red dashed line) and the plasmon in an air/70-nm- SiO_2 /Au interface (green dashed line). The solid lines report the effective index obtained from EIM (see Fig. 5).

ness, and the exact thickness of the SiO_2 layer. For instance, a thickness difference of only 5 nm would shift the upper limit of n_{eff} from 1.154 (70 nm SiO_2) to 1.14 (65 nm SiO_2). We note that the TM_{01} mode was not observed for any of the waveguides, while higher-order modes were detected. This particular mode has an odd symmetry of the field and cannot be excited with a beam impinging along the waveguide direction. This explanation is confirmed by the calculated reflectivity map shown in Fig. 11(h), corresponding to a DL-SPPW of $w=1.5$ μm . For this width, three modes are supported: TM_{00} , TM_{01} , and TM_{02} . However, only TM_{00} and TM_{02} are intersecting with $k_x=0$ value, indicating that they can be excited by a beam parallel to the waveguide. The TM_{01} mode has a signature for $k_x \neq 0$ values and can only be excited with a tilted illumination. The absence of the TM_{01} mode in our experiment indicates that the angular spreading of the beam used to excite the waveguides was not broad enough to excite this mode.

The multimode nature of the DL-SPPWs for w greater than approximately 1.5 μm does not only manifest itself in the Fourier plane but in the LRM images of Figs. 11(b)–11(e). The two wider waveguides $w=1.5$ and 5 μm are certainly multimode and they show modulated intensity patterns. The difference in the intensity distribution inside the waveguides indicates that different modal structures are involved. The 1.5- μm -wide waveguide, for instance, presents two identified modes: TM_{00} and TM_{02} . The field distribution of these two modes shown in Fig. 6 has, respectively, one central maximum and three maxima. The interference between these two modes creates a beating with a chainlike distribution observed in Fig. 11(d). The beating period of the intensity along the center of this waveguide Δ , as calculated from the image, is 7 ± 0.2 μm . Beating of the two considered modes TM_{00} and TM_{02} can be obtained from the expression $\Delta = 2\pi/(k_{\text{TM}_{00}} - k_{\text{TM}_{02}}) = 6.9$ μm , in good agreement with the measured value. Figure 11(f) shows the field intensity distri-

bution along a $1.5 \mu\text{m}$ wide DLSPPW calculated with the differential method and excited by a Gaussian beam. The angular spread of the Gaussian beam was restricted to only excite the TM_{00} and TM_{02} modes. The intensity distribution shows a very similar chainlike pattern as observed in the experimental image.

For waveguides being narrower than $w < 1.5 \mu\text{m}$, only the fundamental mode is excited and the intensity shows no spatial pattern across the waveguide [see Figs. 11(b) and 11(c)]. We have however detected some beating in the intensity along these waveguides whose periodicity is given by $\Delta = 2\pi/(k_{\text{TM}_{00}} - k_{\text{SPP}})$. This beating comes from the interference of the fundamental DLSPPW mode and SPPs propagating on the gold film. Hence, the beating period increases for narrower DLSPPW and, for example, cannot be measured for the 100-nm-wide waveguide.

In summary, since the incident SPPs at the gold/air interface couple simultaneously to all of the available guided modes, the propagation distance and intensity distribution of thin DLSPPW become strongly dependent of w . For $w \geq 1.5 \mu\text{m}$, multiple modes are excited generating a strong beating and L_{SPP} is very close to the SPP decay of a homogeneous gold/SiO₂ interface (about $9 \mu\text{m}$). This reflects the fact that the excited modes are mostly confined laterally within the silica load in this case. When reducing w below $1.5 \mu\text{m}$, the incident energy couples to the TM_{00} mode only. For very narrow DLSPPW, the field extends further into the air resulting in an increase in the propagation length and lower effective index of the mode. Despite low transversal confinement, the figure of merit M_1^{2D} shows a respectable value (see Fig. 7) and efficient guiding is indeed achieved along 100-nm-wide DLSPPW with $L_{\text{SPP}}=20 \mu\text{m}$.

IV. CONCLUSION AND PERSPECTIVE

In this paper, dielectric-loaded surface plasmon polaritons waveguides were theoretically and experimentally investigated by leakage radiation microscopy in direct and Fourier planes. Depending on the thickness of the dielectric load, the figure of merit or mode confinement can be optimized. For a thin load, the large values of the figure of merit allow the propagation of surface plasmon guided modes over distances of several tenths of micrometer in the near-infrared region. For thicker loads, the decay is shorter but the three-dimensional confinement is drastically increased. This regime of thickness is suitable for applications requiring a large density of plasmonic devices. The calculated values of the effective indices and decay lengths of the guided modes obtained with our numerical approach are in agreement with the experimental values. This is encouraging for extending the range of our calculation to telecom bands ($\lambda_0 = 1300 \text{ nm}$ or 1550 nm). Note that at these wavelengths, leakage radiation microscopy is probably not a suitable tool. Radiation losses through the metal are negligible and near field microscopy is more appropriate.^{26–28}

ACKNOWLEDGMENTS

The authors gratefully acknowledge T. Holmgard and S. I. Bozhevolnyi for fruitful discussions. This work was supported by the European Commission through the PLASMO-COM project (under Project No. EC FP6 IST 034754 STREP). M.U.G thanks the Spanish Ministry of Education for funding under the “Ramón y Cajal” program.

*jonathan.grandidier@u-bourgogne.fr

[†]Also at ICRA-Institució Catalana de Recerca i Estudis Avançats, Barcelona, Spain.

¹W. Barnes, A. Dereux, and T. Ebbesen, *Nature (London)* **424**, 824 (2003).

²E. Ozbay, *Science* **311**, 189 (2006).

³R. Charbonneau, P. Berini, E. Berolo, and E. Lisicka-Shrzek, *Opt. Lett.* **25**, 844 (2000).

⁴J. C. Weeber, Y. Lacroute, and A. Dereux, *Phys. Rev. B* **68**, 115401 (2003).

⁵S. I. Bozhevolnyi, V. S. Volkov, E. Devaux, J. Y. Laluet, and T. W. Ebbesen, *Nature (London)* **440**, 508 (2006).

⁶E. Moreno, S. G. Rodrigo, S. I. Bozhevolnyi, L. Martín-Moreno, and F. J. García-Vidal, *Phys. Rev. Lett.* **100**, 023901 (2008).

⁷J. A. Dionne, H. J. Lezec, and H. A. Atwater, *Nano Lett.* **6**, 1928 (2006).

⁸P. Ginzburg and M. Orenstein, *Opt. Express* **15**, 6762 (2007).

⁹B. Steinberger, A. Hohenau, H. Ditlbacher, A. L. Stepanov, A. Drezen, F. R. Aussenegg, A. Leitner, and J. R. Krenn, *Appl. Phys. Lett.* **88**, 094104 (2006).

¹⁰T. Holmgard and S. I. Bozhevolnyi, *Phys. Rev. B* **75**, 245405 (2007).

¹¹A. V. Krasavin and A. V. Zayats, *Appl. Phys. Lett.* **90**, 211101 (2007).

(2007).

¹²B. Steinberger, A. Hohenau, H. Ditlbacher, F. R. Aussenegg, A. Leitner, and J. R. Krenn, *Appl. Phys. Lett.* **91**, 081111 (2007).

¹³T. Holmgard, Z. Chen, S. I. Bozhevolnyi, L. Markey, A. Dereux, A. V. Krasavin, and A. V. Zayats, *Opt. Express* **16**, 13585 (2008).

¹⁴P. Berini, *Opt. Express* **14**, 13030 (2006).

¹⁵A. Hohenau, J. Krenn, A. Stepanov, A. Drezen, H. Ditlbacher, B. Steinberger, A. Leitner, and F. Aussenegg, *Opt. Lett.* **30**, 893 (2005).

¹⁶B. Hecht, H. Bielefeldt, L. Novotny, Y. Inouye, and D. W. Pohl, *Phys. Rev. Lett.* **77**, 1889 (1996).

¹⁷A. Bouhelier, T. Huser, H. Tamaru, H.-J. Güntherodt, D. W. Pohl, F. I. Baida, and D. Van Labeke, *Phys. Rev. B* **63**, 155404 (2001).

¹⁸S. Massenot, J. Grandidier, and A. Bouhelier, G. Colas des Frans, J. -C. Weeber, L. Markey, A. Dereux, J. Renger, M. U. González, and R. Quidant, *Appl. Phys. Lett.* **91**, 243102 (2007).

¹⁹*Handbook of Optical Constants of Solids*, edited by E. D. Palik (Academic, San Diego, 1985).

²⁰R. Buckley and P. Berini, *Opt. Express* **15**, 12174 (2007).

²¹D. Marcuse, *Theory of Dielectric Optical Waveguides* (Academic, New York, 1991).

- ²²M. Nevière and E. Popov, *Light Propagation in Periodic Media, Differential Theory and Design* (Marcel Dekker, New York, 2003).
- ²³S. Massenot, J.-C. Weeber, and A. Bouhelier, G. Colas des Francs, J. Grandidier, L. Markey, and A. Dereux, Opt. Express **16**, 17599 (2008).
- ²⁴J. Renger, S. Grafström, and L.-M. Eng, Phys. Rev. B **76**, 045431 (2007).
- ²⁵A. Bouhelier and G. P. Wiederrecht, Opt. Lett. **30**, 884 (2005).
- ²⁶P. Dawson, F. de Fornel, and J.-P. Goudonnet, Phys. Rev. Lett. **72**, 2927 (1994).
- ²⁷S. I. Bozhevolnyi, V. S. Volkov, E. Devaux, J.-Y. Laluet, and T. W. Ebbesen, Nature (London) **440**, 508 (2006).
- ²⁸T. Holmgård, S. I. Bozhevolnyi, L. Markey, and A. Dereux, Appl. Phys. Lett. **92**, 011124 (2008).

4.2 Gain optique

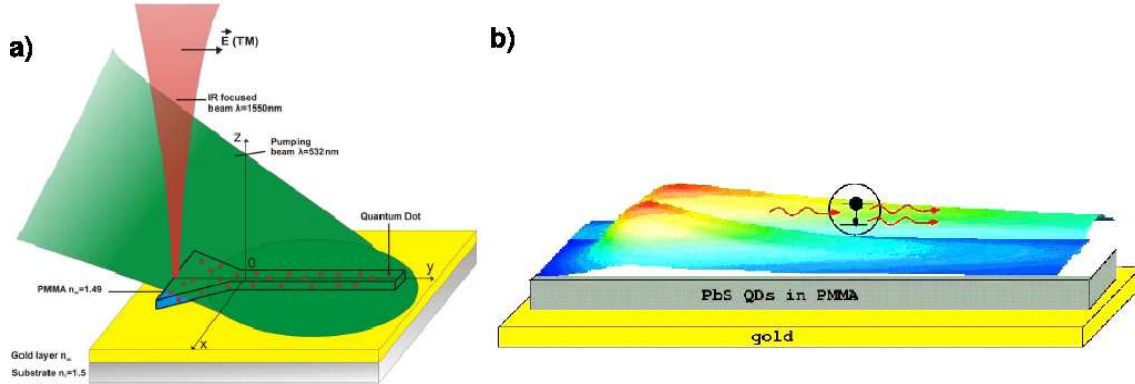


FIG. 4.4 – a) Guide plasmonique dopé avec des puits quantiques (Quantum Dots, QDs). Le mode guidé est excité à $\lambda = 1,55 \mu m$ sur un bord du guide et les QDs sont pompés optiquement à $\lambda = 532nm$. b) Simulation numérique de la propagation assistée par émission stimulée. La propagation en absence de pompage des QDs est représentée à l'avant ($\epsilon'' = 0$). L'augmentation de la longueur de propagation grâce à l'émission stimulée est visible à l'arrière de la figure ($\epsilon'' = -0,007$). ϵ'' représente la partie imaginaire de la constante diélectrique du guide. $\epsilon'' < 0$ décrit un matériau à gain.

Dans ce paragraphe, nous nous intéressons à la compensation des pertes de propagation par émission stimulée de plasmons. La configuration considérée, directement inspirée des amplificateurs optiques, est représentée sur la figure 4.4. Un ruban de polymère (PMMA, épaisseur 600 nm, largeur 400 nm) dopé avec des boîtes quantiques (Quantum Dots, QDs) est déposé sur un film d'or de 50 nm. Le confinement du mode dans le polymère (Fig. 4.3b) assure une bonne interaction avec les QDs pompés optiquement, d'où une possible compensation des pertes par émission stimulée.

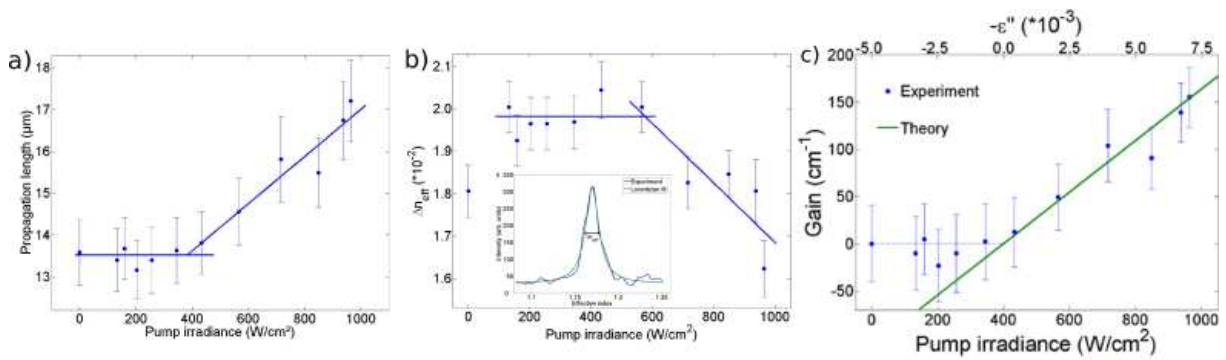


FIG. 4.5 – (a) Longueur de propagation mesurée en fonction de la puissance de pompe. b) Largeur à mi-hauteur de la résonance en fonction de la puissance de pompe. L'insert montre le profil de la résonance mesurée dans le plan de Fourier à pompe nulle. c) Gain intrinsèque déduit de la longueur de propagation [points bleus, $g = 1/L_{SPP} - 1/L_{SPP}(I_p)$] ou calculé en fonction de la partie imaginaire ϵ'' du polymère (courbe verte).

La mesure de la longueur de propagation en fonction de la puissance de pompe (Fig. 4.5a)

fait apparaître un accroissement de près de 30%, avec un net effet de seuil vers 500 W.cm^{-2} , typique du processus d'émission stimulée. Le rétrécissement de la largeur de la résonance, représentée sur la figure 4.2b) confirme le processus d'émission stimulée de plasmons [86]. Des simulations numériques, basées sur un modèle simplifié de l'émission stimulée montre un bon accord avec le gain mesuré (Fig. 4.2c). Sur la base de ces simulations numériques, nous avons estimé qu'une amplification (régénération) du signal à la sortie du guide est envisageable, ouvrant la voie à la réalisation d'un amplificateur plasmonique, composant clé pour la photonique intégrée. Des études sont en cours pour affiner la modélisation de la propagation assistée par émission stimulée. En particulier, il est important de prendre en compte l'inhibition d'émission par transfert non radiatif vers le métal [87]. Il faut souligner tout l'intérêt du travail présenté au chapitre 3 sur la relaxation moléculaire dans ce contexte.

Publication associée

Ce travail est analysé en détail dans l'article suivant

“Gain assisted propagation in a plasmonic waveguide at telecom wavelength”

J. Grandidier, G. Colas des Francs, S. Massenot, A. Bouhelier, L. Markey, J.-C. Weeber,
C. Finot and A. Dereux
Nano Letters **9**, 2935 (2009).

Gain-Assisted Propagation in a Plasmonic Waveguide at Telecom Wavelength

Jonathan Grandidier, Gérard Colas des Francs,* Sébastien Massenot,
Alexandre Bouhelier, Laurent Markey, Jean-Claude Weeber, Christophe Finot,
and Alain Dereux

Institut Carnot de Bourgogne, UMR 5209 CNRS et Université de Bourgogne, 9,
avenue A. Savary, BP 47870, 21 078 Dijon, France

Received April 24, 2009; Revised Manuscript Received June 16, 2009

ABSTRACT

The spatial confinement of surface plasmon polaritons is a promising route for realizing optical on-board interconnects. However, mode losses increase with the confinement factor. To overcome this road block, we investigate propagation assisted by stimulated emission in a polymer strip-loaded plasmonic waveguide doped with nanocrystals. We achieve 27% increase of the propagation length at telecom wavelength corresponding to a 160 cm^{-1} optical gain coefficient. Such a configuration is a step toward integrated plasmonic amplifiers.

At the interface between molecular optics and solid state physics, molecular plasmonics combines chemical engineering and surface plasmon polaritons (SPPs) properties to produce hybrid materials available for biosensing, data storage, photovoltaic cells, or integrated photonic applications.¹ In particular, the design of a surface plasmon circuitry is the object of intense research due to its ability to transfer optical information on a subwavelength scale. In the last years, a large set of passive plasmonic components were integrated to control and manipulate SPPs in a planar circuitry.² Very recently, the feasibility of using SPP waveguides for achieving 10 Gbit/s chip-to-chip data transfer has been demonstrated.³ Recent works also proposed novel configurations to realize all-optical active SPP functionalities^{4–7} or to utilize quantum effects related with SPPs.⁸ These approaches are however plagued by the existing trade-off between confinement and propagation. To overcome this stringent limitation, strategies are emerging to reduce the intrinsic losses associated to SPP modes existing on metal surfaces. In particular, stimulated emission of surface plasmons exploiting optical pumping of molecular dyes^{9,10} or erbium ions¹¹ was recently demonstrated for weakly confined modes. In this letter, we demonstrate an increase of propagation length for confined SPP modes in dielectric-loaded surface plasmon polariton waveguides (DLSPPWs). A DLSPPW typically consists of a dielectric strip - usually a polymer - deposited on a metal film.¹² Efficient integration of passive components based on this technology was recently demonstrated.^{13,14} These waveguid-

ing structures are characterized by a large confinement factor of the mode inside the polymer structure at the expense of a reduced propagation length.¹⁵ To address this shortcoming, we developed a strategy to partially compensate confinement-induced SPP losses by doping the DLSPPW polymer layer with quantum dots (QDs) nanocrystals undergoing stimulated emission. We therefore take advantage of an efficient overlap between the SPP mode and the active material.

Lead sulfide (PbS) QDs (Evident Technologies, concentration in the waveguide $N \sim 9 \times 10^{16}\text{ cm}^{-3}$) were inserted in a polymethylmethacrylate (PMMA) polymer strip waveguide fabricated on a $40 \pm 3\text{ nm}$ thick gold film using a UV-lithography technique (Figure 1, and Supporting Information). These QDs were chosen for their high photostability and tunability.¹⁶ The waveguide thickness and width were adjusted for single mode operation. This waveguide geometry supports a TM (transverse magnetic)-polarized SPP mode propagating along the guide axis. The magnetic field writes

$$\mathbf{H}(x, y, z) = H_0(x, z)\exp(i(k_{\text{SPP}}y - \omega t)\exp(-y/2L_{\text{SPP}})\mathbf{e}_x \quad (1)$$

where k_{SPP} and L_{SPP} are the wave-vector and attenuation length of the mode, respectively. Experimentally, k_{SPP} and L_{SPP} are evaluated from leakage radiation microscopy images recorded in the Fourier and images planes¹⁵ (Supporting Information). In the image plane, the detected intensity is

$$I(x, y) \propto |\mathbf{H}(x, y, z_0)|^2 = |H_0(x, z_0)|^2 \exp(-y/L_{\text{SPP}}) \quad (2)$$

* Corresponding author. E-mail: gerard.colas-des-francs@u-bourgogne.fr.

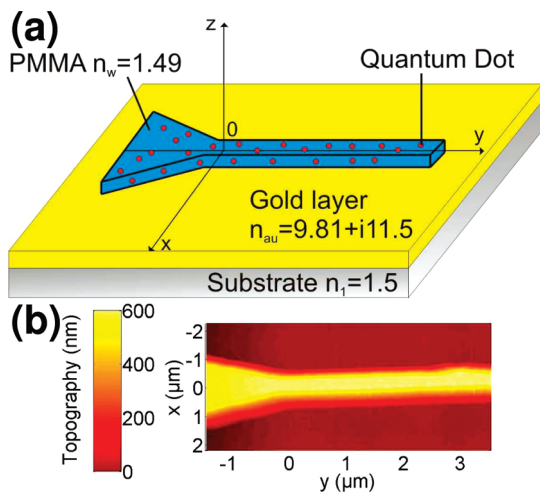


Figure 1. (a) DLSPPW configuration. A PMMA strip confines the plasmon at the gold/polymer interface. An additional tapering structure is designed to efficiently excite the SPP guided mode with an external infrared laser (Figure 3a). The effective indices used in the numerical simulations are indicated on the figure. (b) Atomic force microscopy image of the DLSPPW. The dimensions of the waveguide are 600 nm height, 400 nm width, and 65 μm long.

where z_0 is the objective focal point. Hence, the propagation length L_{SPP} can be readily inferred by measuring the SPP intensity distribution. In the Fourier plane, the recorded signal is

$$I(k_x, k_y) \propto |\tilde{H}(k_x, k_y, z_0)|^2 = \frac{|\tilde{H}_0(k_x, z_0)|^2}{(k_y - k_{\text{SPP}})^2 + (1/2L_{\text{SPP}})^2} \quad (3)$$

where tilde stands for Fourier transform. The intensity recorded in the Fourier plane has a Lorentzian shape centered on the wave-vector of the mode k_{SPP} and with a full-width-at-half-maximum (FWHM) given by $1/L_{\text{SPP}}$.

We first investigated the coupling of QDs emission into waveguide modes (Figure 2). A 532 nm laser was focused on the doped polymer waveguide to pump the QDs in their excited states. The fluorescence emitted around 1500 nm was recorded in the image plane (Figure 2a). A vertical trace extending on either sides of the excitation area indicates a guided mode. Figure 2b shows the modal distribution of effective indices measured in the Fourier plane. The image was obtained for a large excitation area in order to identify all the modes supported by the fabricated structures (see also the inset of Figure 2c). One horizontal line labeled TM_{00} is visible at an effective index $n_{\text{eff}} = k_y/k_0 = 1.18$ (k_0 is the free space wavenumber).¹⁵ This is the signature of a mode propagating inside the DLSPPW with a constant k_y wavevector. Importantly for the following, this mode results from the preferential decay of QDs spontaneous emission into a SPP mode supported by the DLSPPW. The single mode nature of the DLSPPW is evident from Figure 2a,b. Additionally, three arcs of a circle are also visible in Figure 2b, indicating an isotropic propagation of a mode in the surface plane. The inner circle originates from fluorescence coupling to a gold/air SPP mode ($n_{\text{eff}} \sim 1.0$) located on either

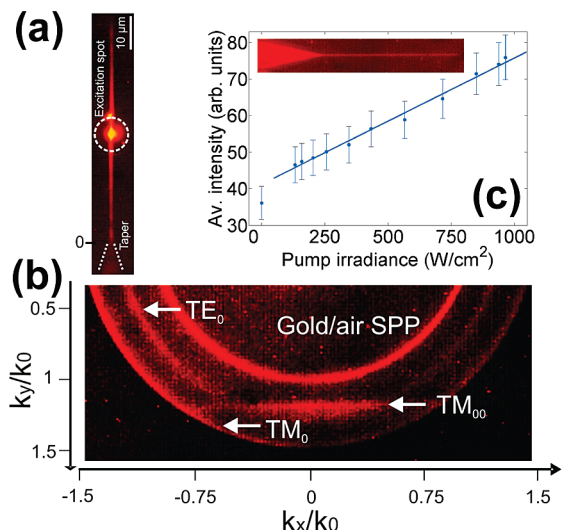


Figure 2. (a) QDs fluorescence (emission wavelength around 1.5 μm) recorded in the image plane. The QDs are excited with a laser ($\lambda = 532 \text{ nm}$, NA = 0.16) focused at the center of the guide (bright spot). Two fluorescence traces extending on both sides of the excitation spot indicates that the emission is coupled to guided modes. (b) QDs fluorescence recorded in the Fourier plane for an extended defocused excitation. The arrows indicate the different effective indices ($n_{\text{eff}} = k_y/k_0$) of the modes existing within the illuminated area. The gold/air SPP mode effective index ($n_{\text{eff}} \sim 1$) and objective numerical aperture (NA = 1.49) were used to calibrate the Fourier plane. The image is saturated for clarity. (c) Averaged spontaneous emission intensity for increasing pump powers (dots, standard deviation indicated) with a linear regression (blue line). The inset shows an homogeneous emission inside the waveguide since an extended illumination was used.

side of the DLSPPW. The two other circles are assigned to film modes existing inside the PMMA tapering region adjacent to the waveguide (Figure 1). Specifically, they are a TM₀ gold/PMMA surface plasmon ($n_{\text{eff}} \sim 1.46$) and a transverse electric TE₀ mode ($n_{\text{eff}} \sim 1.22$) guided into the large tapered PMMA portion. Both TM and TE modes are excited due to the unpolarized emission of the QDs and the multimodal character of the 600 nm thick polymer taper. Using the Differential method,¹⁷ we calculated the effective indices of the detected modes. We obtained $n_{\text{eff}}(\text{TM}_{00}) = 1.18$, $n_{\text{eff}}(\text{TM}_0) = 1.45$, and $n_{\text{eff}}(\text{TE}_0) = 1.20$ at $\lambda = 1.525 \mu\text{m}$ (QDs emission peak) in agreement with the measured values. Finally, Figure 2c shows the QDs spontaneous emission intensity versus pump power. The emission intensity was measured as being the intensity averaged over the complete waveguide homogeneously excited. As expected from spontaneous decay, this signal linearly increases with pump power.

The doped PMMA layer can act as a gain medium for the DLSPPW guided mode if the QDs can undergo stimulated emission into SPPs.¹¹ To this aim, a TM-polarized infrared laser beam ($\lambda = 1.55 \mu\text{m}$) is focused on the tapering region to excite a SPP mode.¹⁸ Figure 3a shows the single-exponential decay of the laser-coupled mode along the waveguide ($L_{\text{SPP}} = 13.6 \pm 0.8 \mu\text{m}$) and its intensity distribution (inset) without pumping the QDs. Because of QDs absorption, L_{SPP} is slightly lower than the propagation length measured in an undoped (passive) waveguide (L_{SPP}

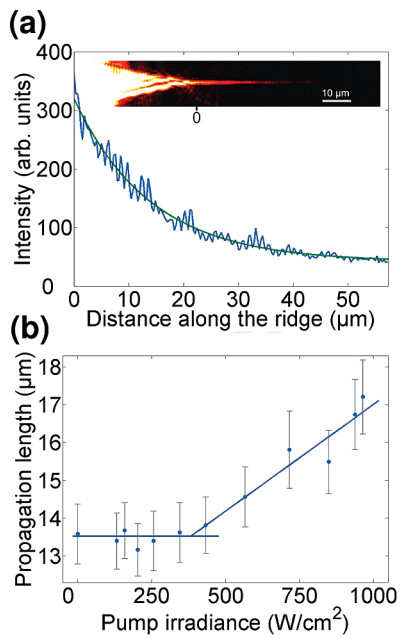


Figure 3. (a) Attenuation length of the SPP mode inside the DLSPPW measured in absence of QDs pumping (blue curve). The data can be fitted by a single exponential decay of the form of eq 2 (green curve) with a decay constant of $13.6 \mu\text{m}$. Inset: Image of the intensity distribution of the mode inside the waveguide. The SPP guided mode is excited by focusing an infrared laser beam ($\lambda = 1.55 \mu\text{m}$) onto the tapering region. (b) Propagation length measured for increasing pump irradiance ($\lambda = 532 \text{ nm}$) at constant IR laser power (dots). The blue curve is a guide for the eyes.

$= 14.1 \pm 0.5 \mu\text{m}$) with the same dimensions. We note that this difference is small due to the low concentration of QDs within the waveguide ($N \sim 9 \times 10^{16} \text{ cm}^{-3}$ corresponding to a volume fraction $f = 7$ per thousand). This low propagation length originates from strong radiative losses. This allows rapid investigation by leakage radiation microscopy, limiting thus QDs photobleaching.

To investigate the influence of the pumped QDs on the SPP guided mode, the waveguide is homogeneously excited by the 532 nm pump beam (see Figure S2 of Supporting Information). Figure 3b presents the fitted propagation lengths $L_{\text{SPP}}(I_p)$ as a function of pump irradiance I_p . The propagation length remains constant around $13.5 \mu\text{m}$ for pump irradiance below $500 \text{ W}\cdot\text{cm}^{-2}$ and increases up to $17.2 \pm 1 \mu\text{m}$ for $1000 \text{ W}\cdot\text{cm}^{-2}$, exceeding the propagation length of the undoped waveguide. This 27% net gain cannot be solely explained by a thermal variation of the optical index of the PMMA,⁴ suggesting a contribution of stimulated emission of SPPs.^{9–11} A signature of stimulated emission is a spectral narrowing of the emitted light.¹⁰ To check this, we used a single-mode fiber-coupled spectrograph working at room temperature. Unfortunately, the combination of coupling losses, weak signal-to-noise ratio at ambient temperature and limited acquisition time (photobleaching) prevented an unambiguous demonstration of a spectral narrowing.

Nevertheless, stimulated emission was qualitatively confirmed by a line width narrowing of the effective index of the DLSPPW mode. Stimulated emission of SPP can be

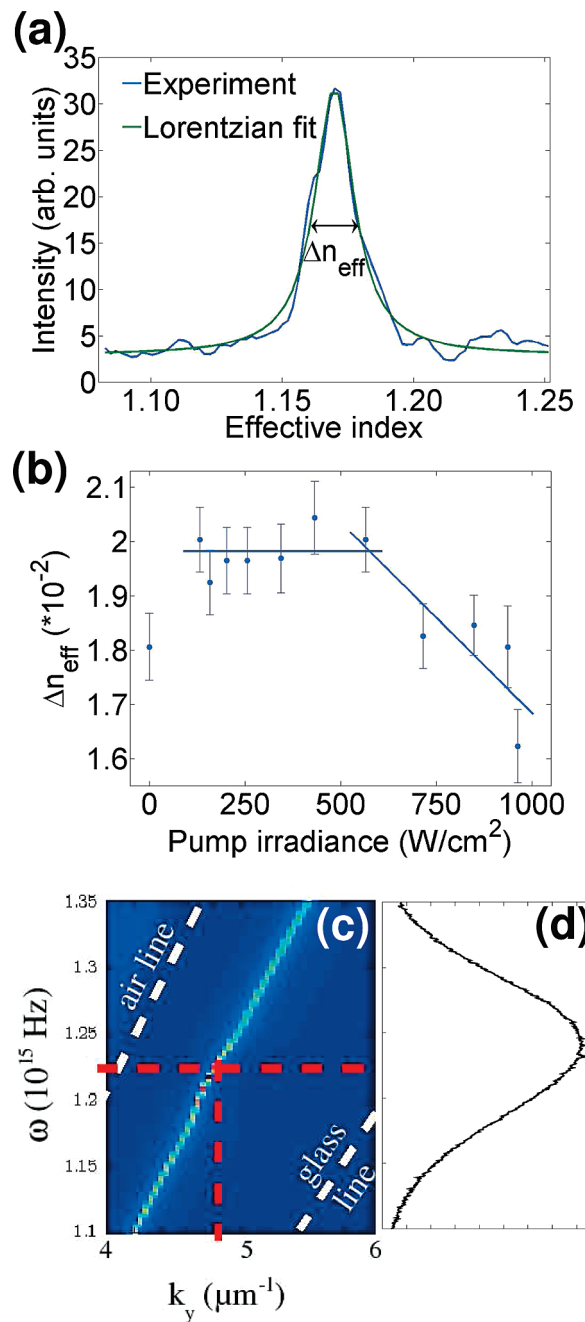


Figure 4. (a) Effective index line width of the DLSPPW mode measured in the Fourier plane without QDs excitation (blue curve). The line width is well approximated by a Lorentzian fit (green curve, see also eq 3). (b) Full-width-half-maximum (FWHM) of the effective index variation Δn_{eff} versus pump irradiance. (c) Density of mode calculated as a function of wave vector k_y and free space frequency ω . Red dotted lines correspond to $\lambda = 1.55 \mu\text{m}$ excitation. (d) QDs emission spectrum. Comparing panels c and d, we see that the mode wave-vector varies from $k_y = 4.5 \mu\text{m}^{-1}$ ($n_{\text{eff}} = 1.17$) to $k_y = 5.4 \mu\text{m}^{-1}$ ($n_{\text{eff}} = 1.24$) on QDs emission spectrum FWHM.

either investigated in frequency space at a fixed mode momentum or in momentum space at a fixed frequency (see, e.g., Figure 2 of ref 10). On the basis of a Fourier analysis of the mode propagation, we report in Figure 4 the effect of stimulated emission on the effective index line width. The stimulated emission is associated with a narrowing of the coupled wave-vectors because the resulting mode is strictly

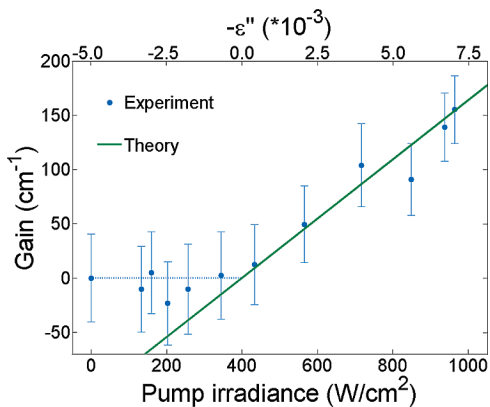


Figure 5. Intrinsic optical gain coefficient $g = [1/L_{\text{SPP}}(0) - 1/L_{\text{SPP}}(I_p)]$ measured versus pump irradiance (blue dots, bottom scale) or calculated as a function of the imaginary part ϵ'' of the DLSPPW dielectric constant (green line, top scale).

identical to the SPP mode responsible for the stimulation. Below the transparency threshold (population inversion), the mode width is mainly governed by the large QDs emission spectrum so that the effective index width remains approximately constant for pump powers below $500 \text{ W}\cdot\text{cm}^{-2}$ (Figure 4b). More precisely, Figure 4c represents the density of modes calculated in the QDs emission spectrum range, revealing the dispersion relation $\omega = f(k_y)$.¹⁹ For low pumping power, the QDs spontaneous emission couples to the DLSPPW mode with a large spectrum, leading to an effective index broadening (see also Supporting Information). When the population inversion is achieved, stimulated emission increases the amount of energy coupled into the mode propagating at $\lambda = 1.55 \mu\text{m}$. Figure 4b clearly shows a decrease of the effective index line width above $500 \text{ W}\cdot\text{cm}^{-2}$. This line width narrowing indicates that stimulated emission of SPP^{10,11} occurs in conjunction with a net increase of L_{SPP} (Figure 3b). Importantly, the observed narrowing of the effective index comes from two contributions, which are not independent. The first contribution originates from a compensation of the losses. Reducing the losses strongly narrows the mode line width since $\Delta k_{\parallel}(\lambda) = 1/L_{\text{SPP}}(\lambda)$. The second contribution is the result of a decrease in the contribution of the spontaneous decay channel in favor of the stimulated emission channel.

Finally, the optical gain coefficient $g = [1/L_{\text{SPP}}(0) - 1/L_{\text{SPP}}(I_p)]$ is reported versus pump irradiance in Figure 5. g was compared to numerical simulations obtained by imposing negative values to the imaginary part ϵ'' of the waveguide dielectric constant. The gold layer thickness was adjusted to 35 nm so that the propagation length calculated for $\epsilon'' = 0$ equalizes the one measured without pump. The small difference with the experimental thickness (40 nm) is explained by additional extrinsic radiative losses due to scattering by gold roughness and PbS nanocrystals. ϵ'' can be estimated¹⁰ from the QDs density ($N \sim 9 \times 10^{16} \text{ cm}^{-3}$), their emission rate ($\gamma \sim 10^6 \text{ s}^{-1}$), their absorption ($\sigma_a = 4.3 \times 10^{-15} \text{ cm}^2$), and their stimulated emission (σ_{st}) cross sections. σ_{st} is an unknown parameter and was adjusted at $3 \times 10^{-15} \text{ cm}^2$ to reproduce the experimental gain at $1000 \text{ W}\cdot\text{cm}^{-2}$. This value is probably underestimated due to

emission quenching near the metal so that more refined models should be considered.²⁰ Nonetheless, the experimental optical gain is qualitatively well reproduced by the theoretical curve above the transparency threshold ($\sim 500 \text{ W}\cdot\text{cm}^{-2}$).

In conclusion, our experimental results unambiguously demonstrate the occurrence of a surface plasmon polariton optical gain by stimulated emission of SPPs in a waveguiding architecture. The gain obtained partially compensates the losses introduced by confining a plasmon. While this does not constitute an amplification, several strategies are possible to realize a plasmonic amplifier. Optical gain in PbS quantum dots is limited due to the 8-fold degeneracy of the first excited states requiring at least four excitons for population inversion.²¹ An optimized gain medium as well as thicker gold films (reduced SPP radiative losses) would certainly contribute to enhance the optical gain. Finally, different strategies for active pumping can also be investigated such as semiconductor electrical pumping.^{22,23} The realization of integrated plasmonics amplifiers could represent a key step toward miniaturized all-optical on-board interconnects.

Acknowledgment. We acknowledge fruitful discussions with S. Bozhevolnyi (University of Southern Denmark), V. Loriot (University of Bourgogne), A. Zayats (University of Belfast), and technical support by G. Bosak from Evident Technologies. This work was supported by the European Community (project PLASMOCOM, EC-FP6 IST 034754 STREP).

Supporting Information Available: Doped waveguide fabrication, leakage radiation microscopy setup, and detailed discussion of effective index broadening. This material is available free of charge via the Internet at <http://pubs.acs.org>.

References

- Van Duyne, P. *Science* **2004**, *306*, 985–986.
- Ebbesen, T.; Genet, C.; Bozhevolnyi, S. *Phys. Today* **2008**, *61*, 44–50.
- Kim, J. T.; Ju, J. J.; Park, S.; Kim, M.; Park, S. K.; Lee, M. H. *Opt. Express* **2008**, *16*, 13133–13138.
- Lereu, A. L.; Passian, A.; Goudonnet, J.-P.; Thundat, T.; Ferrell, T. L. *Appl. Phys. Lett.* **2005**, *86*, 154101.
- Dintinger, J.; Klein, S.; Ebbesen, T. *Adv. Mater.* **2006**, *18*, 1267–1270.
- Wiedermann, G. P.; Hall, J. E.; Bouhelier, A. *Phys. Rev. Lett.* **2007**, *98*, 83801.
- Pacifci, D.; Lezec, H. J.; Atwater, H. A. *Nat. Photonics* **2007**, *1*, 402–406.
- Bergman, D.; Stockman, M. *Phys. Rev. Lett.* **2003**, *90*, 27402.
- Seidel, J.; Grafström, S.; Eng, L. *Phys. Rev. Lett.* **2005**, *94*, 177401.
- Noginov, M. A.; Zhu, G.; Mayy, M.; Ritzo, B. A.; Nogovina, N.; Podolskiy, V. A. *Phys. Rev. Lett.* **2008**, *101*, 226806.
- Ambati, M.; Nam, S. H.; Ulin-Avila, E.; Genov, A.; Bartal, G.; Zhang, X. *Nano Lett.* **2008**, *8*, 3998–4001.
- Hohenau, A.; Krenn, J. K.; Stepanov, A. L.; Drezen, A.; Ditlbacher, H.; Steinberger, B.; Leitner, A.; Aussene, F. R. *Opt. Lett.* **2005**, *30*, 893–895.
- Krasavin, A. V.; Zayats, A. *Phys. Rev. B* **2008**, *78*, 45425.
- Holmgård, T.; Chen, Z.; Bozhevolnyi, S. I.; Markey, L.; Dereux, A.; Krasavin, A. V.; Zayats, A. V. *Appl. Phys. Lett.* **2009**, *94*, 51111.
- Grandidier, J.; Massenot, S.; Colas des Francs, G.; Bouhelier, A.; Weeber, J. C.; Markey, L.; Dereux, A.; Renger, J.; Gonzalez, M. U.; Quidant, R. *Phys. Rev. B* **2008**, *78*, 245419.
- Klimov, V. I.; Mikhailovsky, A. A.; Xu, S.; Malko, A.; Hollingsworth, J. A.; Leatherdale, C. A.; Eisler, H. J.; Bawendi, M. G. *Science* **2000**, *290*, 314–316.

- (17) Massenot, S.; Weeber, J. C.; Bouhelier, A.; Colas des Francs, G.; Grandidier, J.; Markey, L.; Dereux, A. *Opt. Express* **2008**, *16*, 17599–17608.
- (18) Holmgard, T.; Bozhelvolnyi, S.; Markey, L.; Dereux, A. *Appl. Phys. Lett.* **2008**, *92*, 11124.
- (19) Manjacas, A.; Garcia de Abajo, F. J. *Nano Lett.* **2009**, *9*, 1285–1289.
- (20) De Leon, I.; Berini, P. *Phys. Rev. B* **2008**, *78*, 161401(R).
- (21) Hoogland, S.; Sukhovatkin, V.; Howard, I.; Cauchi, S.; Levina, L.; Sargent, E. H. *Opt. Express* **2006**, *14*, 3273–3281.
- (22) Sirtori, C.; Gmachl, C.; Capasso, F.; Faid, J.; Sivco, D. L.; Hutchinson, A. L.; Cho, A. Y. *Opt. Lett.* **1998**, *23*, 1366–1368.
- (23) Kumar, P.; Tripathi, V. K.; Liu, C. S. *J. Appl. Phys.* **2008**, *104*, 33306.

NL901314U

Supplementary Information for

Gain assisted propagation in a plasmonic waveguide at telecom wavelength

Jonathan Grandidier, Gérard Colas des Francs, Sébastien Massenot, Alexandre Bouhelier, Laurent Markey, Jean-Claude Weeber, Christophe Finot and Alain Dereux*

Institut Carnot de Bourgogne, UMR 5209 CNRS et Université de Bourgogne, 9, av. A. Savary, BP 47870, 21 078 Dijon, France

*Corresponding author. E-mail: gerard.colas-des-francs@u-bourgogne.fr

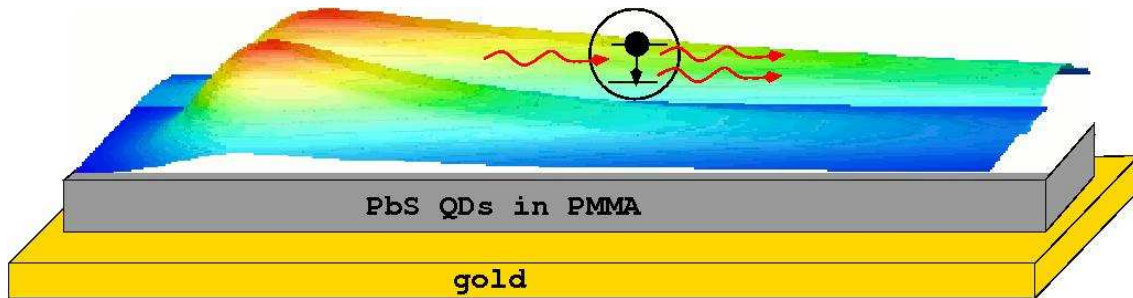


Figure S1 Concept of plasmon loss compensation in confined geometry. The intensity distribution of a plasmon propagating in a QDs doped DLSPPW is calculated when QDs are in their fundamental (front) or are optically pumped to an excited state (back). Stimulated emission of SPPs significantly increases the mode propagation length.

Figure S1 schematically describes the plasmon propagation assisted by stimulated emission investigated in this letter. A plasmon mode propagates along a gold surface and is laterally confined by a PMMA

strip doped with PbS nanocrystals. The intensity is calculated 50 nm above the waveguide with the Differential method¹ for a passive ($\epsilon''=0$) and gain ($\epsilon''=-0.007$) medium. When the QDs are optically pumped, stimulated emission of SPP significantly increases the propagation length of the guided SPP.

Doped DLSPPW fabrication

A dielectric-loaded surface plasmon polariton waveguide doped with PbS nanocrystals is fabricated on a gold film by deep UV lithography according to the following process. A stock solution of PMMA/QDs is first prepared by dissolving 600 μ L of PbS solution (10 mg/mL, toluene solvent, Evident Technologies) into 2.4 mL of PMMA solution (4% w/w in chlorobenzene). Since the toluene dissolves efficiently the PbS nanocrystals and does not phase separate with chlorobenzene, an homogeneous dispersion of the QDs into the PMMA solution is obtained. A 40-nm thick gold film is then prepared by thermal evaporation onto a glass cover slip. A 600 nm thick PMMA/QDs film is then deposited by a two-step spin coating process (1800 rpm, thermal annealing at 170 °C after each spin coating). The 400 nm width waveguides were prepared by deep UV exposure (250 nm wavelength, 1900 mJ/cm²) using a vacuum contact mask aligner (Süss Microtech MJB4) and a commercial chromium mask (Photronics), followed by a chemical development.

Characterization of the mode linewidth in the Fourier plane

Figure S2 schematically represents the leakage radiation microscopy setup. Apart from imaging in the direct plane, it is also possible to investigate the mode propagation in the Fourier plane.

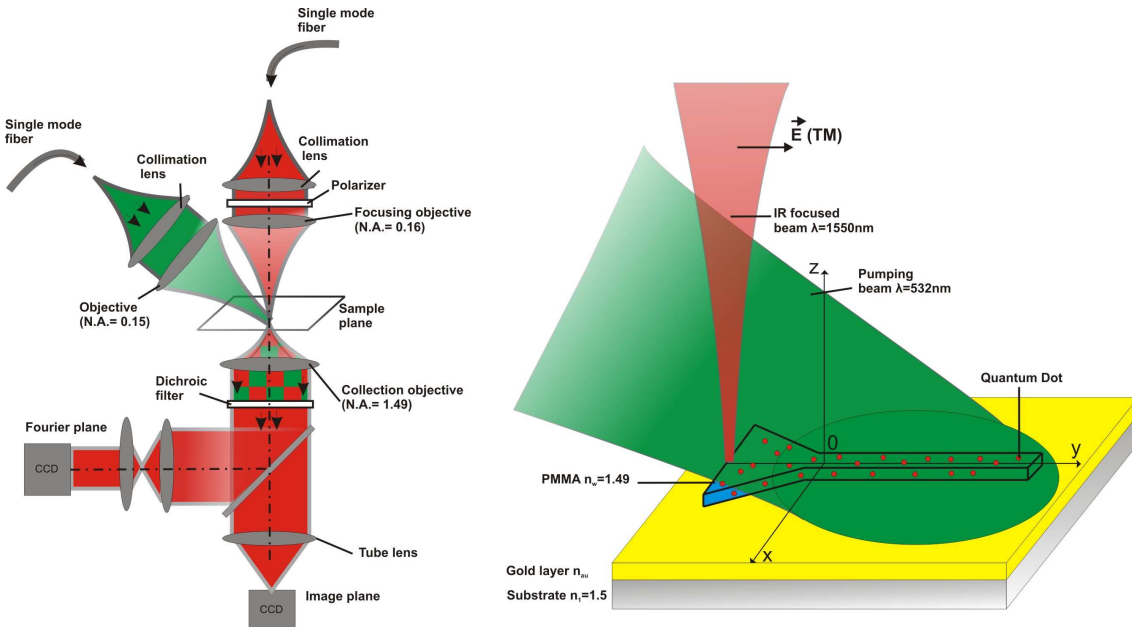


Figure S2 Leakage radiation microscopy setup. The DLSSPW is excited with an infrared laser beam focused on the PMMA tapering portion. A 532 nm laser pump the QDs in their excited state. The signal transmitted below the surface is recorded in the image and Fourier plane at near infrared frequencies. We used a cooled charge-coupled device (CCD) camera to obtain well-defined leakage radiation microscopy images.

Strictly speaking, the signal recorded in the Fourier plane is the Fourier transform of the signal recorded in the image plane as reported in eq. (2) and (3) of the letter. More precisely, direct comparison of eq. (2) and (3) shows that the FWHM Δn_{eff} in the effective index plane is related to the mode propagation length L_{SPP} measured in the image plane at a given wavelength λ by

$$L_{\text{SPP}} = \lambda / (2\pi\Delta n_{\text{eff}}) \quad (\text{S1}).$$

This relation is satisfied for $\lambda = 1.55 \mu\text{m}$ as can be seen from Fig. 3 ($L_{\text{SPP}} = 13.5 \mu\text{m}$) and Fig. 4 ($\Delta n_{\text{eff}} = 1.8 \cdot 10^{-2}$) of the letter.

We propose here to link the signal recorded in the wave-vector plane to the frequency spectrum. This is made possible by the dispersion of the mode $\omega_{\text{SPP}} = f(k_{\parallel})$ relating mode frequency to wave-vector.

Figure 4c in the letter represents the DLSPPW mode dispersion relation. For simplicity, we assume that both QDs emission spectrum $F(\omega)$ and the recorded intensity in the Fourier Plane $I(\omega, k_{\parallel})$ have Lorentzian shapes:

$$F(\omega) = \frac{\Delta\omega}{(\omega - \omega_{\text{fluo}})^2 + \Delta\omega^2} \quad (\text{S2})$$

$$I(\omega, k_{\parallel}) = \frac{\Delta\omega(k_{\parallel})}{[\omega - \omega_{\text{SPP}}(k_{\parallel})]^2 + \Delta\omega(k_{\parallel})^2} \quad (\text{S3})$$

where ω_{fluo} is the emission peak of the QDs.

Therefore, QDs decay into DLSPPW modes is a convolution of these two Lorentzians²,

$$I(k_{\parallel}) = \int d\omega F(\omega) I(\omega, k_{\parallel}) = \frac{\Delta\omega + \Delta\omega(k_{\parallel})}{[\omega_{\text{fluo}} - \omega_{\text{SPP}}(k_{\parallel})]^2 + [\Delta\omega + \Delta\omega(k_{\parallel})]^2} \quad (\text{S4}).$$

Since we characterized the waveguide mode in the effective index plane (Fourier plane), it is useful to rewrite Eq. (S4) as a function of k_{\parallel} . To this aim, using the group velocity of the mode v_g , we approximate the dispersion relation to

$\omega_{\text{SPP}}(k_{\parallel}) = \omega_{\text{fluo}} + v_g [k_{\parallel} - k_{\parallel}(\omega_{\text{fluo}})]$ near the QDs emission wavelength so that Eq. S4 becomes

$$I(k_{\parallel}) = \frac{\Delta\omega + \Delta\omega(k_{\parallel})}{v_g^2 [k_{\parallel} - k_{\parallel}(\omega_{\text{fluo}})]^2 + [\Delta\omega + \Delta\omega(k_{\parallel})]^2} \quad (\text{S5})$$

$I(k_{\parallel})$ has also a Lorentzian shape in the momentum plane. Let us note that the QDs emission is better fitted with a Gaussian profile so that the convoluted intensity is a Voigt profile, which is not analytical. However, the above discussion gives a physical understanding of the signal recorded in the Fourier plane and roughly explains the effective index broadening measured in Fig. 4b below the transparency threshold.

References

1. Grandidier, J.; Massenot, S.; Colas des Francs, G.; Bouhelier, A.; Weeber, J.C.; Markey, L.; Dereux, A.; Renger, J.; Gonzalez, M.U.; Quidant R. *Physical Review B* **78**, 245419 (2008).
2. Chang, S.W.; Adrian Ni, C.Y.; Chuang, S.L. *Optics Express* **16**, 10580-10595 (2008).

4.3 Modélisation de la résonance

Dans le paragraphe précédent, nous avons caractérisé l'émission stimulée par la largeur de la résonance du mode guidé (Fig. 4.2b). En effet, de nombreux phénomènes de résonance suivent un profil lorentzien. Un cas bien connu en physique du solide est un défaut électronique localisé. On peut montrer que la densité d'états électroniques suit alors un profil dit de Breit-Wigner (lorentzien), en fonction de l'énergie. Ce profil caractérise le canal de diffusion électronique induit par la présence de l'impureté. Très récemment, nous nous sommes appuyés sur l'analogie entre les formalismes décrivant la diffusion multiple d'électrons ou d'ondes électromagnétiques pour démontrer que la densité de modes supportés par un guide suit profil similaire [83].

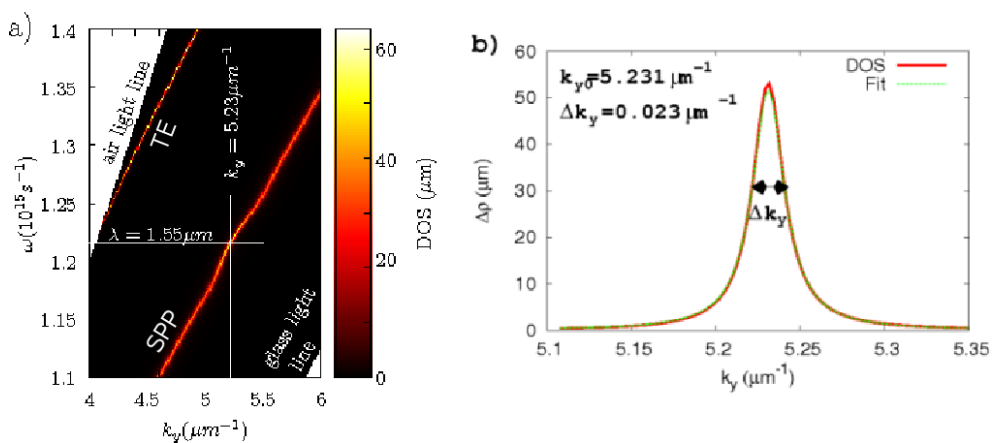


FIG. 4.6 – (a) DOS d'un guide DLSPPW en fonction de la fréquence ω et de la constante de propagation k_y . b) Coupe à ω fixée (correspondant à $\lambda = 1,55\mu m$). La courbe “Fit” est une lorentzienne avec les paramètres indiqués sur la figure.

La figure 4.6a) représente la relation de dispersion d'un DLSPPW déduite de la densité de modes guidés (DOS, density of states) autour de la longueur d'onde telecom. Le mode fondamental est le mode plasmon, noté *SPP* et un second mode, transverse électrique TE_{00} est supporté par le guide au-dessus de $\omega = 1.23 \times 10^{15} s^{-1}$ ($\lambda = 1.53\mu m$). A fréquence fixée, la DOS suit un profil lorentzien, centré sur la constante de propagation k_{y0} du mode et de largeur à mi-hauteur $\Delta k_y = 1/L_{SPP}$, où L_{SPP} est la longueur de propagation du plasmon guidé (Fig. 4.6b). Une comparaison directe avec l'intensité mesurée dans le plan de Fourier en microscopie des fuites radiatives est possible (comparer avec l'insert de la figure 4.5b).

Toutefois, en cas d'excitation non monochromatique du guide, la forme de la résonance mesurée dans le plan de Fourier est plus complexe. Par exemple lors de l'étude du gain au paragraphe précédent, le couplage de l'émission spontanée des QDs avec le guide conduit à un élargissement de la résonance. Ce point est discuté dans le *Supplementary Information* du Nano Letters reproduit à la fin du paragraphe précédent.

Publication correspondante

“Integrated plasmonic waveguides : a mode solver based on DOS formulation”

G. Colas des Francs, J. Grandidier, S. Massenot, A. Bouhelier, J-C. Weeber and A. Dereux
Physical Review B, accepté pour publication (2009).

Integrated plasmonic waveguides: a mode solver based on density of states (DOS) formulation

Gérard Colas des Francs ^{*}, Jonathan Grandidier, Sébastien Massenot[†],

Alexandre Bouhelier, Jean-Claude Weeber and Alain Dereux

*Institut Carnot de Bourgogne, UMR 5209 CNRS - Université de Bourgogne,
9 Av. A. Savary, BP 47 870, 21078 Dijon, FRANCE*

Abstract

We express the density of states (DOS) near guided resonances of plasmonic waveguides by using multiple scattering theory. In direct analogy with the case of localised electronic defect states in condensed matter, we demonstrate that optical DOS variations follow a lorentzian profile near guided modes resonances. The lorentzian shape gives quantitative informations on the guided modes (effective index, propagation length and polarization state). We numerically investigate both leaky and bound (lossy) modes supported by dielectric-loaded surface plasmon polariton waveguides.

PACS numbers: 73.20.Mf, 42.25.Bs, 73.21.-b, 42.82.Et

^{*} Electronic Address: gerard.colas-des-francs@u-bourgogne.fr

[†] present address Institut Supérieur de l'Aéronautique et de l'Espace, Toulouse, France

I. INTRODUCTION

Optical integrated circuits (OICs) are widely used since the 1960's due to their high ability for data communications at small cost. A widely used configuration consists of a strip of dielectric material deposited on top of a planar waveguide. This structure is called a strip-loaded waveguide. The dielectric strip leads to a lateral mode confinement into the planar waveguide [1]. Since the mode does not overlap the loading strip boundaries, scattering losses by the strip corners are limited. Moreover, depending on the dielectric material (polymer, semi-conductor, non linear glass, ...), various optical devices are achievable [1]. In addition, metallic electrodes can also be used as loading striplines with useful applications for designing electro-optical devices [1]. Recently, the concept of dielectric loaded surface plasmon-polariton waveguide (DLSPPW) has been proposed. This configuration, comprised of a dielectric material strip deposited onto a metal film, optimizes the opportunities of combining electrical and optical properties [2–4]. Very recently, we demonstrated loss compensation in strongly confined DLSPPW, in direct analogy with integrated optical amplifier [5]. To this purpose, the dielectric load was made of a polymer strip doped with quantum dots, and played the role of gain medium under optical pumping. Other dielectric materials have to be developed to manage all-optical integrated devices. In particular, ultra-fast photonic circuits can be achieved using non-linear materials such as chalcogenide glasses [6]. These glasses have high-linear indices, so that chalcogenide-DLSPPW support bound modes. However, these bound modes are not easily accessible using e.g differential method which was recently adapted to the DLSPPW configuration [7].

Therefore, we develop here a mode solver based on density of states formulation, available for two-dimensional (2D) waveguides of arbitrary shape and nature. This formulation is directly inspired by the study of localised electronic defects and impurities in condensed matter. Indeed, the electronic density of states presents then a Breit-Wigner (lorentzian) form near scattering resonances, characterizing the scattering channel involved in the process [8]. We will profit here of the strong analogy between light and electronic scattering formalism [9, 10] to fully characterize a guided mode throughout the optical density of states associated to the waveguiding structure.

The paper is organized as follows. Section II will present the theoretical framework. Numerical simulations are reported in section III for the example of a leaky mode already

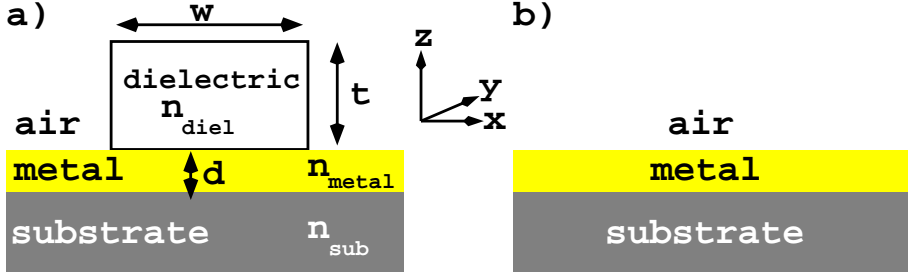


FIG. 1: (color online) a) DLSPPW configuration. A dielectric ridge (thickness t , width w , optical index $n_{\text{diel}} = (\epsilon_{\text{diel}})^{1/2}$) is deposited on a metal film of thickness d and optical index $n_{\text{metal}} = (\epsilon_{\text{metal}})^{1/2}$. The substrate index is $n_{\text{sub}} = (\epsilon_{\text{sub}})^{1/2}$. b) Reference system: substrate/metal/air slab. See text for details.

extensively investigated in the literature. Finally, section IV considers bound modes supported by a high index material.

II. THEORETICAL BACKGROUND

The main idea of this paper is to work with the optical density of states (DOS) of the waveguiding structure. In this first section, we briefly summarize DOS definition and properties, useful for characterizing integrated photonic waveguides. Without loss of generality, we focus on the DLSPPW configuration, described in Fig. (1a). A dielectric load locally modifies the optical index near a metallic film deposited on a substrate. Such a configuration is well-known to support a surface plasmon polariton mode, laterally confined at the metal/dielectric interface [2, 3]. Due to the translational invariance along y -axis, the wavevector component k_y is a constant of the system, that characterizes a guided mode. The electromagnetic density of states $\rho(k_y; \omega)$ is the density of electromagnetic modes in the wavevector interval $[k_y, k_y + dk_y]$ at fixed frequency ω . Since $v = k_y^2$ is the eigenvalue of the wave equation, it is easier to work with $\tilde{\rho}(k_y^2; \omega) = (2k_y)^{-1}\rho(k_y; \omega)$ that is related to the wave equation kernel (2D-Green's dyad) \mathbf{G} associated to the system by [9, 11, 12]

$$\tilde{\rho}(k_y^2; \omega) = -\frac{1}{\pi} \text{Im} \text{Tr} [\epsilon \mathbf{G}(k_y; \omega)] = \frac{d}{dv} \left\{ \frac{1}{\pi} \text{Im} \ln [\det \epsilon \mathbf{G}(k_y; \omega)] \right\}. \quad (1)$$

This relation has to be manipulated with care since it holds only in region where $\epsilon(\mathbf{r})$ does not change sign so that Sturm-Liouville theory applies [13]. Since metallic film possesses a negative dielectric constant, it is convenient to restrict the domain of investigation on the

dielectric strip only. Moreover, the Dyson's equation expresses the Green's dyad \mathbf{G} of any arbitrary system as a function of the Green's dyad \mathbf{G}_{ref} of a reference system [12]

$$\mathbf{G} = [\mathbf{I} - \mathbf{G}_{ref}V]^{-1}\mathbf{G}_{ref}, \quad (2)$$

where $V = k^2(\epsilon_{ref} - \epsilon_{obj})$ represents the perturbation due to the object ($k = \omega/c$). In our case, we choose the substrate/metal/air slab system described in Fig. (1b) as the reference system, so that $V = k^2(1 - \epsilon_{diel})$ inside the dielectric strip and is nul elsewhere. Then, the variation of DOS due to the guiding structure can be written as [14]

$$\begin{aligned} \Delta\tilde{\rho}(k_y^2; \omega) &= \tilde{\rho}(k_y^2; \omega) - \tilde{\rho}_{ref}(k_y^2; \omega) \\ &= -\frac{1}{\pi} \frac{d}{dv} Imln[D(k_y; \omega)], \text{ with} \end{aligned} \quad (3)$$

$$D(k_y; \omega) = \det[\mathbf{I} - \mathbf{G}_{ref}V]. \quad (4)$$

The presence of V in eq. (4) indicates an implicit integration over the perturbation surface. Applying then standard procedure for multiple scattering description, one can demonstrate that the DOS variation has a lorentzian shape near a resonance [8]. For this purpose, we express DOS variations in term of the scattering phase shift $\theta(k_y; \omega) = -\arg[D(k_y; \omega)]$:

$$\Delta\tilde{\rho}(k_y^2; \omega) = \frac{1}{\pi} \frac{d\theta}{dv}. \quad (5)$$

This expression is analogous to the electronic DOS derivation $n(E) = dN(E)/dE$ with $N(E)$ being the number of electronic modes at the energy E . Therefore, θ/π can be seen as the number of electromagnetic modes created in presence of the guiding structure. Due to a change of Riemann sheet, θ varies of π around $Re[D(k_y; \omega)] \approx 0$. After a Taylor expansion of $Re[D(k_y; \omega)]$ near $v_0 = k_{y0}^2$, we obtain, following a procedure similar to that described in ref. [8]

$$\begin{aligned} \Delta\tilde{\rho}(k_y^2; \omega) &\approx \frac{g}{\pi} \frac{\Gamma/2}{(k_y^2 - k_{y0}^2)^2 + (\Gamma/2)^2}, \text{ with} \\ \Gamma &= 2 \frac{ImD(k_y; \omega)}{[dReD(k_y; \omega)/dv]_{v_0}}, \end{aligned} \quad (6)$$

where g is the waveguide degeneracy at ω and k_{y0}^2 . Remembering that $v = k_y^2$, we can now express the DOS variation $\Delta\rho(k_y; \omega) = 2k_y\Delta\tilde{\rho}(k_y^2; \omega)$ near a resonance

$$\Delta\rho(k_y; \omega) \approx \frac{2gk_{y0}}{\pi} \frac{\Gamma/2}{(k_y^2 - k_{y0}^2)^2 + (\Gamma/2)^2}, \quad (7)$$

$$\approx \frac{g}{\pi} \frac{\Delta k_y/2}{(k_y - k_{y0})^2 + (\Delta k_y/2)^2}, \text{ with } \Delta k_y = \frac{\Gamma}{2k_{y0}} \quad (8)$$

where we use $(k_y^2 - k_{y0}^2) \approx 2k_{y0}(k_y - k_{y0})$ near k_{y0} [15].

To summarize, the variation of the density of states presents a lorentzian form near a guided wavector resonance k_{y0} , in exact analogy with the Breit-Wigner (lorentzian) profile followed by the *electronic* density of states in presence of a localised electronic defect. The optical resonance full width at half maximum (FWHM) Δk_y gives the mode propagation length $L_{SPP} = 1/\Delta k_y$. Additionnally, the number of supported mode is $N(\omega) = \int dk_y \Delta\rho(k_y; \omega) = g$. Obviously, the density of created modes is maximum at the resonance and is $\Delta\rho(k_{y0}, \omega) = 2gL_{SPP}/\pi$. In case of DLSPPW configuration, this simple relation shows that *a mode can be supported if and only if its propagation length is long enough* since the collective oscillation of electrons has to establish. Equivalently, the DOS variations can be expressed as a function of ω [16]. The maximum DOS difference expresses then $\Delta\rho(k_{y0}, \omega_0) = 2g\tau/(\pi v_g)$, where τ is the mode lifetime and $v_g = \frac{\partial\omega}{\partial k_y}$ is the mode group velocity. Again, this means that the mode need sufficient time to establish (see also section 9.4.1 of ref. [17]).

Knowing the mode wavector k_{y0} and propagation length L_{SPP} , the mode electric field is computed thanks to the Green's dyad as

$$\mathbf{E}(r_{//}, t) = \mathbf{E}_{2D}(r_{//}) e^{i(k_{y0}y - \omega t)} e^{-y/L_{SPP}}, \text{ with} \quad (9)$$

$$\mathbf{E}_{2D}(\mathbf{r}_{//}) = \mathbf{G}(\mathbf{r}_{//}, \mathbf{r}_{//}^0, k_{y0}) \cdot \mathbf{p} - \mathbf{G}_0(\mathbf{r}_{//}, \mathbf{r}_{//}^0, k_{y0}) \cdot \mathbf{p} \quad (10)$$

where $\mathbf{r}_{//} = (x, z)$ represents the coordinates in the (XZ) plane and \mathbf{p} is a 2D dipoles line source, located at an arbitrary place $\mathbf{r}_{//}^0$ near the waveguide, used to excite the mode. $\mathbf{G}_0(\mathbf{r}_{//}, \mathbf{r}_{//}^0, k_{y0})$ is the free-space Green's dyad so that the second term in the right hand side of eq. (10) removes the excitation field and expression (10) gives the mode field only.

It is worth noting that we do not use expression (3) to evaluate DOS difference since it leads to numerical instabilities because of the difficulty to properly choose the Riemann sheet where the scattering phase shift $\theta(k_y, \omega)$ is defined. Instead, we go back to the generic expression (1). Practically, DOS variation in presence of the waveguide is numerically calculated by

$$\Delta\rho(k_y; \omega) = -\frac{2k_y}{\pi} \text{Im} \int d\mathbf{r}_{//} [\epsilon(\mathbf{r}_{//}) \mathbf{G}(\mathbf{r}_{//}, \mathbf{r}_{//}, k_y, \omega) - \epsilon_{ref}(\mathbf{r}_{//}) \mathbf{G}_{ref}(\mathbf{r}_{//}, \mathbf{r}_{//}, k_y, \omega)], \quad (11)$$

Since we are interested in the waveguide modes, *confined inside the object*, we can limit the integration to the object only [12]. Last, due to the vectorial nature of the electromagnetic

field, one interestingly defined *partial* DOS variations as [18, 19]

$$\Delta\rho_i(k_y; \omega) = -\frac{2k_y}{\pi} \text{Im} \int d\mathbf{r}_{//} [\epsilon(\mathbf{r}_{//})G_{ii}(\mathbf{r}_{//}, \mathbf{r}_{//}, k_y, \omega) - \epsilon_{ref}(\mathbf{r}_{//})G_{ref,ii}(\mathbf{r}_{//}, \mathbf{r}_{//}, k_y, \omega)], (i = x, y, z). \quad (12)$$

The Green's dyad is numerically calculated as described in ref. [20].

III. LEAKY MODES

In this section, we demonstrate the reliability of our approach by considering leaky modes supported by a DLSPPW. These modes have been already theoretically studied using either effective index model [3], finite element numerical simulations [3, 4, 21] or differential method [7] and experimentally investigated by both near-field [22] and leakage radiation microscopies [5, 23].

A. Single mode waveguide

1. Dispersion relation

The DLSPPW characteristics are optimized as indicated in ref. [3] for the telecom wavelength $\lambda = 2\pi c/\omega = 1.55\mu m$. The gold film is $d = 100$ nm thick and the dielectric ridge thickness and width are $t = w = 600$ nm. Figure (2) represents the waveguide modes dispersion around telecom wavelength. Below $\omega = 1.23 \times 10^{15}s^{-1}$ ($\lambda = 1.53\mu m$), the waveguide is monomodal. Apart for $k_y = 0$, one cannot separate TE (transverse electric) and TM (transverse magnetic) polarization in partial DOSs [12, 20]. However, z-DOS is clearly preponderant (Fig. 2d), indicating that TM polarization is concerned. The dispersion relation of this fundamental TM_{00} mode is in good agreement with the figure (1c) of ref. [4]. The first excited mode also appears in Fig. (2a). It is the TE_{00} mode as confirmed using the differential method and noticing the main contribution of the x-DOS (Fig. 2b).

In the following, we fix the wavelength to $\lambda = 1.55\mu m$. The guided SPP mode (TM_{00}) propagation constant is $k_{y0} = 5.23\mu m^{-1}$ at $\lambda = 1.55\mu m$. The DOS variation, presented on Fig. (3), perfectly matches a lorentzian profile as expected from eq. (8). The curve FWHM $\Delta k_y = 0.023 \mu m^{-1}$ corresponds to a propagation length $L_{SPP} = 1/\Delta k_y = 43\mu m$. We also

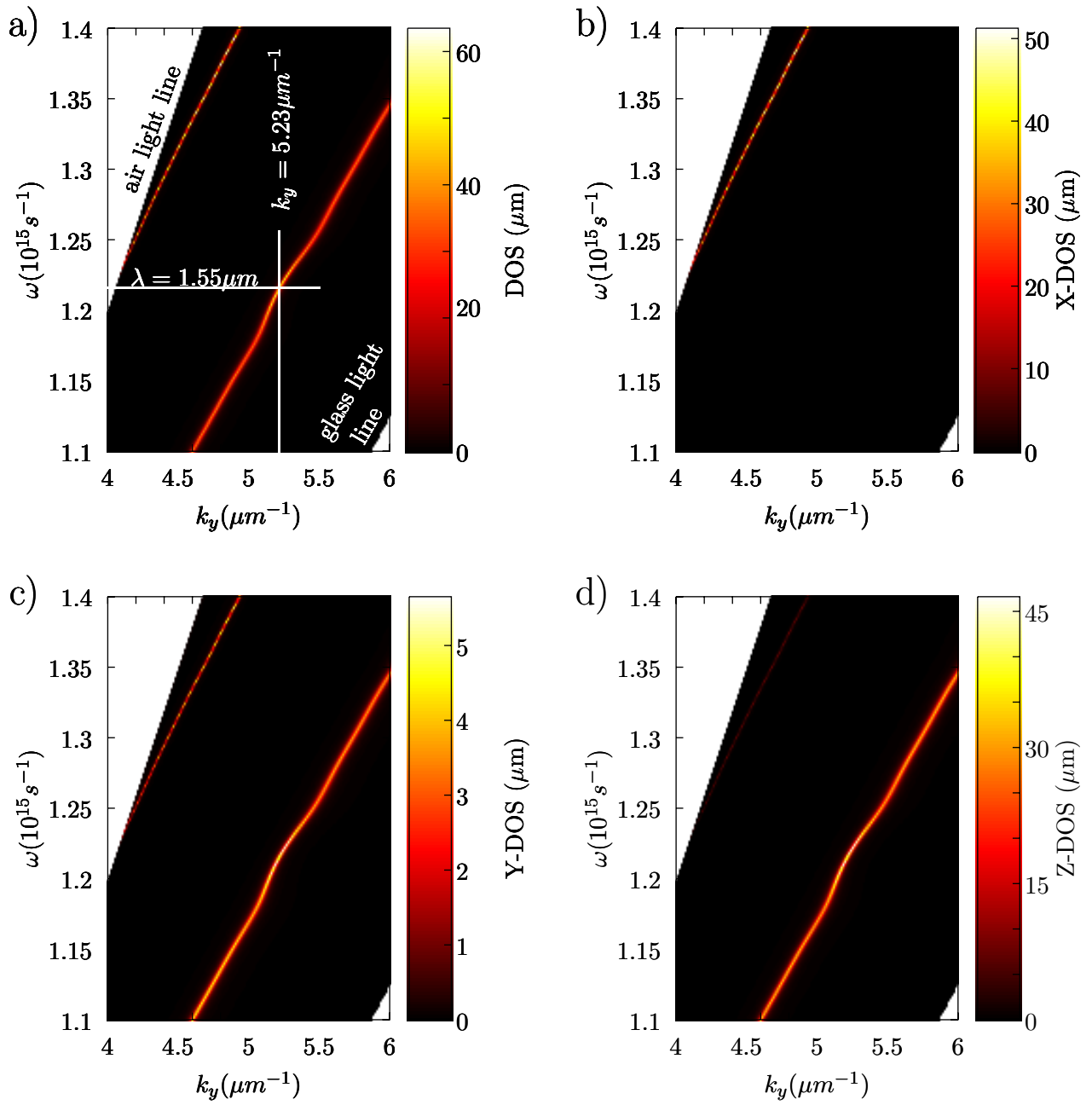


FIG. 2: a) DOS variations calculated for a DLSPPW. The white lines indicate the fundamental mode propagation constant at telecom wavelength $\lambda = 1.55\mu m$. The dispersion curve slope gives a group velocity $v_g/c = 0.6$ at this wavelength. This mode is extensively studied in the following. Figures b,c and d show the x-,y- and z-DOS contributions to the total DOS variation, respectively (note the different scales). The structure is made of a $600\text{ nm} \times 600\text{ nm}$ PMMA strip deposited on a 100 nm gold film. Dielectric constants are taken from ref.[24].

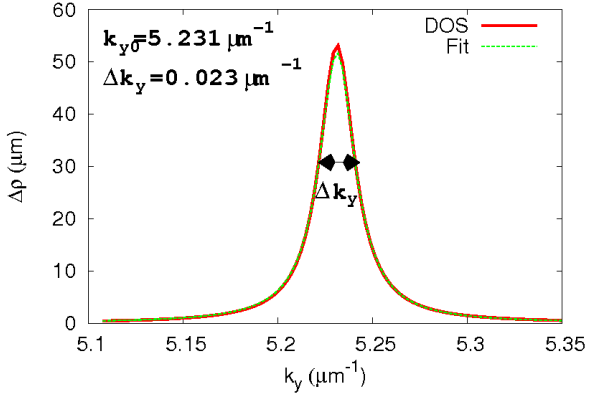


FIG. 3: (color online) Cross-section of dispersion relation (fig. 2) at given frequency (corresponding to $\lambda = 1.55\mu m$). Fit curve is a lorentzian fit (eq. 8) with parameters indicated on the figure.

calculate the DOS variation versus ω at fixed $k_y = 5.23\mu m^{-1}$ (not shown) and obtain a lorentzian profile with a FWHM $\Delta\omega = 3.96 \times 10^{12}s^{-1}$ giving a mode lifetime $\tau = 1/\gamma = 252$ fs [16]. Group velocity satisfies $v_g = L_{SPP}/\tau = 0.57c$ in good agreement with the dispersion slope in Fig. 2.

2. Mode effective index at telecom wavelength

In the following, we work at fixed frequency so that eq. (8) is rewritten

$$\Delta\rho(k_y; \omega) \approx \frac{g}{\pi k_0} \frac{n''}{(k_y/k_0 - n_{eff})^2 + n''^2}, \text{ with } n'' = (\Delta k_y/2k_0) \quad (13)$$

where $n_{eff} = k_{y0}/k_0$ is the mode effective index. n'' is defined so that the mode complex effective index is written as $\tilde{n}_{eff} = n_{eff} + in''$. The mode propagation length is then $L_{SPP} = \lambda/4\pi n''$. Since an image recorded in the Fourier plane by leakage radiation microscopy is easily calibrated in effective indices, it is advantageously compared with expression (13) [23, 25]. Specifically, it presents the same Lorentzian profile (apart from amplitude) [5].

Figure (4a) represents the partial DOSS variations. A resonance clearly appears at $k_y/k_0 = 1.291$. As indicated previously, the z-DOS is clearly preponderant near the resonance, since the mode is TM polarized. There is also a non negligible y-DOS contribution as expected for a *longitudinal* plasmon mode. We deduce the mode effective index $n_{eff} = 1.291$ and propagation length $L_{SPP} = \lambda/(4\pi n'') = 43.2\mu m$ ($n'' = 2.85 \times 10^{-3}$) in

agreement with previous studies [3, 7, 21]. The guided mode is also characterized considering a TM polarized 2D gaussian excitation. The mode intensity decaying in the near-field of the waveguide clearly appears in Fig. (4b). An exponential fit gives $L_{SPP}^{2D} = 44.4\mu m$. Note that the difference between the propagation lengths deduced from DOS FWHM and from gaussian beam propagation originates from 3D and 2D mode shape [21]. Importantly, the exact 3D mode characteristics associated with the 2D waveguide are obtained through DOS shape. The mode pattern, calculated in Fig. (4c), demonstrates the good confinement [23]. Finally, the mode intensity at a given time is shown in Fig. (4d). The collective charge oscillation, mode enhancement and confinement at the metal/dielectric interface, typical from a surface plasmon mode are visible. The plasmon mode wavelength $\lambda_{SPP} = 1.202\mu m = \lambda/n_{eff}$ is again consistent with $n_{eff} = 1.29$.

B. Coupling strength

In order to demonstrate the versatility and efficiency of DOS formulation as a mode solver, we now investigate coupling strength between two identical waveguides. The DOS variation for two DLSPPWs separated by 500 nm (edge to edge) is presented in Fig. (5a). Comparing DOS amplitudes in Fig. (5a) and Fig. (3), it appears that no new mode is created but modes coupling breaks the degeneracy as expected. Due to the coupling between the two isolated waveguide modes, a symmetric and antisymmetric supermodes appear at effective index $n_{eff}^s = 1.309$ and $n_{eff}^a = 1.269$ respectively. These two modes present identical propagation length $L_{SPP}^s = L_{SPP}^a = (\lambda/4\pi n'') = 41.4\mu m$, slightly below the isolated waveguide mode propagation length since some additional leakages occur during energy transfer to the nearby waveguide. Finally, the coupling length between the two waveguides obeys

$$L_C = \frac{\lambda}{2(n_{eff}^s - n_{eff}^a)}. \quad (14)$$

We obtain $L_C = 19.2\mu m$ for $d = 500nm$. We again compare this result with the direct calculation considering excitation of one of the two guides. The electric intensity shown on fig. (5b) presents typical oscillation due to energy transfer from one guide to the other. The coupling length is in excellent agreement with the number obtained previously. Figure (5b) represents the supermodes effective indices as a function of guide separation distance. Finally, the evanescent coupling between the two waveguides, follows an exponential law

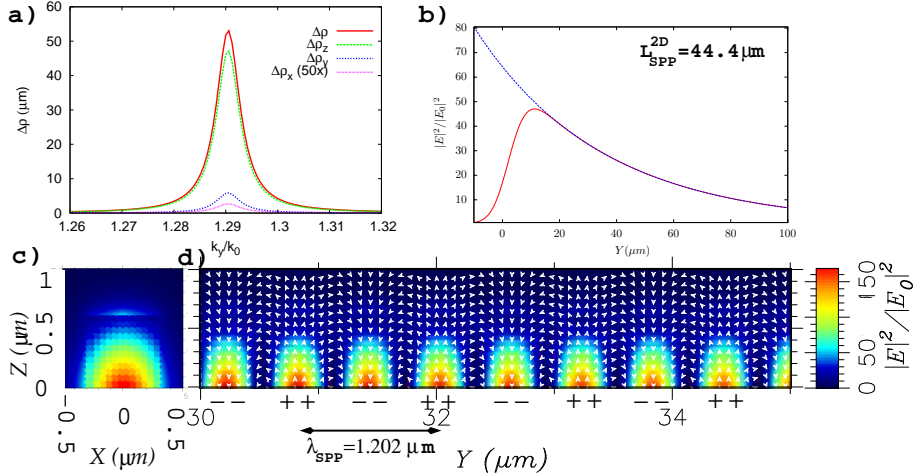


FIG. 4: (color online) Single waveguide characterization. a) Partial DOSs calculated as a function of k_y/k_0 . xDOS is magnified 50 \times to be visible. b) (Time-averaged) electric intensity calculated 50 nm above the dielectric ridge when the system is excited by a (2D-) gaussian beam by total internal reflection from the substrate centered at incident angle $\arcsin(n_{eff}/n_{sub}) = 53.8^\circ$. The blue curve is an exponential fit with decay length $L_{SPP}^{2D} = 44.4 \mu m$. c) Mode intensity pattern $\mathbf{E}_{2D}(\mathbf{r}_{//})$. d) Electric field intensity computed at a certain time, far from the incident excitation spot (see Fig. (4b)), revealing the mode propagation. The white arrows indicate the electric field orientation. “- -” and “+ +” represent the charges density signs at the metal surface, deduced from the field polarization. The dielectric ridge ($n_{diel} = 1.535$) is $t = 600$ nm thick and $w = 600$ nm width. The gold film and glass substrate optical indices are $n_{metal} = 0.55 + i11.5$ and $n_{sub} = 1.6$ respectively. Incident vacuum wavelength is $\lambda = 1.55 \mu m$. Electric intensity is normalized with respect to the incident intensity at the focal point ($y=0, z=0$).

with a lateral wavevector component $k_x = 1/290 \text{ nm}^{-1}$ (Fig. (5c)), in good agreement with finite element study done in ref. [21], and indicating a strong field confinement near the guide.

We would like to draw a temporary conclusion here. The DOS computation in presence of a complex waveguiding structure allows direct and complete characterization of the supported mode: propagation constant and length, as well as polarization state. In addition coupling between two waveguides is also easily described.

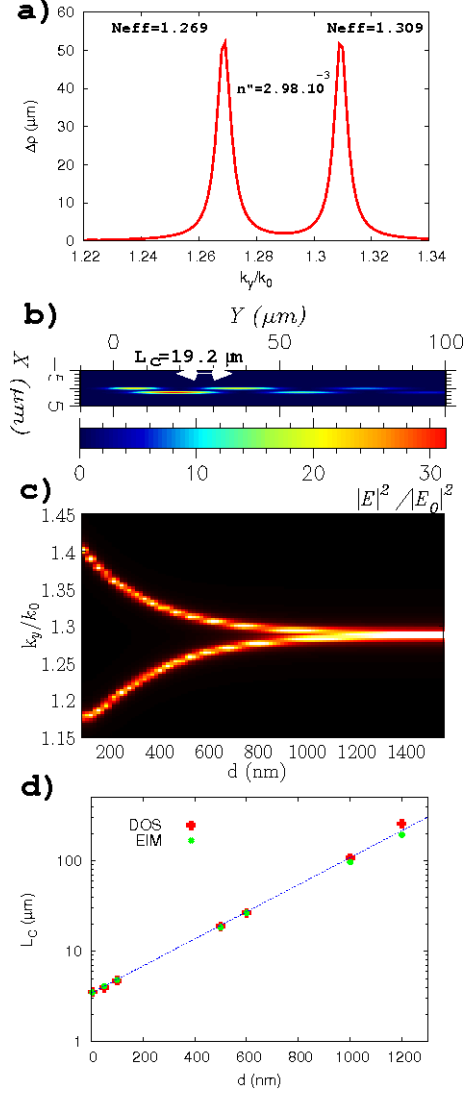


FIG. 5: (color online) Coupled DLSPPWs.a) DOS difference computed for two guides separated by $d = 500$ nm (edge to edge). b) Electric intensity calculated 50 nm above the DLSPPWs when the top waveguide is excited with a (spatially truncated) 2D-gaussian beam at incident angle 53.8° . c) Coupled waveguides DOS as a function of separation distance. d) Coupling length for several separation distance deduced from DOS variations ('DOS') or effective index model ('EIM'). The dotted line is an exponential fit with a slope $k_x = 1/290 \text{ nm}^{-1}$.

IV. BOUND MODES

In this last section, we apply the DOS method to bound (lossy) modes. The modes investigated above have effective indices below the substrate optical index so that they

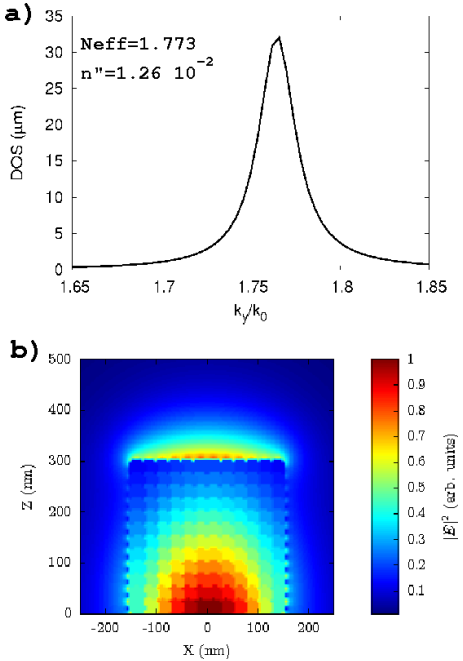


FIG. 6: (color online) a) DOS variation for a high index ($n = 2.437$) strip above a 50 nm gold film. b) Mode intensity profile in the (XZ) plane.

radiatively leak into the substrate. In order to improve the mode confinement, we now investigate bound modes in DLSPPW. They are characterized by effective indices higher than substrate and superstrate (air) optical indices and can be obtained with high index dielectric materials. In this section, we consider a dielectric strip of optical index $n = 2.437$ that corresponds for instance to chalcogenide glasses [26] or BM4i4i polymer, two materials that present strong non-linear properties promising for all-optical integrated photonic [6].

Using effective index model, we first roughly determine the strip thickness and width that optimize the mode confinement and insure monomodal conditions [3, 23]. We found that a strip with square section of 300 nm side allows for a good mode confinement, and supports a single mode (TM_{00}). We deduce from DOS variation (Fig. 6a) the mode effective index ($n_{eff} = 1.773$) and propagation length ($L_{SPP} = 9.8\mu\text{m}$). The mode profile, represented on Fig. (6b) is similar to PMMA leaky mode (Fig. 4c). However, although being a bound mode (effective index higher than the substrate index), this mode has a very low propagation length compared to the leaky PMMA mode. This is due to the high dielectric index that *pushes* the mode field into the lossy metal. This can be clearly seen considering thin gold films. Figure (7) represents the mode profile for leaky and bound modes for two gold thicknesses.

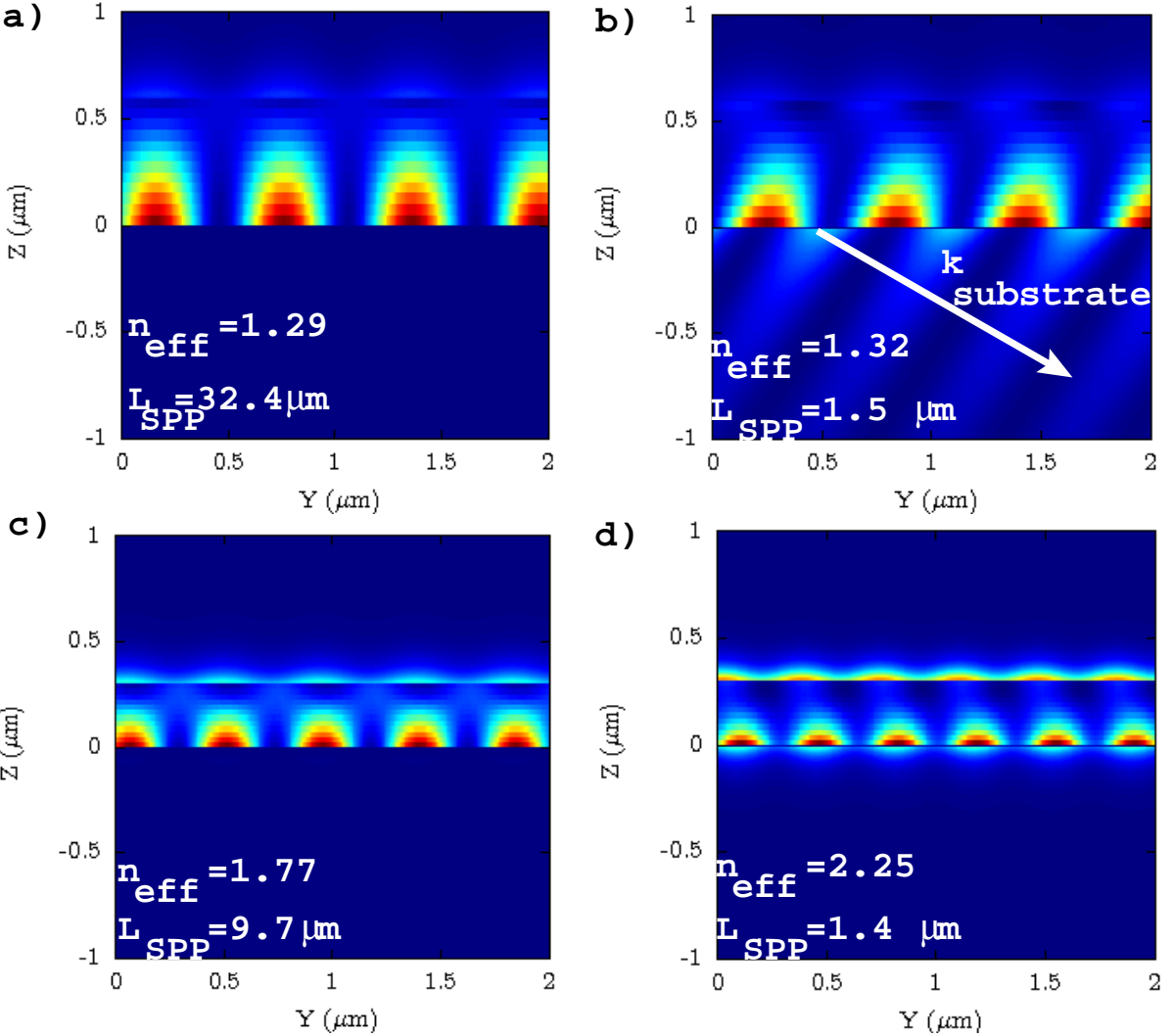


FIG. 7: (color online) Mode intensity profile in the (YZ) plane for a,b) PMMA ($t = w = 600\text{nm}$) and c,d) chalcogenide ($t = w = 300\text{nm}$) DLSPPW. The gold film thickness is 50 nm (a,c) or 10 nm (b,d). The vacuum wavelength is $\lambda = 1.55\mu\text{m}$. In b), $k_{\text{substrate}}$ represents the leaky mode wavevector into the substrate. The mode effective indices and propagation length obtained from DOS calculation are indicated on the figures.

As the gold film thickness decreases, radiative losses of the leaky modes into the substrate increase so that the PMMA-DLSPPW mode propagation length drops to $L_{\text{SPP}} = 1.5\mu\text{m}$ for 10 nm gold film (Fig. 7b). In case of bound mode, no radiative loss is observed (Fig. 7d) but due to the high mode effective index, strong mode penetration into the lossy gold film is visible so that rather low propagation length ($L_{\text{SPP}} = 1.4\mu\text{m}$) is also obtained.

Finally, this study shows that one has to avoid high index materials for DLSPPW ap-

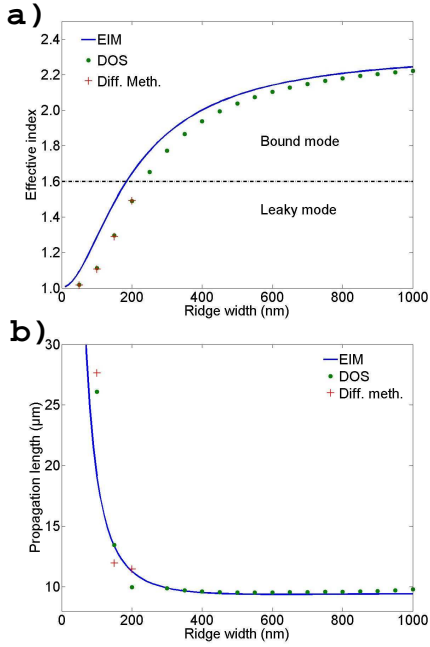


FIG. 8: (color online) Comparison of the effective indices (a) and propagation length (b) obtained with either effective index model, differential method or DOS calculation. The chalcogenid strip thickness is 300 nm and its width varies from 0 to 1 μm . In a), the horizontal line at the substrate index separates bound and leaky modes.

plication, in contrasts to standard dielectric integrated waveguides [27]. Figure (8a) also compares effective indices obtained using approximated effective index model [3] and two exact numerical methods, namely the differential method and the DOS variations. Numerical methods are in excellent agreement for leaky modes. Bound modes can not be easily investigated by the differential method, since it generally relies on mode excitation through the substrate [7], but they are accessible using DOS formulation. The agreement is within 10% as far as propagation length is concerned (Fig. 8b).

V. CONCLUSION

In conclusion, the evaluation of density of modes modification in presence of a photonic waveguiding structure allows direct estimation of both mode effective index and propagation length for either leaky and bound modes. Moreover, a close inspection of partial DOSs, that build up the density of modes, directly reveals the mode polarization state. Finally, it is worthwhile noting that although we investigated a specific configuration, namely DLSPPW,

this method is general and is available for any 2D guiding structure. Last, we would like to mention that this method intrinsically concerns lossy modes. In case of absolutely no loss (neither by leakage, absorption nor corners scattering), it could be applied by artificially adding an extremely small absorption to the waveguide.

Acknowledgments

The authors gratefully acknowledge F. Smektala for fruitful discussion on chalcogenide glass properties. This work is supported by the European Commission (project PLASMO-COM, EC FP6 IST 034754 STREP).

- [1] R. G. Hunsperger, *Integrated Optics: theory and technology* (Springer, 2002).
- [2] B. Steinberger, A. Hohenau, H. Ditlbacher, A. L. Stepanov, A. Drezet, F. R. Aussenegg, A. Leitner, and J. R. Krenn, Appl. Phys. Lett. **88**, 94104 (2006).
- [3] T. Holmgard and S. I. Bozhevolnyi, Physical Review B **75**, 245405 (2007).
- [4] A. V. Krasavin and A. V. Zayats, Physical Review B **78**, 045425 (2008).
- [5] J. Grandidier, G. Colas des Francs, S. Massenot, A. Bouhelier, L. Markey, J. Weeber, C. Finot, and A. Dereux, Nano Letters **9**, 2935 (2009).
- [6] V. Ta'eed, N. J. Baker, L. Fu, K. Finsterbusch, M. R. E. Lamont, D. J. Moss, H. C. Nguyen, B. J. Eggleton, D.-Y. Choi, S. Madden, et al., Optics Express **15**, 9205 (2007).
- [7] S. Massenot, J.-C. Weeber, A. Bouhelier, G. Colas des Francs, J. Grandidier, L. Markey, and A. Dereux, Optics Express **16**, 17599 (2008).
- [8] J. Callaway, *Quantum Theory of the Solid State* (Academic Press, Inc., 1976).
- [9] A. Lagendijk and B. Tiggelen, Physics Reports **270**, 143 (1996).
- [10] G. Colas des Francs, C. Girard, J.-C. Weeber, C. Chicanne, T. David, A. Dereux, and D. Peyrade, Physical Review Letters **86**, 4950 (2001).
- [11] A. Dereux, J. P. Vigneron, P. Lambin, and A. A. Lucas, Phys. Rev. B **38**, 5438 (1988).
- [12] O. J. F. Martin, C. Girard, D. R. Smith, and S. Schultz, Phys. Rev. Lett. **82**, 315 (1999).
- [13] P. Morse and H. Feshbach, *Methods of theoretical physics* (1953).

- [14] A. Dereux, Ph.D. thesis, Namur (1991).
- [15] A slightly different definition is also possible. Writting $\delta(k_y'^2 - k_y^2) = \frac{1}{2|k_y|}[\delta(k_y' - k_y) + \delta(k_y' + k_y)]$, we obtain $\rho(k_y^2) = \frac{1}{2k_y}[\rho(k_y) + \rho(-k_y)]$ ($k_y > 0$). Moreover, $\rho(-k_y) = \rho(k_y)$ since $\pm k_y$ simply defines forward and backward propagations. This lead to $\Delta\rho(k_y; \omega) = \frac{g}{2\pi} \frac{\Delta k_y/2}{(k_y - k_{y0})^2 + (\Delta k_y/2)^2}$ instead of eq. (8) and a degeneracy $g/2$, excluding forward/backward propagation degeneracy.
- [16] DOS can also be expressed in the frequency space for fixed momentum k_y . Noticing that θ is a function of both ω and $v = k_y^2$, we use the identity $\frac{\partial\theta}{\partial\omega}|_v \frac{\partial\omega}{\partial v}|_\theta \frac{\partial v}{\partial\theta}|_\omega = -1$ that leads to $\frac{\partial\theta}{\partial\omega}|_{k_y} = -\frac{\partial v}{\partial\omega}|_v \frac{\partial\theta}{\partial v}|_\omega = -2k_y/v_g \pi \Delta\tilde{\rho}(k_y^2; \omega) = -\pi/v_g \Delta\rho(k_y; \omega)$. A Taylor expansion near the resonance frequency ω_0 gives then $\Delta\rho(k_y; \omega) \approx \frac{gv_g}{\pi} \frac{\Delta\omega/2}{(\omega - \omega_0)^2 + (\Delta\omega/2)^2}$, with $\Delta\omega = -2 \frac{\text{Im}D(\omega_0; k_y)}{[\partial\text{Re}D(\omega; k_y)/\partial\omega]|_{(\omega=\omega_0)}} = 1/\tau = v_g/L_{SPP}$, and τ is the mode lifetime. See also M. Kretschmann and A. A. Maradudin, Physical Review B **66**, 245408 (2002)
- [17] C. Bohren and D. Huffman, *Absorption and scattering of light by small particles* (1983).
- [18] G. Colas des Francs, C. Girard, and A. Dereux, Journal of Chemical Physics **117**, 4659 (2002).
- [19] G. Lévéque, G. Colas des Francs, C. Girard, J.-C. Weeber, C. Meier, C. Robilliard, R. Mathivet, and J. Weiner, Physical Review E **65**, 36701 (2002).
- [20] M. Paulus, P. Gay-Balmaz, and O. Martin, Physical Review E **63**, 66615 (2001).
- [21] A. V. Krasavin and A. V. Zayats, Applied Physics Letters **90**, 211101 (2007).
- [22] T. Holmgaard, S. Bozhevolnyi, L. Markey, and A. Dereux, Applied Physics Letters **92**, 011124 (2008).
- [23] J. Grandidier, S. Massenot, G. Colas des Francs, A. Bouhelier, J.-C. Weeber, L. Markey, A. Dereux, J. Renger, M. U. González, and R. Quidant, Physical Review B **78**, 245419 (2008).
- [24] E. D. Palik, *Handbook of Optical Constants of Solids* (Academic Press - Elsevier, 1998).
- [25] A. Drezet, A. Hohenau, D. Koller, A. Stepanov, H. Ditlbacher, B. Steinberger, F. Aussenegg, A. Leitner, and J. Krenn, Materials Science and Engineering B **149**, 220 (2008).
- [26] G. Boudebs, S. Cherukulappurath, M. Guignard, J. Troles, F. Smektala, and F. Sanchez, Optics Communications **230**, 331 (2004).
- [27] R. Quidant, J.-C. Weeber, A. Dereux, D. Peyrade, G. Colas des Francs, C. Girard, and Y. Chen, Physical Review E **64**, 66607 (2001).

4.4 Conclusion

Les guides plasmoniques confinés par un ruban diélectrique, décrit dans ce chapitre, constituent une première étape pour réaliser des dispositifs plasmoniques actifs. Outre une amélioration du gain, nous allons travailler dans les prochaines années à démontrer d'autres fonctions en utilisant des matériaux diélectriques variés (polymère thermo-optique, verre non linéaire, etc.). Un important travail de recherche de matériaux compatibles avec un guide plasmonique et ouvrant la voie à la réalisation de portes logiques s'impose. Un effort tout particulier doit être fait aussi pour assurer la compatibilité avec la technologie silicium, incontournable pour proposer une alternative à l'industrie électronique.

Ce dernier point est l'objectif du projet européen PLATON (2009-2012) auquel notre équipe participe. L'ambition de ce projet est de réaliser des composants plasmoniques intégrés permettant des transferts de données de l'ordre du Tb/s. Pour cela, il reprend le concept de DLSPPW, inséré dans une plateforme photonique intégrée silicium. Cette configuration est un premier pas vers les composants opto-électroniques intégrés en surface profitant de la technologie plasmonique et offre une alternative originale au tout électronique ou tout optique.

Toutefois, de nombreux défis restent à relever. En premier lieu, la réalisation de dispositifs actifs, basés sur la technologie plasmonique, évoquée plus haut. Un autre point important concerne taux d'intégration de ces composants plasmoniques. En effet, même si certaines configurations, comme un nanofil métallique, ne possède pas de taille de coupure, la plupart des configurations testées jusqu'à aujourd'hui ne permet pas de dépasser l'état de l'art atteint par la photonique intégrée. Bien que la combinaison de guidage optique et électronique sur une même structure métallique constitue en soi un atout majeur des circuits plasmoniques, un effort important doit être fait pour penser à des configurations originales. La question des pertes restent aussi cruciale. La propagation assistée par gain optique, démontrée dans ce chapitre, constitue une réponse, mais cela n'évite pas de réfléchir à de nouveaux matériaux plasmoniques à faibles pertes. L'utilisation de structures métalliques hautement cristallines, réalisables par voie chimique, est une piste prometteuse.

Conclusion et perspectives de recherches

Au cours de ces six dernières années, j'ai développé une activité de plasmonique moléculaire. Sur la base de simulations numériques et en m'appuyant sur le parc d'instruments déjà présent dans l'équipe ou développé avec l'aide de doctorants, post-doctorants et de collègues, j'ai pu démontrer l'intérêt de la plasmonique pour contrôler le signal de fluorescence de molécules uniques. Ce travail repose aussi sur des collaborations avec des groupes ayant une bonne connaissance de la fluorescence de molécules individuelles.

D'autre part, je participe activement à l'activité de développement de micro-circuits optiques ou opto-électroniques basés sur les propriétés de mode plasmon-polaritons de surface. Cette activité se fait en lien étroit avec Alain Dereux, Jean-Claude Weeber et Alexandre Bouhelier.

Enfin, depuis peu, il a été proposé d'adapter la notion d'antenne au domaine optique (voir l'introduction du chapitre 3, page 75). Ce nouveau concept d'*antennes optiques* [52, 53] propose d'utiliser des nanoparticules plasmoniques pour confiner efficacement une onde propagative vers un domaine très nettement sub-longueur d'onde avec de fortes potentialités allant de l'amélioration du rendement des cellules photovoltaïques [15] jusqu'à la réalisation de sources de photons uniques performantes [45, 47]. Comme discuté à plusieurs reprises dans ce mémoire, les antennes optiques sont généralement des structures métalliques supportant des modes localisés (confinés) mais aussi des modes délocalisés (propagatifs).

Fort de l'expérience acquise dans l'étude et la conception de guides à plasmons et de la spectroscopie exaltée, j'ai débuté une activité sur ce thème avec le projet PlasTips (2009-2013) et le co-encadrement de la thèse de Pierre Bramant, démarrée en octobre 2008.

Le projet PlasTips, que je coordonne, est consacré à la réalisation, la caractérisation et l'optimisation de sondes plasmoniques pour le champ proche optique. Ces sondes se composent de structures métalliques déposées sur une fibre optique effilée. Une originalité de ce projet est d'utiliser des structures métalliques synthétisées et déposées par voie chimique et non déposées par évaporation thermique. Nous bénéficierons ainsi de la cristallinité du métal limitant les pertes par effet Joule. Un axe fort de ce projet concerne l'étude du couplage entre un émetteur quantique unique et les sondes plasmoniques. Ceci pourrait mener à la réalisation d'une source de photons uniques efficacement couplée à une fibre optique. Une telle configuration serait un excellent outil pour étudier de manière approfondie le comportement d'une source de photons uniques. Le développement d'une nouvelle technologie basée sur le comportement quantique de la lumière pourrait en bénéficier. Ainsi, les sources de photons uniques sont un élément essentiel dans de nombreuses expériences de cryptographie quantique [88]. L'adaptation de cette configuration en version photonique intégrée peut aussi ouvrir la voie à la réalisation de nouveaux dispositifs de calcul quantique assimilable à une puce photonique.

Bibliographie

- [1] L. Novotny and B. Hecht, *Principles of Nano-Optics*, Cambridge University Press, 2006.
- [2] Optical Constants of the Noble Metals
P. Johnson and R. Christy, *Physical Review B* **6**, pp. 4370–4379 (1972).
- [3] E. D. Palik, *Handbook of Optical Constants of Solids*, Academic Press - Elsevier, 1998.
- [4] C. Kittel, *Introduction to solid state physics*, 5th ed., 1976.
- [5] H. Raether, *Surface Plasmons on Smooth and Rough Surfaces and on Gratings*, Springer Verlag, 1986.
- [6] C. Bohren and D. Huffman, *Absorption and scattering of light by small particles*, 1983.
- [7] Molecular Plasmonics
R. P. V. Duyne, *Science* **306**, pp. 985–986 (2004).
- [8] www.biacore.com.
- [9] K. Kneipp, M. Moskovits, and H. Kneipp, eds., *Surface-Enhanced Raman Scattering–Physics and Applications*, Springer-Verlag, 2006.
- [10] Photothermal Imaging of Nanometer-Sized Metal Particles Among Scatterers
D. Boyer, P. Tamarat, A. Maali, M. Orrit, and B. Lounis, *Science* **297**, pp. 1160–1163 (2002).
- [11] Temperature mapping around plasmonic nanostructures using fluorescence polarization anisotropy
G. Baffou, M. P. Kreuzer, F. Kulzer, and R. Quidant, *Optics Express* **17**, pp. 3291–3298 (2009).
- [12] Photo-thermal tumor ablation in mice using near-infrared-absorbing nanoparticles
D. O’Neal, L. Hirsch, N. Halas, J. Payne, and J. West, *Cancer Letters* **209**, pp. 171–176 (2004).

- [13] A Cellular Trojan Horse for Delivery of Therapeutic Nanoparticles into Tumors
M. Choi, K. Stanton-Maxey, J. Stanley, C. Levin, R. Bardhan, D. Akin, S. Badve, J. Sturgis, J. Robinson, R. Bashir, N. Halas, and S. Clare, *Nano Letters* **7**, pp. 3759–3765 (2007).
- [14] Nanoshell-Enabled Photothermal Cancer Therapy : Impeding Clinical Impact
S. Lal, S. Clare, and N. Halas, *Accounts of Chemical Research* **41**, pp. 1842–1851 (2008).
- [15] Plasmonic solar cells
K. Catchpole and A. Polman, *Optics Express* **16**, pp. 21793–21800 (2008).
- [16] Surface plasmon subwavelength optics
W. Barnes, A. Dereux, and T. Ebbesen, *Nature* **424**, pp. 824–830 (2003).
- [17] Surface plasmon circuitry
T. Ebbesen, C. Genet, and S. Bozhevolnyi, *Physics Today* **61**, pp. 44–50 (2008).
- [18] Molecule-Surface Plasmon Interactions in Hole Arrays : Enhanced Absorption, Refractive Index Changes, and All-Optical Switching
J. Dintinger, S. Klein, and T. W. Ebbesen, *Advanced Materials* **18**, pp. 1267 – 1270 (2006).
- [19] Control of Molecular Energy Redistribution Pathways via Surface Plasmon Gating
G. P. Wiederrecht, J. E. Hall, and A. Bouhelier, *Physical Review Letters* **98**, p. 083001 (2007).
- [20] All-optical modulation by plasmonic excitation of CdSe quantum dots
D. Pacifici, H. J. Lezec, and H. A. Atwater, *Nature Photonics* **1**, pp. 402–406 (2007).
- [21] Near-field optics-light Microscopy for life science
U. Fischer and A. Naber, *Photonik International* **5**, pp. 82–85 (2006).
- [22] Enhanced light confinement in a near-field optical probe with a triangular aperture
A. Naber, D. Molenda, U. Fischer, H. Maas, C. Hoppenre, N. Lu, and H. Fuchs, *Physical Review Letters* **21**, p. 210801 (2002).
- [23] Enhanced light confinement in a triangular aperture : Experimental evidence and numerical calculations
G. Colas des Francs, D. Molenda, U. Fischer, and A. Naber, *Physical Review B* **72**, p. 165111 (2005).
- [24] Analysis and Numerical Computation of Diffraction of an Optical Field by a Subwavelength-Size Aperture in a Thick Metallic Screen by Use of a Volume Integral Equation

- K. Tanaka and M. Tanaka, Applied Optics **43**, pp. 1734–1746 (2004).
- [25] Transmission of an obliquely incident beam of light through small apertures in a metal film
E. Bortchagovsky, G. Colas des Francs, D. Molenda, A. Naber, and U. Fischer, Applied Physics B **84**, p. 49 (2006).
- [26] On the optimum form of an aperture for a confinement of optically excited electric near-field
E. Bortchagovsky, G. Colas des Francs, D. Molenda, A. Naber, and U. Fischer, Journal of Microscopy (NFO9) **229**, p. 223 (2008).
- [27] Near field microscopy and near field optics
D. Courjon and C. Bainier, Rep. Prog. Phys. **57**, pp. 989–1028 (1994).
- [28] W. Göhde and U. Fischer and H. Fuchs and J. Tittel and Th. Basché and Ch. Bräule and A. Herrmann and K. Mullen
F. Blinking and P. of Single Terrylenediimide Molecules Studied with a Confocal Microscope, Journal of Physical Chemistry A **102**, pp. 9109–9116 (1998).
- [29] Nano-optics with single quantum systems
B. Hecht, Phil. Trans. R. Soc. Lond. A **362**, pp. 881–899 (2004).
- [30] Far-Field Optical Nanoscopy
S. W. Hell, Science **316**, pp. 1153–1158 (2007).
- [31] Near-Field Optical Study of Protein Transport Kinetics at a Single Nuclear Pore
M. Herrmann, N. N. J. Wissler, J. Prez, D. Gradl, and A. Naber, NanoLetters ASAP (2009).
- [32] Optical microscopy using a single-molecule light source
J. Michaelis, J. M. C. Hettich, and V. Sandoghdar, Nature **405**, pp. 325–328 (2000).
- [33] A single gold Particle as a probe for apertureless SNOM
T. Kalkbrenner, M. Ramstein, J. Mlynek, and V. Sandoghdar, Journal of Microscopy **202**, pp. 72–76 (2001).
- [34] Tomographic plasmon spectroscopy of a single gold nanoparticle
T. Kalkbrenner, U. Hakanson, and V. Sandoghdar, Nano Letters **4**, pp. 2309–2314 (2004).
- [35] Energy transfer in near-field optics
G. Colas des Francs, C. Girard, M. Juan, and A. Dereux, Journal of Chemical Physics **123**, p. 174709 (2005).

- [36] SNOM signal near plasmonic nanostructures : an analogy with fluorescence decay channels
G. Colas des Francs, C. Girard, A. Bruyant, and A. Dereux, Journal of Microscopy (NFO9) **229**, pp. 302–306 (2008).
- [37] Near-Field optical imaging of plasmon modes in gold nanorods
K. Imura, T. Nagahara, and H. Okamoto, Journal of Chemical Physics **122**, p. 154701 (2005).
- [38] Local Excitation, Scattering, and Interference of Surface Plasmons
B. Hecht, H. Bielefeldt, L. Novotny, Y. Inouye, and D. W. Pohl, Phys. Rev. Let **77**, pp. 1889–1892 (1996).
- [39] Far-field imaging of the electromagnetic local density of optical states
C. Huang, A. Bouhelier, G. Colas des Francs, G. Legay, J.-C. Weeber, and A. Dereux, Optics Letters **33**, pp. 300–302 (2008).
- [40] Gain, detuning and directivity of nanoparticles optical antennas
C. Huang, A. Bouhelier, G. Colas des Francs, A. Bruyant, A. Guénot, E. Finot, J.-C. Weeber, and A. Dereux, Physical Review B **78**, p. 155407 (2008).
- [41] Generalized Bloch equations for optical interactions in confined geometries
C. Girard, O. Martin, G. Lévêque, G. Colas des Francs, and A. Dereux, Chemical Physics Letters **404**, p. 44 (2005).
- [42] Theory of molecular excitation and relaxation near a plasmonic device
G. Colas des Francs, C. Girard, T. Laroche, G. Lévêque, O. Martin, and A. Dereux, Journal of Chemical Physics **127**, p. 34701 (2007).
- [43] Rationale for 10^{14} enhancement factor in single molecule Raman spectroscopy
S. G. an D.V. Guzatov, ArXiv (2008).
- [44] Laser-Induced Resonance Shifts of Single Molecules Self-Coupled by a Metallic Surface
O. Labeau, P. Tamarat, H. Courtois, G. S. Agarwal, and B. Lounis, Physical Review Letters **98**, p. 143003 (2007).
- [45] Quantum Optics with Surface Plasmons
D. Chang, A. Sørensen, P. Hemmer, and M. Lukin, Physical Review Letters **97**, p. 053002 (2006).
- [46] Generation of single optical plasmons in metallic nanowires coupled to quantum dots
A. Akimov, A. Mukherjee, C. Yu, D. Chang, A. Zibrov, P. Hemmer, H. Park, and M. Lukin, Nature **450**, pp. 402–406 (2007).

- [47] Plasmon-Enhanced Single Photon Emission from a Nanoassembled Metal-Diamond Hybrid Structure at Room Temperature
 S. Schietinger, M. Barth, T. Aichele, and O. Benson, *Nano Letters* **9**, pp. 1694–1698 (2009).
- [48] Wave-particle duality of single surface plasmon polaritons
 R. Kolesov, B. Grotz, G. Balasubramanian, R. J. Stöhr, A. A. L. Nicolet, P. R. Hemmer, F. Jelezko, and J. Wrachtrup, *Nature Physics* **5**, pp. 470–474 (2009).
- [49] Plasmonic field enhancement and SERS in the effective mode volume picture
 S. Maier, *Optics Express* **14**, pp. 1957–1964 (2006).
- [50] Fluorescence near metal tips : the roles of energy transfer and surface plasmon polaritons
 N. Issa and R. Guckenberger, *Optics Express* **15**, pp. 12131–12144 (2007).
- [51] Near-field optics seen as an antenna problem
 D. W. Pohl, in *Near-field Optics, Principles and Applications*, X. Zhu and M. Ohtsu, eds., World Scientific, Singapore, 2000, pp. 9–21.
- [52] Resonant Optical Antennas
 P. Mühlischlegel, H.-J. Eisler, O. J. F. Martin, B. Hecht, and D. W. Pohl, *Science* **308**, pp. 1607 – 1609 (2005).
- [53] $\lambda/4$ resonance of an optical monopole antenna probed by single molecule fluorescence
 T. H. Taminiau, R. J. Moerland, F. B. Segerink, L. Kuipers, and N. F. van Hulst, *Nano Lett.* **7**, pp. 28–33 (2007).
- [54] Effective wavelength scaling for optical antennas
 L. Novotny, *Physical Review Letters* **98**, p. 266802 (2007).
- [55] Optical antennas focus in on biology
 M. F. Garcia-Parajo, *Nature Photonics* **2**, pp. 201–203 (2008).
- [56] Optical antennas tuned to pitch
 L. Novotny, *Nature* **455**, p. 887 (2008).
- [57] A Monopole Antenna at Optical Frequencies : Single-Molecule Near-Field Measurements
 T. H. Taminiau, F. B. Segerink, and N. F. van Hulst, *IEEE Transactions on antennas and propagation* **55**, pp. 3010–3017 (2007).
- [58] Thermal radiation scanning tunnelling microscopy
 Y. D. Wilde, F. Formanek, R. Carminati, B. Gralak, P. Lemoine, K. Joulain, J. Mulet,

- Y. Chen, and J. Greffet, *Nature* **444**, pp. 740–743 (2006).
- [59] Single molecules probe local density of modes (LDOS) around photonic nanostructures
G. Colas des Francs, G. Sanchez-Mosteiro, M. Ujue-Gonzalez, L. Markey, N. van Hulst, and A. Dereux, *Journal of Microscopy (NFO9)* **229**, pp. 210–216 (2008).
- [60] The single molecule probe : nanoscale vectorial mapping of photonic mode density in a metal nanocavity
J. P. Hoogenboom, G. Sanchez-Mosteiro, G. Colas des Francs, D. Heinis, G. Legay, A. Dereux, and N. F. van Hulst, *Nano Letters* **9**, pp. 1189–1195 (2009).
- [61] Influencing the Angular Emission of a Single Molecule
H. Gersen, M. F. García-Parajó, L. Novotny, J. A. Veerman, L. Kuipers, and N. F. van Hulst, *Physical Review Letters* **85**, pp. 5312–5315 (2000).
- [62] Fluorescence Quenching of Dye Molecules near Gold Nanoparticles : Radiative and Nonradiative Effects
E. Dulkeith, A. C. Morteani, T. Niedereichholz, T. A. Klar, J. Feldmann, S. A. Levi, F. C. J. M. van Veggel, D. N. R. and M. Möller, and D. Gittins, *Physical Review Letters* **89**, p. 203002 (2002).
- [63] Nanoparticle Induced Fluorescence Lifetime Modification as Nanoscopic Ruler : Demonstration at the Single Molecule Level
J. Seelig, K. Leslie, A. Renn, S. KÅ^{1/4}hn, V. Jacobsen, M. van de Corput, C. Wyman, and V. Sandoghdar, *Nano Letters* **7**, pp. 685–689 (2007).
- [64] Enhancement and quenching of single molecule fluorescence
P. Anger, P. Bharadwaj, and L. Novotny, *Phys. Rev. Lett.* **96**, p. 113002 (2006).
- [65] Enhancement of single molecule fluorescence using a gold nanoparticle as an optical nano-antenna
S. Kühn, U. Hakanson, L. Rogobete, and V. Sandoghdar, *Phys. Rev. Lett.* **97**, p. 017402 (2006).
- [66] Plasmon-enhanced luminescence near noble-metal nanospheres : Comparison of exact theory and an improved Gersten and Nitzan model
H. Mertens, A. Koenderink, and A. Polman, *Physical Review B* **76**, p. 115123 (2007).
- [67] Fluorescence relaxation in the near-field of a mesoscopic metallic particle : distance dependence and role of plasmon modes
G. Colas des Francs, A. Bouhelier, E. Finot, J.-C. Weeber, A. Dereux, C. Girard, and E. Dujardin, *Optics Express* **16**, pp. 17654– 17666 (2008).

- [68] Molecule non-radiative coupling to a metallic nanosphere : an optical theorem treatment
G. Colas des Francs, International Journal of Molecular Science **10**, pp. 3931–3936 (2009).
- [69] J. Jackson, Classical electrodynamics, John Wiley & Sons, Hoboken, third ed., 1998.
- [70] Molecular quenching and relaxation in a plasmonic tunable nanogap
G. Baffou, C. Girard, E. Dujardin, G. Colas des Francs, and O. Martin, Physical Review B **77**, p. 121101(R) (2008).
- [71] C. Cohen-Tannoudji, J. Dupont-Roc, and G. Grynberg, Processus d'interaction entre photons et atomes, CNRS Editions, Paris, 1996.
- [72] Electromagnetic field quantization in absorbing dielectrics
R. Matloob, R. Loudon, S. M. Barnett, and J. Jeffers, Physical Review A **52**, pp. 4823–4838 (1995).
- [73] Spontaneous decay in the presence of dispersing and absorbing bodies : General theory and application to a spherical cavity
H. T. Dung, L. Knöll, and D.-G. Welsch, Physical Review A **62**, p. 053804 (2000).
- [74] Surface Plasmon Amplification by Stimulated Emission of Radiation : Quantum Generation of Coherent Surface Plasmons in Nanosystems
D. J. Bergman and M. I. Stockman, Physical Review Letters **90**, p. 027402 (2003).
- [75] Demonstration of a spaser-based nanolaser
M. A. Noginov, G. Zhu, A. M. Belgrave, R. Bakker, V. M. Shalaev, E. E. Narimanov, S. Stout, E. Herz, T. Suteewong, and U. Wiesner, Nature **460**, pp. 1110–1112 (2009).
- [76] Guiding of a one-dimensional optical beam with nanometer diameter
J. Takahara, S. Yamagishi, H. Taki, A. Morimoto, and T. Kobayashi, Optics Letters **22** **22**, pp. 475–477 (1997).
- [77] Unidirectional Plasmon Propagation in Metallic Nanowires
R. M. Dickson and L. Lyon, Journal of Physical Chemistry B **104**, pp. 6095–6098 (2000).
- [78] Silver Nanowires as Surface Plasmon Resonators
H. Ditlbacher, A. Hohenau, D. Wagner, U. Kreibig, M. Rogers, F. Hofer, F. R. Aussenegg, and J. R. Krenn, Physical Review Letters **95**, p. 257403 (2005).
- [79] Crystalline structure's influence on the Near-field optical properties of single plasmonic nanowires
T. Laroche, A. Vial, and M. Roussey, Applied Physics Letters **91**, p. 123101 (2007).

- [80] The Moore's Law for photonic integrated circuits
 L. Thylen, S. He, L. L. Wosynki, and D. Dai, Journal of Zhejiang University Science A **7**, pp. 1961–1967 (2006).
- [81] R. G. Hunsperger, Integrated Optics : theory and technology, Springer, 2002.
- [82] Differential method for modelling dielectric-loaded surface plasmon polariton waveguides
 S. Massenot, J.-C. Weeber, A. Bouhelier, G. Colas des Francs, J. Grandidier, L. Markey, and A. Dereux, Optics Express **16**, pp. 17599–17608 (2008).
- [83] Integrated plasmonic waveguides : a mode solver based on density of states (DOS) formulation
Gérard Colas des Francs, J. Grandidier, S. Massenot, A. Bouhelier, J. Weeber, and A. Dereux, accepted (2009).
- [84] Polymer-metal waveguides characterization by Fourier plane leakage radiation microscopy
 S. Massenot, J. Grandidier, A. Bouhelier, G. Colas des Francs, J.-C. Weeber, L. Markey, and A. Dereux, Applied Physics Letters **91**, p. 243101 (2007).
- [85] Dielectric-loaded surface plasmon polariton waveguides : figures of merit and mode characterization by image and Fourier plane leakage microscopy
 J. Grandidier, S. Massenot, G. Colas des Francs, A. Bouhelier, J.-C. Weeber, L. Markey, A. Dereux, J. Renger, M. U. González, and R. Quidant, Physical Review B **78**, p. 245419 (2008).
- [86] Gain assisted propagation in a plasmonic waveguide at telecom wavelength
 J. Grandidier, Gérard Colas des Francs, S. Massenot, A. Bouhelier, L. Markey, J. Weeber, C. Finot, and A. Dereux, Nano Letters **9**, pp. 2935–2939 (2009).
- [87] Theory of surface plasmon-polariton amplification in planar structures incorporating dipolar gain media
 I. D. Leon and P. Berini, Physical Review B **78**, p. 161401 (2008).
- [88] Photons uniques et cryptographie quantique
 G. Messin and F. Treussart, Images de la Physique (CNRS), pp. 118–125 (2005).

Troisième partie

Annexes - Reproductions d'articles

A.1-Publications relatives au chapitre 2

"SNOM signal near plasmonic nanostructures : an analogy with fluorescence decay channels"

G. Colas des Francs, C. Girard, A. Bruyant and A. Dereux

Journal of Microscopy **229**, 302-306 (2008).

"Gain, detuning and directivity of nanoparticles optical antennas"

C. Huang, A. Bouhelier, G. Colas des Francs, A. Bruyant, A. Guénot, E. Finot, J.-C. Weeber and A. Dereux

Physical Review B **78** 155407 (2008).

"Generalized Bloch equations for optical interactions in confined geometries"

C. Girard, O. Martin, G. Lévêque, G. Colas des Francs and A. Dereux

Chemical Physics Letters **44**, 204 (2005).

SNOM signal near plasmonic nanostructures: an analogy with fluorescence decays channels

G. COLAS DES FRANCS*, C. GIRARD†, A. BRUYANT*

& A. DEREUX*

*Institut Carnot de Bourgogne, UMR 5209 CNRS, Université de Bourgogne, 9 avenue A. Savary,
F-21078 Dijon, France

†Centre d'Elaboration de Matériaux et d'Etudes Structurales (CNRS), 29, rue Jeanne Marvig BP
4347, F-31055 Toulouse, France

Key words. Antenna, fluorescence decay rate, Green's dyadic, plasmon, SNOM.

Summary

Scanning Near-field Optical Microscope (SNOM) is based on local excitations of nanostructures deposited on a substrate (illumination mode). Ideally, the local source behaves like a dipolar emitter so that the SNOM signal is strongly similar to the fluorescence decay rates of an excited molecule that would be located at the SNOM tip position. We present here how the SNOM signal near plasmonic nanostructures can be used to analyze radiative and non-radiative contribution to the fluorescence decay rate.

Introduction

In illumination mode, the scanning near-field optical microscope (SNOM) is used to excite locally nanostructures on a substrate (Novotny & Hecht, 2006). When the whole light (forbidden and allowed light) transmitted below the substrate is detected, the SNOM signal can be related to the local density of photonic states (LDOS) at the probe position (Chicanne *et al.*, 2002). This is of great interest in studying molecule fluorescence in confined geometry since the fluorescence rate depends on LDOS as described by the Fermi's golden rule. In addition, plasmonic nanostructures present strong field enhancement properties so that it is possible to increase significantly the fluorescence signal near plasmonic structures like in SERS (surface enhanced Raman spectroscopy) (Barnes, 1998; Stefani *et al.*, 2005; Anger *et al.*, 2006; Kühn *et al.*, 2006).

In this context, SNOM is a useful tool to characterize the plasmonic nanostructures properties (Imura *et al.*, 2005a). However, near the resonance, plasmonic structures present strong dissipation that can strongly affect the SNOM signal

(Colas des Francs *et al.*, 2005), in strong analogy with the fluorescence decay channels for a molecule located near a metallic system. We propose here to precise the analogy between the SNOM signal and the fluorescence rate and to explicitly detail how SNOM signal can be used to qualitatively evaluate the radiative and non-radiative channels contributions to the spontaneous relaxation of an excited molecule.

Fluorescence decay rate

Fermi's Golden rule in confined system

Due to its coupling to the environment, an excited molecule (with energy $\hbar\omega_0$) spontaneously relaxes to its ground level with the probability given by Fermi's golden rule in case of weak coupling

$$\Gamma(\mathbf{r}_m) = \frac{1}{\hbar\epsilon_0} \left(1 + \coth \frac{\hbar\omega_0}{2kT} \right) |\mu_0|^2 \text{Im}[\mathbf{u} \cdot \mathbf{S}(\mathbf{r}_m, \mathbf{r}_m, \omega_0) \cdot \mathbf{u}] \quad (1)$$

where \mathbf{S} is the field-susceptibility of the molecule surroundings, $\mu_0 = \mu_0 \mathbf{u}$ is the molecular emission dipole moment and \mathbf{r}_m represents the molecule position in the system. It is worthwhile to note that this relation remains valid for molecule near absorbing structures. At ambient temperature and for standard optical transitions, the term in bracket tends towards two so. Equation (1) simplifies to

$$\Gamma(\mathbf{r}_m) = \frac{2}{\hbar\epsilon_0} |\mu_0|^2 \text{Im}[\mathbf{u} \cdot \mathbf{S}(\mathbf{r}_m, \mathbf{r}_m, \omega_0) \cdot \mathbf{u}]. \quad (2)$$

This expression indicates how the presence of the surroundings perturbs the fluorescence decay rate Γ . Indeed, in vacuum, this expression reduces to the well-known level broadening

$$\Gamma_0 = \frac{|\mu_0|^2 \omega_0^3}{3\pi\epsilon_0\hbar c^3}. \quad (3)$$

Correspondence to: G. Colas des Francs, e-mail: gerard.colas-des-francs@u-bourgogne.fr

In addition, for a molecule placed in close vicinity of nanostructures, the decay rate is then modified according to Eqs (1)–(3):

$$\frac{\Gamma(\mathbf{r}_m)}{\Gamma_0} = 1 + \frac{6\pi}{k_0^3} \text{Im}[\mathbf{u} \cdot \mathbf{S}_{\text{obj}}(\mathbf{r}_m, \mathbf{r}_m, \omega_0) \cdot \mathbf{u}]. \quad (4)$$

In this expression, we have explicitly isolated the object contribution \mathbf{S}_{obj} to the field-susceptibility ($\mathbf{S} = \mathbf{S}_0 + \mathbf{S}_{\text{obj}}$ where \mathbf{S}_0 denotes the free-space field susceptibility). Relation (4) is strictly equivalent to the power radiated by a unit dipole \mathbf{u} normalized with its free-space power $P_0 = \omega_0^4 |\mathbf{u}|^2 / 12\pi c^3 \epsilon_0$. This leads to the classical description of fluorescence rate perturbation in confined geometry (Novotny & Hecht, 2006). In the following, we will only refer to this classical model as it is sufficient to describe the fluorescence rate modification. In this classical point of view, \mathbf{S} corresponds to the electric Green's dyad of the molecule surroundings (actually, the field-susceptibility is proportional to the electric Green's dyad: $\mathbf{S} = k_0^2 \mathbf{G}$ and the dipolar electric field is $\mathbf{E}(\mathbf{r}) = 1/\epsilon_0 \mathbf{S}(\mathbf{r}, \mathbf{r}_m, \omega_0) \cdot \mathbf{u}$).

Finally, the object contribution is easily deduced from the Dyson's equation ($\Delta\epsilon = \epsilon - 1$ with ϵ the object relative permittivity)

$$\mathbf{S}(\mathbf{r}, \mathbf{r}', \omega) = \mathbf{S}_0(\mathbf{r}, \mathbf{r}', \omega) + \mathbf{S}_{\text{obj}}(\mathbf{r}, \mathbf{r}', \omega) \quad (5)$$

$$\begin{aligned} \mathbf{S}(\mathbf{r}, \mathbf{r}', \omega) &= \mathbf{S}_0(\mathbf{r}, \mathbf{r}', \omega) + \int_{\text{obj}} d\mathbf{r}'' \mathbf{S}_0(\mathbf{r}, \mathbf{r}'', \omega) \\ &\times \Delta\epsilon(\mathbf{r}'', \omega) \mathbf{S}(\mathbf{r}'', \mathbf{r}', \omega). \end{aligned} \quad (6)$$

This self-consistent equation can be numerically solved by discretizing the object in N small cells of volume V_n ($n = 1, \dots, N$) and permittivity ϵ_n . The singularity of the free-space field-susceptibility \mathbf{S}_0 at the origin has to be treated very carefully. This leads to (Lakhtakia & Mulholland, 1993; Novotny & Hecht, 2006)

$$\begin{aligned} \mathbf{S}(\mathbf{r}_i, \mathbf{r}_j, \omega) &= \mathbf{S}_0(\mathbf{r}_i, \mathbf{r}_j, \omega) \sum_{n=1, N, n \neq i} \mathbf{S}_0(\mathbf{r}_i, \mathbf{r}_n, \omega) \\ &\times \Delta\epsilon_n V_n \mathbf{S}(\mathbf{r}_n, \mathbf{r}_j, \omega) + (\mathbf{M}_i \Delta\epsilon_i - \mathbf{L}) \mathbf{S}(\mathbf{r}_i, \mathbf{r}_j, \omega) \\ &\times (i, j = 1, \dots, N, j \neq i) \end{aligned} \quad (7)$$

where \mathbf{M}_i and \mathbf{L} come from the singularity treatment at the origin. More precisely, \mathbf{L} is the depolarization term and \mathbf{M}_i generalizes the radiative reaction of the finite size cell (Lakhtakia & Mulholland, 1993). They depend on the cell shape and can be evaluated for simple geometries analytically (Jaghjiani, 1980) or numerically (Chaumet *et al.*, 2004). For spherical cells of radius a , they are given by (Lakhtakia & Mulholland, 1993)

$$\mathbf{M} = \frac{2}{3} [(1 - ik_0 a) e^{ik_0 a} - 1] \mathbf{I} \quad (8)$$

$$\mathbf{L} = \frac{1}{3} \mathbf{I}. \quad (9)$$

The physical meaning of these equations appears clearer when considering one single nanoparticle of small radius ($k_0 a \ll 1$), located at \mathbf{r}_s . Then, the Dyson's equation is solved and the particle polarizability $\alpha(\omega)$ appears (Lakhtakia & Mulholland, 1993):

$$\mathbf{S}_{\text{obj}}(\mathbf{r}_i, \mathbf{r}_j, \omega) = \mathbf{S}_0(\mathbf{r}_i, \mathbf{r}_s, \omega) \cdot \alpha(\omega) \cdot \mathbf{S}_0(\mathbf{r}_s, \mathbf{r}_j, \omega) \text{ with} \quad (10)$$

$$\alpha(\omega) = \left[1 - \frac{k_0^2}{4\pi a \epsilon} \alpha_0(\omega) - i \frac{k_0^3}{6\pi \epsilon} \alpha_0(\omega) \right]^{-1} \alpha_0 \quad (11)$$

where $\alpha_0 = 4\pi a^3 (\epsilon(\omega) - 1) / (\epsilon(\omega) + 2)$ is the quasi-static polarizability of the nanoparticle. For a molecule at a distance d from the nanoparticle and with a dipole moment parallel to the particle surface (1), this leads to the following expression for the decay rate

$$\begin{aligned} \frac{\Gamma(\mathbf{r}_m)}{\Gamma_0} &= 1 + \frac{3k_0^3}{8\pi} \text{Im} \left[\alpha(\omega_0) \exp(2ik_0 d) \right. \\ &\times \left. \left(\frac{1}{(k_0 d)} + \frac{i}{(k_0 d)^2} - \frac{1}{(k_0 d)^3} \right)^2 \right]. \end{aligned} \quad (12)$$

In this expression, the term in bracket is the electric field backscattered at the molecule position by the excited nanoparticle, leading to the so-called driven-field description of the decay rate perturbation (Novotny & Hecht, 2006).

Decay channels

The spontaneous relaxation process can occur through two channels: the radiative emission of a photon and the non-radiative coupling to the sample with Joule dissipation into the metallic structure. These two terms can be calculated, respectively, as the power radiated in far-field and the power absorbed by the dissipative sample for an oscillating dipole modelling the excited molecule. Actually, it is simpler to calculate both the total rate Γ and the non-radiative rate Γ_{NR} so that the normalized radiative rate is the difference $\Gamma_{\text{rad}}/\Gamma_0 = \Gamma/\Gamma_0 - \Gamma_{\text{NR}}/\Gamma_0 = \Gamma/\Gamma_0 - Q_{\text{abs}}/P_0$ where Q_{abs} is the power absorbed in the sample, given by (Jackson, 1998; Colas des Francs *et al.*, 2005)

$$Q_{\text{abs}}(\mathbf{r}_m) = \frac{\omega_0 \epsilon_0}{2} \int_{\text{object}} \text{Im}[\epsilon(\mathbf{r}, \omega_0)] |\mathbf{E}(\mathbf{r}, \omega_0)|^2 d\mathbf{r} \quad (13)$$

$$= \frac{\omega_0}{2\epsilon_0} \int_{\text{object}} \text{Im}[\epsilon(\mathbf{r}, \omega_0)] |\mathbf{S}(\mathbf{r}, \mathbf{r}_m, \omega_0) \cdot \mathbf{u}|^2 d\mathbf{r}. \quad (14)$$

The normalized probability for relaxation through the non-radiative channel simplifies to the following analytical form considering a molecule coupled to a single nanoparticle

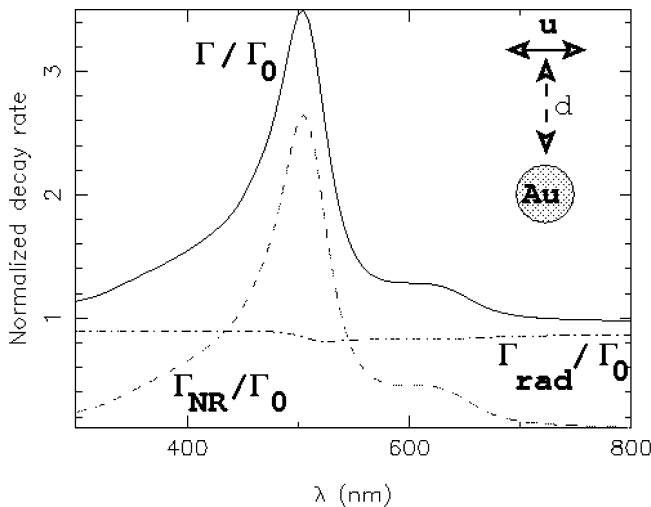


Fig. 1. Normalized decay rate calculated for a molecule located 15 nm above a 20 nm diameter gold nanoparticle. Solid line: decay rate, dotted line: non-radiative rate and dash-dotted line: radiative rate. The dipole moment is parallel to the particle surface. The gold permittivity is taken from Palik (1985).

(Fig. 1):

$$\frac{\Gamma_{NR}(\mathbf{r}_m)}{\Gamma_0} = \frac{Q_{abs}(\mathbf{r}_m)}{P_0} = \frac{3k_0^3}{8\pi} \left| \frac{1}{(k_0 d)} + \frac{i}{(k_0 d)^2} - \frac{1}{(k_0 d)^3} \right|^2 \left[Im(\alpha(\omega_0)) - \frac{k_0^3}{6\pi} |\alpha(\omega_0)|^2 \right]. \quad (15)$$

It appears here that the non-radiative rate is simply the extinction cross-section minus the scattering cross-section as expected from energy conservation considerations (Das & Puri, 2002; Colas des Francs *et al.*, 2005; Carminati *et al.*, 2006).

Figure 1 represents the decay rates contributions calculated near a gold nanoparticle. The total decay rate is only weakly perturbated except near the plasmon resonance (around 510 nm) where strong dissipation appears, opening a new decay channel (Gersten & Nitzan, 1981; Dulkeith *et al.*, 2002; Colas des Francs *et al.*, 2005; Carminati *et al.*, 2006). Unfortunately, the non-radiative process dominates the spontaneous relaxation, so that a very low fluorescence quantum yield is observed near the plasmon resonance (Colas des Francs *et al.*, 2005; Carminati *et al.*, 2006; Anger *et al.*, 2006; Kühn *et al.*, 2006).

SNOM signal

We now consider the signal recorded with a SNOM setup. In SNOM configuration, a sample deposited on a transparent surface is locally excited with a probe tip and the light transmitted below the surface is collected with a high numerical aperture. Every SNOM tip is generally based on two principles: a localized source or a subwavelength sink is built in the cut-off region of an optical fiber. The localized source can

be either a fluorescent molecule, a quantum dot, a plasmonic edge mode or a metallic nanoparticle. The subwavelength sink is simply an aperture opened inside a metal coated optical fiber, which has been elongated below its cut-off diameter. Very recently, it was also proposed and achieved to gather these two principles, forming a ‘tip on aperture’ with a highly confined electromagnetic field (Frey *et al.*, 2004; Taminian *et al.*, 2007). Another improvement can also be obtained by coupling the source with a resonant antenna, in a bowtie antenna (for a recent review, see the chapter 6 of ref. Novotny & Hecht, 2006, and reference therein).

The exact nature of the emitted signal strongly depends on the tip shape and nature and is beyond the scope of this paper. Nevertheless, some important feature can be easily deduced from a multipole expansion for localized source or aperture in waveguide (Jackson, 1998). Obviously, the multipole expansion converges satisfactorily for a small source or hole so that it is well adapted to near-field optical probes. Apart from the aperture probes which behaves like a magnetic dipole, the SNOM can be generally modelled by an electric dipole (Novotny & Hecht, 2006). We propose to analyze SNOM images within this model. More precisely, the SNOM tip is modelled by an effective dipole not necessarily located at the tip end and the signal recorded below the surface when the tip is raster scanned above the sample is easily deduced from the Green’s dyad formalism. We do not reproduce here the equations since they can be found in the literature (Colas des Francs *et al.*, 2002; Novotny & Hecht, 2006). Using this formalism, we have demonstrated both theoretically and experimentally, that the SNOM signal is a good approximation of the normalized fluorescence decay rate when considering poorly dissipative system (Chicanne *et al.*, 2002). Here we attempt to generalize this result and to show how the SNOM signal can be used to determine the decay channel available for a molecule located close to plasmonic nanostructures. Obviously, this comparison relies on the dipolar like emission of the SNOM tip. This point is in good agreement with previous experiments done even near plasmonic structures (Novotny *et al.*, 1997).

Let us consider a gold nanorod as a typical sample for our numerical study. Such plasmonic structures are widely studied for possible applications for subwavelength waveguiding (Ditlbacher *et al.*, 2005) or spectroscopic enhancement (Bouhelier *et al.*, 2005; Imura *et al.*, 2005). The calculated spectrum is given on Fig. 2, showing a plasmonic resonance at wavelength 633 nm which could be easily excited with standard He–Ne laser.

We reproduce on Fig. 3 the different contributions to the decay rate of a molecule located near the gold nanorod. We have also represented on Fig. 4 the normalized SNOM signal calculated considering an effective dipole which is scanned over the same sample. Strictly speaking, the normalized radiative decay rate is equivalent to the total intensity detected *below and above* the substrate when a dipole is scanned over the sample.

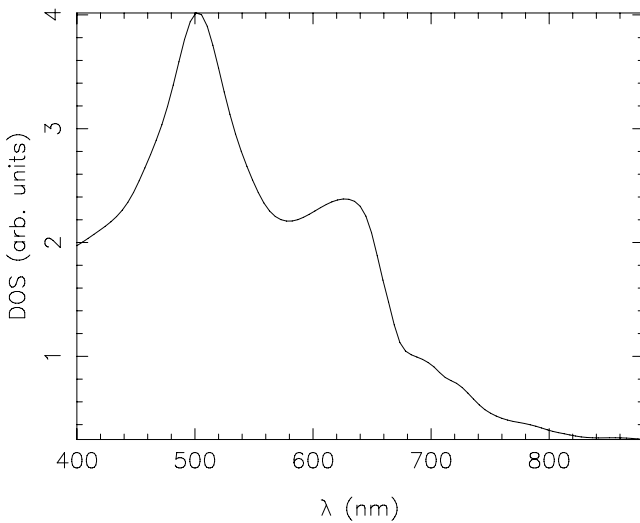


Fig. 2. DOS spectrum of a gold nanorod ($20 \times 20 \times 420 \text{ nm}^3$) deposited on a glass substrate.

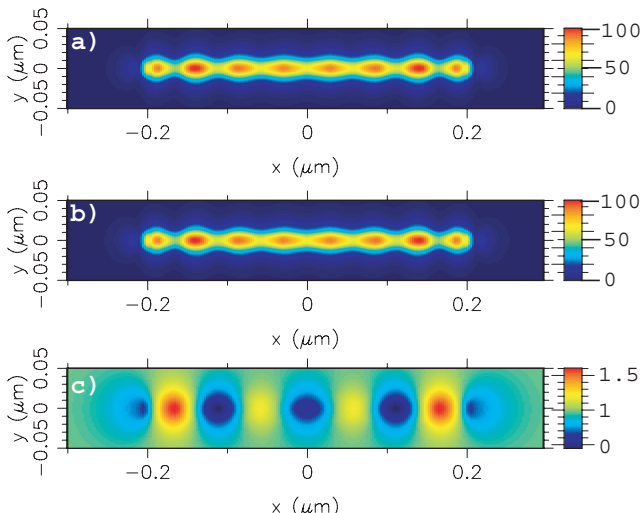


Fig. 3. (a) Normalized decay rate map above the gold nanorod at $\lambda = 633 \text{ nm}$. (b) Non-radiative contribution to the decay rate. (c) Radiative contribution to the decay rate obtained as the difference between (a) and (b). The transition dipole is along the long axis of the rod (x -axis) and located 10 nm above the nanorod.

However, we observe that the agreement with the transmitted signal only remains qualitatively good (compare Figs 3c and 4a). Therefore, SNOM setup with high numerical aperture should reveal some interesting information about the decay channels for an excited molecule located in close proximity of plasmonic structures. Let us mention that considering non-absorbing system, the agreement between the transmitted SNOM signal and the decay rate is almost perfect (Colas des Francs *et al.*, 2001).

Recently, in a original experiment Imura *et al.* demonstrated that the SNOM signal goodly reproduces the total decay rate, even near plasmonic resonances (Imura *et al.*, 2005a).

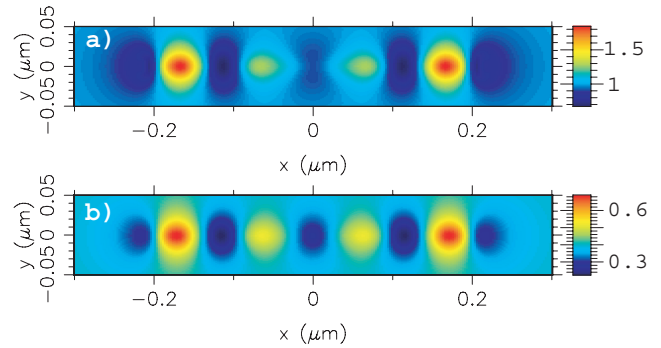


Fig. 4. (a) Normalized transmitted intensity detected below the surface when the effective dipole modellizing the SNOM tip is scanned 10 nm above the nanorod ($\lambda = 633 \text{ nm}$). (b) Normalized reflected intensity that should be detected above the substrate in reflection SNOM mode. The effective dipole is along the x -axis. The signals are normalized with respect to the intensity recorded without the rod on the surface.

Particularly, they measure the dispersion curve of gold nanorods. Although the SNOM tip end they used was in close proximity of the nanorods during the scan, their images do not reproduce the expected perturbation due to Joule dissipation inside the metallic structures. This indicates that the effective dipole that should modellize the SNOM tip is further away from the very tip end (Radko *et al.*, 2006).

Conclusion

We have demonstrated that SNOM setup with high numerical aperture should delivered a signal similar to the normalized radiative decay rate of a molecule located at the tip position. This is of great interest for qualitative and versatile study of metallic sample before doing more precise dynamical fluorescent measurement. Moreover, the formalism detailed in section II is also relevant for numerical study of fluorescent decay rates near plasmonic structures of arbitrary shape.

Acknowledgments

This work benefits from the financial support of the Specific Target Research Project (STREP) ASPIRENT (contract No. NMP-CT-2003-001601) and of the Network of Excellence (NoE) Plasmo-Nano-Devices (contract No. FP6 2002-IST-1-507879) in the sixth Framework Program of the European Community.

References

- Anger, P., Bharadwaj, P. & Novotny, L. (2006) Enhancement and quenching of single-molecule fluorescence. *Phys. Rev. Lett.* **96**, 113002.
- Barnes, W.L. (1998) Fluorescence near interfaces: the role of photonic mode density. *J. Modern Opt.* **45**, 661–699.
- Bouhelier, A., Bachelot, R., Lerondel, G., Kostcheev, S., Royer, P. & Wiederrecht, G.P. (2005) Surface plasmon characteristics of tunable photoluminescence in single gold nanorods. *Phys. Rev. Lett.* **95**, 267405.

- Carminati, R., Greffet, J., Henkel, C. & Vigoureux, J. (2006) Radiative and non-radiative decay of a single molecule close to a metallic nanoparticle. *Opt. Commun.* **261**, 368–375.
- Chaumet, P.C., Sentenac, A. & Rahmani, A. (2004) Coupled dipole method for scatterers with large permittivity. *Phys. Rev. E* **70**, 36606.
- Chicanne, C., David, T., Quidant, R. et al. (2002) Imaging the local density of states of optical corrals. *Phys. Rev. Lett.* **88**, 97402–1–4.
- Colas des Francs, G., Girard, C. & Dereux, A. (2002) Theory of near-field imaging with a single molecule light source. *J. Chem. Phys.* **117**, 1–8.
- Colas des Francs, G., Girard, C., Juan, M. & Dereux, A. (2005) Energy transfer in near-field optics. *J. Chem. Phys.* **123**, 174709.
- Colas des Francs, G., Girard, C., Weeber, J.C. & Dereux, A. (2001) Relationship between scanning near-field optical images and local density of states. *Chem. Phys. Lett.* **345**, 512–515.
- Das, P. & Puri, A. (2002) Energy flow and fluorescence near a small metal particle. *Phys. Rev. B* **65**, 155416.
- Ditlbacher, H., Hohenau, A., Wagner, D. et al. (2005) Silver nanowires as surface plasmon resonators. *Phys. Rev. Lett.* **95**, 257403.
- Dulkeith, E., Morteani, A.C., Niedereichholz, T. et al. (2002) Fluorescence quenching of dye molecules near gold nanoparticles: radiative and nonradiative effects. *Phys. Rev. Lett.* **89**, 203002.
- Frey, H., Witt, S., Felderer, K. & Guckenberger, R. (2004) High-resolution imaging of single fluorescent molecules with the optical near-field of a metal tip. *Phys. Rev. Lett.* **93**, 200801.
- Gersten, J. & Nitzan, A. (1981) Spectroscopic properties of molecules interacting with small dielectric particles. *J. Chem. Phys.* **75**, 1139–1152.
- Imura, K., Nagahara, T. & Okamoto, H. (2005a) Near-field optical imaging of plasmon modes in gold nanorods. *J. Chem. Phys.* **122**, 154701.
- Imura, K., Nagahara, T. & Okamoto, H. (2005b) Near-field two-photon-induced photoluminescence from single gold nanorods and imaging of plasmon modes. *J. Phys. Chem. B* **109**, 13214–13220.
- Jackson, J. (1998) Classical electrodynamics. Hoboken, 3rd edn. John Wiley & Sons, New York.
- Jaghjiani, A.D. (1980) Electric dyadic green's functions in the source region. *Proc. IEEE* **68**, 248–263.
- Kühn, S., Hakanson, U., Rogobete, L. & Sandoghdar, V. (2006) Enhancement of single-molecule fluorescence using a gold nanoparticle as an optical nanoantenna. *Phys. Rev. Lett.* **97**, 17402.
- Lakhtakia, A. & Mulholland, G. W. (1993) On two numerical techniques for light scattering by dielectric agglomerated structures. *J. Res. Natl. Inst. Standards Technol.* **98**, 699–716.
- Novotny, L., Hecht, B. & Pohl, D. W. (1997) Interference of locally excited surface plasmons. *J. Appl. Phys.* **81**, 1798–1806.
- Novotny, L. & Hecht, B. (2006) Principles of nano-optics. Cambridge University Press, New York.
- Palik, Z. (1985) *Handbook of Optical Constants of Solids*. Academic, San Diego, CA.
- Radko, I., Bozhevolnyi, S. & Gregersen, N. (2006) Transfer function and near-field detection of evanescent waves. *Appl. Opt.* **45**, 4051–4061.
- Stefani, F.D., Vasilev, K., Bocchio, N., Stoyanova, N. & Kreiter, M. (2005) Surface-plasmon-mediated single-molecule fluorescence through a thin metallic film. *Phys. Rev. Lett.* **94**, 23005.
- Taminiau, T., Moerland, R., Segerink, F., Kuipers, L. & van Hulst, N. (2007) $\lambda/4$ Resonance of an optional monopole antenna probed by single molecule fluorescence. *Nano. Lett.* **7**, 28–33.

Gain, detuning, and radiation patterns of nanoparticle optical antennas

C. Huang, A. Bouhelier,* G. Colas des Francs, A. Bruyant,[†] A. Guenot, E. Finot, J.-C. Weeber, and A. Dereux
Institut Carnot de Bourgogne, CNRS-UMR 5209, Université de Bourgogne, 21078 Dijon, France
 (Received 4 August 2008; published 7 October 2008)

For their capability to localize and redirect electromagnetic field, metal nanoparticles have been recently viewed as efficient nanoantenna operating in the optical regime. In this article, we experimentally investigated the optical responses of coupled gold antenna pairs and measured the critical parameters defining antenna characteristics: resonant frequencies and bandwidths, detuning and gains, and radiation patterns.

DOI: 10.1103/PhysRevB.78.155407

PACS number(s): 42.30.Va, 73.22.Lp, 78.67.Bf

I. INTRODUCTION

Optical antennas are fundamental devices for interfacing light wave to nanoscale elements because of their capability to drastically confine and direct incoming radiation to relevant dimensions.^{1–3} In the optical regime, this property originates from surface plasmon resonances and scattering properties of metal nanoparticle(s) constituting an optical antenna. Understanding the optical response of antenna/metal nanoparticles has therefore been a center of interest from the designer point of view. It is interesting to note that mainly two particle-dependent quantities are driving research efforts for fabricating optimal optical antennas. First, it was realized that radiowave antenna concepts are not fully applicable in the optical regime. To correctly design the dimensions of an optical antenna, an effective wavelength taking into account the surface plasmon resonant frequency was introduced.^{4–7} Single-particle dark-field spectroscopy is usually employed to provide the spectral location of resonances, giving thus insights about dimensions of an antenna⁸ and possible near-neighbor coupling mechanisms.^{9,10} Second, optical antennas characterized by strong plasmon resonances provide an important mechanism for locally amplifying electromagnetic field. This characteristic is of particular interest to enhance weak optical responses such as single-molecule Raman scattering.¹¹ The field enhancement factor of a given antenna geometry is generally deduced from measurements involving the optical response to amplify: Raman scattering,¹² fluorescence,⁷ or nonlinear photoluminescence.^{1,13,14} While these type of signals inform about antenna's amplification at the molecular probe *emission* wavelength, they do not directly provide antenna's property at the wavelength used to *excite* them. Furthermore, the spectroscopic response of metal nanoparticles is known to be extremely sensitive to the surrounding environment. An external molecular reporter has therefore a perturbative influence on antenna characteristics.¹⁵

In this article, we report on nonperturbative experimental investigations of single optical antennas constituted of individual gold nanoparticles and dimers. In particular, we measured important parameters defining an optical antenna: spectral coverage, detuning, bandwidth, gain, and partial radiation pattern. To the difference with previous studies involving molecular probes, we are measuring antennas' characteristics at the excitation frequency, providing thus an important experimental tool to the designer.

II. EXPERIMENT

Our approach essentially relies on the experimental measurement of the partial local electromagnetic density of states (LDOS) obtained by integrating the differential scattering cross section of the antenna.¹⁶ The LDOS uniquely describes the available optical eigenmodes in which photons can exist at a specific spatial location,¹⁷ and any resonances occurring in an antenna will be encoded in the measured signal. Our apparatus, schematically described in Fig. 1(a), is based on efficient Fourier filtering of the specular scattered modes. As opposed to confocal dark-field microscopy,¹⁸ our detection scheme retains only the frustrated evanescent components of the antenna (a more detailed description can be found in Ref. 16). The integrated forward-scattered intensity is detected in the image plane of the microscope by a photomultiplier (PMT) in a confocal-type arrangement. The antennas are scanned through the excitation and detection volumes to reconstruct an image of the scattering magnitude. The alignment of the illumination and detection was adjusted in the axial direction to maximize the scattered intensity detected and to reduce the point-spread function to a diffraction-limited response. To obtain the radiation diagram of the antennas, a charge-coupled device (CCD) appropriately placed at the Fourier plane (conoscopic detection) records the angular distribution of the evanescent modes collected by the 1.45 N. A. collection objective. More details on the arrangement will be given in Sec. IV.

The antennas were fabricated by electron-beam lithography followed by standard lift-off procedure and gold thermal evaporation. The nanoparticles forming the antennas have a varying diameter ranging from 66 to 90 nm and a height of ca. 70 nm. For the dimer antennas, the distance between particles (edge-to-edge) was systematically varied from 140 nm down to contact with a minimum separation distance of 10 ± 2 nm. Figure 1(b) shows electron micrographs of dimer antennas together with close up images of selected pairs. The spacing between dimers was kept constant to 3 μm to avoid any significant array-induced optical coupling between dimers.

III. DETUNING AND GAIN OF OPTICAL ANTENNAS

Figure 2 shows a two-dimensional scan of the scattered intensity from an array of individual antennas at an excitation wavelength $\lambda_{\text{exc}}=633$ nm. The polarization of the inci-

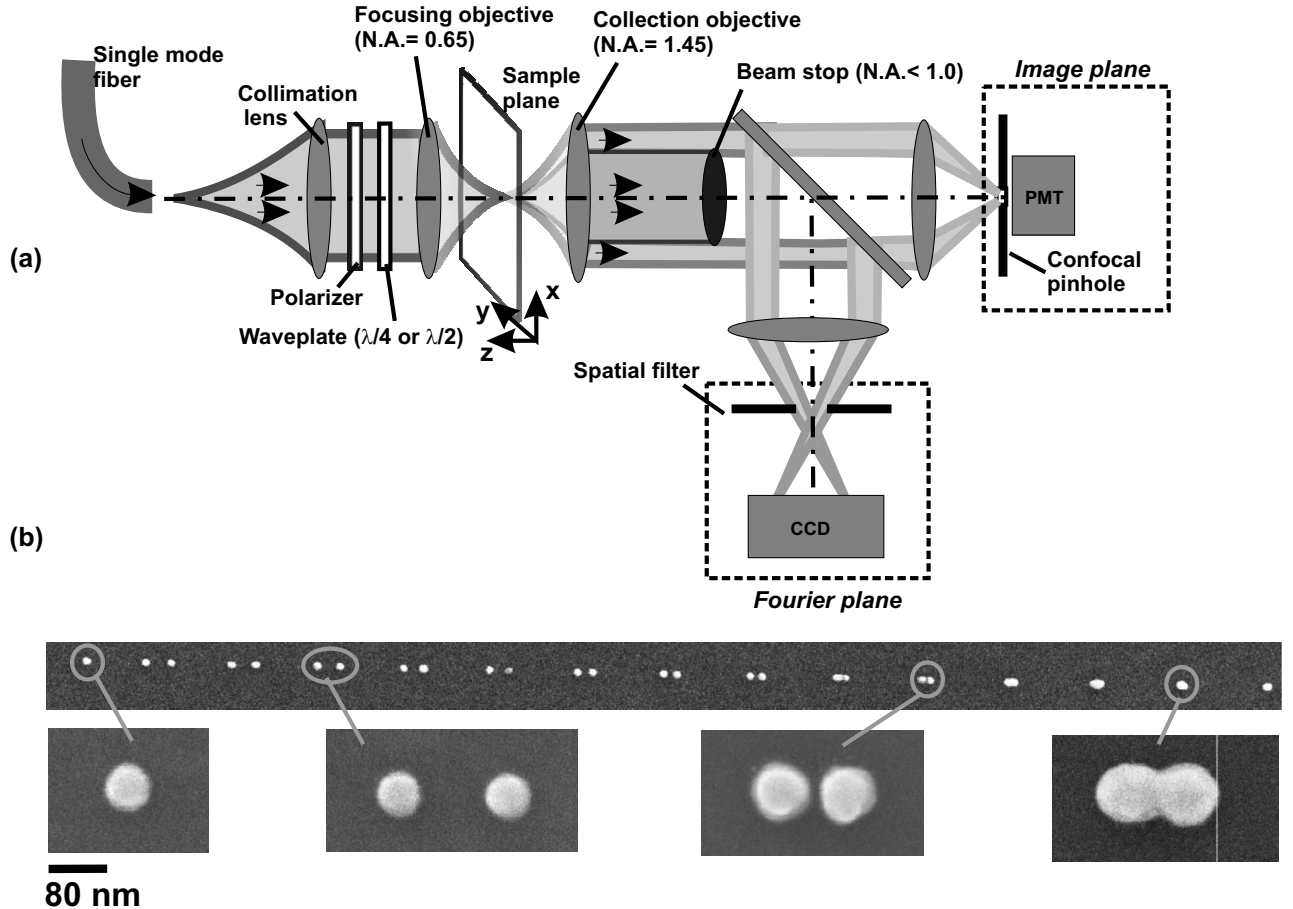


FIG. 1. (a) Experimental scheme. The antennas are illuminated by a 0.65 N. A. objective and the scattered components are collected by a 1.45-N. A. lens. The evanescent scattered angular spectrum is Fourier selected by a beam stop. (b) Electron micrographs of some of the antennas characterized in this study.

dent light was oriented along the dimer [Fig. 2(a)] or perpendicular to it [Fig. 2(b)] as indicated by the white arrows. The diameter of the antennas and the gap distance were systematically varied within the array [dotted arrows on the left and on the top of Fig. 2(a)] from 66 nm to 90 nm and from contact to approx. 140 nm, respectively. The first column on the left corresponds to scattering from single gold nanoparticles whereas the last two columns on the right of the array are bridged particles [see electron micrographs in Fig. 1(b)].

For a given polarization, the magnitude of the scattered intensity is not constant within the array. In Fig. 2(a) for instance, the brightest antennas appear for larger particle diameters and smaller gaps consistent with an increase in the scattering cross section for larger particles. Figures 2(c) and 2(d) are three-dimensional (3D) renderings of the boxed lines in Figs. 2(a) and 2(b). For a polarization oriented along the dimer, the scattered intensity increases by reducing the gap between dimers before an abrupt falloff for the last two antennas (bridged particles: red circle). Interestingly, Fig. 2(d) shows an almost constant intensity regardless of the gap even for the two particles that are in contact (red circle).

To gain understanding on these intensity variations, we systematically measured scattered spectra from individual coupled antennas using dark-field spectroscopy. Typical spectra scattered from a single dimer with an approximate

10-nm gap and 70-nm diameter are shown in Fig. 3(a) for unpolarized illumination and for a polarization parallel and perpendicular to the dimer axis, respectively. As the result of a strong coupling between the two interacting particles, a well-known hybridization of the resonance occurs.^{19,20} Figure 3(b) shows typical dependence of the resonance maxima λ_{sp} for varying gaps and for particle diameter of 80 nm. The vertical bars indicate the full width at half maximum of the resonances. The splitting of λ_{sp} starts for particle separation below 30 nm and a redshift of λ_{sp} is observed for a polarization oriented along the main axis of the antennas in accordance with the literature.^{21,22} We note that averaged measurements on large arrays of coupled nanoparticles revealed a small blueshift of the resonance for an electric field perpendicular to the main axis.²¹ We do not see such a shift in our single-dimer measurements. Instead, we measured a systematic redshift of the resonances [Fig. 3(b)]. We attribute this difference to the unique fingerprints of individual dimers. These individual different responses can also be observed from dimers with large gaps (>50 nm) whereby the position of the maxima exhibits spectral oscillations despite nominally comparable particles [Fig. 3(b)].

To correlate the variations in the scattered intensity at the laser frequency with the spectral signature of the antenna, we define the amount of detuning $|\delta\lambda|$ by differentiating the la-

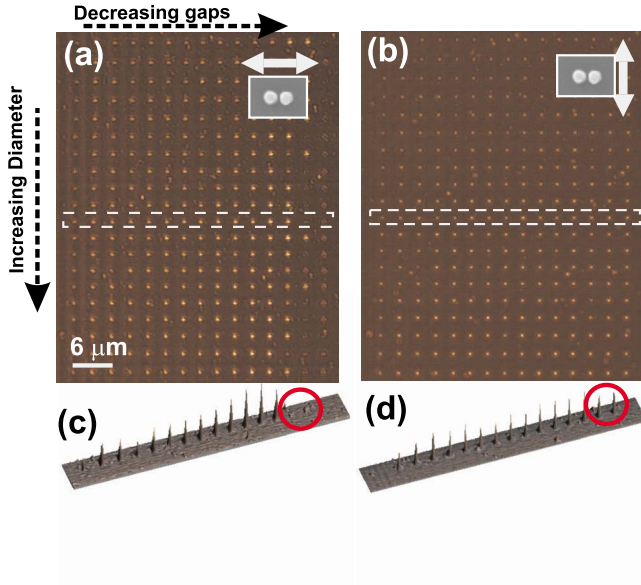


FIG. 2. (Color online). (a) and (b): Scattering intensities at $\lambda = 633$ nm from single antennas constituted of gold nanoparticle dimers for a polarization parallel to the dimer axis and perpendicular to it, respectively (white arrows). The first column on the left is single-particle antenna, and the two last columns on the right are bridged particles. Top line displays particles with diameter of 60 nm increasing up to 90 nm for the bottom line. (c) and (d) are 3D rendering of the dotted line in (a) and (b).

ser wavelength to the resonance maxima: $|\delta\lambda| = |\lambda_{\text{exc}} - \lambda_{\text{sp}}|$. Let us also introduced the relative gain G of an antenna. In antenna theory, G describes the ability of an antenna to increase scattered intensity in the direction of the peak radiation. This parameter is usually normalized from a reference radiator, i.e., a dipole.²³ For small particles compared to the wavelength of light, an isolated spherical nanoparticle behaves essentially like a dipole. We therefore define G by measuring the magnitude of the scattered intensities I_d originating from dimers and normalizing it to the one issued from single-particle antennas I_s of the same diameter: $G = I_d/I_s$. This definition assumes that the scattered angular distribution and the collection efficiency of our experimental setup are constant regardless of the particle arrangement. The validity of this assumption will be asserted in Sec. IV.

Figure 4(a) shows the evolution of the parameters $|\delta\lambda|$ and G by reducing the gap between the dimer and for an excitation field at 633 nm polarized along the dimer axis. For large gaps (>50 nm), detuning from the excitation laser $|\delta\lambda|_{633 \text{ nm}}$ is kept below 25 nm, indicating that the antennas are close to resonance with the laser line. This is confirmed by the trend of the G factor, which varies around 2.5. For a group of identical particles characterized by a weak mutual optical interaction, G should scale linearly with the number of particle present in the detection volume if the excitation is homogeneous. However, the measured value is slightly larger than the expected value ($G=2$). We think this small difference originates from the polarization-sensitive inhomogeneous field distribution inside the excitation and detection volumes.^{24,25}

For smaller gaps, a strong electromagnetic coupling between the particles constituting the antenna rapidly increases

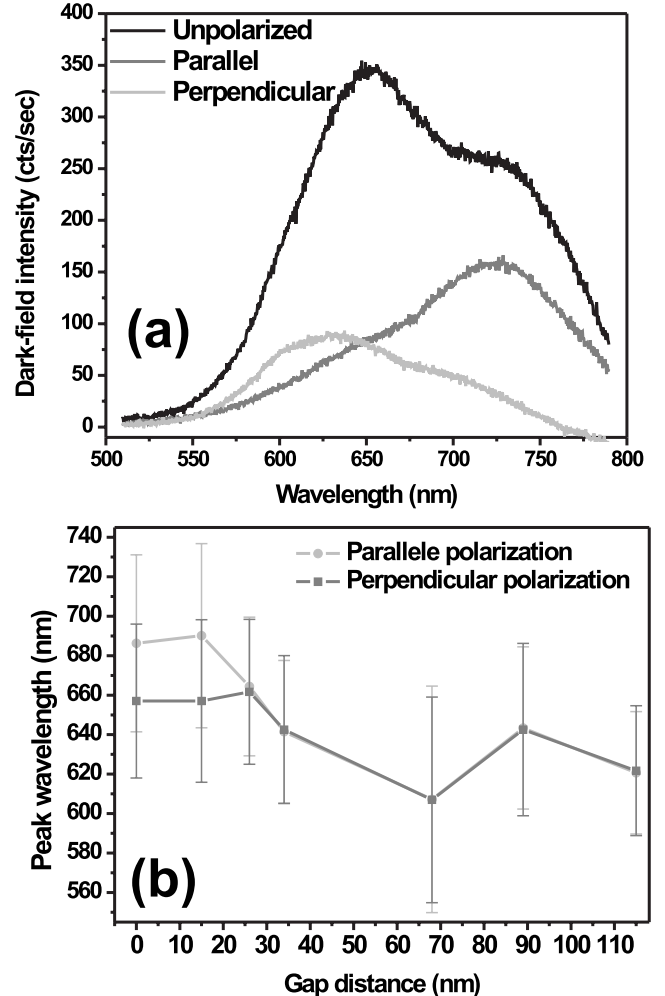


FIG. 3. (a) Characteristic spectra for an isolated strongly coupled dimer. The unpolarized spectrum (black) features two polarization-sensitive resonances identified by a polarized excitation (dark gray and gray). Gap ~ 10 nm and particle diameter 70 nm. (b) Dependence of the dimer resonance(s) on the gap values. For small gaps, a redshift and a hybridization of the resonances are observed. The vertical bars indicate the breadth of the resonances. The particle diameter is 80 nm.

the amount of detuning and $|\delta\lambda|_{633 \text{ nm}}$ reaches 55 nm for a 15-nm gap. In this coupling regime, G dramatically drops from a maximum of 3.3 to a value of 0.3 for the bridged dimer, indicating that the optical antenna is detuned from its optimum excitation frequency.

Figure 4(b) shows the trend of $|\delta\lambda|_{633 \text{ nm}}$ and G for a polarization oriented perpendicular to the dimer. $|\delta\lambda|_{633 \text{ nm}}$ oscillates around 15 nm and stays within the full width at half maximum of the surface plasmon resonances [see Fig. 3(b)]. The gain features two plateaus of almost constant G values ($G=2.3$ and 1.6 with variations $\sim 10\%$) for gaps below 50 nm and gaps above 50 nm, respectively. Since $|\delta\lambda|_{633 \text{ nm}}$ stays near resonance with the excitation line and G is close to its expected value of 2, we also attribute these two plateaux to the particularity of the focal field distribution: it's only when the particles are close to each other that the excitation intensity can be assumed to be spatially constant. We

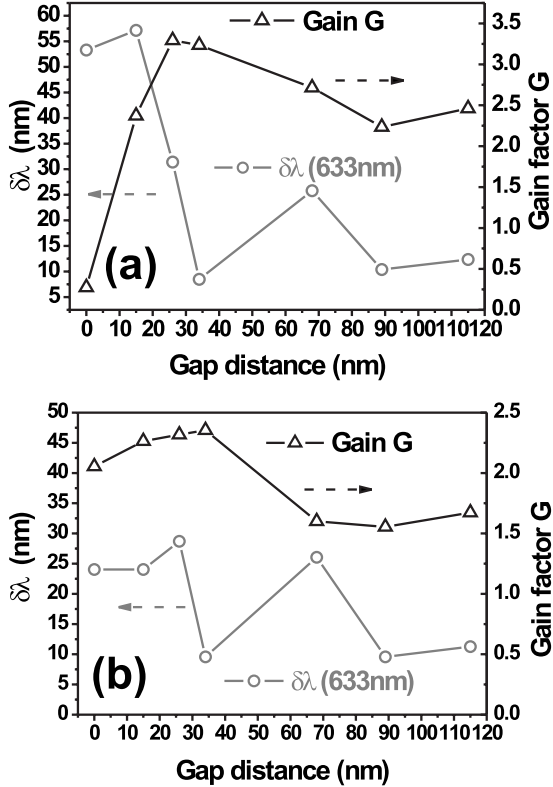


FIG. 4. (a) and (b): Detuning factor $|\delta\lambda|_{633 \text{ nm}}$ (gray) and gain factor G (black) for parallel and perpendicular polarizations with respect to the dimer axis, respectively. Particle diameter: 80 nm.

note that the experimental magnitude of G does not reach very large enhancement values as predicted from strongly coupled nanoparticle pairs and small gaps.^{26,27} This relatively low gain have also been observed in Ref. 28. It is worth emphasizing that the enhancement factors calculated in the literature are usually normalized to the applied field, whereas in the present work we compare G to a reference dipolar antenna. We note that $|\delta\lambda|_{633 \text{ nm}}$ and to some extend G show some oscillatory behavior with increasing gap distance. This particularity is observed regardless of the particle size within the fabricated array and polarization orientation. We did not see in our measurement a systematic correlation between the positions of the oscillatory peaks and the interparticle distance. We therefore believe that the observed oscillations are resulting from variations in the antenna morphology inherent to the fabrication process.

In only one instance in the study of the array depicted in Fig. 2(a) was G significantly increased. Figure 5 shows experimental values of G and $|\delta\lambda|_{633 \text{ nm}}$ for the upper most line of the array (particle diameter is 66 nm) and a polarization oriented along the axis joining the dimers. In this graph, we observed typical spectral variation in $|\delta\lambda|_{633 \text{ nm}}$ for large gaps already seen in Fig. 4(a). The gain factor is constant for the two largest gaps ($G \sim 2$) and displays a small increase for the 37-nm-gap dimer consistent with the low value of $|\delta\lambda|_{633 \text{ nm}}$. For smaller gaps however, the antennas are being detuned and yet G keeps increasing to reach a value of 6.3 for the 18-nm-gap dimer. G undergoes then an abrupt falloff for the bridged pair. Despite the antennas being detuned with

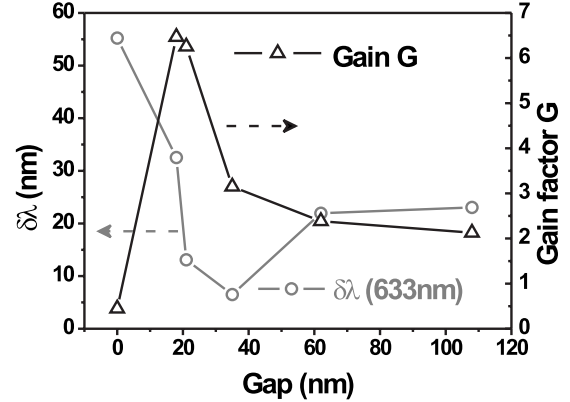


FIG. 5. Detuning factor $|\delta\lambda|_{633 \text{ nm}}$ and gain factor G for parallel with respect to the dimer axis, respectively. Particle diameter is 66 nm.

respect to the laser line, the optical coupling and field amplification characterizing these particular antennas were sufficient to not only compensate G for the detuning of the antenna but also enhance it by a sixfold factor. The measured gain for this coupled antenna was not reproduced inside the fabricated array and emphasizes the difficulty to design electromagnetic hotspots by such fabrication technique.

To validate our approach, we investigated the antenna array depicted in Fig. 2 at a laser wavelength of 780 nm. Figure 4(a) demonstrated a rapid decrease in G when the antennas are red detuned from the excitation at 633 nm. It is therefore expected that by reducing the detuning by using a 780-nm laser line, the gain will be restored. Figure 6(a) displays the evolution of G and $|\delta\lambda|_{780 \text{ nm}}$ for the same set of antennas featured in Fig. 4(a) and for a polarization parallel to the dimer. For decreasing gaps, $|\delta\lambda|_{780 \text{ nm}}$ also decreases as a consequence of the redshift of the resonance, and as hypothesized, strongly coupled dimers exhibit a significant recovering of G . To the difference with an illumination at 633 nm, antennas characterized by small gaps are tuned toward resonance for a 780-nm-excitation line. It should be noted that the relatively high values of G (up to $G \sim 17$) originate from the weak intensity I_s scattered by the referenced single particle. This single-particle antenna is not at resonance at 780 nm.

Figure 6(b) showed the case for a perpendicular polarization. $|\delta\lambda|_{780 \text{ nm}}$ indicates that the antenna is significantly detuned for this polarization regardless of the gap size. Accordingly, the antenna gains have low values compared to the orthogonal polarization. Nonetheless, a slow decrease in $|\delta\lambda|_{780 \text{ nm}}$ for small gaps is observed concomitant to a two-fold increase in G .

IV. RADIATION PATTERNS OF OPTICAL ANTENNAS

With radio-frequency antenna,²³ the radiated power at large distances is the parameter of interest, and radiation patterns are traditionally measured considering the antenna in an homogenous dielectric medium. Optical antennas, however, are typically fabricated on a substrate and the presence of an interface considerably modifies the radiation pattern.

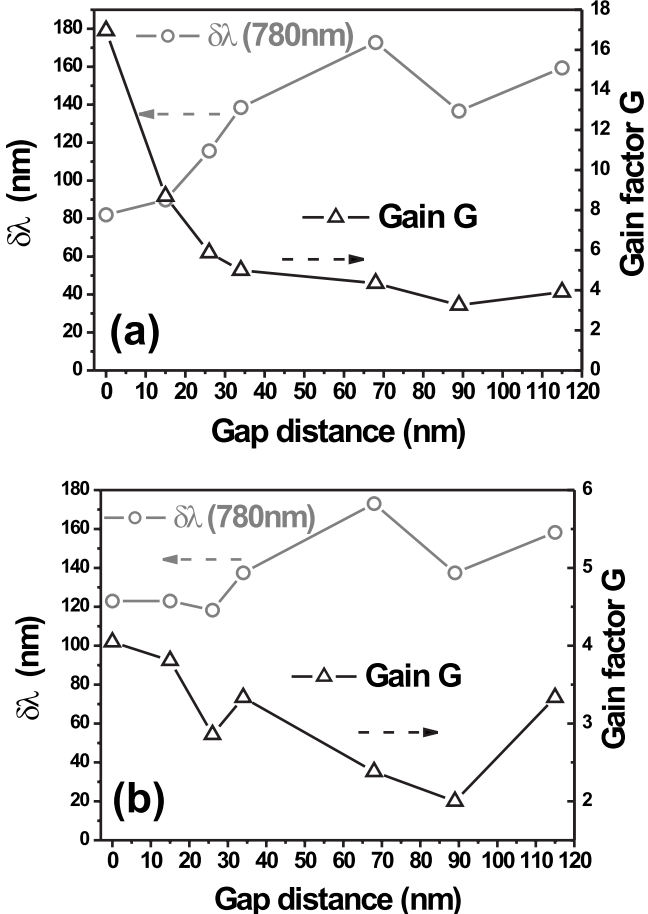


FIG. 6. (a) and (b) Detuning factor $|\delta\lambda|_{780 \text{ nm}}$ and gain factor G for a 780-nm excitation wavelength and for a polarization oriented along the dimer axis and perpendicular to it, respectively. Particle diameter is 80 nm.

For small particles behaving like dipoles close to a dielectric interface, the radiated power is principally emitted in the denser medium at the critical angle,²⁹ and backward scattering can be neglected. We use a 1.45 oil-immersion objective [Fig. 1(a)] to retrieve this forward-scattered contributions. At the exit pupil of the objective, i.e., the primary Fourier plane, the angular distribution of the scattered intensity is a direct measure of the radiation pattern in the substrate. With modern objective lenses, however, this primary Fourier plane is located inside the objective's body, and relay lenses are usually employed to image the objective's back aperture at a secondary Fourier plane.^{30–34}

To retrieve the near-field contribution and to discriminate it from the overwhelming illumination contribution, a beam stop removes the part of the light angularly distributed below the critical angle as sketched in Fig. 1(a). The filtering only retains radiated intensity corresponding to frustrated evanescent modes of the antenna collected by our objective, i.e., its partial induction field. In the following, the term radiation patterns will be referred to the angular distribution of the scattered intensity located above the critical angle and is therefore a partial measure of the total pattern.

Figure 7 shows experimental scattered diagrams for an optical antenna constituted of a single colloidal 80-nm Au

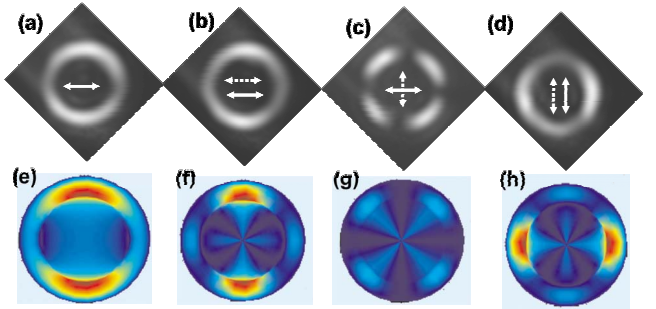


FIG. 7. (Color online). (a) to (d) Angular distributions of the intensity scattered by a single Au nanoparticle. The white arrow indicates the incident polarization and the broken arrow the analyzer orientation. The intensity peaks at the critical angle. (e) to (h) are the corresponding calculated intensity distributions.

nanoparticle illuminated by $\lambda_{\text{exc}}=633$ nm. Here we choose to utilize perfectly spherical nanoparticles from a colloidal solution to set a reference for the following and to avoid any shape-induced artifacts remnant with electron-beam lithography. Figure 7(a) represents the intensity distribution for a polarization indicated by the thick arrow. Two lobes perpendicularly oriented to the polarization are observed peaking at the critical angle. These lobes are characteristic from a dipole emission oriented parallel to a dielectric interface.³¹ This scattered pattern is in very good agreement with our numerical calculation of a dipole emission shown in Fig. 7(e). Figures 7(b) and 7(c) display the scattered diagram of the same particle analyzed through parallel and cross polarizers, respectively (broken arrow). Note that all the experimental images are rotated to compensate for a 45° tilt of the outport of our microscope. Figures 7(f)–7(h) are numerical simulations of the dipole emissions corresponding to the experimental polarizer and analyzer orientations. Note that all angles below θ_c were included in the calculations. A significant portion of the intensity is located in the vicinity of θ_c , indicating that our Fourier filtering rejects a negligible portion of the scattered diagram.

We now turn our attention to the scattered pattern of the antennas constituted of coupled pairs of nanoparticles. Arrangement of strongly interacting core-shell nanoantennas were predicted to significantly modify radiation patterns.³⁵ For coupled dimers, however, the angular emission is almost unaffected and only the intensity distribution is modified. Figures 8(a)–8(c) shows diagrams for selected antennas with gap values of 126, 68, and 15 nm, respectively. The diameter of individual nanoparticles was fixed at 80 nm. The polarization is aligned with the dimer axis and the illumination wavelength is 633 nm. Figure 8(d) shows the 15-nm-gap antenna pattern for a polarization oriented perpendicularly to the dimer axis. These scattered diagrams do not significantly differ from the diagrams characterizing the single-particle antenna showed in Fig. 7: the intensity distribution is peaked at the critical angle and the two-lobe patterns are readily recognized. These antennas essentially have a dipolar response of their radiation pattern. However, a close inspection reveals some differences. Let us define the contrast ratio η :

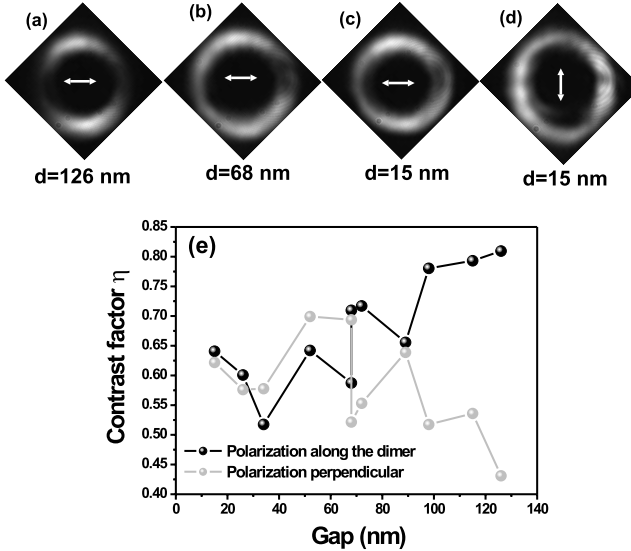


FIG. 8. (a) to (c) Angular distributions of the intensity scattered by dimers with varying gaps d and with an excitation field oriented along the dimer. (d) Polarization oriented perpendicular to a 15-nm-gap dimer. (e) Evolution of the contrast η for the two polarizations.

$$\eta = \frac{I_{\max} - I_{\min}}{I_{\max} + I_{\min}}, \quad (1)$$

where I_{\max} and I_{\min} are the orthogonal intensity maxima and minima of the scattered diagram. The η parameter indicates the deviation of the antennas' scattered diagram from an ideal dipole pattern. For reference, the values of contrast ratio extracted from the colloidal particle emission pattern of Fig. 7(a) and calculated dipolar diagram of Fig. 7(e) are in agreement at $\eta=0.5$. Here, however the reference isolated single particle yields a higher value of $\eta=0.72$ for the two polarizations and does not significantly change with the diameter of the particles investigated. The difference of contrast between the scattered diagram of a colloidal nanoparticle and lithographed particle of nominally similar diameters remains unclear, but is probably linked to the different morphology of the later particle type. Figure 8(e) shows the evolution of the contrast ratio η for varying gaps and for the two orthogonal orientations of the incident field. Interestingly, θ_c has an opposite trend between the two polarizations. For an incident field oriented along the axis of the dimer and for wider gaps, η increases and reaches a value comparable to the reference isolated particle ($\eta=0.72$). This is clearly indi-

cating a reduced interaction between the two particles for large gaps. On the contrary, for a polarization perpendicular to the dimer, η is approaching the reference contrast of an isolated particle for the shortest dimer separation. The magnitude of I_{\max} does not significantly vary across the different antennas (variation <5%). The evolution of η is mainly governed by the value of I_{\min} . We attribute the trends of η to a modification of the azimuthal radiation direction for antennas characterized by interacting nanoparticles: for a polarization along the dimer, the particles are more likely to interact in the near field since the far-field radiation pattern of individual particles are oriented perpendicular to the electric field. For the orthogonal polarization, however, the far-field radiation patterns of the two particles are aligned with the main axis of the dimer, and the interaction is therefore stronger for larger gaps.

V. CONCLUSIONS

For their ability to interface free-space radiation with nanoscale elements and devices, optical antennas are likely to play a major role in the next generation of photonic devices and sensors. Knowing the important parameters defining the properties of individual optical antennas is therefore essential for this goal. We have developed experimental techniques to rapidly compare the basic units constituting an optical antenna and measure their critical performances. By only retaining a part of the evanescent spectrum scattered by individual nanoantennas and by correlating the magnitude of this signal with their spectral characteristics, we experimentally measured the gain and the detuning factors for a given excitation wavelength. We also recorded radiation patterns of various type of antennas and found that their partial radiation pattern is essentially dipolar in nature. Important is the fact that our approach allows us to characterize the antennas at the excitation frequency. It does not require the use of reporter molecules or nonlinear phenomena to probe the antenna's response and is therefore completely nonperturbative.

ACKNOWLEDGMENTS

A.B. is grateful to R. Zia (Brown University) for his helpful comments about Fourier planes. The authors thank the Agence Nationale de la Recherche (ANR) under Grants Antares (PNANO 07-51) and Photohybrid (BLANC 07-2-188654), as well as the Regional Council of Burgundy (program FABER) for funding. C. H. acknowledges stipend from the People's Republic of China.

*Corresponding author: alexandre.bouhelier@u-bourgogne.fr

[†]Present address: Laboratoire de Nanotechnologie et d'Instrumentation Optique ICD CNRS-FRE 2848, Université de Technologie de Troyes, 10000 Troyes, France.

¹P. Mühlischlegel, H.-J. Eisler, O. J. F. Martin, B. Hecht, and D. W. Pohl, Science **308**, 1607 (2005).

²E. Cubukcu, E. A. Kort, K. B. Crozier, and F. Capasso, Appl.

Phys. Lett. **89**, 093120 (2006).

³T. Taminiau, F. D. Stefani, and N. F. Van Hulst, Opt. Express **16**, 16858 (2008).

⁴J. Aizpurua, G. W. Bryant, L. J. Richter, F. J. García de Abajo, B. K. Kelley, and T. Mallouk, Phys. Rev. B **71**, 235420 (2005).

⁵P. J. Burke, S. Li, and Z. Yu, IEEE Trans. Nanotechnol. **5**, 314 (2006).

- ⁶L. Novotny, Phys. Rev. Lett. **98**, 266802 (2007).
- ⁷T. H. Taminiua, R. J. Moerland, F. B. Segerink, L. Kuipers, and N. F. van Hulst, Nano Lett. **7**, 28 (2007).
- ⁸J. Mock, M. Barbic, D. R. Smith, D. A. Schultz, and S. Schultz, J. Chem. Phys. **116**, 6755 (2002).
- ⁹D. P. Fromm, A. Sundaramurthy, P. J. Schuck, G. Kino, and W. E. Moerner, Nano Lett. **4**, 957 (2004).
- ¹⁰A. Bouhelier, R. Bachelot, J. Im, G. P. Wiederrecht, G. Lerondel, S. Kostcheev, and P. Royer, J. Phys. Chem. B **109**, 3195 (2005).
- ¹¹K. Kneipp, H. Kneipp, and J. Kneipp, Acc. Chem. Res. **39**, 443 (2006).
- ¹²S. Lal, N. K. Grady, G. P. Goodrich, and N. J. Halas, Nano Lett. **6**, 2338 (2006).
- ¹³P. J. Schuck, D. P. Fromm, A. Sundaramurthy, G. S. Kino, and W. E. Moerner, Phys. Rev. Lett. **94**, 017402 (2005).
- ¹⁴A. Bouhelier, R. Bachelot, G. Lerondel, S. Kostcheev, P. Royer, and G. P. Wiederrecht, Phys. Rev. Lett. **95**, 267405 (2005).
- ¹⁵J. N. Anker, W. P. Hall, O. Lyandres, N. C. Shah, J. Zhao, and R. P. Duyne, Nature Mater. **7**, 442 (2008).
- ¹⁶C. Huang, A. Bouhelier, G. Colas des Francs, G. Legay, J.-C. Weeber, and A. Dereux, Opt. Lett. **33**, 300 (2008).
- ¹⁷G. Colas des Francs, C. Girard, J. C. Weeber, C. Chicane, T. David, A. Dereux, and D. Peyrade, Phys. Rev. Lett. **86**, 4950 (2001).
- ¹⁸O. L. Muskens, V. Giannini, J. A. Sánchez-Gil, and J. Gómez Rivas, Opt. Express **15**, 17736 (2007).
- ¹⁹H. Tamaru, H. Kuwata, H. T. Miyazaki, and K. Miyano, Appl. Phys. Lett. **80**, 1826 (2002).
- ²⁰P. Nordlander, C. Oubre, E. Prodan, K. Li, and M. I. Stockman, Nano Lett. **4**, 899 (2004).
- ²¹W. Rechberger, A. Hohenau, A. Leitner, J. Krenn, B. Lamprecht, and F. Aussenegg, Opt. Commun. **220**, 137 (2003).
- ²²I. Romero, J. Aizpurua, G. W. Bryant, and F. J. García de Abajo, Opt. Express **14**, 9988 (2006).
- ²³T. A. Milligan, *Modern Antenna Design* (Wiley, New York, 2005).
- ²⁴L. Novotny, D. R. Grober, and K. Karrai, Opt. Lett. **26**, 789 (2001).
- ²⁵M. R. Beversluis, A. Bouhelier, and L. Novotny, Phys. Rev. B **68**, 115433 (2003).
- ²⁶H. Xu and M. Käll, Phys. Rev. Lett. **89**, 246802 (2002).
- ²⁷E. Hao and G. C. Schatz, J. Chem. Phys. **120**, 357 (2004).
- ²⁸A. L. Lereu, G. Sanchez-Moistero, P. Ghenuche, R. Quidant, and N. F. V. Hulst, J. Microsc. **229**, 254 (2008).
- ²⁹W. Lukosz and R. E. Kunz, J. Opt. Soc. Am. **67**, 1607 (1977).
- ³⁰A. Bouhelier, M. Beversluis, A. Hartschuh, and L. Novotny, Phys. Rev. Lett. **90**, 013903 (2003).
- ³¹A. Lieb, J. M. Zavislan, and L. Novotny, J. Opt. Soc. Am. B **21**, 1210 (2004).
- ³²A. Drezet, A. Hohenau, A. L. Stepanov, H. Ditlbacher, B. Steinberger, N. Galler, F. R. Aussenegg, A. Leitner, and J. R. Krenn, Appl. Phys. Lett. **89**, 091117 (2006).
- ³³M. U. González, A. L. Stepanov, J. C. Weeber, A. Hohenau, A. Dereux, R. Quidant, and J. R. Krenn, Opt. Lett. **32**, 2704 (2007).
- ³⁴S. Massenot, J. Grandidier, A. Bouhelier, G. Colas des Francs, L. Markey, J.-C. Weeber, A. Dereux, J. Renger, M. U. González, and R. Quidant, Appl. Phys. Lett. **91**, 243102 (2007).
- ³⁵J. Li, A. Salandrino, and N. Engheta, Phys. Rev. B **76**, 245403 (2007).

Generalized bloch equations for optical interactions in confined geometries

Christian Girard ^{a,*}, Olivier J.F. Martin ^b, Gaëtan Lévèque ^b,
Gérard Colas des Francs ^c, Alain Dereux ^c

^a Centre d'Elaboration des Matériaux et d'Etudes Structurales (CNRS), 29 Rue Jeanne Marvig, F-31055 Toulouse, France

^b Nanophotonics and Metrology Laboratory, Swiss Federal Institute of Technology Lausanne (EPFL) CH-1015 Lausanne, Switzerland

^c Equipe d'Optique Submicronique, Laboratoire de Physique de l'Université de Bourgogne 9 Av. A. Savary, F-21078 Dijon, France

Received 25 August 2004; in final form 29 December 2004

Abstract

By combining the field-susceptibility technique with the optical Bloch equations, a general formalism is developed for the investigation of molecular photophysical phenomena triggered by nanometer scale optical fields in the presence of complex environments. This formalism illustrate the influence of the illumination regime on the fluorescence signal emitted by a single molecule in a complex environment. In the saturated case, this signal is proportional to the optical local density of states, while it is proportional to the near-field intensity in the non-saturated case.

© 2005 Elsevier B.V. All rights reserved.

1. Introduction

Over the last decade, numerous experimental configurations have been proposed for studying single molecule photophysical phenomena triggered by nanometer size light fields [1–8]. These configurations involve the interaction of microscopic entities with their macroscopic environment. Similar situations, where elements exhibiting very different length scales interact, exist also in solid state physics and materials science [9].

The main objective of this communication is to propose a formalism for analyzing a large class of experimental configurations where various molecular photophysical processes are induced by highly confined optical fields in the presence of a complex environment. The approach is based on the combination of the *field-susceptibility/Green's-tensor technique* [10,11] with the *optical Bloch equations* [12,13]. The former provides an

accurate electromagnetic description of the system, including the local electric field and local density of states (LDOS) [14]. These parameters are then introduced into the optical Bloch equations to obtain the population evolution of the molecular energy levels and deduce the molecular fluorescence signals [15–17].

Our approach relies on the fact that quantum-mechanical calculations can be restricted to the molecular system, while the complex optical environment can be treated classically using the Green's tensor. This contrasts markedly with earlier theoretical works on fluorescence in confined geometries where the molecule was treated as a classical emitting dipole [18–21]. Indeed, in the present approach the population equations can be solved in a non-perturbative manner, irrespective of the complexity of the environment seen by the molecules. Like this, one or several molecules including an arbitrary number of energy levels can be investigated. Different experimental illumination regimes can be investigated and effects such as saturation are readily accessible to the technique. These complex effects play

* Corresponding author. Fax: +33 5 62 25 79 99.

E-mail address: girard@cemes.fr (C. Girard).

a central role in the interpretation of single molecule experiments in the presence of highly confined optical fields.

The Letter is organized as follows: A general formalism for the evolution of the different fluorescence signals generated by a molecule placed in a complex environment is first developed. Two limiting cases are then studied in detail to illustrate the dependence of the fluorescence signal on the illumination conditions.

2. Formalism

Let us consider a molecular system located at the position \mathbf{r}_m in a complex environment and characterized by its dipole operator $\hat{\mu}$ and Hamiltonian H_0 (Fig. 1). The Fourier transform $\mathbf{E}(\mathbf{r}_m, \omega)$ of the local electric field $\mathbf{E}(\mathbf{r}_m, t)$ can be obtained everywhere in the system from the generalized field propagator $\mathbf{K}(\mathbf{r}, \mathbf{r}', \omega)$ [10]:

$$\mathbf{E}(\mathbf{r}_m, \omega) = \int_v \mathbf{K}(\mathbf{r}_m, \mathbf{r}', \omega) \cdot \mathbf{E}_0(\mathbf{r}', \omega) d\mathbf{r}', \quad (1)$$

where $\mathbf{E}_0(\mathbf{r}', \omega)$ represents the Fourier transform of the illumination field $\mathbf{E}_0(\mathbf{r}, t) = \mathbf{E}_0 \cos(\omega_0 t - \mathbf{k}_0 \cdot \mathbf{r})$, and the integral runs over the entire environment. The dyad $\mathbf{K}(\mathbf{r}, \mathbf{r}', \omega)$ can be expressed in terms of the optical field susceptibility tensor $\mathbf{S}(\mathbf{r}, \mathbf{r}', \omega)$ associated with the entire system

$$\mathbf{K}(\mathbf{r}, \mathbf{r}', \omega) = \delta(\mathbf{r} - \mathbf{r}') + \mathbf{S}(\mathbf{r}, \mathbf{r}', \omega) \cdot \boldsymbol{\chi}(\mathbf{r}', \omega), \quad (2)$$

where $\boldsymbol{\chi}$ is the optical susceptibility of the complex environment. Eq. (1) can be solved using a recursive series of Dyson's equations associated with \mathbf{S} , leading to the field $\mathbf{E}(\mathbf{r}, \omega)$ in the system [10]. The dipolar coupling Hamiltonian $W(t) = -\hat{\mu} \cdot \mathbf{E}(\mathbf{r}_m, t)$ can then be obtained from the generalized propagator (2). Applying the usual rotating waves approximation that neglects non-resonant terms in the interaction process [12], one obtains

$$W(t) = \sum_{\alpha=x,y,z} \frac{\hbar \Omega_\alpha(\mathbf{r}_m)}{2} \{ e^{-i(\omega_0 t + \phi_\alpha(\mathbf{r}_m))} |2\rangle\langle 1| + C.C. \}, \quad (3)$$

where $\Omega_\alpha(\mathbf{r}_m)$ is the α -component of the vectorial Rabi frequency. This quantity is proportional to the α -component of the absorption transition dipole μ_2

$$\Omega_\alpha(\mathbf{r}_m) = -\frac{\mu_{2,\alpha} \mathbf{E}_\alpha(\mathbf{r}_m)}{\hbar}, \quad (4)$$

with

$$\mathbf{E}_\alpha(\mathbf{r}_m) = \left| \sum_{\beta=x,y,z} \int \mathbf{K}_{\alpha\beta}(\mathbf{r}_m, \mathbf{r}', -\omega_0) e^{-i\mathbf{k}_0 \cdot \mathbf{r}'} d\mathbf{r}' E_{0,\beta} \right|. \quad (5)$$

In Eq. (3), the three phase factors $\phi_\alpha(\mathbf{r}_m)$ (with $\alpha = x, y$ or z) are obtained by taking separately the phase of the three components of the complex number $\mathbf{E}(\mathbf{r}_m, \omega)$. This splitting of both the phase factor and the Rabi frequency into three distinct components originates from the presence of evanescent fields [22,23].

At this stage, we have all the ingredients required to write Liouville's equation that governs the matrix density evolution of the molecule

$$\dot{\rho}(t) = \frac{1}{i\hbar} [H_0 + W(t), \rho(t)] + [\mathcal{R}_{\text{spont}} + \mathcal{R}_{\text{vib}}] \rho(t), \quad (6)$$

where the two Redfield operators $\mathcal{R}_{\text{spont}}$ and \mathcal{R}_{vib} , describe, respectively, the couplings with the photons bath and the internal vibrational states of the molecule [12]. This leads to a coupled system of four optical Bloch equations [12]:

$$\dot{\rho}_{33}(t) = K \rho_{22}(t) - \Gamma_3 \rho_{33}(t), \quad (7)$$

$$\dot{\rho}_{22}(t) = -(K + \Gamma_2) \rho_{22}(t) - i\Omega^- \rho_{12}(t) + i\Omega^+ \rho_{21}(t), \quad (8)$$

$$\dot{\rho}_{12}(t) = \left[i\delta_L - \frac{\Gamma_2}{2} \right] \rho_{12}(t) - i\Omega^+ (2\rho_{22}(t) + \rho_{33}(t) - 1), \quad (9)$$

$$\dot{\rho}_{21}(t) = - \left[i\delta_L + \frac{\Gamma_2}{2} \right] \rho_{21}(t) + i\Omega^- (2\rho_{22}(t) + \rho_{33}(t) - 1), \quad (10)$$

with

$$\Omega^{-/+} = \sum_{\alpha=x,y,z} \frac{\Omega_\alpha(\mathbf{r}_m)}{2} e^{(-/+i\phi_\alpha(\mathbf{r}_m))}. \quad (11)$$

When the phase factors $\phi_\alpha(\mathbf{r}_m)$ weakly vary from one field component α to another, we can put $\phi_\alpha(\mathbf{r}_m) \equiv \phi(\mathbf{r}_m)$ for

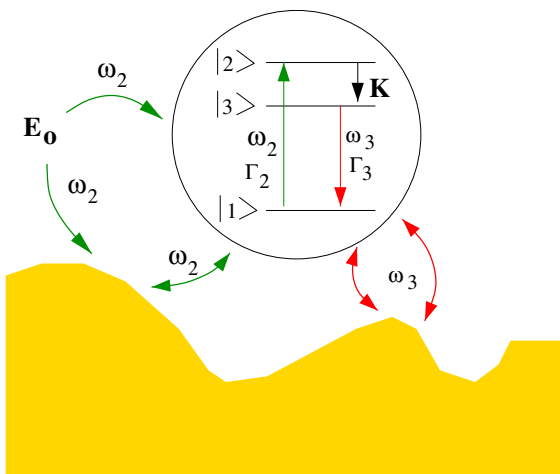


Fig. 1. Schematic representation of a three levels molecular system in interaction with a complex optical environment. Symbols $|1\rangle$ and $|3\rangle$ represent ground singlet state and first excited singlet, respectively. K characterizes the vibrational relaxation decay of state $|2\rangle$ and \mathbf{E}_0 is the amplitude of the illumination field.

$\alpha = x, y$ or z . In this case, the two factors Ω^+ and Ω^- can be related to the usual Rabi frequency $\Omega(\mathbf{r}_m)$:

$$\Omega^+ = (\Omega^-)^* = \frac{\Omega(\mathbf{r}_m)}{2} e^{i\phi(\mathbf{r}_m)}. \quad (12)$$

In Eqs. (7)–(10), we have also introduced four useful parameters, namely, (i) the detuning $\delta_L = \omega_2 - \omega_0$ between the laser and the resonant absorption frequency of the molecule, (ii) the vibrational relaxation constant K between the excited state and the first excited singlet, and finally (iii) the two radiative decay rates of the molecule [15]:

$$\Gamma_{2/3} = \Gamma_{2/3}^{(0)} + \frac{2\mu_{2/3}^2}{\hbar} \text{Im}\{\mathbf{S}(\mathbf{r}_m, \mathbf{r}_m, \omega_{2/3})\} : \mathbf{u}\mathbf{u}, \quad (13)$$

where \mathbf{u} is a unit vector that characterizes the molecule orientation, $\mu_{2/3}$ represent the transition dipole between the ground state and the $|2\rangle/|3\rangle$ levels, and $\Gamma_{2/3}^{(0)}$ are the spontaneous decay rates of the isolated molecule (Fig. 1). These parameters appear in the optical Bloch equations after application of the Redfield operator on the matrix density operator. In the present case, symmetry considerations imply that several Redfield operator matrix elements vanish [12]. The stationary population ρ_{33} of the first singlet state $|3\rangle$ gives direct access to the detected fluorescence signal when the molecule is illuminated in permanent regime. In this case, the four terms on the left-hand side of Bloch equations tend simultaneously to zero. This leads to

$$\rho_{33} = \left[1 + \left(\frac{2}{K} + A_1 + A_2 \right) \Gamma_3 \right]^{-1}, \quad (14)$$

with

$$A_1 = \frac{\delta_L^2}{\Omega^+ \Omega^-} \left\{ \frac{1}{K} + \frac{1}{\Gamma_2} \right\} \quad (15)$$

and

$$A_2 = \frac{\Gamma_2}{4\Omega^+ \Omega^-} \left\{ 1 + \frac{\Gamma_2}{K} \right\}. \quad (16)$$

The fluorescence signals generated by the molecule is then given by

$$I_{\text{fluo}}(\mathbf{r}_m) = \frac{\hbar\omega_3 \Gamma_3}{1 + \left(\frac{2}{K} + A_1 + A_2 \right) \Gamma_3}. \quad (17)$$

Eq. (17) together with Eqs. (15) and (16) demonstrate the possibility of self-consistently bridging the gap between molecular and macroscopic scales. The entire optical information related to the dielectric environment is implicitly contained, via the field-susceptibility \mathbf{S} , in the factors $\Gamma_{2/3}$ and $\Omega^{+/-}$. Consequently, this approach is well-suited for investigating a large class of photophysical phenomena in confined geometries.

3. Limiting cases for different illumination modes

Another important advantage of this approach should also be emphasized. As illustrated by the previous analysis, a proper selection of the only active molecular levels for a given photophysical process leads to quasi-analytical expressions for the fluorescence signals. For example, two limiting cases particularly pertinent to on-going single molecule near-field optical experiments can be extracted from Eq. (17).

3.1. Saturated absorption regime

When the laser frequency ω_0 excites the molecule at the absorption frequency ω_2 , the detuning factor δ_L in Eq. (15) and the factor A_1 tend towards zero. The magnitude of the excitation power can then be adjusted to approach the so-called saturation regime that occurs when the product $A_2 \Gamma_3$ is much smaller than unity in Eq. (17). This condition is fulfilled when the Rabi frequency $\Omega(\mathbf{r}_m)$ verifies the following relation (see Eqs. (12) and (16)):

$$\Omega(\mathbf{r}_m) \gg \sqrt{\Gamma_2 \Gamma_3}. \quad (18)$$

Moreover, for customary fluorescent molecules, the term $2 \Gamma_3/K$ in Eq. (17) remains always much smaller than unity. Consequently, within this asymptotic case, the fluorescence signal becomes merely proportional to the radiative decay Γ_3 :

$$I_{\text{sat}}(\mathbf{r}_m) \simeq \hbar\omega_3 \Gamma_3(\mathbf{r}_m, \omega_3). \quad (19)$$

After substitution of Eq. (13) into Eq. (19), the variation of $I_{\text{fluo}}(\mathbf{r}_m)$ with respect to the molecule location \mathbf{r}_m is found to be proportional to the imaginary part of the field susceptibility \mathbf{S} associated with the entire environment,

$$I_{\text{sat}}(\mathbf{r}_m) \simeq \hbar\omega_3 \Gamma_3^{(0)} + 2\mu_3^2 \omega_3 \text{Im}\{\mathbf{S}(\mathbf{r}_m, \mathbf{r}_m, \omega_3)\} : \mathbf{u}\mathbf{u}. \quad (20)$$

For a specific orientation of the molecule along the α -direction, the factor $\text{Im}\{\mathbf{S}(\mathbf{r}_m, \mathbf{r}_m, \omega_{2/3})\} : \mathbf{u}\mathbf{u}$ can be related to the partial photonic LDOS $n_\alpha(\mathbf{r}_m, \omega_3)$ at the fluorescence frequency ω_3 [14],

$$n_\alpha(\mathbf{r}_m, \omega_3) = \frac{1}{2\pi^2 \omega_3} \text{Im}\{\mathbf{S}_{\alpha,\alpha}(\mathbf{r}_m, \mathbf{r}_m, \omega_3)\}. \quad (21)$$

Finally, substitution of Eq. (21) into Eq. (20) leads to

$$I_{\text{sat}}(\mathbf{r}_m) = \hbar\omega_3 \Gamma_3^{(0)} + 4\omega_3^2 \mu_3^2 \pi^2 n_\alpha(\mathbf{r}_m, \omega_3). \quad (22)$$

Consequently, when the saturation regime is reached, the molecule tends to gradually forget any initial information related to the structure of the excitation field. In this case, the molecule loses the history of the successive absorption events and emits fluorescence photons that probe the partial photonic LDOS associated with the environment. Such experimental conditions can be obtained by working at low temperature in order to

minimize the absorption linewidth Γ_2 of the molecular probe. Very recently, Michaelis et al. succeeded in operating a low temperature SNOM configuration where the source of light was reduced to a single fluorescing terrylene molecule embedded in a paraterphenyl microcrystal, which itself was glued on the apex of a sharpened optical fiber [7,24]. At 1.4 K, the terrylene linewidth is about 47 MHz, which provides ideal conditions to observe, under saturated conditions, the variations of the LDOS as the micro-crystal is raster-scanned [25].

A simulation of this operation mode is presented in Fig. 2b, where a single terrylene molecule raster-scans the sample depicted in Fig. 2a. The fluorescence wavelength $\lambda_3 = 2\pi c/\omega_3$ of terrylene is 630 nm and its fluorescence transition dipole μ_3 oriented along the y -axis. According to Eq. (22), the molecule signal is modulated by the partial y -LDOS computed at the fluorescence wavelength λ_3 . The presence of symmetrical ripples around the dielectric cylinders indicates that a LDOS map characterizes a given system independently of the illumination mode [26]. Let us note that the other partial x -LDOS can be probed by rotating the molecule by $\pi/2$ in the xy -plane.

3.2. Off-saturation absorption regime [27]

In this second asymptotic case, we also maintain the detuning factor δ_L close to zero and consider the fluores-

cence signal when the molecule is excited at a low Rabi frequency. This regime is described by the following inequality,

$$\Omega(\mathbf{r}_m) \ll \sqrt{\Gamma_2 \Gamma_3}, \quad (23)$$

which corresponds to the condition $A_2 \Gamma_3 \gg 1$. The fluorescence signals $I_{\text{off-sat}}(\mathbf{r}_m)$ reads then

$$I_{\text{off-sat}}(\mathbf{r}_m) \simeq \frac{\hbar \omega_3}{A_2} = \frac{4\hbar \omega_3 K \Omega_+ \Omega_-}{\Gamma_2(K + \Gamma_2)}. \quad (24)$$

In the case of low near-field phase variations (Eq. (12)), this signal becomes proportional to the square of the Rabi frequency $\Omega(\mathbf{r}_m)$ at the molecule location:

$$I_{\text{off-sat}}(\mathbf{r}_m) = A \Omega^2(\mathbf{r}_m), \quad (25)$$

with $A = \hbar \omega_3 K / \Gamma_2(K + \Gamma_2)$. For a particular orientation of the molecule along the α -direction, $\Omega^2(\mathbf{r}_m) = \mu_2^2 \mathbf{E}_\alpha^2(\mathbf{r}_m)$, and the molecule probes the local near-field intensity [27,28],

$$I_{\text{off-sat}}(\mathbf{r}_m) = A \mu_2^2 \mathbf{E}_\alpha^2(\mathbf{r}_m). \quad (26)$$

This result shows that, unlike what happened in the fluorescence saturation regime where the molecule probed the photonic LDOS (Eq. (22)), the off-saturation regime leads to a fluorescence signal that is proportional to the local near-field intensity. According to Eq. (23), this condition is easily verified when the Rabi frequency is small compared to the absorption linewidth. These

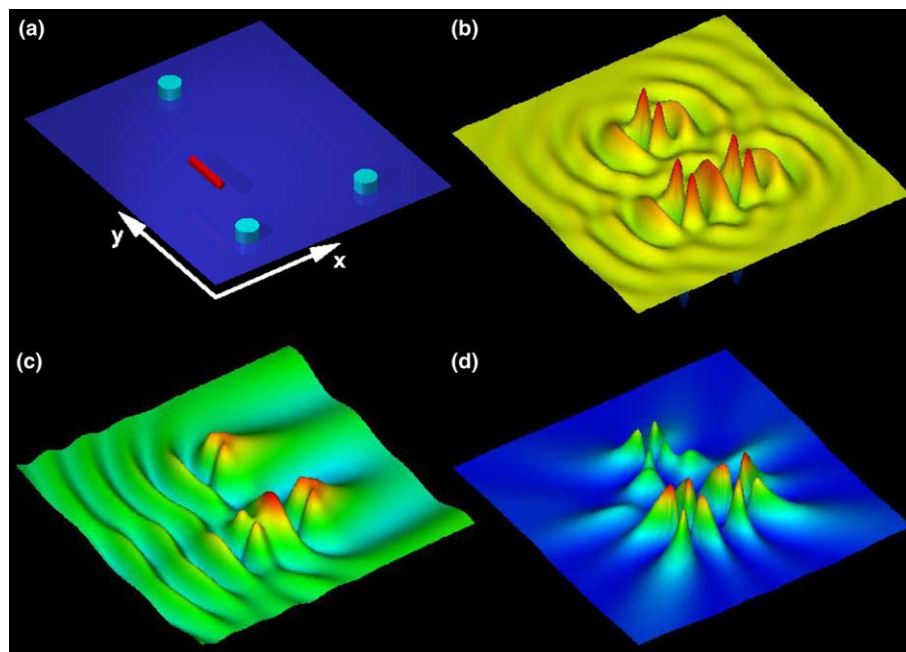


Fig. 2. (a) Geometry used for the calculation: three dielectric cylindrical protrusions (diameter 100 nm, height 60 nm, $\epsilon = 4.41$) are placed at the corners of an isosceles triangle with base 600 nm and perpendicular 1000 nm on a glass surface ($\epsilon = 2.25$). The red ellipsoid represents the molecule that raster-scans the sample at a constant height $z = 150$ nm above the surface. The system is illuminated from underneath in total internal reflection with s-polarization. (b) Fluorescence signal computed in the saturation regime (Eq. (22)) when the molecule raster-scans the sample. (c) and (d) Fluorescence signal computed in the off-saturation regime (Eq. (26)), for two different propagation directions of the illumination field: y -direction (c) and x -direction (d). Map dimensions: (a) $1.2 \times 1.4 \mu\text{m}^2$, (b)–(d) $3 \times 3 \mu\text{m}^2$.

conditions have been used in a series of beautiful experiments performed at room temperature where the detection of local signals emitted by individual molecules was reported [2,28]. In particular, it was demonstrated in Ref. [2] how individual fluorescing molecules were able to precisely map the electric field intensity generated at the apex of a metal coated tip, thereby providing the first direct verification of Bethe's theory of light diffraction by a subwavelength aperture.

Two simulations of this off-saturation mode, calculated at the illumination wavelength $\lambda_2 = 578$ nm, are given in Figs. 2c and d. In this case, it may be seen that the molecule probes the intensity E_y^2 associated with the y -component of the optical electric near-field confined by the environment. Unlike what happened in the saturated absorption regime (Fig. 2b), the recorded fluorescence signal dramatically depends on the illumination conditions and does not provide direct information on the sole topography of the sample.

3.3. Arbitrary illumination regime

When neither conditions examined under (i) or (ii) apply, no evident simplification can be made and the detected fluorescence signal must be computed from the general relation (17). In this case, information related to the electric field distribution is entangled with local information related to the LDOS calculated at the fluorescence frequency.

4. Summary

In conclusion, we have developed a unified formalism to describe molecular photophysical processes in a confined geometry. This approach includes a non-perturbative quantum treatment of all the different active molecular levels, as well as the complex and rapidly varying field distributions associated with a complicated optical environment. The combination of these two features renders the method particularly powerful for the accurate analysis of experiments performed with local probe techniques and single active molecules. The obtained equations provide new insights into the signal effectively radiated in the near-field by a single molecule. Important limiting cases in the saturated and off-saturated absorption regimes can be recovered from this general formalism.

Acknowledgements

O.J.F.M. gratefully acknowledges support from the Swiss National Science Foundation. This work was supported in part by the European Network of Excellence (NoE) *Plasmo-Nano-Devices* (Contract No. 507879).

References

- [1] K. Lieberman, S. Harush, A. Lewis, R. Kopelman, *Science* 247 (1990) 59.
- [2] E. Betzig, R.J. Chichester, *Science* 262 (1993) 1422.
- [3] W.E. Moerner, T. Plakhotnik, T. Irngartinger, U.P. Wild, D.W. Pohl, B. Hecht, *Phys. Rev. Lett.* 73 (1994) 2764.
- [4] E. Betzig, J.K. Trautman, J.D. Harris, J.S. Weiner, R.L. Kostelack, *Science* 251 (1991) 1468.
- [5] W.L. Barnes, *J. Modern Opt.* 45 (1998) 661.
- [6] W.E. Moerner, M. Orrit, *Science* 283 (1999) 1671.
- [7] J. Michaelis, J.M.C. Hettich, V. Sandoghdar, *Nature* 405 (2000) 325.
- [8] P. Andrew, W.L. Barnes, *Science* 290 (2000) 785.
- [9] J.A. Nieminen, S. Paavilainen, *Phys. Rev. B* 60 (1999) 2921.
- [10] O.J.F. Martin, C. Girard, A. Dereux, *Phys. Rev. Lett.* 74 (1995) 526.
- [11] P. de Vries, D.V. van Coeverden, A. Lagendijk, *Rev. Mod. Phys.* 70 (1998) 447.
- [12] C. Cohen-Tannoudji, J. Dupont-Roc, G. Grynberg, *Processus D'interaction Entre Photons Et Atomes*, InterEditions, Paris, 1988.
- [13] C.M. Bowden, J.P. Dowling, *Phys. Rev. A* 47 (1993) 1247.
- [14] G. Colas des Francs, C. Girard, J.C. Weeber, C. Chicanne, T. David, A. Dereux, D. Peyrade, *Phys. Rev. Lett.* 86 (2001) 4950.
- [15] G.S. Agarwal, *Phys. Rev. A* 12 (1975) 1475.
- [16] P. Das, H. Metiu, *J. Phys. Chem.* 89 (1982) 4680.
- [17] N. Vats, S. John, K. Busch, *Phys. Rev. A* 65 (2002) 43808.
- [18] C. Girard, O.J.F. Martin, A. Dereux, *Phys. Rev. Lett.* 75 (1995) 3098.
- [19] L. Novotny, *Appl. Phys. Lett.* 69 (1996) 3806.
- [20] C. Henkel, V. Sandoghdar, *Opt. Commun.* 158 (1998) 250.
- [21] G. Parent, D. VanLabeke, D. Barchiesi, *J. Microscopy* 194 (1999) 281.
- [22] R. Carminati, *Phys. Rev. E* 55 (1997) R4901.
- [23] M.L.M. Balistreri, J.P. Korkerik, L. Kuipers, N.F. Van Hulst, *Phys. Rev. Lett.* 85 (2000) 294.
- [24] V. Sandoghdar, *Phys. World* 14 (2001) 29.
- [25] G. Colas des Francs, C. Girard, A. Dereux, *J. Chem. Phys.* 117 (2002) 4659.
- [26] G. Lévéque, G. Colas des Francs, C. Girard, J.C. Weeber, C. Meier, C. Robillard, R. Mathevret, J. Weiner, *Phys. Rev. E* 65 (2002) 36701.
- [27] T. Plakhotnik, E. Donley, U.P. Wild, *Ann. Rev. Phys. Chem.* 48 (1997) 181.
- [28] B. Sick, B. Hecht, L. Novotny, *Phys. Rev. Lett.* 85 (2000) 4482.

A.2-Publications relatives au chapitre 3

“Single molecules probe local density of modes (LDOS) around photonic nanostructures”

G. Colas des Francs, G. Sanchez-Mosteiro, M. Ujue-Gonzalez, L. Markey, N. van Hulst
and A. Dereux

Journal of Microscopy **229**, 210-216 (2008).

“Molecular quenching and relaxation in a plasmonic tunable system”

G. Baffou, C. Girard, E. Dujardin, G. Colas des Francs and O. Martin
Physical Review B, **77**, 122101(R) (2008).

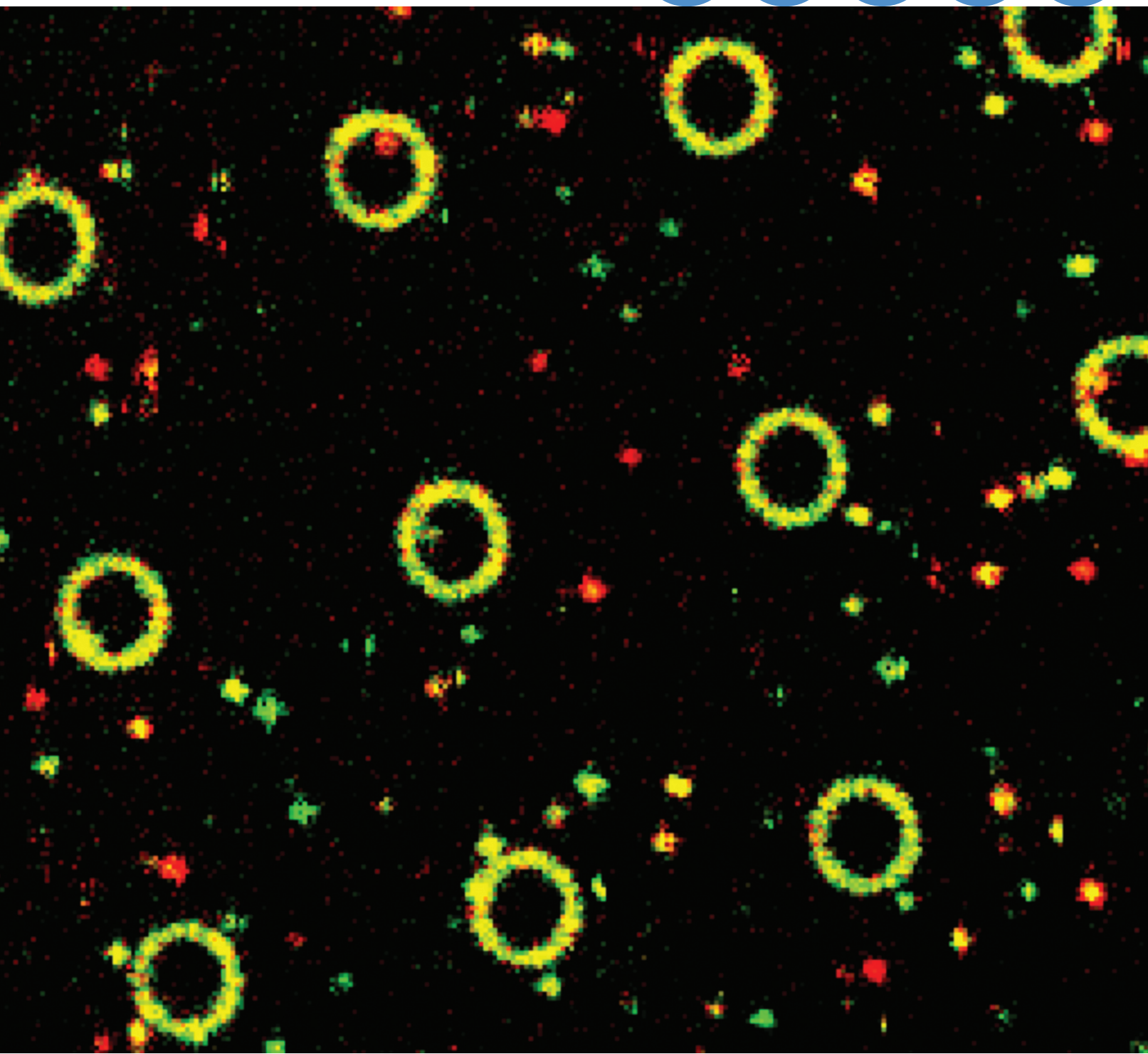
Journal of

ISSN 0022-2720

Microscopy

Blackwell Publishing

Volume 229, Part 2, February 2008



Single molecules probe local density of modes (LDOS) around photonic nanostructures

G. COLAS DES FRANCS*, G. SANCHEZ-MOSTEIRO†,
M. UJUE-GONZALEZ*·†, L. MARKEY*, N. VAN HULST†,
A. DEREUX*

*Institut Carnot de Bourgogne, CNRS UMR 5209-Université de Bourgogne, 9 avenue A. Savary,
F-21078 Dijon, France

†ICFO-Institut de Ciències Fotòniques, 08860 Castelldefels (Barcelona) Spain

Key words. Fluorescence lifetime, LDOS, purcell effect, single molecule detection.

Summary

According to Fermi's golden rule, the fluorescence decay rate is directly proportional to the projected local density of photonic modes (LDOS) at the molecule location. The relevant LDOS depends on the molecule orientation. In this paper, the direct measurement of the fluorescence lifetime near gold dot photonic structures is investigated and compared to calculated LDOS. Detailed analysis of the decay channels is presented on the basis of numerical simulations.

Introduction

Since the work of Purcell, it is well known that spontaneous emission is governed by the local density of photonic modes (LDOS) ρ (Purcell, 1946). Considering weak coupling between the excited molecule and the electromagnetic environment, Fermi's golden rule expresses the fluorescence decay rate Γ (inverse of fluorescence lifetime τ) in terms of the number of allowed electromagnetic modes available for the emission of a photon:

$$\Gamma(\mathbf{r}_m) = \frac{\pi\omega_0}{\hbar\epsilon_0} |\mu|^2 \rho_u(\mathbf{r}_m, \omega_0), \quad (1)$$

In this expression, $\rho_u(\mathbf{r}_m, \omega_0)$ is the projected LDOS (PLDOS) along the direction \mathbf{u} of the transition dipole moment $\mu = \mu\mathbf{u}$ at the molecule position \mathbf{r}_m and fluorescence frequency ω_0 (Novotny and Hecht, 2006). Because of boundary conditions, ρ_u depends strongly on the molecule location and orientation in the system. This property can be used to tune the fluorescence rate by tailoring the optical surroundings of

the molecule. For instance, by placing an emitter in a microcavity, one can cancel all transitions except the one in resonance with the cavity, with applications in single photon source elaboration (Lounis & Orrit, 2005). On the other hand, Rigneault *et al.* recently proved that increasing the fluorescence decay avoids saturation effects in fluorescence correlation spectroscopy studies (Rigneault *et al.*, 2005).

We report here the measurement of the single molecule fluorescence lifetime near photonic structures (in the 'experiment' section). In the 'Discussion' section, the lifetime is compared to the PLDOS numerically evaluated inside the system. Moreover, a detailed analysis of the PLDOS reveals the decay channels for the molecule relaxation.

Experiment

We place the molecule in so-called *optical corrals* because it has been previously demonstrated that it is possible to modulate differently the X, Y and Z-LDOS inside the corral (Chicanne *et al.*, 2002). Optical corrals of various shapes are obtained by standard electron beam lithography technique. They are made of gold pads of 100-nm diameter and 45-nm height on a thin glass substrate forming a circle, an ellipse or stadium, as shown in Fig. 1(a). Dye molecules (DiD, molecular probes, Invitrogen, Carlsbad, CA, USA) are diluted in polymethylmethacrylate (PMMA, Acros, USA) at concentration 10^{-8} mol. L⁻¹ and spin coated on the substrate. Fluorescence intensity is collected by confocal scanning fluorescence microscopy (Zeiss Axiovert 200, inverted microscope, Carl Zeiss Ltd, UK) with an oil immersion objective lens (Olympus NA 1.3, 100× Olympus UK Ltd, Watford, UK) (Sánchez-Mosteiro *et al.*, 2006). Circularly polarized light ($\lambda_{\text{exc}} = 635$ nm, ps laser diode head LDH-635, PicoQuant) was used as excitation through the same objective and separated from the excitation light by the

Correspondence to: G. Colas des Francs. Tel: 03 80 39 9067; fax: 03 80 39 6024;
e-mail: gerard.colas-des-francs@u-bourgogne.fr

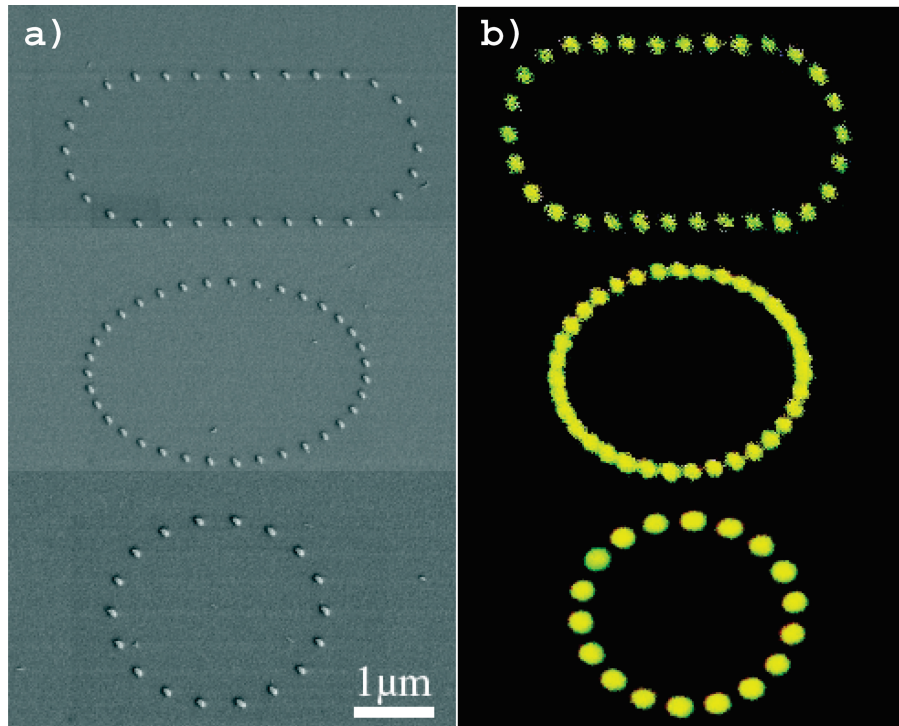


Fig. 1. (a) SEM images of gold optical corrals lithographed on 170- μm glass substrate. (b) Luminescence scan of the photonic structures at excitation wavelength 635 nm and detection wavelength above 665 nm.

combination of a dichroic mirror (Omega 650DRLP) and a long pass filter (Omega 665ALP). The fluorescence light was then sent to two avalanche photodiodes (APD, SPCM-AQ-14, EG&G Electro Optics). A polarizing beam splitter in front of the APDs separates the light into two orthogonal polarizations. Because of the gold luminescence (see Fig. 1b), the optical corrals are clearly seen, so that it is possible to locate with confocal resolution the position of molecules inside the system. Typical fluorescence images are represented in Fig. 2. The optical corrals are easily identified and each spot is the fluorescence signal of individual molecules spread on the substrate. Direct analysis of the far-field emission reveals the molecule orientation, which is indicated by a false colour code. Green pixels refer to horizontal polarized light, red pixels refer to vertical polarization. Finally, focusing on each spot, we record the fluorescence lifetime for each molecule. In this preliminary study, we present a statistical analysis of the lifetime modification by the optical corral. The distribution of recorded lifetimes is reported in Fig. 2(d).

Molecules far away from any structure present a lifetime distribution ranging from 1.6 ns to 3 ns, as has been previously reported in a similar configuration (Vallée *et al.*, 2001). This distribution is clearly broadened for molecules located inside the stadium. The fluorescence lifetime of these molecules ranges from very short lifetimes (not detected) resulting from quenching, up to 35% larger than the lifetimes of molecules situated far away from any structure.

Discussion

Formalism

The LDOS involved in the Fermi's golden rule [Eq. (1)] is a classical quantity that is related to the classical electric Green's dyad \mathbf{G} associated with the molecule surroundings. This dyad describes the electric field scattered at any point \mathbf{r} of the system by a dipole \mathbf{u} located at \mathbf{r}_m :

$$\mathbf{E}(\mathbf{r}) = \frac{k_0^2}{\epsilon_0} \mathbf{G}(\mathbf{r}, \mathbf{r}_m, \omega_0) \cdot \mathbf{u}, \quad k_0 = \omega_0/c$$

is the free-space wavenumber

(2)

and the PLDOS can be expressed as (unit is in s. m^{-3})

$$\rho_u(\mathbf{r}, \omega) = \frac{2\omega}{\pi c^2} \text{Im}[\mathbf{u} \cdot \mathbf{G}(\mathbf{r}, \mathbf{r}_m, \omega) \cdot \mathbf{u}].$$
(3)

Because the dipolar transition moment of the molecule is unknown, it is easier to consider the normalized decay rate

$$\gamma = \frac{\Gamma(\mathbf{r}_m)}{\Gamma_0} = \frac{6\pi}{k_0} \text{Im}[\mathbf{u} \cdot \mathbf{G}(\mathbf{r}_m, \mathbf{r}_m, \omega_0) \cdot \mathbf{u}].$$
(4)

in which $\Gamma_0 = 1/\tau_0 = (3.5 \text{ ns})^{-1}$ is the free-space molecule decay rate considered as a parameter.

The expression of Green's dyad is analytical only for a few highly symmetric systems but can be numerically evaluated for any arbitrary system (Girard & Dereux, 1996). In the following, we describe the construction of Green's dyad associated with

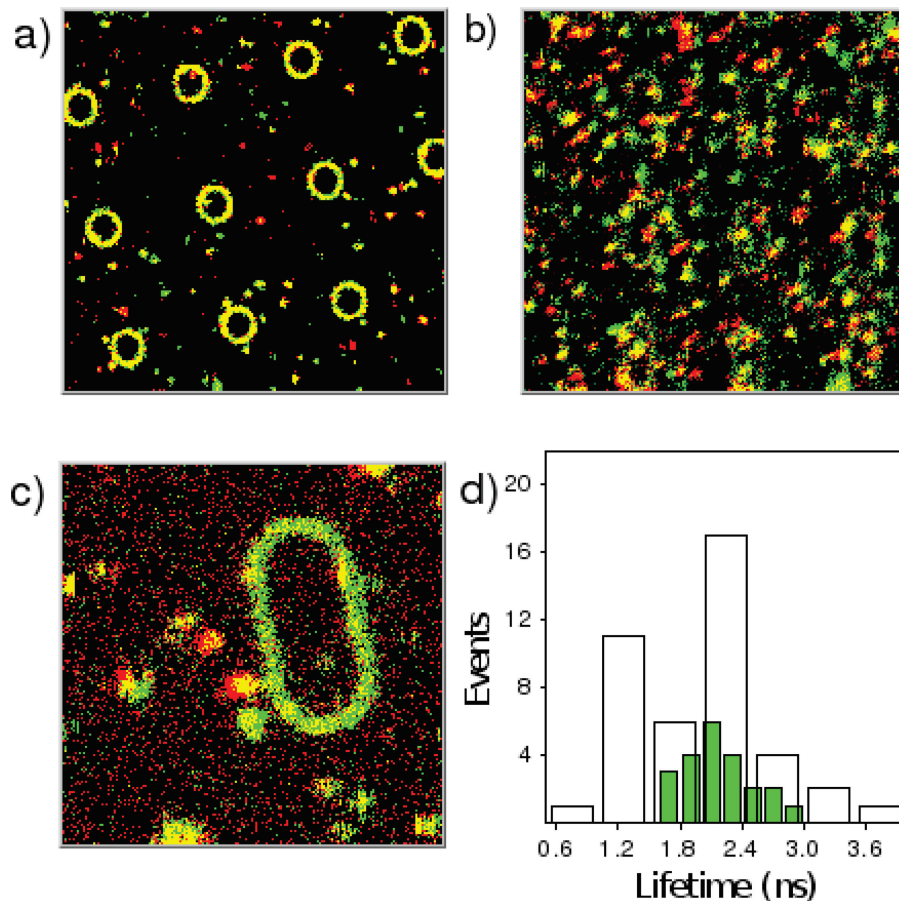


Fig. 2. Fluorescence images of single molecules spread on optical corrals. Red/green colour indicates the molecule's dipole orientation in the substrate plane. (a) $30 \times 30 \mu\text{m}^2$ image of circular corrals, (b) $30 \times 30 \mu\text{m}^2$ image of corral stadiums. (c) $10 \times 10 \mu\text{m}^2$ image of a single corral stadium and (d) fluorescence lifetime distribution for molecules far from (filled bars) and inside (open bars) the stadium corrals.

the optical system of the experiment described above, the gold dots stadium embedded in the polymer slab. We first described Green's dyad associated with the bare slab that has to be considered to analyze the fluorescence lifetime

distribution far from the structures. Using Dyson's equation, the stadium perturbation is then numerically evaluated and compared to the lifetimes measured inside the optical corral.

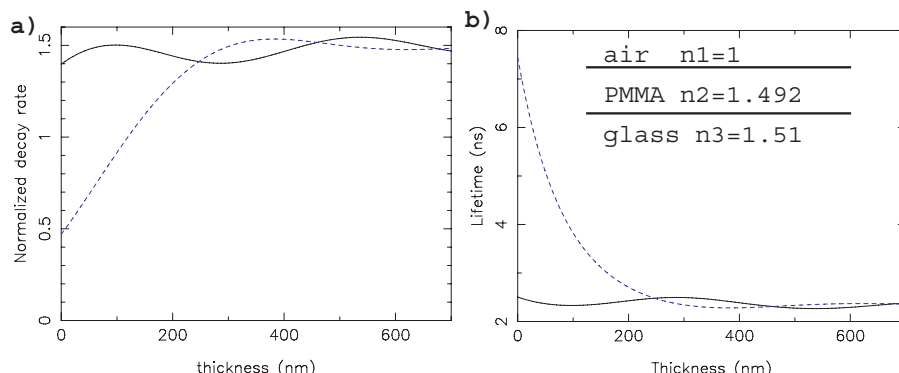


Fig. 3. (a) Normalized decay rate calculated for a molecule parallel (solid line) or perpendicular (dashed line) to the surface and located in the middle of the PMMA slab when varying the thickness. (b) Corresponding fluorescence lifetime. For a thick film, the normalized decay rate tends towards its value in a homogeneous PMMA background ($\gamma = n_2 = 1.49$). The index of refraction is given in the inset of Fig. b).

Lifetime dispersion inside the PMMA slab

We define first the reference system as the PMMA film lying on the glass substrate and exposed to air (see the inset of Fig. 3b). The fluorescence decay rate is easier expressed considering the angular spectrum representation of the dipole field (Novotny & Hecht, 2006):

$$\gamma_{\text{slab}}(\mathbf{r}_m) = \frac{6\pi}{k_0} \text{Im}[\mathbf{u} \cdot \mathbf{G}_{\text{slab}}(\mathbf{r}_m, \mathbf{r}_m, \omega_0) \cdot \mathbf{u}] = \int_0^\infty dk_p P(k_p), \quad (5)$$

where the normalized power $P(k_p)$ emitted by a dipole embedded inside the dielectric slab is straightforwardly expressed as a function of the Fresnel coefficients (Novotny & Hecht, 2006). The decay rate and corresponding lifetime of a single molecule embedded in the PMMA slab are represented in Fig. 3 for several slab thickness. Small interferences oscillations appear because of reflections at the interfaces. Because the tangential electric field is continuous at the interfaces, the parallel lifetime is only weakly perturbed by the polymer. On the contrary, the perpendicular lifetime is strongly modified below thickness of about half wavelength (Lukosz, 1980; Rahmani *et al.*, 1997). Finally, as the number of allowed modes (decay channels) decreases, the lifetime increases up to 7.5 ns.

The plane wave spectrum of the emitted power, represented in Fig. 4, provides some information about the available decay channels. For a dipole perpendicular to the surface, almost all the light is radiated into the substrate, whereas the main contribution for a horizontal transition dipole moment comes from light tunnelled from the PMMA into the glass substrate ($1.492 < k_p/k_0 < 1.51$) (Fan *et al.*, 1997; Danz *et al.*, 2002). Finally, the measured lifetime distribution is in good agreement with this model as described before (Vallée *et al.*, 2001). However, in the previous experiment, polystyrene ($n_2 = 1.58$) was used instead of PMMA. The calculated lifetime dependence on the position inside the PMMA film is given in Fig. 5. Although a lifetime dispersion ranging from 2.2 ns to 7.5 ns

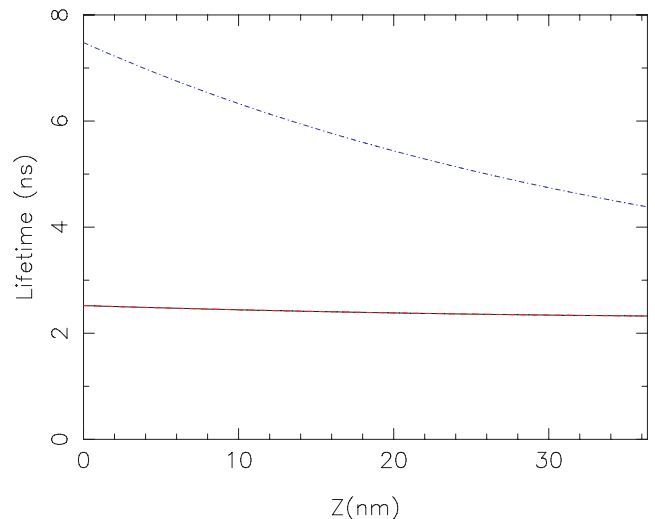


Fig. 5. Fluorescence lifetime calculated inside the film for an in-plane (solid line) and out-of-plane (dotted line) oriented dipole.

is expected from dipolar model, the experimental data present a lifetime distribution from 1.6 ns to 3 ns for molecules far from the stadium. Confocal single molecule detection mainly shows in-plane or close to in-plane molecules, because of the in-plane excitation field component. As a result, the long lifetimes up to 7.5 ns are not found in the experiment (Vallée *et al.*, 2001). The presence of a range of lifetimes reveals the inhomogeneity of the polymer film (Vallée *et al.*, 2001, 2003, 2005).

Lifetime dispersion inside the optical corral

LDOS modulation inside the optical corral. Green's dyad associated with the optical corral embedded into the PMMA slab is deduced from the bare slab dyad thanks to Dyson's equation ($\Delta\epsilon = \epsilon - \epsilon_2$ with ϵ the object (gold) dielectric function (Palik, 1985) and $\epsilon_2 = n_2^2$ the PMMA dielectric

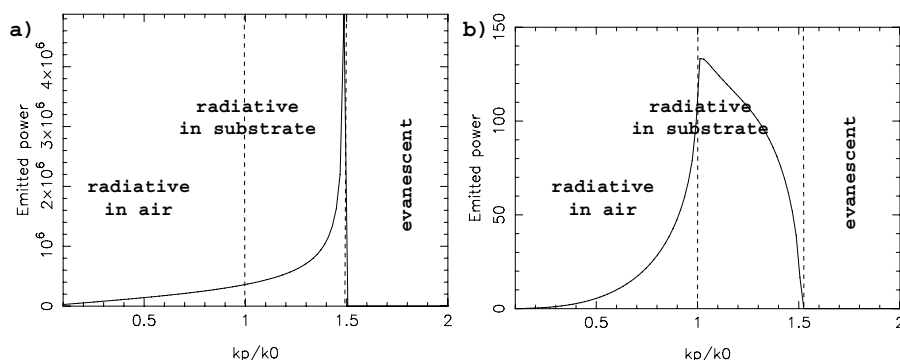


Fig. 4. Angular spectrum dependence of the normalized emitted power $P(k_p)$. The molecule is placed at the centre of a 35 nm PMMA slab. (a) Parallel decay rate and (b) perpendicular decay rate. Vertical lines indicate the limits for radiative mode in air ($k_p/k_0 < 1$) or in substrate ($k_p/k_0 < 1.51$).

function) (Martin & Piller, 1998):

$$\begin{aligned} \mathbf{G}(\mathbf{r}, \mathbf{r}', \omega) = & \mathbf{G}_{\text{slab}}(\mathbf{r}, \mathbf{r}', \omega) \\ & + k_0^2 \int_{\text{dots}} d\mathbf{r}'' \mathbf{G}_{\text{slab}}(\mathbf{r}, \mathbf{r}'', \omega) \Delta\epsilon(\mathbf{r}'', \omega) \mathbf{G}(\mathbf{r}'', \mathbf{r}', \omega). \end{aligned} \quad (6)$$

This self-consistent equation can be numerically solved by discretizing the gold dots (Girard & Dereux, 1996). Then, the PLDOS and fluorescence lifetime are obtained from Eqs (3) and (4), respectively.

The calculated Z-LDOS inside the stadium is shown in Fig. 6. To avoid time calculation limitations, we consider a single interface air/PMMA because the substrate and the PMMA film have very similar optical index. Moreover, we use the nonretarded (static) form for Green's dyad (Gay-Balmaz & Martin, 2000). Obviously, this forbids us to take into account the slab modes discussed above. This point will be discussed hereafter. The LDOS's maps show characteristic modulations inside the stadium as previously studied using a scanning near-field optical microscope (SNOM) (Chicanne *et al.*, 2002). The retardation effect (dynamic theory) is included in the numerical simulations of Fig. 6(b). We present both X-and Z-LDOS compared to the bare slab. Because of new boundaries conditions, similar variations are expected for both in-plane and out-of-plane molecules. Nevertheless, even in the most favourable situation (out-of-plane molecule, dynamic theory), the LDOS decrease (lifetime increase), does not explain the observed change in the fluorescence lifetime (3% instead of 35%). Indeed, LDOS variation inside the corral is small. Nevertheless, these first calculations show that the main effects appear near the gold dots. We explore this point in more details in the next paragraph.

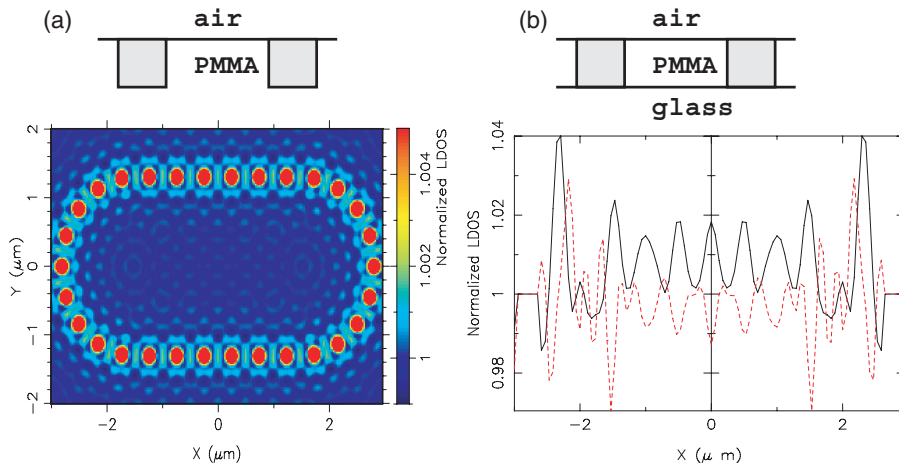


Fig. 6. (a) Normalized Z-LDOS inside the stadium corral. The configuration is schematized on the inset: single air/PMMA interface is considered (static theory). The Z-LDOS is calculated 10 nm below the interface. Scale is saturated to reveal LDOS modulation inside the optical corral. (b) Cross-section of normalized X-(solid line) and Z-(dashed line) LDOS calculated inside the corral, taking into account the slab configuration (dynamic theory). The normalization is carried out with respect to the LDOS calculated 10 nm below the air/PMMA interface without gold structures, this in order to reveal exclusively the stadium effect only.

Decay channels

A better insight of the relaxation process can be achieved throughout Green's dyad formalism. Indeed, applying the classical point of view for the fluorescence emission, the dissipative contribution to the fluorescence decay rate writes (Kuhn, 1970; Jackson, 1998; Colas des Francs *et al.*, 2005):

$$\gamma_{\text{nonrad}}(\mathbf{r}_m) = \frac{6\pi}{k_0} \int_{\text{dots}} \text{Im}[\epsilon(\mathbf{r}, \omega_0)] |\mathbf{G}(\mathbf{r}, \mathbf{r}_m, \omega_0) \cdot \mathbf{u}|^2 d\mathbf{r}. \quad (7)$$

Obviously, the radiative contribution is the difference $\gamma_{\text{rad}} = \gamma - \gamma_{\text{nonrad}}$. Figure 7 shows both the radiative and nonradiative decay channels' contribution to the total decay rate calculated near one gold pad inside the PMMA film. The real PMMA slab is considered here.

The number of allowed modes increases dramatically near the gold pad (Fig. 7a). Figure 7(b) clearly shows that the dissipative coupling to the metallic nanostructures is responsible for the opening of new decay channels, hence a strong quenching of the fluorescence. Finally, as the main effects occur near the metallic structures, we report in Fig. 8 the lifetime calculated inside the cavity formed by two gold dots inside the PMMA slab. The distance between the two pads is fixed at 500 nm, which corresponds to the experimental mean distance measured in the lithographed optical corrals. In the centre of the cavity, the lifetime is near the lifetime calculated in the bare slab (about 6 ns). However, strong lifetime enhancement of about 15% appears near the gold dots just before the fluorescence quenching. This enhancement is only 10% when considering molecules slightly out of plane (dipole moment making an angle of 30° with the interface plane). This is in good qualitative

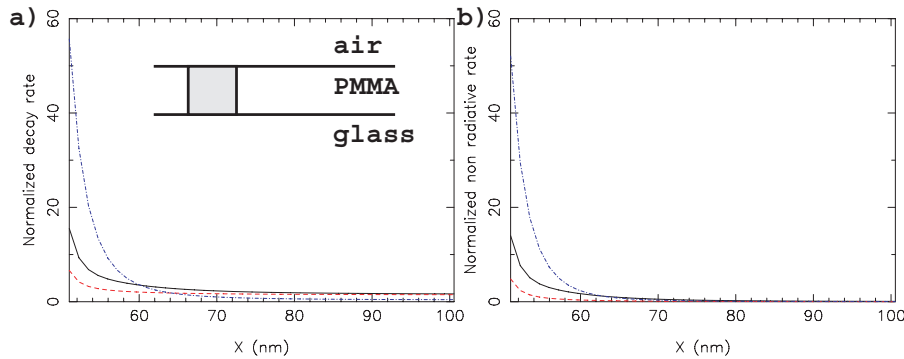


Fig. 7. (Colour online) Normalized decay rate γ (a) and dissipative contribution γ_{nonrad} (b) calculated near a single gold dot embedded into the PMMA slab. The molecule is located 10 nm below the air/PMMA interface and the abscissae indicates the distance from the dot centre ($x = 50$ nm corresponds to the contact). The dipole is oriented along the O_x (solid line), O_y (red dashed line) or O_z (blue dashed-dotted line) axis.

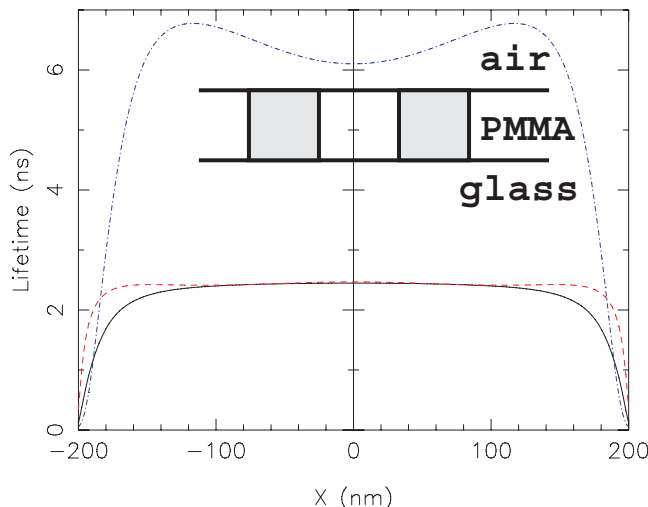


Fig. 8. Fluorescence lifetime calculated inside the 3D cavity formed by two gold dots separated by 500 nm (centre to centre) into the PMMA slab. Other parameters are identical to Fig. 7.

agreement with the measured shift of the maximum lifetime measured in Fig. 2(d). Therefore, according to Fermi's golden rule, the broadening of the fluorescence lifetime distribution can be attributed to the stadium perturbation of the LDOS. Indeed, although lifetime up to 7.5 ns can be expected in the PMMA slab alone for molecules oriented out of plane (see Fig. 5), the experiment is mainly sensitive for in-plane molecules with lower lifetime. Thus, the fact that a significant number of molecules show both shorter and longer lifetimes is attributed to the stadium effect.

Conclusion

Using confocal scanning microscopy, we have measured fluorescence lifetime of a single molecule near photonic nanostructures. The observed broadening of the lifetime distribution compared to molecules far from any structures is

correlated to the LDOS modulation inside the optical corrals. Numerical simulations based on dyadic Green's function technique identify the channels involved in the relaxation process, where it is possible to discriminate radiative and nonradiative decay rate. Moreover, the slab effect on the radiative decay rate is analyzed. Further investigation is planned. Particularly, direct comparison between PLDOS and individual lifetime, taking into account the molecule orientation, is needed for more quantitative understanding.

Acknowledgments

The authors gratefully acknowledge Aurélien Bruyant and Romain Quidant for fruitful discussions and help in the sample fabrication. This work benefits from the financial support of the Specific Target Research Project (STREP) ASPIRE (contract no. NMP-CT-2003-001601) in the sixth Framework Program of the European Community and G. S-M is financially supported by FOM, the Dutch Foundation for Fundamental Research of Matter.

References

- Chicanne, C., David, T., Quidant, R., et al. (2002) Imaging the local density of states of optical corrals. *Phys. Rev. Lett.* **88**, 97402–97406.
- Colas des Francs, G., Girard, C., Juan, M. & Dereux, A. (2005) Energy transfer in near-field optics. *J. Chem. Phys.* **123**, 174709–174715.
- Danz, N., Waldhaäusl, R., Bräuer, A., & Kowarschik, R. (2002) Dipole lifetime in stratified media. *J. Opt. Soc. Am. B* **19**, 412–419.
- Fan, S., Villeneuve, P.R., Joannopoulos, J. & Schubert, E. (1997) High extraction efficiency of spontaneous emission from slabs of photonic crystals. *Phys. Rev. Lett.* **78**, 3294.
- Gay-Balmaz, P. & Martin, O. (2000) Validity of non-retarded Green's tensor for electromagnetic scattering at surfaces. *Opt. Commun.* **184**, 37–47.
- Girard, C. & Dereux, A. (1996) Optical near-field theories. *Rep. Prog. Phys.* **59**, 657–699. (Note the minus sign between our definition and the definition used in this reference for the Green's dyad.)
- Jackson, J. (1998) Classical Electrodynamics, 3rd edition. John Wiley & Sons, Hoboken, NJ.

- Kuhn, H. (1970) Classical aspects of energy transfer in molecular systems. *J. Chem. Phys.* **53**, 101–108.
- Lounis, B. & Orrit, M. (2005) Single photon sources. *Rep. Prog. Phys.* **68**, 1129–1179.
- Lukosz, W. (1980) Theory of optical-environment-dependent spontaneous-emission rates for emitters in thin layers. *Phys. Rev. B* **22**, 3030.
- Martin, O.J.F. & Piller, N.B. (1998) Electromagnetic scattering in polarizable backgrounds. *Phys. Rev. E* **58**, 3909–3915.
- Novotny, L. & Hecht, B. (2006) Principles of Nano-Optics. Cambridge University Press, New-York.
- Palik, Z.D. (1985) Handbook of Optical Constants of Solids. Academic Press Inc., London.
- Purcell, E. (1946) Spontaneous emission probabilities at radio frequencies. *Phys. Rev.* **69**, 681.
- Rahmani, A., Chaumet, P., de Fornel, F. & Girard, C. (1997) Field propagator of a dressed junction: fluorescence lifetime calculations in a confined geometry. *Phys. Rev. A* **56**, 3245.
- Rigneault, H., Capoulade, J., Dintinger, J., Wenger, J., Bonod, N., Popov, E., Ebbesen, T. & Lenne, P.-F. (2005) Enhancement of single-molecule fluorescence detection in subwavelength apertures. *Phys. Rev. Lett.* **95**, 117401–117404.
- Sánchez-Mosteiro, G., van Dijk, E., Hernando, J., et al. (2006) DNA-based molecular wires: multiple emission pathways of individual constructs. *J. Phys. Chem. B* **110**, 26349–26353.
- Vallée, R., Tomczak, N., Gersen, H., van Dijk, E.M.H.P., Garcia Parajo, M.F., Vancso, G.J. & van Hulst, N.F. (2001) On the role of electromagnetic boundary conditions in single molecule fluorescence lifetime studies of dyes embedded in thin films. *Chem. Phys. Lett.* **348**, 161–167.
- Vallée, R., Tomczak, N., Vancso, L.K.G. & van Hulst, N. (2003) Single molecule lifetime fluctuations reveal segmental dynamics in polymers. *Phys. Rev. Lett.* **91**, 38301–38304.
- Vallée, R., Tomczak, N., Vancso, G., Kuipers, L. & van Hulst, N. (2005) Fluorescence lifetime fluctuations of single molecules probe local density fluctuations in disordered media: a bulk approach. *J. Chem. Phys.* **122**, 114704–114712.

Molecular quenching and relaxation in a plasmonic tunable system

Guillaume Baffou

Laboratoire de Photophysique Moléculaire (CNRS), Université Paris XI, F-91405 Orsay, France

Christian Girard and Erik Dujardin

Centre d'Elaboration des Matériaux et d'Etudes Structurales (CNRS), 29 Rue J. Marvig, F-31055 Toulouse, France

Gérard Colas des Francs

Institut Carnot de Bourgogne, UMR 5209 CNRS-Université de Bourgogne, 9 Avenue A. Savary, Boîte Postale 47870, F-21078 Dijon, France

Olivier J. F. Martin

Nanophotonics and Metrology Laboratory, Swiss Federal Institute of Technology Lausanne (EPFL), CH-1015 Lausanne, Switzerland

(Received 14 February 2008; published 19 March 2008)

Molecular fluorescence decay is significantly modified when the emitting molecule is located near a plasmonic structure. When the lateral sizes of such structures are reduced to nanometer-scale cross sections, they can be used to accurately control and amplify the emission rate. In this Rapid Communication, we extend Green's dyadic method to quantitatively investigate both radiative and nonradiative decay channels experienced by a single fluorescent molecule confined in an adjustable dielectric-metal nanogap. The technique produces data in excellent agreement with current experimental work.

DOI: 10.1103/PhysRevB.77.121101

PACS number(s): 73.20.Mf, 34.35.+a, 07.79.Fc

The emission characteristic of a single quantum system excited by an external source of electrons or photons and interacting with metallic nanostructures is governed by a subtle balance between the radiative and nonradiative energy channels available in the vicinity of the metal.¹ In many experiments, the excitation mechanism generally involves pure optical^{2–9} or electro-optical^{10–12} processes. For example, in near field optics experiments, molecules deposited on dielectric surfaces are generally excited by an external laser beam or by the optical field generated at the tip apex of a near field optical microscope.^{4,6,7} In scanning tunneling microscope (STM), inelastic tunnel electronic events can also be used to excite fluorescent molecules.^{11,12} In spite of the fundamental difference between these two excitation modes, the fluorescence decay of the excited channels is governed by the same mechanisms. Actually, three emission regimes can be defined by comparing the absolute value of the *tip-molecule distance* to the *fluorescence wavelength* λ_0 . (i) In the wave zone,¹ emission rate smoothly oscillates around the free space value Γ_0 due to interferences with the sample surface. (ii) When entering the subwavelength distance range, the total decay rate of the molecule is significantly modified (enhanced or partially canceled) by its transition dipole image.¹³ (iii) At even shorter distances, ranging from few nanometers to the physical contact with the metallic structure, a second mechanism tends to increase the total decay rate. This effect, which is responsible for fluorescence quenching, corresponds to the opening of a new decay channel by absorption of fluorescence photons in the metallic structure itself.^{6,7,14,15} Over the past few years, these well-known physical concepts have been applied to possible new plasmonic devices, with the aim of achieving (i) high density integrated photonic components, (ii) low threshold detection of biological and chemical species, and to supply (iii) new molecular-scale characterization techniques for biomolecules.¹⁶ In this rapidly growing

field, systems consisting of isolated molecules interacting with noble metal nanostructures are used as prototype models to test and validate new schemes for active plasmonic devices. Recently, a new step toward *molecular plasmonics* was achieved with the demonstration of the control of fluorescent resonant energy transfer through thin layers of plasmonic materials.¹⁷ These experiments use the excitation of surface plasmons to enhance and control the efficiency of the optical transfer between two remote molecular sites. Such controlled light transfer in highly reduced geometries can pave the way for future optical technologies, integrable and scalable down to molecular dimensions.¹⁸ Finally, in a closely related context involving the spatial control of sharp metal tips or the effective realization of nanoparticle plasmon waveguides, single molecules are often used as efficient local sensors for the plasmonic near-field intensity.¹⁹ In this Rapid Communication, we present a fully self-consistent framework relevant for the interpretation of recent experiments involving molecular quenching and relaxation in a plasmonic tunable nanogap. Our model includes the complex physics involved in quantum systems coupled with plasmonic environments. In the presence of plasmonic devices that sustain localized plasmon modes, such an analysis requires a specific attention to properly include local field enhancements, Ohmic losses, and radiative decay rates. In particular, we apply Green's dyadic method (also called field-susceptibility technique) to treat these different phenomena in the presence of finite plasmonic structures.

In near-field experimental setups based either on electrons or photons detection, the central element is the tip of a metallic stylus that is raster scanned across the sample. We consider the case of such a sharp metallic probe facing a plane dielectric surface on which N identical fluorescing molecules have been adsorbed (Fig. 1). The tip is modeled as a paraboloid enclosed in a surface of equation $Ax^2 + Ay^2 = z$. The pa-

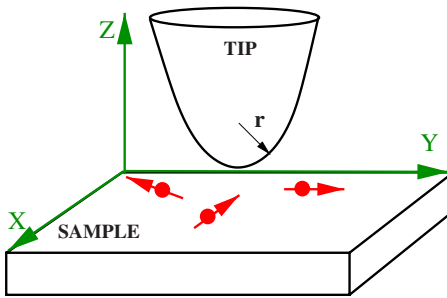


FIG. 1. (Color online) Schematics of the geometry used to model light emission by molecules located in the gap between a paraboloid metallic tip and a planar dielectric surface. The curvature radius \mathbf{r} of the tip apex is fixed at 8 nm.

parameter A can then be adjusted to modify the sharpness of the tip. In the numerical scheme used in this Rapid Communication, the physical volume limited by this surface will be discretized on a Cartesian grid stacking layers of meshes in a closed packed arrangement. When we neglect any optical coupling between the individual molecules, the total fluorescence energy released by the sample at the frequency ω_0 is given by

$$I(\mathbf{R}_{tip}) = \sum_{i=1}^N \hbar \omega_0 \rho(\mathbf{r}_i, \mathbf{u}_i, \omega_0) \Gamma(\mathbf{r}_i, \mathbf{u}_i, \omega_0), \quad (1)$$

where \mathbf{R}_{tip} labels the position of the tip apex, \mathbf{r}_i represents the location of the i th molecule deposited on the surface, and the units vectors \mathbf{u}_i have been introduced to define the orientations of their transition dipole moment \mathbf{P}_{eg} with respect to an absolute surface frame. In addition, the two factors $\rho(\mathbf{r}_i, \omega_0)$ and $\Gamma(\mathbf{r}_i, \omega_0)$ define the population rate and the total decay rate associated with the i th molecule, respectively. Both quantities depend on the orientation and the location of the molecules. The first one, $\Gamma(\mathbf{r}_i, \mathbf{u}_i, \omega_0)$, is given by

$$\Gamma(\mathbf{r}_i, \mathbf{u}_i, \omega_0) = \Gamma_0 + \frac{2P_{eg}^2}{\hbar} \text{Im}\{\mathcal{S}(\mathbf{r}_i, \mathbf{r}_i, \omega_0)\} : \mathbf{u}_i \mathbf{u}_i. \quad (2)$$

The field-susceptibility $\mathcal{S}(\mathbf{r}_i, \mathbf{r}_i, \omega_0)$ that enters the total decay rate is defined in Ref. 20. This dyadic tensor describes the dipolar response of the whole *tip-surface* system. It obeys Dyson's equation that can be numerically solved with an algorithm that relies on a three-dimensional discretization of the metal tip.²¹

In Eq. (1), the population rate $\rho(\mathbf{r}_i, \mathbf{u}_i, \omega_0)$ is directly related to the mechanism we used to excite the molecules. For example, in the case of optical excitations with a laser light source at the frequency ω_L , it can be easily obtained from the Maxwell–Bloch equation scheme (see Ref. 20). In particular, a two-level molecular model predicts the following Lorentzian law:

$$\rho(\mathbf{r}_i, \mathbf{u}_i) = \frac{\Omega^2(\mathbf{r}_i, \mathbf{u}_i, \omega_L)}{4\delta_L^2 + \Gamma^2(\mathbf{r}_i, \mathbf{u}_i, \omega_0) + 2\Omega^2(\mathbf{r}_i, \mathbf{u}_i, \omega_L)}, \quad (3)$$

where $\delta_L = \omega_L - \omega_0$ is the detuning factor and $\Omega(\mathbf{r}_i, \mathbf{u}_i, \omega_0)$ defines the Rabi frequencies at the molecule locations \mathbf{r}_i . As

indicated by Eq. (3), the molecular population rate ρ intricately depends both on the Rabi frequency and the excited state decay rate. The Rabi frequency is proportional to the optical near-field intensity at the molecule location. The saturation regime occurs when this quantity is significantly larger than Γ . In the case of a two-level model, the population rate stabilizes around the ratio of 1/2 for zero detuning. In the following numerical applications, we will assume that this saturation regime has been reached.

When the tip enters the subwavelength approach distance range, the total decay rate $\Gamma(\mathbf{r}_i, \mathbf{u}_i, \omega_0)$ of the molecules is significantly enhanced compared to its free-space value Γ_0 . For a selected molecule, which is located at the position \mathbf{r}_i , the enhancement factor can be derived from

$$\eta(\mathbf{r}_i, \mathbf{u}_i, \omega_0) = \Gamma(\mathbf{r}_i, \mathbf{u}_i, \omega_0) / \Gamma_0 = 1 + \frac{2P_{eg}^2}{\hbar\Gamma_0} \text{Im}\{\mathcal{S}(\mathbf{r}_i, \mathbf{r}_i, \omega_0)\} : \mathbf{u}_i \mathbf{u}_i. \quad (4)$$

This well-known phenomenon is associated with an increase (or decrease) of the local density of available photonic states when the tip is approaching the molecule.⁴ However, in the vicinity of dissipative materials, a second mechanism will significantly reduce the radiative decay rate. This effect, responsible for fluorescence quenching, corresponds to the absorption of fluorescence photons by the metallic structure itself. To compute this dissipated power $Q(\mathbf{R}_{tip})$, we consider that each emitting molecule behaves as a fluctuating dipole defined by

$$\mathbf{m}_i(t) = P_{eg} \mathbf{u}_i \cos(\omega_0 t). \quad (5)$$

In turn, these dipoles give rise to an electric field inside the metal,

$$\mathbf{E}_{tip}(\mathbf{r}, \omega_0) = \sum_i \mathcal{S}(\mathbf{r}, \mathbf{r}_i, \omega_0) \cdot P_{eg} \mathbf{u}_i, \quad (6)$$

which oscillates at the fluorescence frequency ω_0 . The dissipated power $Q(\mathbf{R}_{tip})$ is given by the integral of the square modulus of $\mathbf{E}_{tip}(\mathbf{r}, \omega_0)$ over the volume occupied by the tip. This scalar quantity can be normalized by the free-space power $\hbar\omega_0\Gamma_0$. After using Eq. (6), it reads

$$\bar{Q}(\mathbf{R}_{tip}) = \frac{3}{2k_0^3} \int_{tip} \sum_i \text{Im}[\chi(\omega_0)] |\mathcal{S}(\mathbf{r}, \mathbf{r}_i, \omega_0) \cdot \mathbf{u}_i|^2 d\mathbf{r}, \quad (7)$$

where $\text{Im}[\chi(\omega_0)]$ represents the imaginary part of the metal susceptibility. In the numerical work presented in this Rapid Communication, we have chosen a paraboloid-shaped gold tip facing a planar glass surface (optical index $n=1.5$) located at the coordinate $Z=0$. The tip displays a circular cross section in the (XOY) plane. The aperture angle and tip radius of the paraboloid are fixed at 30° and 8 nm, respectively. A volume discretization of the tip based on a hexagonal mesh is used to compute the retarded field susceptibility around the system. The molecules, which are characterized by a fluorescence wavelength λ_0 and a natural linewidth Γ_0 , are adsorbed at 1 nm from the glass substrate. From Eqs. (1), (4), and (7), we can deduce the total fluorescence signal collected by a remote detector placed in the far-field zone above the sample.²²

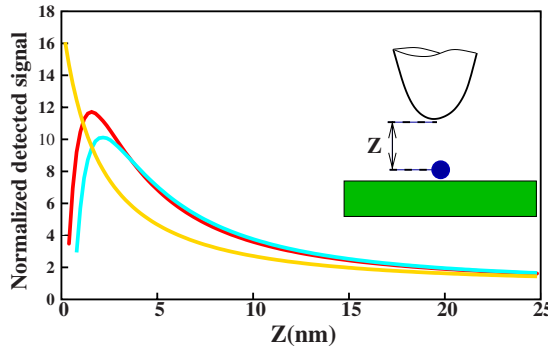


FIG. 2. (Color online) Total fluorescence signal computed as a function of the tip-sample distance. Three different fluorescence wavelengths are investigated: red curve (dark gray) $\lambda_0=620$ nm, cyan curve (gray) $\lambda_0=534$ nm, and yellow curve (light gray) $\lambda_0=780$ nm. The molecule is perpendicular to the surface.

$$I_{det}(\mathbf{R}_{tip}) = \hbar\omega_0\Gamma_0 \sum_{i=1}^N \rho(\mathbf{r}_i, \mathbf{u}_i, \omega_0) [\eta(\mathbf{r}_i, \mathbf{u}_i, \omega_0) - \bar{\mathcal{Q}}(\mathbf{R}_{tip})]. \quad (8)$$

This expression [Eq. (8)] together with Eq. (7) has been implemented numerically on a parallel supercomputer to investigate several photophysical properties of molecules coupled with plasmonic tips. In Eqs. (8) and (7), the field susceptibility \mathcal{S} is computed *outside* and *inside* the metal by iteratively solving a sequence of Dyson's equations. The corresponding numerical results are shown in Figs. 2–5. In Fig. 2, a series of three typical tip-molecule distance curves computed for three different fluorescence wavelengths λ_0 shows the dramatic variation of the far-field intensity [Eq. (8)] when the molecule approaches the metal quenching zone.

We observe that significant fluorescence quenching occurs at very short distances from the metallic tip [e.g., few nanometers for the red (dark gray) and cyan (gray) curves in Fig. 2]. In these two examples, the dissipated power totally cancels the radiative emission rate before reaching the physical contact of the molecule with the metal. Conversely, at $\lambda_0=780$ nm, this behavior does not occur because the imagi-

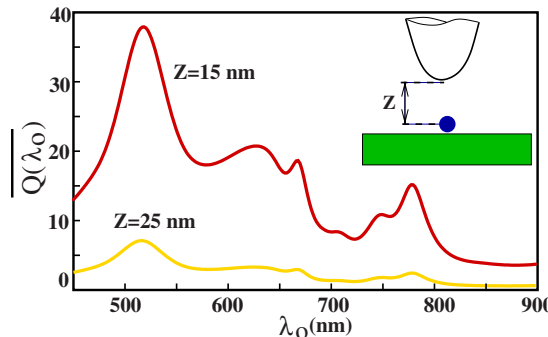


FIG. 3. (Color online) Variation of the power dissipated by an arbitrary molecule versus its fluorescence wavelength λ_0 . The power is normalized to the power $\hbar\omega_0\Gamma_0$ delivered by the molecule in vacuum.

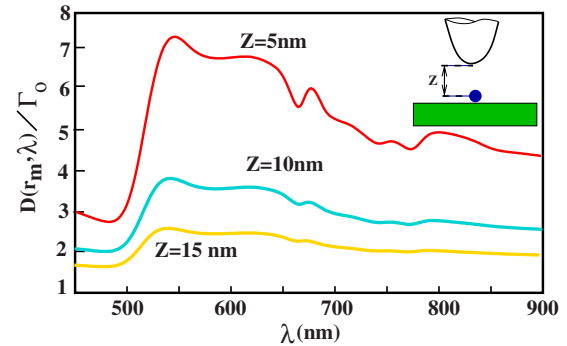


FIG. 4. (Color online) Evolution of the far-field intensity as a function of the fluorescence wavelength (λ_0). Three approach distances Z are considered: red curve (dark gray) $Z=5$ nm, cyan curve (gray) $Z=10$ nm, and yellow curve (light gray) $Z=15$ nm. The signal is normalized to the power $\hbar\omega_0\Gamma_0$ delivered by the molecule in vacuum.

nary part of the gold dielectric constant decreases in this frequency range.

Very recently, Issa and Guckenberger²³ have analyzed the role of the surface plasmon polaritons mode in the relaxation processes. They separate the local energy transfer to the very tip and the long range energy losses during the propagation of the plasmon surface wave along the tip-air interface. In the present analysis, these two contributions are taken into account in the nonradiative rate [Eq. (7)]. Generally, let us note that because of the plasmon propagation at long distance, direct calculation of the radiative decay rate is extremely difficult since it includes the energy transported by the plasmon mode that should be totally dissipated by Joule effect for infinitely extended gold tip.^{23,24} More generally, when exploring the visible range spectrum, the simulations indicate that the fluorescence enhancement varies between 10 and 16. We conclude that energy losses, which are intrin-

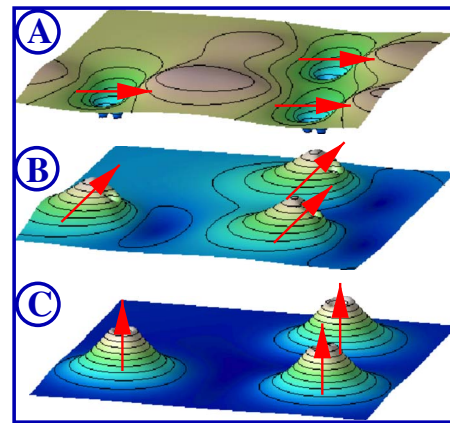


FIG. 5. (Color online) Sequence of three maps of the fluorescence intensity scattered in the far-field zone. The rainbow color (gray) scale increases from blue (dark gray) to pale red (light gray). The tip-molecule distance is fixed at 2.5 nm and three orientations of the transition dipole moments (red arrows) are investigated: (A) parallel to the sample surface, (B) tilted with an angle of 45°, and (C) perpendicular to the surface.

sic to the metal tip, considerably reduce the expected fluorescence amplification effect. The amplitude variation of these losses can be predicted with our model. In the visible frequency range, two spectra of the power dissipated in the gold tip by a single molecule are plotted in Fig. 3 as a function of the fluorescence wavelength λ_0 . In these two examples, the molecule is perpendicularly aligned to the surface. We observe well-contrasted signatures of the power dissipated in the metal as a function of the fluorescence wavelength λ_0 . Apart from the main plasmon resonance of the tip (≈ 520 nm), the number of fluorescence photons absorbed by the metal increases. This phenomenon produces an enhancement of the normalized factor \bar{Q} between 8 and 38 when the tip-molecule distance decreases from 25 to 15 nm. These results can be compared with the spectra of the total signal collected by a remote sensor (see Fig. 4). Figure 4 shows that the spectral variation of this signal—described as the difference between two quantities of the same magnitude order [$I(\mathbf{R}_{tip})$ and $Q(\mathbf{R}_{tip})$]—is generally smoother than the variation of the sole dissipated power $Q(\mathbf{R}_{tip})$. With the gold tip considered here, the optimal enhancement effect is obtained when working with fluorescence wavelengths λ_0 between 520 and 630 nm.

To conclude this analysis, Fig. 5 shows a sequence of three maps for the normalized detected signal. The maps are computed by scanning the tip in the constant distance mode. The planar glass sample supports three identical fluorescing molecules for which three molecular orientations have been investigated, keeping the same tip-sample distance (2.5 nm). In the first map [Fig. 5(a)], the transition dipole moments are parallel to the surface. In this geometry, individual molecules

appear as elongated depressions perpendicularly oriented to their transition dipoles and surrounded by two-lobed patterns. Furthermore, the two closest molecules simulated in this figure exhibit a pattern with three lobes and two depressions, which is in fairly good agreement with the results of Ref. 14. In the second map Fig. 5(b), the dipole moments are tilted out of the sample plane with an angle of 45°. Here, each molecule produces an asymmetrical protrusion with a small depression localized on its right side. Finally, these patterns gradually transform into regular truncated conical protrusions with a small depression on their apex when the molecules are perpendicularly aligned to the surface. These orientational behaviors are found in perfect agreement with recent experimental data measured in similar tip-sample geometries.^{6,7,14}

To summarize, we have described a versatile scheme well suited for describing and predicting photophysical mechanisms triggered by the vicinity of complex plasmonic devices. When applied to an adjustable plasmonic nanogap geometry, this framework successfully reproduces experimental signals. Consequently, this numerical tool can be used to support current experimental work developed in the field of *molecular plasmonics*. In particular, it can be applied to any geometrical configuration, to the accurate computation of the dissipation losses, and to the research of strategies to minimize them. Finally, by introducing an appropriate model for the excitation rate parameter $\rho(\mathbf{r}_i, \mathbf{u}_i)$, the method could be extended to the description of optical relaxation of single molecules located in an STM nanogap.^{10,11}

This work was supported in part by the European Network of Excellence (NoE) *Plasmo-Nano-Devices* (Contract No. 507879).

- ¹R. R. Chance, A. Prock, and R. Silbey, *Adv. Chem. Phys.* **37**, 1 (1978).
- ²F. D. Stefani, K. Vasilev, N. Bocchio, N. Stoyanova, and M. Kreiter, *Phys. Rev. Lett.* **94**, 023005 (2005).
- ³B. C. Buchler, T. Kalkbrenner, C. Hettich, and V. Sandoghdar, *Phys. Rev. Lett.* **95**, 063003 (2005).
- ⁴W. Trabesinger, A. Kramer, M. Kreiter, B. Hecht, and U. P. Wild, *Appl. Phys. Lett.* **81**, 2118 (2002).
- ⁵A. Cvitkovic, N. Ocelic, J. Aizpurua, R. Guckenberger, and R. Hillenbrand, *Phys. Rev. Lett.* **97**, 060801 (2006).
- ⁶P. Anger, P. Bharadwaj, and L. Novotny, *Phys. Rev. Lett.* **96**, 113002 (2006).
- ⁷S. Kuhn, U. Hakanson, L. Rogobete, and V. Sandoghdar, *Phys. Rev. Lett.* **97**, 017402 (2006).
- ⁸G. P. Wiederrecht, J. E. Hall, and A. Bouhelier, *Phys. Rev. Lett.* **98**, 083001 (2007).
- ⁹O. Labea, Ph. Tamarat, H. Courtois, G. S. Agarwal, and B. Louonis, *Phys. Rev. Lett.* **98**, 143003 (2007).
- ¹⁰J. Aizpurua, G. Hoffmann, S. P. Apell, and R. Berndt, *Phys. Rev. Lett.* **89**, 156803 (2002).
- ¹¹M. Sakurai, C. Thirstrup, and M. Aono, *Phys. Rev. Lett.* **93**, 046102 (2004).
- ¹²X. H. Qiu, G. V. Nazin, and W. Ho, *Phys. Rev. Lett.* **93**, 196806 (2004).

- ¹³W. Barnes, *J. Mod. Opt.* **45**, 661 (1998).
- ¹⁴H. G. Frey, S. Witt, K. Felderer, and R. Guckenberger, *Phys. Rev. Lett.* **93**, 200801 (2004).
- ¹⁵G. Colas des Francs, C. Girard, M. Juan, and A. Dereux, *J. Chem. Phys.* **123**, 174709 (2005).
- ¹⁶T. Neumann, M.-L. Johansson, D. Kambhampati, and W. Knoll, *Adv. Funct. Mater.* **12**, 575 (2002); G. Stengel and W. Knoll, *Nucleic Acids Res.* **33**, 7 (2005); J. R. Lakowicz, *Anal. Biochem.* **337**, 171 (2005).
- ¹⁷P. Andrews and W. L. Barnes, *Science* **306**, 1002 (2004).
- ¹⁸D. E. Chang, A. S. Sørensen, P. R. Hemmer, and M. D. Lukin, *Phys. Rev. Lett.* **97**, 053002 (2006).
- ¹⁹H. Ditlbacher, J. R. Krenn, N. Felidj, B. Lamprecht, G. Schider, M. Salerno, A. Leitner, and F. R. Aussenegg, *Appl. Phys. Lett.* **80**, 404 (2002).
- ²⁰C. Girard, O. J. F. Martin, G. Leveque, G. Colas des Francs, and A. Dereux, *Chem. Phys. Lett.* **404**, 44 (2005).
- ²¹O. J. F. Martin and M. Paulus, *J. Microsc.* **205**, 147 (2002).
- ²²For simplicity, we have omitted the angular dependency of the detected signal.
- ²³During the review process, a related article has been published: N. Issa and R. Guckenberger, *Opt. Express* **15**, 12131 (2007).
- ²⁴F. Kaminski, V. Sandoghdar, and M. Agio, *Chem. Abstr.* **4**, 635 (2007).

A.3-Publications relatives au chapitre 4

“Polymer-metal waveguides characterization by Fourier plane leakage radiation microscopy”

S. Massenot, J. Grandidier, A. Bouhelier, Colas des Francs, J.-C. Weeber, L. Markey and A. Dereux
Applied Physics Letters **91**, 243101 (2007).

“Differential method for modelling dielectric-loaded surface plasmon polariton waveguides”

S. Massenot, J.-C. Weeber, A. Bouhelier, Colas des Francs, J. Grandidier, L. Markey and A. Dereux
Optics Express **16**, 17599-17608 (2008).

Polymer-metal waveguides characterization by Fourier plane leakage radiation microscopy

S. Massenot,^{a)} J. Grandidier, A. Bouhelier, G. Colas des Francs, L. Markey, J.-C. Weeber, and A. Dereux
Institut Carnot de Bourgogne, UMR 5209 CNRS-Université de Bourgogne, 9 Av. A. Savary, BP 47 870, F-21078 Dijon Cedex, France

J. Renger, M. U. González, and R. Quidant
ICFO-Institut de Ciències Fotòniques, Castelldefels 08860 Barcelona, Spain

(Received 2 October 2007; accepted 24 November 2007; published online 10 December 2007)

The guiding properties of polymer waveguides on a thin gold film are investigated in the optical regime. The details of propagation in the waveguides are studied simultaneously in the object and Fourier planes, providing direct measurement of both the real and imaginary parts of the effective index of the guided mode. A fair agreement between theoretical analysis provided by the differential method and experimental leakage radiation microscopy data is shown. All these tools bring valuable information for designing and understanding such devices. © 2007 American Institute of Physics.
[DOI: 10.1063/1.2824840]

Due to their high bandwidth, integrated optical components have raised considerable interests in the race to overcome data transfer limitation in electronic circuits. For instance, interconnections between chips realized in the optical domain could significantly increase their bit rate. Among the different existing optical waveguiding technologies, polymeric elements lying on a metal film offer a number of advantages. On the one hand, they dispose of a high index contrast required for large scale integration and, on the other hand, the presence of a metal layer let foresee the possibility to develop plasmonic components, which present interesting properties such as field confinement and exaltation at dielectric/metal interfaces.¹ Compared to silicon-on-insulator technology, these waveguides are intrinsically lossy. However, they are still of interest when propagation lengths involved are short, typically a few tens of micrometers. It is notably true in the near-infrared domain, i.e., standard telecommunications spectral bands, where the losses associated with noble metal substrates are relatively low.

The integration of polymer onboard interconnects requires the understanding and optimization of light propagation in basic structures such as the straight waveguide. Such structures were theoretically investigated by the effective index model and by finite elements analysis, in particular for structures supporting plasmon modes.^{2,3} Propagation losses of $0.1 \text{ dB}/\mu\text{m}$ have been calculated for a wavelength of 1550 nm and the preliminary guiding demonstration was experimentally observed on metal/polymer structure⁴ (for $\lambda = 632.8 \text{ nm}$). Closely related, SiO_2 dielectric waveguides (straight and bent) have also been investigated and propagation lengths versus bent radii were characterized^{5,6} (for $\lambda = 800 \text{ nm}$). However, the use of polymer waveguides instead of SiO_2 brings additional advantages. The polymers are widely accessible, presenting a variety of chemical and optical specificities, sensibilities, and dopings. The latter feature can be of importance in the development of active and dynamic functionalities (modulators or switches, for example) addressed either optically or electrically.

The recent interest for dielectric elements on metal films increases the need of powerful design and characterization techniques and it is the aim of this letter to present suitable tools. The structures are modeled using the differential method, which is particularly suited in the investigation of this kind of waveguide since it calculates the field inside and outside the waveguide and provides the complex effective index of the guided mode. The characteristics of the waveguides are experimentally measured by direct and Fourier plane leakage radiation microscopy.^{7–10} This dual-plane imaging technique allows to retrieve the real and imaginary parts of the effective index of the supported modes without requiring advanced scanning near-field imaging techniques¹¹ or mode profiling of the output end.

The geometry of the structure is schematically shown in Fig. 1. It consists of a polymer waveguide composed of polymethylmethacrylate (PMMA) (refractive index n_w) deposited on a gold metal layer (50 nm thick, refractive index n_m) lying on a glass substrate (refractive index n_1). The waveguide is illuminated from the substrate with a plane wave or a Gaussian beam with an angle of incidence θ and an azimuth δ . $\delta = 90^\circ$ corresponds to an incident wavevector parallel to the longitudinal axis of the waveguide.

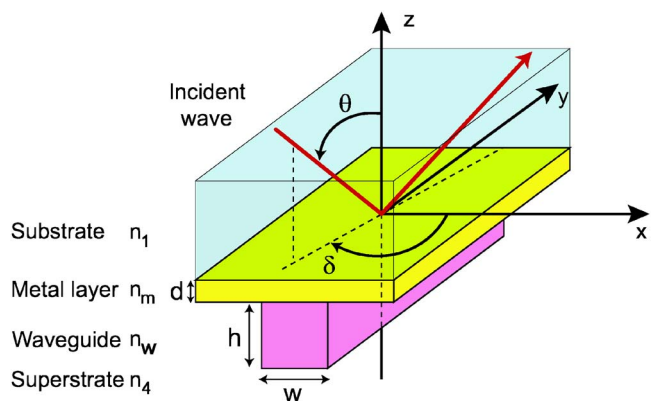


FIG. 1. (Color online) Sketch of the polymer waveguide studied and associated notations.

^{a)}Electronic mail: sebastien.massenot@u-bourgogne.fr.

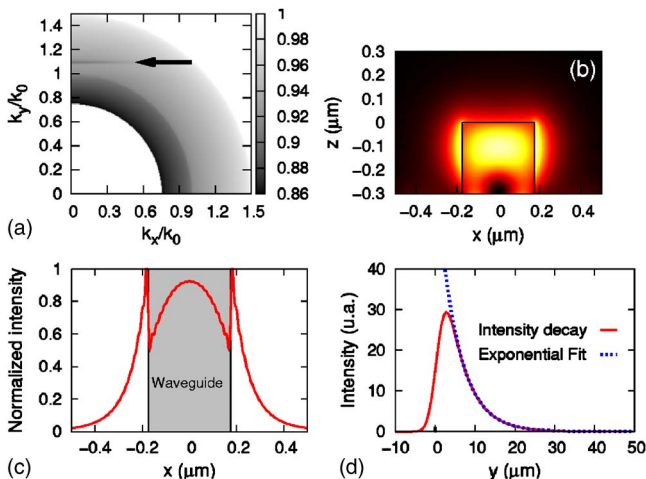


FIG. 2. (Color online) (a) Fourier plane (reflectivity map of the structure) for a TE polarized incident plane wave. (b) Normalized intensity profile of the TE mode supported by the structure. (c) Mode profile at $z=-0.1 \mu\text{m}$. (d) Calculated intensity distribution along the longitudinal axis.

The excitation condition of a guided mode in the structure is given by the phase matching condition:¹² $k_0 n_1 \sin \theta \sin \delta = \Re(\beta) = k_0 \Re(n_{\text{eff}})$ (1), where k_0 is the free-space wavevector, β the propagation constant of the considered guided mode, and n_{eff} , its associated complex effective index ($n_{\text{eff}} = \nu + i\alpha$). The real part of n_{eff} is used in Eq. 1 because of the presence of the metal layer which is a source of Ohmic and radiative losses. The propagation length of the mode, corresponding to the attenuation of the intensity at $1/e$, is defined by $L_\alpha = \lambda_0 / 4\pi\alpha$, where λ_0 is the wavelength in vacuum.

This waveguide structure is theoretically analyzed using the differential method,¹³ originally dedicated to the study of diffraction gratings. It is relatively easy to extend this method to a nonperiodic structure by avoiding coupling effects between the periodic units and considering a grating period much larger than the typical lateral extension of the mode supported by the system of interest. A scattering matrix algorithm helps to propagate in the different layers of the structure without numerical instabilities.¹⁴ By using angular spectrum decomposition, it is possible to extend the calculation to arbitrary excitation profiles.¹⁵

Following notations of Fig. 1, the parameters of the considered waveguide are $n_1 = 1.5$, $n_w = 1.493$, $n_4 = 1.0$, $d = 50 \text{ nm}$, $h = 300 \text{ nm}$, $w = 350 \text{ nm}$, and $\lambda = 632.8 \text{ nm}$. The refractive index of gold n_m is calculated from Ref. 16 with piecewise cubic Hermite interpolation. By analyzing the reflectivity of this structure for all the angles θ and δ , Fourier planes can be established (they contain the spatial information associated to the angular response of the structure). Figure 2(a) shows the reflectivity map calculated over $30^\circ < \theta < 89^\circ$ and $0^\circ < \delta < 90^\circ$ for TE incident plane waves. The darker areas in Fig. 2(a) are regions of lower reflectivity. A horizontal dark fringe is observed, that corresponds to a constant value of the k_y component of the incident wave. Following Eq. (1), this line can be interpreted as being the signature of a guided mode in the structure. The position of the line gives a direct measure of the real part of the mode effective index, here $\nu = 1.095$. The single mode operation is confirmed by Figs. 2(b) and 2(c) showing the calculated distribution of intensity across the waveguide. To estimate the propagation length of the mode, the evolution of the intensity

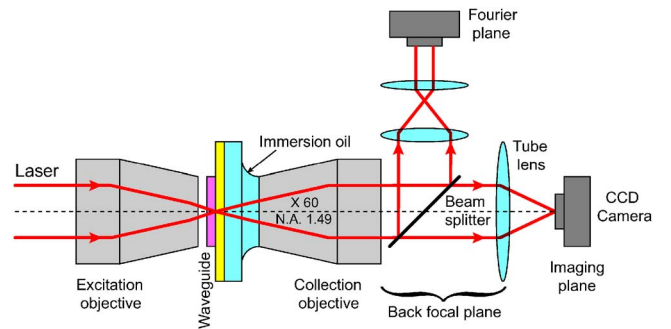


FIG. 3. (Color online) Principle of leakage radiation microscopy.

along the waveguide is calculated by replacing the plane wave illumination by a Gaussian excitation. Figure 2(d) shows an exponential decay of the intensity with a characteristic length $L_\alpha = 5.2 \mu\text{m}$.

To experimentally verify the theoretical values of the complex effective index of the guided mode, polymer waveguides were fabricated on a 50-nm-thick gold layer using standard electron-beam lithography and the size parameters were those used in the calculations.

The waveguide was optically characterized by leakage radiation microscopy.^{7,8,17} This method uses optical index matching through a high-numerical aperture lens to collect radiation losses occurring in the waveguide during propagation. These losses are mainly emitted into the substrate through the gold layer. Imaging this leakage radiation gives valuable information of the guided mode structure. A schematic of the setup is shown in Fig. 3. Depending on where leakage radiations are detected on the optical path, the image can be conjugated either with the object plane or with the Fourier plane, thus, permitting to access both direct and reciprocal spaces.^{9,18} The guided mode was excited here using a diascopic illumination with a 20 \times objective opened at 0.35 numerical aperture. Scattering on a waveguide defect generates a continuum of wavevectors, some of them fulfilling the condition given by Eq. (1), thereby exciting the supported mode. In this case, two counterpropagating modes are excited [see Fig. 4(a)]. The polarization direction was aligned perpendicularly to the axis of the waveguide and parallel to the substrate (TE). Contrary to Fig. 1, this setup is not a measure of the reflectivity. Only the leakage radiations collected by the immersion objective will be detected and the signature of the guided mode in the Fourier plane will appear as a bright line and not as an absorption dip.

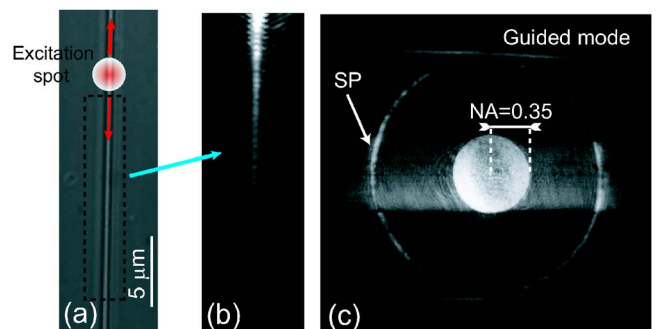


FIG. 4. (Color online) (a) Optical micrograph of the polymer waveguide fabricated on a gold substrate. Leakage radiation microscopy observations of the propagation in the waveguide: (b) imaging plane and (c) Fourier plane.

Figure 4(b) is the corresponding leakage image acquired in direct space showing the mode propagating from top to bottom inside the polymer waveguide (the excitation area is outside the field of view of the camera). An exponential fit of the intensity along the waveguide gives a propagation length $L_\alpha = 4.8 \pm 0.5 \mu\text{m}$ in good agreement with the calculated value. The intensity distribution in the waveguide demonstrates the single mode nature of the mode. This characteristic is confirmed by the reciprocal Fourier image, shown in Fig. 4(c). The signature of the guided mode appears as a single bright horizontal line in Fourier space corresponding to the propagating mode, displayed in Fig. 4(b) [two lines are present; they correspond to the two counterpropagating modes, as shown in Fig. 4(a)]. It is worth to note that these lines are the direct consequences of the field confinement of the guided mode in the transverse direction. Indeed, the Fourier transform of such a confined field distribution features necessarily a wide angular spectrum in the transverse (i.e., x axis) direction and a single value of the wavevector in longitudinal direction corresponding to the propagation constant of the guided mode. Additionally, the thin film surface plasmon excitation appears as a bright ring in the image (as a polarized beam is focused on the structure, it contains vertical components of the field allowing the excitation of a surface plasmon). The large central band simply reveals light diffraction perpendicular to the line structure. Knowing the full numerical aperture of the excitation and the collection objectives, it is easy to calibrate the image and extract $\Re(n_{\text{eff}})$ of the guided mode. From the image, a value of $\nu = 1.08 \pm 0.03$ is obtained, which is also in very good agreement with the theoretical value given by the differential method.

In conclusion, polymer waveguides lying on a metal film have been studied by using the differential method and leakage radiation microscopy in direct and reciprocal spaces. These numerical and experimental tools are providing powerful characterization of the nature of the modes propagating inside the structure. In particular, the complex effective index of the modes can be theoretically estimated and experimen-

tally determined. Fair agreements have been obtained. These techniques are well suited to characterize dielectric-loaded surface plasmon waveguides (or other structures presenting radiation losses) and to evaluate their potential for information processing devices.

The authors gratefully acknowledge S. I. Bozhevolnyi and T. Holmgård for initial design inputs. This work was financially supported by the European Commission (PLAS-MOCOM Project EC FP6 IST 034754 STREP).

- ¹W. Barnes, A. Dereux, and T. Ebbesen, *Nature (London)* **424**, 824 (2003).
- ²T. Holmgård and S. Bozhevolnyi, *Phys. Rev. B* **75**, 245405 (2007).
- ³A. Krasavin and A. Zayats, *Appl. Phys. Lett.* **90**, 211101 (2007).
- ⁴R. Kiyan, C. Reinhardt, S. Passinger, A. L. Stepanov, A. Hohenau, J. Krenn, and B. Chichkov, *Opt. Express* **15**, 4205 (2007).
- ⁵B. Steinberger, A. Hohenau, H. Ditlbacher, A. Stepanov, A. Drezet, F. Ausseneegg, A. Leitner, and J. Krenn, *Appl. Phys. Lett.* **88**, 094104 (2006).
- ⁶B. Steinberger, A. Hohenau, H. Ditlbacher, F. Ausseneegg, A. Leitner, and J. Krenn, *Appl. Phys. Lett.* **91**, 081111 (2007).
- ⁷A. Bouhelier and G. Wiederrecht, *Opt. Lett.* **30**, 884 (2005).
- ⁸A. Hohenau, J. Krenn, A. Stepanov, A. Drezet, H. Ditlbacher, B. Steinberger, A. Leitner, and F. Ausseneegg, *Opt. Lett.* **30**, 893 (2005).
- ⁹M. González, A. Stepanov, J.-C. Weeber, A. Hohenau, A. Dereux, R. Quidant, and J. Krenn, *Opt. Lett.* **32**, 2704 (2007).
- ¹⁰J. Jägerskå, N. Le Thomas, R. Houdré, J. Bolten, C. Moormann, T. Wahlbrink, J. Čtyroký, M. Waldow, and M. Först, *Opt. Lett.* **32**, 2723 (2007).
- ¹¹I. Stefanon, S. Blaize, A. Bruyant, A. Aubert, G. Lerondel, R. Bachet, and P. Royer, *Opt. Express* **13**, 5553 (2005).
- ¹²A. Snyder and J. Love, *Optical Waveguide Theory* (Chapman and Hall, London, 1983).
- ¹³M. Nevière and E. Popov, *Light Propagation in Periodic Media, Differential Theory and Design* (Dekker, New York, 2003).
- ¹⁴L. Li, *J. Opt. Soc. Am. A* **13**, 1024 (1996).
- ¹⁵J. Goodman, *Introduction to Fourier Optics* 2nd ed. (McGraw-Hill, New York, 1996).
- ¹⁶E. Palik, *Handbook of Optical Constants of Solids* (Academic, New York, 1985).
- ¹⁷B. Hecht, H. Bielefeldt, L. Novotny, Y. Inouye, and D. Pohl, *Phys. Rev. Lett.* **77**, 1889 (1996).
- ¹⁸A. Drezet, A. Hohenau, A. Stepanov, H. Ditlbacher, B. Steinberger, N. Galler, F. Ausseneegg, A. Leitner, and J. Krenn, *Appl. Phys. Lett.* **89**, 091117 (2006).

Differential method for modelling dielectric-loaded surface plasmon polariton waveguides

S. Massenot*, J.-C. Weeber, A. Bouhelier, G. Colas des Francs, J. Grandidier, L. Markey and A. Dereux

*Institut Carnot de Bourgogne, UMR 5209 CNRS-Université de Bourgogne,
9 Av. A. Savary, BP 47 870, F-21078 DIJON Cedex, FRANCE
sebastien.massenot@u-bourgogne.fr*

Abstract: This paper demonstrates the efficiency of the differential method, a conventional grating theory, to investigate dielectric loaded surface plasmon polariton waveguides (DLSPPWs), known to be a potential solution for optical interconnects. The method is used to obtain the mode effective indices (both real and imaginary parts) and the mode profiles. The results obtained with the differential method are found to be in good agreement with those provided by the effective index method or finite elements. The versatility of the differential method is demonstrated by considering complex configurations such as trapezoidal waveguides or DLSPPWs lying on a finite width metal stripe.

© 2008 Optical Society of America

OCIS codes: (130.2790) Guided waves; (240.6680) Surface plasmons; (050.1960) Diffraction theory.

References and links

1. J.-H. Yeh and R. K. Kostuk , “Substrate-mode holograms used in optical interconnects: design issues,” *Appl. Opt.* **34**, 3152-3164 (1995).
2. S. H. Song, S. Park, C. H. Oh, P. S. Kim, M. H. Cho and Y. S. Kim, “Gradient-index planar optics for optical interconnections,” *Opt. Lett.* **23**, 1025-1027 (1998).
3. S. Kawai, “Handbook of optical interconnects,” Marcel Dekker Inc., New-York 2005.
4. J.-C. Weeber, Y. Lacroute, and A. Dereux, “Optical near-field distribution of surface plasmon waveguide modes,” *Phys. Rev. B* **68**, 115401 (2003).
5. T. Holmgard and S. I. Bozhevolnyi, “Theoretical analysis of dielectric-loaded surface plasmon-polariton waveguides,” *Phys. Rev. B* **75**, 245405 (2007).
6. A. V. Krasavin and A. V. Zayats, “Passive photonic elements based on dielectric-loaded surface plasmon polariton waveguides,” *Appl. Phys. Lett.* **90**, 211101 (2007).
7. B. Steinberger, A. Hohenau, H. Ditlbacher, A. L. Stepanov, A. Drezet, F. R. Aussenegg and J. R. Krenn, “Dielectric stripes on gold as surface plasmon waveguides,” *Appl. Phys. Lett.* **88**, 094104 (2006).
8. B. Steinberger, A. Hohenau, H. Ditlbacher, F. R. Aussenegg, A. Leitner, and J. R. Krenn, “Dielectric stripes on gold as surface plasmon waveguides: Bends and directional couplers,” *Appl. Phys. Lett.* **91**, 081111 (2007).
9. A. Hohenau, J. R. Krenn, A. L. Stepanov, A. Drezet, H. Ditlbacher, B. Steinberger, A. Leitner, and F. R. Aussenegg, “Dielectric optical elements for surface plasmons,” *Opt. Lett.* **30**, 893-895 (2005).
10. R. Kiyan, C. Reinhardt, S. Passinger, A. L. Stepanov, A. Hohenau, J. R. Krenn, and B. N. Chichkov, “Rapid prototyping of optical components for surface plasmon polaritons,” *Opt. Express* **15**, 4205-4215 (2007).

11. S. Massenot, J. Grandidier, A. Bouhelier, G. Colas des Francs, L. Markey, J.-C. Weeber, A. Dereux, J. Renger, M. U. González and R. Quidant, "Polymer-metal waveguides characterization by Fourier plane leakage radiation microscopy," *Appl. Phys. Lett.* **91**, 243102 (2007).
 12. E. Ameniogiannis, E. N. Glytsis and T. K. Gaylord, "Determination of guided and leaky modes in lossless and lossy planar multilayer optical waveguides: Reflection pole method and Wavevector density method," *J. Light-wave Technol.* **17**, 929-941 (1999).
 13. K. Kawano and T. Kitoh, "Introduction to optical waveguide analysis," Wiley, New-York (2001).
 14. M. Nevière and E. Popov, "Light Propagation in Periodic Media, Differential Theory and Design," Marcel Dekker Inc., New-York (2003).
 15. L. Li, "Formulation and comparison of two recursive matrix algorithms for modelling layered diffraction gratings," *J. Opt. Soc. Am. A* **13**, 1024-1035 (1996).
 16. P. Dawson, F. de Fornel and J.-P. Goudonnet, "Imaging of surface plasmon propagating and edge interaction using a photon scanning tunnelling microscope," *Phys. Rev. Lett.* **72**, 2927 (1994).
 17. S.-D. Wu, T. K. Gaylord, E. N. Glytsis, and Y.-M. Wu, "Three-dimensional converging-diverging Gaussian beam diffraction by a volume grating," *J. Opt. Soc. Am. A* **22**, 1293-1303 (2005).
 18. P. Berini, "Plasmon-polariton waves guided by thin lossy metal films of finite widths: Bound modes of asymmetric structures," *Phys. Rev. B* **63**, 125417 (2001).
 19. R. Zia , J. A. schuller and M. L. Brongersma, "Near-field characterization of guided polariton propagation and cutoff in surface plasmons waveguides," *Phys. Rev. B* **74**, 165415 (2006).
-

1. Introduction

Optical interconnects are promising for very short distance communications applications in their ability to support higher bandwidths than conventional metal wires or stripes used for carrying data from board to board, chip to chip or component to component within a single chip. Several solutions have been studied including free-space (substrate-mode holograms, grin substrates for example) [1, 2], plastic optical fibers or integrated optics [3]. In a logic of massive integration, the latter solution seems the more suitable especially if the refractive index contrast of the components is high. This can be obtained with Silicon On Insulator (SOI) technology or metal based components for example. If SOI is a more mature technology, metal based integrated components keep a potential practical interest since they can combine both the electronic and optical properties of metals by using surface plasmon polaritons (SPP).

If SPP are generally propagating along a metal / dielectric interface, it is preferable to confine them in the lateral direction by using metal stripes or dielectric loaded surface plasmon polariton waveguides (DLSPPWs) on a metal film [4, 5]. The latter are the more promising to confine SPPs in submicron structures hence their interest for large scale integration. The fact that DLSPP waveguides are intrinsically lossy due to the presence of the metal is not necessary an inconvenient if propagation lengths involved are not too high in order to keep a sufficient signal to noise ratio. It is well known that surface plasmon based devices are strongly polarization dependant and intrinsically not well suited for telecommunications applications. If low polarization dependence is a crucial parameter for transport and access networks due to the presence of polarization dependant losses, it is a criteria of lower relevance for on-board optical interconnects hence the possibility of using surface plasmon polaritons to carry the information.

DLSPPWs have recently rise a great interest [5–11], in this context, it is highly desirable to dispose of suitable tools for the design of the waveguides. In particular, it is of great importance to assess the fundamental properties of these waveguides such as the complex effective index or the cross-section mode profile from which the mode confinement, the propagation length (such waveguides are intrinsically lossy) or the optimum coupling conditions can be determined. The goal of this paper is to demonstrate the suitability of a diffraction grating theory known as the differential method to study DLSPPWs. In this respect, the differential method can be an easy-to-implement alternative to more conventional method such as FDTD or finite elements. In section 2, the principle of the differential method is reminded and the modifications allowing the study of DLSPPWs are presented. Next a comparison with results obtained for DLSPPWs

with other numerical methods, effective index (EIM) and finite elements (FEM), is given in section 3. Once the reliability of the differential method has been established for modelling DLSPPWs, the properties of waveguides having triangularly shaped profile or lying on a finite-width metal stripe are investigated in section 4.

2. Presentation of the differential method

2.1. Principle

The differential method belongs to rigorous vector diffraction theories. It allows the study of diffraction grating and more generally periodic media [14]. Several works during the last decade [15] improved the performance of this method especially in terms of convergence rate and numerical stability. The aim of this section is to remind briefly its principle.

The geometry of the problem to be solved is shown in Fig. 1. It is comprised of a modulated layer (e.g. the grating) and two homogeneous semi-infinite media (noted I and III in Fig. 1).

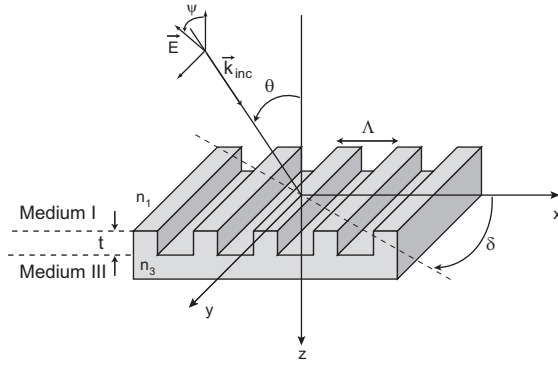


Fig. 1. Illustration of the notations used by the differential method for a lamellar grating in conical diffraction.

Λ is the grating period, θ the incident angle, δ the azimuthal angle ($\delta \neq 0$ corresponds to a conical diffraction regime), Ψ is the polarisation angle in the local system of axis of the field and t the grating thickness.

The method relies on the fact that the electromagnetic field is pseudo-periodic in the modulated layer. This field can Fourier-expanded and injected into Maxwell equations. From this, the field in the two homogeneous media on both sides of the grating can be written as plane-waves series called Rayleigh expansions. For example, the more general form of the E_y component of the field is given in Eq. 1:

$$E_y^{(i)}(x, y, z) = \sum_{m=-N}^N A_m^{(i)} \exp \left[i \left(k_{x,m}^{(i)} x + k_y^{(i)} y - k_{z,m}^{(i)} z \right) \right] + B_m^{(i)} \exp \left[i \left(k_{x,m}^{(i)} x + k_y^{(i)} y + k_{z,m}^{(i)} z \right) \right] \quad (1)$$

where $k_{x,m}^{(i)} = k_0 n_i \sin \theta \cos \delta + m \frac{2\pi}{\Lambda}$, $k_y^{(i)} = k_0 n_i \sin \theta \sin \delta$ and $k_{z,m}^{(i)} = [k_0^2 n_i^2 - k_{x,m}^{(i)} - k_y^{(i)}]^1/2$ (k_0 being the vacuum wavevector, $k_0 = 2\pi/\lambda$).

A_m and B_m are the Rayleigh coefficients and correspond respectively to the amplitudes of the downgoing and upgoing waves of the structure. N is the number of Fourier harmonics retained

for the calculation. The output of the differential method is the set of A_m and B_m coefficients in media I and III from which the diffraction efficiencies of the grating can be computed.

The computation of A_m and B_m coefficients requires the propagation of the electromagnetic field through the modulated region. Writing Maxwell-Faraday and Maxwell-Ampère equations leads to a linear system of coupled differential equations for the transverse components of the field E_x , E_y , H_x and H_y . By introducing the Fourier expansions of each field component (using the correct factorization rules [14]), one obtain a system that can be noted:

$$\frac{dF}{dz} = M(z)F \quad (2)$$

where $F = [E_m^x \ E_m^y \ H_m^x \ H_m^y]^T$, the size of this system is $4(2N+1)$ (subscript m corresponds to the m^{th} Fourier harmonic of the field component). Two different cases can be considered: if the profile of the grating is constant along the vertical coordinate (lamellar grating for example), the system 2 has constant coefficients and it can be solved by calculating the eigenvalues and eigenvectors of matrix M . In the other case, $M = M(z)$ and the system is solved by a standard routine for ordinary differential equations. An example is given in section 3.2.1 where a trapezoidal profile is considered.

Practically the computation of the unknowns of the problem (the Rayleigh coefficients) can be achieved by means of a shooting method leading to the scattering matrix of the modulated zone. At this stage it is worth to note that the use of a scattering matrix instead of a transfer matrix to describe the propagation of the electromagnetic field through the modulated zone is necessary to prevent numerical contaminations [15]. Once the scattering matrix of the grating is known, the electromagnetic field can be computed from the Rayleigh expansions in each homogeneous medium surrounding the structure. In addition, it is also possible to consider modelling of multilayer structures comprising either homogeneous (with arbitrary dielectric permittivity) or periodically modulated layers (having the same period as the initial grating).

2.2. Modelling DLSPPWs with the differential method

As reminded in the previous section, the differential method is dedicated to the study of periodic objects. However this method can also be used to investigate isolated structures provided that the grating period is large enough in order to avoid coupling effects between isolated elements. A typical DLSPPW structure is shown in Fig. 2(a). A dielectric waveguide is loaded on a metal layer. A TM polarized incident light field with a plane of incidence parallel to the longitudinal axis of the waveguide ($\delta = 90^\circ$) is used to excite the guided modes (see Fig. 2(b)), the incident wave comes now from the bottom of the structure for convenience contrary to Fig. 1). By adjusting the angle of incidence θ , the k_y component of the incident wavevector can be chosen such that it matches the phase constant of the considered mode allowing a selective excitation of either the modes guided within the dielectric stripe or the surface plasmon at the gold / air interface.

Because of the presence of the metal, the modes supported by DLSPPW are intrinsically lossy. For a full characterization of these modes, the complex effective index ($n_{\text{eff}} = v + i\alpha$) and the mode profile inside and outside the waveguide must be computed.

The real part v of the effective index can be obtained from the computation of the reflectivity of the structure versus θ . Indeed, as expected for an ATR (Attenuated Total Reflection) setup, the excitation of a guided mode manifests itself as an absorption dip into the reflectivity angular spectrum. The real part of the effective index is then computed from the angular position θ of the dip by $v = n_1 \sin \theta \sin \delta$ ($\delta = 90^\circ$ in this case).

For the computation of α , the most straightforward solution consists in searching for the poles of the scattering matrix of the structure. However, from a numerical point of view this

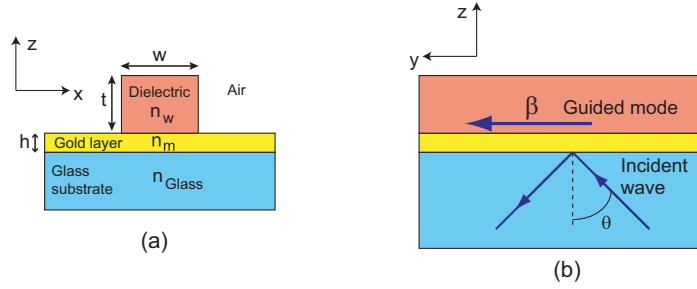


Fig. 2. Illustration of a dielectric loaded surface plasmon polariton waveguide, cross-section (a) and excitation scheme in ATR along the longitudinal axis of the waveguide (b).

technique requires the use of optimisation routines searching for complex roots that are rather time consuming. A less elaborate, but numerically more efficient solution to compute α is to excite the structure with a finite size beam and to determine the $1/e$ damping distance L_{spp} of the field intensity guided mode [16]. In this way, α is obtained according the relation $L_{spp} = \lambda/4\pi\alpha$. The excitation of the guided mode with a finite-size beam is performed by using a plane wave decomposition of a gaussian beam (see [17] for example). Expression 3 gives the amplitude of the Gaussian beam and its angular spectrum (plane wave) decomposition. For the numerical simulations, this decomposition is first restricted to a an interval of values for k_x and k_y and then converted to a discrete sum. Each plane wave of the decomposition is associated to a couple of angles (θ, δ) (see [17] for example).

$$E_{inc} = \exp \left[-\frac{x^2 + y^2}{w_0^2} \right] = \frac{w_0^2}{4\pi} \int \int \exp \left[-\frac{(k_x^2 + k_y^2) w_0^2}{4} \right] \exp [i(k_x x + k_y y)] dk_x dk_y \quad (3)$$

Then, the total field is reconstructed and the near field intensity above the waveguide (in the xy plane) can be computed. An exponential fit along the longitudinal axis of the waveguide with the formula $I = I_0 \exp \left(-\frac{y}{L_{spp}} \right)$ provides directly the damping distance (hence α). To simplify the problem and to reduce the computation time, it is possible to use a two-dimensional Gaussian beam instead of the expression given by Eq. 3 (the beam is infinite along the x-axis).

Concerning the mode profiles, they are calculated in the case of a single plane wave excitation with an angle of incidence $\theta = \arcsin \left(\frac{\Re(n_{eff})}{n_1} \right)$. The profiles are obtained by performing an additional integration of Maxwell equations by taking as initial values the field components obtained from solving the two-point boundary value problem. In addition to the mode profile in the cross-section, it is possible to obtain the confinement factor Γ of the considered guided mode (Γ is defined as the ration between the mode power in the waveguide and the whole space).

3. Application of the method to DLSPPWs

3.1. Rectangular profile

In this section, the fundamental mode supported by the DLSPPW structure shown in Fig. 2 is studied. It corresponds to the plasmon mode confined along the metal / dielectric interface [5] contrary to conventional waveguides where the energy is usually located near the center of the guide. Without dielectric, only the metal / air plasmon mode exists with an effective index

#93728 - \$15.00 USD

(C) 2008 OSA

Received 11 Mar 2008; revised 14 Jun 2008; accepted 15 Jun 2008; published 17 Oct 2008

27 October 2008 / Vol. 16, No. 22 / OPTICS EXPRESS 17604

To check the validity of the differential method, several profiles have been studied especially by changing the width of the dielectric waveguide (all the other parameters being unchanged compared the reference structure). The complex effective indices have been determined and compared to those obtained with FEM and the effective index method EIM [5], which is known to be an approximate method rather easy to implement [13]. The results are given in table 1 for both the real part of the effective index and the damping distance.

Table 1. Comparison of the results obtained by the differential method (DM) to those provided by the Effective Index Method (EIM) and Finite Elements (FEM) for waveguides of different widths ($t=600$ nm, $n_w = 1.535$, $n_m = 0.55 + 11.5i$ and $\lambda = 1.55 \mu\text{m}$)

Waveguide width w (nm)	200	300	400	500	600	700	800
$\Re(n_{eff})$ DM	1.064	1.133	1.198	1.250	1.291	1.323	1.348
$\Re(n_{eff})$ FEM	1.064	1.133	1.198	1.250	1.291	1.323	1.348
$\Re(n_{eff})$ EIM	1.094	1.162	1.221	1.268	1.305	1.334	1.357
$L_{spp} (\mu\text{m})$ DM	80.4	59.1	50.1	46.0	44.0	42.8	42.2
$L_{spp} (\mu\text{m})$ FEM	81.3	59.1	50.1	46.4	44.4	42.8	42.2
$L_{spp} (\mu\text{m})$ EIM	89.7	63.4	53.0	48.1	45.5	44.0	43.2

Good agreements are observed between the different methods, which validates the use of the differential method for studying DLSPPWs. The differences in the propagation lengths obtained with the differential method and FEM could be due to the quality of the exponential fitting, whereas the approximate nature of the EIM is at the origin of the discrepancies.

The intensity distributions of the guided modes in the cross-section of different waveguides are shown in Fig. 4. For these four waveguides, the fundamental mode is clearly confined at the metal / dielectric interface demonstrating the plasmonic nature of this guided mode. The confinement factor Γ has been calculated for each waveguide and the best value is obtained for the 600 nm \times 600 nm waveguide ($\Gamma=72.2\%$). The high field intensity observed at the top of the waveguide especially for the case 300 nm \times 300 nm is due to the discontinuity of the E_z component of the electric field and that the mode tends to behave as the plasmon mode of the gold / air interface.

3.2. Extension to other structures

3.2.1. Trapezoidal profiles

Practically, DLSPPWs are realized by UV or e-beam lithography and their profiles are generally not perfectly rectangular due to proximity effects or exposition parameters. It is then important to know the impact of the realistic waveguide profile on the propagation properties. The case of trapezoidal waveguides is considered first since it has been observed that such profiles can be obtained for specific exposure parameters in photolithography. It can be anticipated that the effective index of the modes supported by a trapezoidal DLSPPW will be different from that of a rectangular waveguide, however the impact of the waveguide geometrical profile change onto the damping distance of the guided mode is not straightforward and deserves a carefull examination.

Keeping the same notations as in Fig. 2, the trapezoidal profile of the waveguides is defined by two parameters w_1 and w_2 corresponding to the width respectively at the top and the bottom of the waveguide (Fig. 5). In all the subsequent calculations, w_2 is kept at 600 nm whereas w_1 is changed from 600 nm to 510 nm.

The real effective index and the damping distances of the fundamental mode supported by

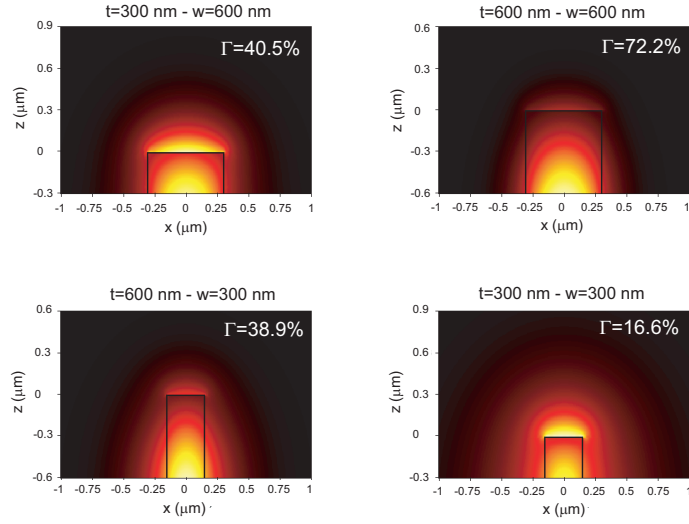


Fig. 4. Intensity mode profiles and confinement factors Γ for DLSPPWs having different structural parameters (thicknesses and widths).

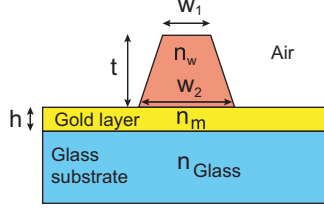


Fig. 5. Illustration of the studied trapezoidal DLSPPW.

each waveguide are given in table 2. For decreasing values of w_1 , a decrease of the real part of the effective index of the guided mode is observed. This can be understood from the reduction of the waveguide cross-section surface when decreasing w_1 . One can also observe that the change of waveguide geometry does not impact significantly the damping distance L_{spp} leading to the conclusion that tolerance exists on the fabrication parameters of the DLSPPW. This conclusion is supported by the results obtained in the case of a triangularly shaped cross-section waveguide obtained with $w_1=0$ nm and $w_2=600$ nm. In this case, the real part of the effective index of the mode is, as expected, significantly lower than for the rectangular profile ($n_{eff}=1.161$) whereas the damping distance is only reduced by 5% for the triangular waveguide ($L_{spp}=42$ μm) compared to the rectangular one. This rather weak impact of parameter w_1 onto the attenuation constant of the guided modes can be understood from the fact that the modes we consider originate from a SPP resonance and thus exhibit a field confinement at the surface of the metal. It is then likely that the properties of those modes are more affected by the metal / dielectric interface conditions rather than by a change in the volume of the waveguide.

3.2.2. Rectangular waveguide on a finite-width metal stripe

In this last paragraph, a situation that is of practical interest in the perspective of DLSPPW integration is investigated. A rectangular DLSPPW is lying onto a finite-width metal stripe

Table 2. Calculated effective index and propagation length for different trapezoidal DLSP-PWs with the differential method

w_1 (nm)	600	570	540	510
v	1.291	1.286	1.276	1.269
L_{spp} (μm)	44.0	44.6	45.4	46.02

instead of an infinitely extended thin metal film (see Fig. 6(a)). It has been already shown that plasmonic waveguides consisting of metal stripe have a cutoff width [18, 19]. The goal of this calculation is then to establish the minimum width of the metal stripe that does not degrade the propagation length of a given DLSPPW. To that aim the 600 nm \times 600 nm waveguide investigated in section 3.1 is considered. It is deposited on a metal stripe of different widths. From a numerical point of view, this situation is modelled with the differential method as a stack of two lamellar gratings having the same period. The propagation lengths obtained for metal stripe width ranging from 0.8 μm to 4 μm are plotted in Fig. 6(b) and it is shown that a metal stripe width of 3 μm is necessary to recover a propagation length similar to that of an infinite thin gold film (noted L_{spp}^∞ in Fig. 6(b)). This result can be attributed to the larger damping distance of the SPP modes supported by metal stripes compared to an infinite thin film and demonstrates unambiguously the plasmonic nature of the fundamental mode supported by the DLSPPW.

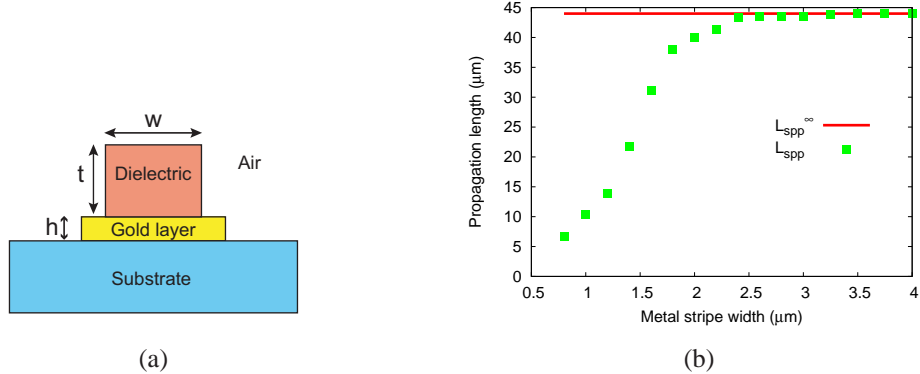


Fig. 6. (a): Illustration of a DLSPPW on a finite-width metal stripe; b: Evolution of the propagation length of the guided mode according the width of the metal stripe. The parameters are $w=600$ nm, $t=600$ nm and $h=100$ nm.

4. Conclusion

In summary, The suitability of the differential method for studying dielectric-loaded surface plasmon polariton waveguides has been demonstrated. This numerically effective method provides results in excellent agreement with those obtained with more sophisticated techniques, such as the finite element method for example. The versatility of the differential method has been used to investigate DLSPPWs with realistic profiles. In particular, it has been shown that the properties of DLSPPWs are not significantly modified by changing the geometrical profile of the waveguides, provided that these changes do not impact the metal / dielectric interface. In addition, it has been shown that when deposited on a metal stripe, the damping distance

of the DLSPPW modes depends drastically on the stripe width. This property that proves unambiguously the plasmonic nature of the DLSPPW modes must be taken into account for a practical implementation of such waveguides.

Acknowledgment

This work was financially supported by the European Commission (PLASMOCOM Project - EC FP6 IST 034754 STREP).